# DATING THE ATERIAN USING TECHNIQUES OF LUMINESCENCE DATING AND IMPLICATIONS FOR MAPPING THE DISPERSAL OF MODERN *HOMO SAPIENS*

## VOLUME I

**Laine Clark-Balzan**

Research Laboratory for Archaeology and the History of Art
Keble College
University of Oxford

Thesis submitted for the degree of
Doctor of Philosophy

Michaelmas Term 2012

# Abstract

The Aterian is a Middle Stone Age technocomplex that occurs throughout North Africa, typically identified by the presence of pedunculates. Due to widespread radiocarbon dating of contaminated samples, most Aterian sites are not well-dated. The use of more appropriate absolute dating techniques, including optically stimulated luminescence (OSL), has renewed interest in the Aterian technocomplex--several sites with remarkable behavioural innovations have been the source of surprisingly early ages.

This OSL dating project had two separate but complementary aims. First, OSL ages were obtained for samples from four significant Aterian sites (Taforalt, Dar es-Soltan I, Rhafas, and Chaperon Rouge II). High density sampling strategies were used in concert with independent dating methods and Bayesian modeling in order to obtain accurate and precise OSL ages. This study suggests that the Aterian technocomplex began by at least 70 ka in Taforalt, though Middle Palaeolithic archaeology exists earlier, and likely before ~100 ka at the coastal site Dar es-Soltan I. Single grain analysis was carried out for a previously dated sample from the open air site Chaperon Rouge II (Rhodes, 1990), and it indicated that the sample was likely highly bioturbated. Conversely, sediment trapped within a potentially Aterian human femur (Rhafas) seems to be less than 10,000 years old, though the bone itself may be older.

Second, the feasibility of imaging ultraviolet OSL via electron-multiplying charge coupled device (EMCCD) cameras was investigated. Key requirements for an OSL imager were evaluated, scientific cameras from several manufacturers were compared, and an optical system was created. Experiments have shown that a back-thinned, back-illuminated EMCCD camera is sensitive enough in the UV regime (365 nm) to successfully detect OSL emissions from natural quartz grains. Additionally, quantitative information can be derived from such image sequences and used to calculate equivalent dose.

# Acknowledgements

The process of creating a coherent DPhil project, and, indeed, a book, has been far harder and longer than I thought possible. I would like to thank everyone that has supported me through this process.

First, of course, must be my advisors, Dr. Jean-Luc Schwenninger and Professor Nick Barton. Thank you for helping me to love field work, and allowing me to explore sites containing thousands of years of shared human history. Thank you, too, for fostering the curiosity and care necessary to enjoy the precise lab-based processes necessary to unravel the true chronologies of such sites.

I am also deeply indebted to the Boise Fund, without whose support I would not have been able to complete this work. Thanks to your generosity, I have been able to both educate myself, and add a few small pieces to the colossal puzzle of human evolution.

To Dave Peat, the master of the lab, thanks for both teaching and listening! You taught me how to prepare samples, listened to me gripe about setbacks, and forgave me when I misplaced things in the carefully arranged laboratory. I'd also like to thank everyone else in the luminescence group, for discussions about theory and work and a few (too few!) nights out discussing everything else.

My methodological work is also indebted to a large number of people. Special thanks go to Hamamatsu, Andor, and QImaging for providing equipment for initial experiments, and Martin Franks for building a number of test rigs. More recently, many thanks go to Christian Bradley, who designed a lovely little instrument for our use.

Finally, and most of all, I appreciate the constant support of my family—my mom, all of my family in Tennessee and California, and especially Forrest Brennen. As hard as the last few years have been for me, I'm sure they have not been easy for you either (I'm certainly not the easiest person to be around when I'm stressed!). And I thank you for encouraging me to work, and sometimes to stop working and try to stay sane. Whatever sanity I still have is thanks to you!

# Table of Contents

# Chapter One

## *INTRODUCTION*

The advent of modern chronological methods has encouraged a paradigm shift in the study of deep prehistory. By means of chronological data, individual sites can be placed within larger cultural and climatic frameworks to contextualize and so augment excavation data. Databases of age information may be applied to test theories of human migration patterns, adaptations to different environments, climatic forcing, and technological transfers with time depths spanning centuries to tens of thousands of years or more.

The proliferation of chronological studies has of course increased the demand for accurate and precise dates. Inaccurate dates, in particular, may derail scientific thought in a number of related fields due to these productive interconnections. Therefore, modern chronological methods tend to emphasize the application of several independent dating methods in order to cross-check findings. However, it is necessary and desirable to have quality checks intrinsic to each method. This entails carefully validating assumptions and introducing reliability tests.

The ramifications of inaccurate chronologies have shaped the last half-century of North African archaeological research, specifically the convoluted history of the Aterian technocomplex. Known for their distinctive tanged lithics, Aterian sites have been assigned in succession to the Upper Palaeolithic (Reygasse, 1921; Caton-Thompson, 1952), Middle Palaeolithic ca. 20-40 ka (Camps, 1974), Middle Stone Age (N. Barton, pers. comm.) and are now thought to be at least twice as old and a potential proxy for the spread of modern *Homo sapiens* in North Africa (McBrearty and Brooks, 2000). Each of these intellectual transformations has been directly related to the application of a modern dating method, first radiocarbon dating and then (primarily) trapped charge dating.

The transition between radiocarbon and trapped charge dating studies in particular is an interesting study in the significance of inaccurate ages, the effects of which are still felt. Due to the vagaries of academic inquiry (see section 2.1.9), the corpus of accurate ages for the Moroccan Aterian is so far small. Therefore, the true significance of the Moroccan material, which includes relatively high numbers of *Homo sapiens* fossils and early evidence of symbolic thought, is still unknown. If the Aterian can indeed be linked with modern *Homo sapiens*, the Moroccan evidence will be vital.

Therefore, this study has two separate but complimentary aims. First, optically stimulated luminescence (OSL) was used to date samples from several Aterian sites, in order to expand the available chronological database. Samples have been measured via multi- and single grain methods from both inland (Taforalt, in the Beni Snassen Mountains, and Rhafas, in the Oujda uplands), and coastal sites (Dar es-Soltan I and Chaperon Rouge, both on the Atlantic Coast). The limits of current OSL dating, i.e. accuracy, precision, and quality control methods, are investigated by comparison with several independent dating techniques at Taforalt. In addition, a number of methods for enhancing age precision are applied, including the development of a micro-sampling technique, detailed dose rate calculations, and Bayesian modeling of final ages.

Second, a feasibility study was conducted to investigate the use of scientific imaging equipment for spatially-resolved optically stimulated luminescence (SR-OSL) measurements. Though scientists are now able to measure absorbed doses from disaggregated single grains, there is little understanding of how dose rates vary in natural sediment. The few studies that have been done suggest that spatial variation is likely for many natural samples, and that such effects may cause significant error in OSL ages calculated via standard methods (Nathan et al., 2003; Guerin et al., 2011; Mayya et al., 2011). Mathematical approximations based on the homogeneity of radiation in sediments can no longer be assumed correct, but should be tested for each sample. If spatial gradients in dose rate exist, it will be necessary to combine modeled dose rate information and measured equivalent dose for each grain in order to generate accurate ages.

SR-OSL involves making absorbed dose measurements via imaging or scanning techniques, so that measured values can be associated with particular emission sources in the sample. Development of this technique is the first step towards the more accurate and precise OSL dating methodology described above. Technological innovations in imaging, such as the recent invention of electron-multiplying charge coupled device cameras (EMCCDs), may permit practical SR-OSL dating studies.

This dissertation comprises eight chapters. Necessary background to both methodological and applied research is presented in Chapter 2. A discussion of the Aterian is presented first, including excavation findings, the history of applied chronological research, recently suggested implications for human evolution, and the importance of further investigation. Next, the fundamental mechanisms of OSL dating, development of methodology, and pressing need for new equivalent dose measurement technologies are discussed. Sampling methods are described for each of the four studied sites (Taforalt, Dar es-Soltan I, Rhafas, and Chaperon Rouge) in Chapter 3, and the standard OSL dating methods are outlined in Chapter 4. OSL analyses, final ages, and Bayesian models are presented in Chapter 5, organized by site.

Chapter 6 comprises a report on the development of an EMCCD camera-based SR-OSL measurement technique, including experimental results. The discussion (Chapter 7) integrates both OSL ages and the methodological research by examining the accuracy and precision of OSL ages, methods of determining OSL age reliability, and the implications for Aterian archaeology in Morocco. Finally, conclusions and suggestions for further work are presented in Chapter 8.

# Chapter Two

## *PROJECT BACKGROUND*

The combination of applied dating and methodological development in this dissertation has arisen naturally from the desire for accurate, precise, and comprehensive chronological databases in the archaeological record. The use of luminescence dating has revolutionized the study of the Middle Palaeolithic/Middle Stone Age in general (Feathers, 1996; McBrearty and Brooks, 2000; Henshilwood et al., 2002), and the Aterian specifically (see Section 2.1.9), but much more archaeological and chronological research is necessary. This chapter will describe the historical and theoretical background to both the archaeological study of the Aterian and the development of luminescence dating. As will become clear, each field of study is currently in a state of intellectual flux.

## 2.1 Archaeology

Though recent detailed studies have shed more light on the range of sites, regional settlement patterns, and resource utilization recorded in the Aterian (see Sections 2.1.2 through 2.1.10), there are a number of outstanding enigmas which will be outlined in this section. Among others, these include the geographical origins and spread of this Middle Stone Age (MSA)

culture, its connection to other technocomplexes in North Africa, and its relationship to the dramatically changing environment of the prehistoric Sahara. Additionally, the discovery of a number of hominin fossils associated with the Aterian combined with the use of more appropriate dating techniques has led to the intriguing theory that the Aterian may serve as a proxy for the spread of modern *Homo sapiens* into and through North Africa. For each issue to be satisfactorily resolved, any archaeological model must be tested against a secure chronological database.

### 2.1.1 Terminology

It has been argued persuasively that archaeological terminology should reflect the Aterian's African setting and affiliation (McBrearty and Brooks, 2000). Both "Middle/Upper Palaeolithic" and "Mousterian" were defined by European site characteristics, and it is unlikely that the same archaeological development would prevail on another continent with no proven interrelations. In addition, the Middle/Upper Palaeolithic transition of Europe implies by analogy the biological replacement of Neanderthal populations by modern *Homo sapiens* (Garcea, 2012). Though this same evolutionary replacement was originally identified in Morocco (Ennouchi, 1962; Arambourg, 1965), reexamination of the evidence shows that Neanderthals did not inhabit North Africa and were thus not responsible for North African "Mousterian" archaeology (see Section 1.7). This paper will therefore use the more accurate "Middle/Later Stone Age" (MSA/LSA), however, the term "Mousterian" will be retained due to the lack of a better alternative.

Another issue for which there is no satisfactory accord relates to the identification of Aterian sites and occupation layers. Bir el Ater, Algeria is nominally regarded as the type-site for the Aterian (Reygasse, 1921). The distinctiveness of the characteristic tang and the high number of surface scatters, however, has led to an implicit equivalence between the Aterian and tanged lithic artifacts. This rigid approach leads to anomalous cases such as that of El Guettar, Tunisia (Aouadi-Abdeljaouad and Belhouchet, 2012). Originally identified as Mousterian by the

excavator (Gruet, 1950), it was reclassified as Aterian by Clark (1982) due to the presence of pedunculates. Even now, it is unclear exactly what typifies an Aterian site besides pedunculates, or if the Aterian can be considered a coherent archaeological entity in itself. For example, based on excavations at Ifri n'Ammar and the alternating presence and absence of pedunculates, Richter et al. (2012) suggest:

> "The technology of tanging cannot be related to a certain epoch, technocomplex, culture, etc., as it frequently is, but, rather, represents aspects of mobility, subsistence strategies, and a reflection of cognitive skills related to contact and exchange of groups" (75).

Conversely, other groups undertaking syntheses of evidence in Morocco (Bouzouggar et al., 2007a; Bouzouggar and Barton, 2012) and Libya (Garcea and Giraudi, 2006; Garcea, 2012) have concluded that the Aterian is a coherent technocomplex, with recognizable settlement organization, a 'flexible' toolkit that includes but should not be defined solely by the presence of pedunculates, and early instances of intriguingly modern behavior.

For practical purposes, it is not within the scope of this thesis to reevaluate particular sites according to a standardized and modern definition of the Aterian. Instead, the author relies on the identifications made in cited studies and refers to the Aterian as a 'technocomplex' (i.e. multifaceted technology).

### 2.1.2 Range

Aterian sites and scattered tanged implements have been identified across North Africa, west from the Moroccan Atlantic coast (Ruhlmann, 1936; 1951), east through the Sahara (Reygasse, 1921; Cremaschi, 1996; Aouadi-Abdeljaouad and Belhouchet, 2012), and south into Niger (Clark, 1971) and Chad (Tillet, 1985). It should be noted, however, that the Aterian does not appear to be present at the well-known Libyan site of Haua Fteah (Moyer, 2003). To the east, the Aterian is found at least as far as Kharga Oasis (Caton-Thompson, 1952) and Bir Tarfawi (Wendorf et al., 1987) in the Western Desert of Egypt, but reports of finds in the Nile Valley and the Eastern desert have never been confirmed (van Peer et al., 1998). Selected sites are shown in Fig. 2-1.

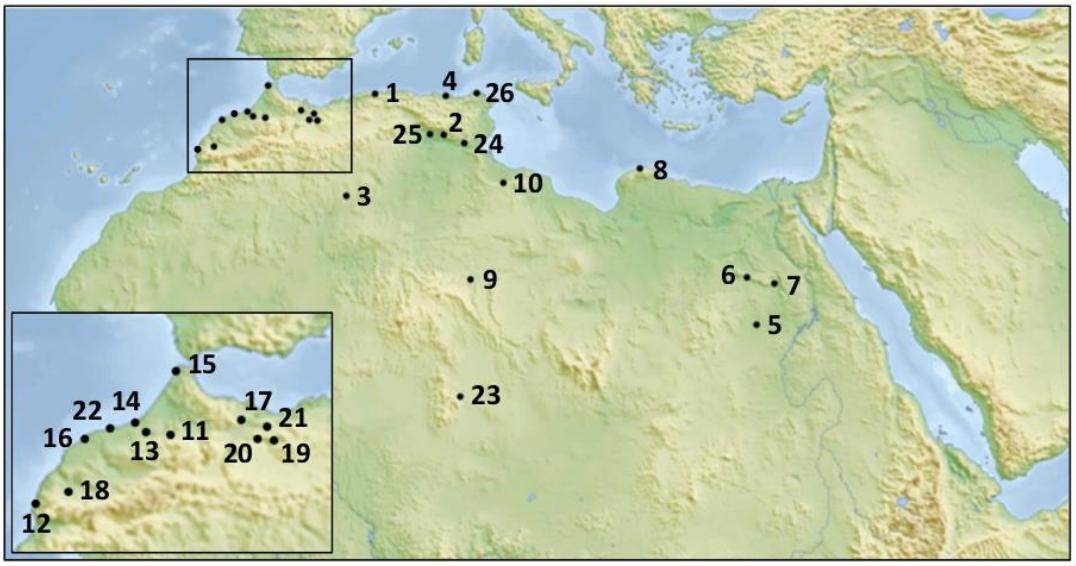


**Algeria**
(1) Bérard
(2) Bir el Ater
(3) Bou Hadid
(4) Herbillon

**Egypt**
(5) Bir Sahara
(5) Bir Tarfawi
(6) Dakleh Oasis
(7) Kharga Oasis

**Libya**
(8) Haua Fteah*
(9) Uan Afuda
(9) Uan Tabu
(10) Wadi Sel

**Morocco**
(11) Aïn Maarouf
(12) Bizmoune
(13) Chaperon Rouge I/II
(14) Contrebandiers
*Témara*
(14) Dar es-Soltan I/II
(15) El Aliya
(14) El Harhoura
*Zouhra*
(16) El Khenzira I/II
(14) El Mnasra
(17) Ifri n'Ammar
(18) Jebel Irhoud*
(19) Oued Thalma
(19) Rhafas
(20) Station Metéo
(21) Taforalt
(22) Tit Mellil

**Niger**
(23) Adrar Bous

**Tunisia**
(24) Aïn El-Guettar
(25) Aïn Métherchem
(26) Cap Blanc
(24) El Guettar

*Included for reference, not Aterian.

**FIG. 2-1.** Aterian sites (excluding Jebel Irhoud and Haua Fteah) discussed in Chapter 2.

The highest concentration of sites is in the Maghreb, particularly from the Atlantic Coast of Morocco and along the Mediterranean border of Algeria into Tunisia. Morocco itself contains at least 35 major Aterian sites, including four with both early MSA and Aterian levels (Bouzouggar and Barton, 2012). These sites comprise a unique archaeological record due to the high proportion that contain extensive, stratified Aterian occupation levels. These include El Mnasra (El Hajraoui, 1993; Nespoulet et al., 2008b), Ifri n'Ammar (Mikdad et al., 2004), El Aliya (Howe, 1967), El Khenzira (Ruhlmann, 1936), Dar es-Soltan I (Ruhlmann, 1951) and II (Debénath, 1972), Rhafas (Wengler, 1993), and Taforalt (Roche, 1972).

Both cave and open air sites are known for this technocomplex. Open air sites are typically associated with sources of water, such as the palaeolake at Adrar Bous, Niger (Williams, 1976), the artesian springs of Tunisia (Aouadi-Abdeljaouad and Belhouchet, 2012), both seasonal wadis and permanent springs in Libya (Barich et al., 2006; Garcea and Giraudi, 2006) and the previously mentioned Egyptian oases.

### 2.1.3 Origin

The origins of the Aterian are no more straightforward than any other aspect of this widespread industry, as the stratigraphic relationship between the Aterian and the Mousterian, its presumed predecessor, is unclear. In part, this ambiguity is due to the low ratio of Mousterian to Aterian sites. The Mousterian is virtually unknown from the Central Sahara (Clark, 1982). Even in the densely populated Maghreb, there are many fewer Mousterian sites, and most of these are inland (Balout, 1965). It is also rare for a stratified site to contain both Mousterian and Aterian archaeology. Of those that do, most evince a stratigraphic progression from Mousterian to Aterian, including Tit Mellil (Antoine, 1938), Cap Blanc (Vaufrey, 1955), Kharga Oasis (Caton-Thompson, 1952), Aïn Métherchem (Bordes, 1976-77), and the Moroccan sites of Taforalt (Roche, 1972), Rhafas (Wengler, 1993; Mercier et al., 2007), and Station Météo (Wengler, 1997). Ifri n'Ammar, however, does contain layers that alternate between presence and absence of pedunculates (Richter et al., 2010; Richter et al., 2012), and Aïn El-Guettar

yielded Aterian lithics >1.4 m below a Mousterian level (Aouadi-Abdeljaouad and Belhouchet, 2012).

The technological ancestry of the distinctive Aterian toolkit is likewise ambiguous. It may be the result of an indigenous North African adaptation, as originally believed by Caton-Thompson (1946). Conversely, elements may have been introduced from further south or via the Nile Valley (van Peer et al., 1998) or "humid corridors" through the Sahara (Osborne et al., 2008). One candidate for a possible sub-Saharan origin is the Lupemban of the Congo, due to claimed similarities between foliate types (Clark, 1964).

### 2.1.4 Lithics

Defining a standard lithics typology for the Aterian is confounded by the noted variability in assemblages (Ferring, 1975), varying standards used during surface collections and old excavations, and the lack of consensus about Aterian identification. Nevertheless, there do seem to be some identifiable themes. The Aterian is a Levallois-based (Caton-Thompson, 1946), Middle Stone Age industry, sharing some elements in common with the Mousterian (e.g. side-scrapers) and including more advanced 'Upper Palaeolithic' tool types (e.g. end-scrapers, burins, pedunculates, and bifacial foliates) (Fig. 2-2) (Bordes, 1976-77; Clark, 1982). Filling in more detail is problematic, largely because of the near impossibility of disentangling regional and chronological differences without secure dating.

The Moroccan Aterian is distinguished by several local characteristics. Overall, there is an increased prevalence of tanged lithics and decreased emphasis on foliates and endscrapers, which is notable even when compared with the nearby Algerian Aterian (Clark, 1982). This trend is not absolute, however, as both El Aliya and Taforalt have significantly higher numbers of bifacial foliates than tanged lithics (Bouzouggar et al., 2002; Bouzouggar et al., 2007b). It has been suggested that there is an inverse relationship between the presence of foliates and pedunculates (Bouzouggar and Barton, 2012). Blades and laminar flakes are also present, but seem to be restricted primarily to eastern and northern Morocco (Bouzouggar and Barton,

**FIG. 2-2.** A selection of characteristic Aterian lithics from Dar es-Soltan I, Morocco (courtesy of R.N.E. Barton). From left to right, these are a tanged point, Mousterian point, foliate, retouched blade, and another tanged point.

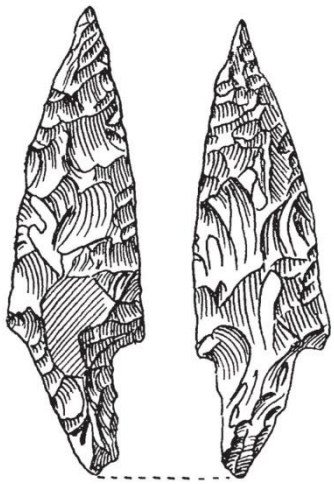

**FIG. 2-3.** A *Pointe Marocaine*, adapted from Caton-Thompson's (1946:117) Fig. 9.

**FIG. 2-4.** A possible Aterian bone tool from Layer 5, El Mnasra (after Nespoulet et al., 2008a: 372, Fig. 15).

2012). Finally, the *Pointe Marocaine* (Fig. 2-3), is an elongated, bifacial, tanged point that has so far only been identified in the Moroccan Aterian (Bouzouggar and Barton, 2012).

Some chronological shifts have been noted, such as the apparent increase in endscraper use through time (Ferring, 1975), the increased variation of tanged tool types (Barton et al., 2009), and a proposed movement from what might be thought of as a Mousterian-plus-tang ('proto-Aterian') to a fully-fledged technocomplex (Bordes, 1976-77; Mercier et al., 2007). However, most attempts to distinguish regional chronological trends from stylistic and typological variation have been essentially unsuccessful due to insufficient or inaccurate chronological data. For example, the identification of a 'late' Aterian at Dar es-Soltan I (Ruhlmann, 1951) has been repudiated by recent absolute dating (Barton et al., 2009).

Lithic raw materials in the Aterian consisted primarily of locally-derived flints and quartzites. These were often sourced up to ~20 km from the site, according to findings from Dar es-Soltan I (Barton et al., 2009), El Mnasra, and El Harhoura II (Nespoulet et al., 2008b). The extensive Aterian occupation layers at Dar es-Soltan I and El Khenzira II indicate a shift to higher quality raw materials over time (Caton-Thompson, 1946; Ruhlmann, 1936; 1951), though this may have been occurring at a local level only. Worked bone and ivory are rare, but present in some assemblages. Ruhlmann's (1951) lower Aterian assemblage at Dar es-Soltan I included two ivory items, a point and a *plaquette.* El Mnasra, too, yielded several bone objects (Fig. 2-4). These points and polishers were apparently produced from large herbivore ribs (Nespoulet et al., 2008b). Hematite has also been discovered in the form of a seemingly unique flake at Dar es-Soltan I (Ruhlmann, 1951; Barton et al., 2009).

The Aterian of the central Sahara and Egypt's Western Desert is similar to the Moroccan record in some respects, but local variations are significant. Aterian levels at both Adrar Bous and Dakhleh Oasis are distinguished from earlier MSA ones at the same sites by a marked increase in retouched pieces, in addition to the appearance of tangs and foliates (Clark, 1993; Hawkins, 2001). Hawkins suggests that this may be related to a shift from predominantly on-site

tool use to the creation of “mobile personal gear” (Hawkins, 2012: 170). Increased variation in both core preparation strategies and finished lithics have also been noted in the Egyptian Aterian (van Peer, 1991). Raw material selection, however, is very different. There is continuity in Egypt between the earlier MSA and the Aterian, with preference given to a local chert that was transported up to 40 km (Hawkins and Kleindienst, 2002). At Adrar Bous, however, a preference for locally sourced raw material in the earlier MSA was replaced by the exploitation of a silicified vitric tuff that was sourced nearly 300 km away (Clark, 1993).

Returning for a moment to the characteristic Aterian tang, its function and the reason for its widespread adoption is still under investigation. Similarities have been noted between tanged points and arrow-heads (Caton-Thompson, 1946), but a number of recent studies suggest that few, if any, points would have functioned as projectiles. Shea (2006) found that the tip cross-sectional area of Aterian tools was different than a comparative database of projectiles, which included arrowheads and dart tips. Garcea (2012) also found morphological differences between Aterian point proportions and known projectiles, noting that Aterian tangs were significantly shorter than one would expect for a hafted projectile.

Instead, the tang is likely to reflect significantly increased efficiency in both hunting and butchery due to hafting technology (Clark, 1982). Use-wear and fracture studies on pedunculates from Rhafas and Contrebandiers (Bouzouggar et al., 2007a) and Taforalt (Bouzouggar and Barton, 2012) indicate that tanged lithics were likely hafted and used in scraping and for butchery. Traces of working with both hard and soft materials were noted. Iovita (2011) also found evidence for hafting based on a morphometric study of over 500 tools from both surface and excavation collections. The studied pedunculates were probably retouched and re-sharpened sequentially from the tip, thereby conserving the tang, and preferentially used on one active edge as a knife or scraper. Some tanged points may have been hafted and used as thrusting spears, as Shea (2006) suggests.

### 2.1.5 Subsistence and environment

Periodic reviews have tended to place the Aterian within an environmental regime that was more humid than the present day but already deteriorating from a climatic optimum (Caton-Thompson, 1946; Ferring, 1975; Clark, 1982). Indeed, lithostratigraphic evidence from the Algerian coast (Roubet, 1972), central Tunisia (Bouchra et al., 1998), southern Libya (Cremaschi and Di Lernia, 1999; Cremaschi et al., 1998), Adrar Bous (Williams, 1971), and western Egypt (Smith et al., 2004; Hawkins, 2012) supports aridification during or immediately post-Aterian.

The available floral and faunal analyses of Aterian sites provide a bit more detail, hinting at probable regional and chronological variations. Geraads (2012) recently reviewed published faunal records for Northwest Africa, and found that there is evidence for significantly arid, steppe-like or sub-desertic conditions and local extinctions on the Moroccan Atlantic Coast during the Aterian. He suggests that the Algerian coast, in contrast, may have escaped the worst effects. Small mammal remains from the Moroccan Atlantic (El Harhoura II) also indicate alternating aridic steppic and wooded, humid periods during Aterian occupation, though further archaeological and chronological analysis is necessary to draw any conclusions about human adaptation to climate (Stoetzel et al., 2011). Faunal evidence is scarce for the interior of Morocco, but a sedimentological and charcoal-based study of Rhafas and Oued Thalma corroborate the suggestion of cyclical humid and dry phases during the Aterian (Wengler, 1993). Even less evidence exists further east, as no faunal remains have been found associated with Aterian layers at central Sahara sites such as Adrar Bous (Clark, 1993) or in Egypt's Western Desert (Hawkins, 2012).

Aterian subsistence strategies are relatively unknown. Based on extant collections, it is probable that hunting was opportunistic, and some scavenging may have occurred (Nespoulet et al., 2008b; Michel et al., 2009). Steele (2012), though, warns that the existing corpus of evidence from Morocco is not sufficient for firm conclusions of this nature. Garcea and Giraudi (2006)

propose that the new settlement patterns introduced by Aterians in the Jebel Gharbi (northwest Libya) would be linked with utilization of lacustrine resources. In a similar vein, Erlandson (2001) reviews evidence for aquatic adaptation by hominins, and notes that—if Aterian sites can be linked with early modern *Homo sapiens*—the evidence for a significant subsistence shift towards aquatic resources is marked.

### 2.1.6 Site organization and symbolism

Aterian sites have yielded a number of cultural innovations potentially indicative of behavioral modernity. *Nassarius* shell beads associated with Aterian layers have been identified at Taforalt, Ifri n'Ammar, Contrebandiers, Rhafas and possibly Bizmoune (Bouzouggar and Barton, 2012). Though the *Nassarius* from El Mnasra and four of five from Rhafas are not securely associated with particular levels (d'Errico et al., 2009), dating of secure contexts at Taforalt indicates their antiquity (Bouzouggar et al., 2007b). The Taforalt shells are perforated, and use-wear analyses indicate that they were likely strung as beads (Fig. 2-5). Additionally, both the beads from Taforalt and Ifri n'Ammar have red ochre residues (Bouzouggar et al., 2007b; d'Errico et al., 2009). Pigment has also been identified in the form of hematite blocks from Layer 7 of El Mnasra (Nespoulet et al., 2008b). The blocks appear to have been scraped, and were found near a quartzite nodule with pigment residue.

Various constructed stone features also appear during the Aterian. A 'cairn' comprising around 60 limestone spheres, ~4.5 to 18.0 cm in diameter, bone, and retouched tools has been excavated near the fossil spring at El Guettar (Fig. 2-6; Clark, 1982). Clark notes that other spheroids are known from Mousterian sites in the Maghreb, so this may be a haphazard collection rather than a built feature. Better evidence for intentional construction has been discovered at El Mnasra (Nespoulet et al., 2008b). Known features include fireplaces delineated by limestone slabs, and a large (~ 1 $m^2$ and 15 cm deep) collection of flat stones. Within a localized depression, nine layers of stones have been deposited in a mostly horizontal manner

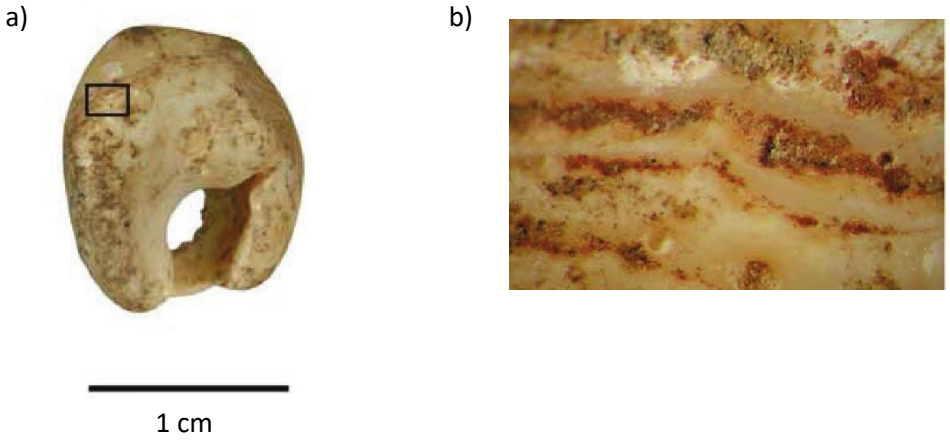


**FIG. 2-5.** Taforalt *Nassarius* gibbosulus bead (a) with close up of ochre residue (b) (adapted from Bouzouggar et al., 2007b: SI Fig. 9).

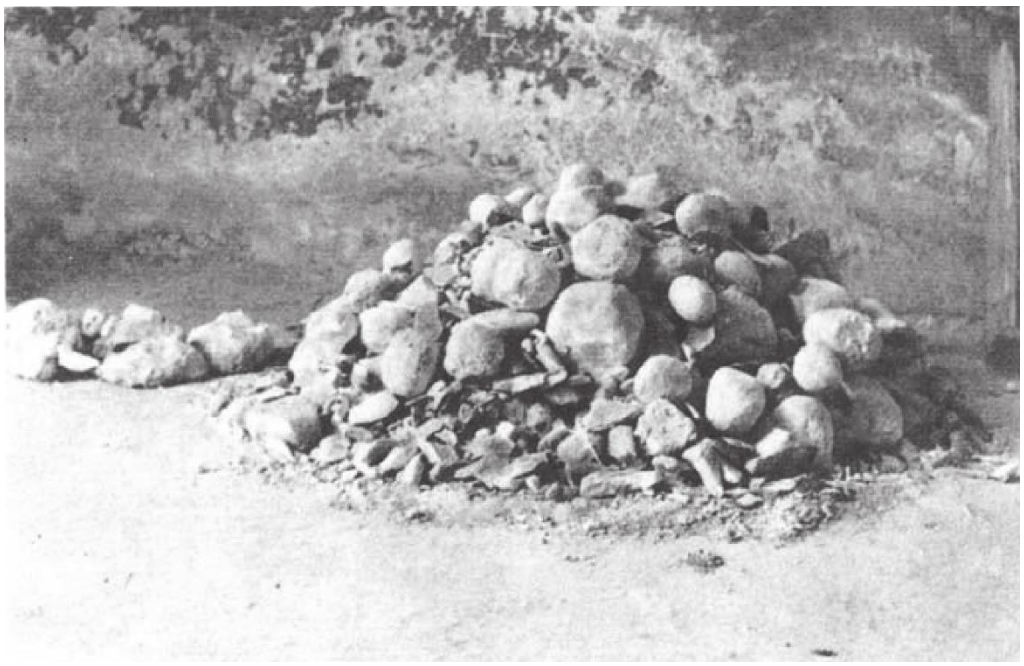

**FIG. 2-6.** Spheroids, bones, and tools at El Guettar (after Gruet and Zelle, 1955: 460).

with a few wedged pieces. The excavators did not find any artifacts within the feature, though there are many throughout the rest of the level.

### 2.1.7 Human fossils

Pleistocene-age *Homo sapiens* fossils have been discovered at a number of Moroccan sites (Hublin, 1992; McBrearty and Brooks, 2000):

- Contrebandiers (Témara)
- Dar es-Soltan II
- El Aliya (Tangier)
- El Harhoura
- Jebel Irhoud.

An earlier review by Debénath et al. (1982) also included a skull found by Bouiybaouiene in 1980 at Carrières de Skhirat. No other reference has been found that mentions this discovery, though a Neolithic necropolis was found at Skhirat (Lacombe et al., 1990) so this may be a misidentification.

Human fossils from the first four sites are believed to relate to Aterian archaeological levels; the Jebel Irhoud remains are associated with the Mousterian (Arambourg, 1965). Fossils were documented *in situ* at El Harhoura (Debénath et al., 1982) and Dar es-Soltan II (Ferembach, 1976). According to Debénath et al. (1982), the El Harhoura remains and the Dar es-Soltan remains were found within and below Aterian levels, respectively. Attribution to the Aterian is not always straightforward, though. Re-excavations in the case of Contrebandiers (Hublin, 1992) and chemical comparisons with fauna at El Aliya (Wrinn and Rink, 2003) have been necessary to affiliate fossil remains with particular archaeological layers. Together, the Moroccan Aterian fossils are a uniquely rich record of potentially early human evolution.

These incomplete skeletal elements have been included in a number of different classification schemes over time. Particularly notable is the early identification of a fossil from Contrebandiers as Acheulian, and the attribution of several to a Neanderthaloid variety as reviewed by Hublin (1992). Close comparisons of skull metrics (Hublin, 1992) and dental morphology (Minugh-Purvis, 1993) and development (Smith et al., 2007) have all pointed to an

inclusion of the listed fossils within modern *Homo sapiens*. In particular, Aterian tooth morphology is similar to that of MSA anatomically modern humans in both the Levant and East Africa, and Aterian teeth lack a number of characteristic Neanderthaloid features (Hublin et al., 2012). It is also sometimes noted that Jebel Irhoud skulls show a more archaic morphology than the presumed Aterian population (Hublin 1992; McBrearty and Brooks 2000).

### 2.1.8 End of the Aterian

From Morocco east through the Sahara, Aterian occupation often seems to have terminated during hyper-arid conditions, as previously mentioned. Stratigraphic and chronological evidence suggests the presence of a significant hiatus between the last Aterian and earliest Later Stone Age, known as the Iberomaurusian (Camps, 1974; 1975). Other sites, particularly those in the central Sahara, are not inhabited again until a Holocene humid phase or are never reoccupied (Cremaschi et al., 1998).

What happened to the potentially sizeable, or at least archaeologically prolific, Aterian population is still an open question. Connections between the late Aterian and industries in nearby regions have been suggested, but further analysis has negated most of these. Reygasse (1921) and Pericot (1942) noted striking similarities between Aterian and Spanish Solutrean bifacial points, however, mounting chronological evidence indicates that the last Aterian pre-dated the earliest Solutrean by a significant period (see Section 2.1.9.2 and discussion). Turning east, a small number of lithics from the Arabian peninsula were identified as potentially Aterian by McClure (1994). A more recent analysis suggests that the affiliation is not supported by modern comparative techniques (Scerri, 2012). Furthermore, no specifically Aterian influence has been noted in Middle Palaeolithic Levantine assemblages (Beyin, 2006), though lithic evidence for thrusting spears may suggest a commonality in the function of various tools between Africa and the Levant (Shea, 2010).

### 2.1.9 Dating the Aterian

Prior to the advent of radiocarbon dating, the Aterian, like all prehistoric evidence in the early 20th century, was dated according to relative stratigraphy within sites, faunal associations, stratigraphic correlations according to geological members across regions, and axioms concerning cultural evolution over time. While surface scatters in the Sahara initially pointed scholars towards a relatively moist period in Northern Africa, early theories about the temporal position of the Aterian were dependent upon the discovery of stratified sites in the central areas of its occurrence in Morocco and Algeria. The assignment of calendar dates was essentially pure speculation and only rarely attempted (Smith, 1935). Subsequently, the application of absolute dating techniques has significantly altered the place of the Aterian in North African prehistory.

#### *2.1.9.1 Relative dates*

Of the many stratigraphic and geomorphic associations that have been analyzed to provide a chronological framework for the Aterian, uplifted fossil beach sediments in Morocco (Lecointre, 1916) and Algeria (Roubet, 1972) have been some of the most extensively utilized. Unlike more localized formations, it was believed that these deposits could be rigorously correlated over extensive areas. Deposits were grouped into synchronous events based on altitude and lithology, often being incorporated into Mediterranean-wide chronostratigraphies. Such altitude-based correlations were instrumental in establishing that the Aterian post-dated the Mousterian (or Levalloiso-Mousterian), and that it was likely contemporaneous with the European Gravettian and Solutrian (Caton-Thompson, 1946: 119). The former conclusion is now questioned, and the latter is undoubtedly incorrect.

The rich Quaternary deposits in the Casablanca area of Morocco (Lecointre, 1916), which comprise a complex sequence of uplifted marine and aeolianite terraces, have been particularly fruitful for dating studies. Neuville and Ruhlmann (1941) identified four local beach relicts, which they correlated with similar features in the Mediterranean basin and associated with pluvial phases. These same deposits were the basis for Biberson's (1961) oft-cited cyclical

framework of marine and continental stages, and have been recently reanalyzed. It is now apparent that the Casablanca terraces record a complicated series of transgressions and lithification events that are not necessarily easily relatable to modern Marine Isotope Stages (MIS) (Lefèvre and Raynal, 2002; Texier et al., 2002). With direct relevance to early Aterian research, Texier et al. (2002) have noted that correlation of regional facies across hundreds of miles must be invalid due to the localized influences of sedimentation and tectonics. Nevertheless, pinning absolute ages to the Casablanca terraces offers significant promise for understanding local archaeology. U-series (Stearns and Thurber, 1965), OSL (Rhodes et al., 2006), and a number of other techniques (see review by Raynal et al., 2004) are clarifying the time-depth involved.

Relative dating efforts have more recently included the application of amino- and biostratigraphy. Both methods involve comparison of particular biological characteristics to a local reference database. Aminostratigraphy is based on the progressive racemization of amino acids in mollusk shells. The rate of enantiomer conversion after death depends strongly on temperature, therefore by itself it can serve only as a relative chronological marker (Mitterer, 1974). A group has attempted to pin racemization rates to radiocarbon dates on the Moroccan Atlantic coast, thereby providing a pseudo-absolute dating technique, but estimated ages have in general been too young for Aterian sites with independent age control (Occhietti et al., 1993; Raynal and Occhietti, 2012).

Biostratigraphy is simply the comparison of the faunal record to a reference collection; based on presence/absence of certain fauna and morphological variations within species, chronological sequences may be constructed. For example, the earliest (highest) of the Casablanca beach terraces is likely to be of Miocene age based on a micromammal study of Lissasfa Quarry (Raynal et al., 1999). Compilations of faunal remains for Late Pleistocene archaeological sites have generally focused on the presence/frequency of various macrofauna as palaeoenvironmental proxies (Ferring, 1975), which do contain implicit chronological

assumptions but were not generally used to assign a specific age range. Only rarely has fauna formed the basis of a more explicitly chronological analysis, as for the Mousterian site of Jebel Irhoud (Amani and Geraads, 1993). Microfaunal analyses, particularly tooth morphology, are almost unknown for most sites in Northwest Africa but may be productive in the future (Geraads, 2012).

#### *2.1.9.2 Absolute dating*

It is difficult to overestimate the importance of accurate chronological information to Aterian studies. By pinning archaeological successions to a fixed calendar, absolute chronologies allow testing of theories including development, succession, and association. Due to use of inappropriate chronometric techniques (radiocarbon), however, nearly the entire database of Aterian-related ages must be considered inaccurate. Partial adoption of more appropriate methods (trapped charge dating and U-series) resulted in a "bimodal" age distribution that skewed archaeological interpretations for more than two decades. This section reviews the scientific history of Aterian dating studies and their repercussions for current knowledge. Only chronometric data published prior to the commencement of this project has been included in this section; for all publications, see the Discussion (Chapter 7).

Radiocarbon

The advent of radiocarbon dating resulted in the first major paradigm shift in Aterian studies. Between the 1950's and the mid-1970's, radiocarbon dates from Aterian levels at Bérard, Dar es-Soltan I, and Taforalt demonstrated that the earliest Aterian was at least 30,000 years old (Camps, 1974; 1975). The push to date organic and carbonate samples from Aterian sites continued, so that by the mid-1980s dates from at least 10 major sites had been published (Table 1). These dates clustered between 20 ka and 40 ka, and this age range became the oft-cited, standard chronology (Debénath et al., 1986). It was also believed that the last major pluvial, i.e. a period of enhanced moisture, dated from this period (Alimen et al., 1966): the presence of the Aterian in North Africa was associated with evidence of the Ouljian marine

**TABLE 2-1.** Radiocarbon dates obtained from Aterian sites.

| Site | Lab Code | Sample Type | Context | Date (14C yrs BP) | Source |
|---|---|---|---|---|---|
| **Algeria** | | | | | |
| Bérard | I-3951 | Shell (marine) | Silt with Aterian | 31,800 ± 1,900 | Camps, 1974 |
| Bir el Ater | MC-657 | Shell (*Helix*) | Not given | > 35,000 | Ibid. |
| Bou Hadid | I-1761 | Not given | Upper lignite | >38,000 | Alimen et al., 1966 |
| | I-1787 | Not given | Lower lignite | >39,900 | Ibid. |
| Herbillon | MC-630 | Shell (marine) | Sandstone under Aterian | 25,850 ± 1,000 | Morel, 1974 |
| | MC-631 | Shell (marine) | Fossil beach | 31,450 ± 2,000 | Ibid. |
| | NY-170 | Shell (marine) | Base of offshore bar | 27,870 +800/ -700 | Hassko et al., 1974 |
| | NY-172 | Charcoal | Sandy deposit with Moustero-Aterian tools | 30,330 +1,870/ -1,520 | Ibid. |
| **Egypt** | | | | | |
| Bir Sahara | SMU-75 | Shell (Pelecypod) | Surface and Lacustrine Silt (B.S. 15) | 30,870 ± 1,000 | Haynes and Haas, 1974 |
| | SMU-79 | Shell (Gastropod) | Lacustrine Silt (B.S. 15) | >44,680 | Ibid. |
| | SMU-80 | Shell | Surface (B.S. 13) | 32780 ± 900 | Ibid. |
| | SMU-81 | Shell (Gastropod) | Pond marl (B.S. 16) | >41,450 | Ibid. |
| | SMU-82 | Shell | B.S. 16 | 40,710 ± 3,270 | Ibid. |
| | SMU-95 | Humates | B.S. 16 | 37,740 ± 1,980 | Close, 1980 |
| | SMU-108 | Humates | B.S. 16 | 28,000 ± 1,250 | Ibid. |
| | SMU-177 | Shell (Gastropod) | B.S. 14 | 44,190 ± 3,000 | Ibid. |
| | SMU-205 | Bone collagen | B.S. 14 | 26,530 ± 470 | Ibid. |
| | SMU-215 | Charcoal | B.S. 16 | 34,600 ± 970 | Ibid. |
| | SMU-218 | Humates | B.S. 16 | 33,080 ± 1,120 | Ibid. |
| Bir Tarfawi | SMU-214 | Not given | B.T.16 | 21,950 ± 490 | Ibid. |
| **Libya** | | | | | |
| Wadi Sel | Beta-167098 | Not given | Soil with Aterian | 43,530 ± 2,110 | Garcea, 2004 |
| **Morocco** | | | | | |
| Aïn Maarouf | GRN-3165 | Shell (Gastropod) | Above atypical Aterian | 32,000 ± 600 | Choubert et al., 1967 |
| Dar es-Soltan I | UCLA-678A | Charcoal | Lower Aterian (Layer I) | >30,000 | Berger et al. , 1965 |
| | UCLA-678B | Charcoal | Upper Aterian (Layer C2) | >27,000 | Ibid. |
| Dar es-Soltan II | TO-2045 | Shell (marine) | Aterian | 37,220 ± 290 | Occhietti et al., 1993 |
| | TO-2046 | Shell (*Helix*) | "migration dans Atérien" | 16,090 ± 90 | Ibid. |
| El Harhoura I | TO-2047 | Shell (*Helix*) | Aterian | 25,580 ± 130 | Ibid. |

**TABLE 2-1.** (Continued)

| Site | Lab Code | Sample Type | Context | Date (14C yrs BP) | Source |
|---|---|---|---|---|---|
| **Morocco (cont.)** | | | | | |
| Contrebandiers | Gif-2576 | Shell (marine) | Level 8 | 22,630 ± 500 | Delibrias et al., 1982 |
| | Gif-2577 | Bone | Level 8 | 12,500 ± 170 | Ibid. |
| | Gif-2578 | Shell (marine) | Level 9 | 35,200 ± 2,100 | Ibid. |
| | Gif-2579 | Bone | Level 9 | 14,460 ± 200 | Ibid. |
| | Gif-2580 | Bone | Level 10 | 12,320 ± 600 | Ibid. |
| | Gif-2581 | Shell (marine) | Level 11 | >40,000 | Ibid. |
| | Gif-2582 | Bone | Level 11 | 24,500 ± 600 | Ibid. |
| | Gif-2583 | Bone | Level 12 | 12,170 ± 160 | Ibid. |
| | Gif-2584 | Shell (marine) | Level 12 | >35,000 | Ibid. |
| | Gif-2585 | Carbonaceous earth | Level 12 | 23,700 ± 1,000 | Ibid. |
| Ifri n'Ammar | KIA-8823 | Charcoal | Lower OS | 38,740 +2,290/-1,780 | Richter et al., 2012 |
| | KIA-8824 | Charcoal | Lower OS | 51,480 +1,470/-1,240; 51,370 +2,490/-1,900 | Ibid. |
| Rhafas | GIF-6489 | Bone | Unit 2, Level 2 | 14,060 ± 150 | Mercier et al., 2007 |
| Taforalt | GIF-2276 | Shell (Gastropod) | Epipal./Aterian transition | >32,370 +2,470/-1,890 | Delibrias et al., 1982 |
| | GIF-2277 | Shell (Gastropod) | Level 19 | >34,550 +3,200/-2,280 | Ibid. |
| | GIF-2278 | Shell (Gastropod) | Level 21 | 19,080 ± 250; 19,400 ± 250 | Ibid. |
| | GIF-2279 | Shell (Gastropod) | Level 23 | >40,000 | Ibid. |
| | GIF-2280 | Shell (Gastropod) | Level 26 | 21,860 ± 330 | Ibid. |
| | GIF-2588 | Carbonaceous earth | Base of Level 19 | >40,000 | Ibid. |
| | GIF-2589 | Carbonaceous earth | Top of Level 19 | >40,000 | Ibid. |
| | Not given | Shell (marine) | Level 18 | 32,370 ± ? | Camps, 1974 cites Roche, 1970-71 |
| | Not given | Shell (*Helix*) | Not given | 34,550 ± ? | Ibid. |
| **Niger** | | | | | |
| Bilma | GIF-1788 | Limestone | Above Aterian | 33,400 ± 2,500 | Delibrias et al., 1974 |

transgression along the Mediterranean coast, and this high-stand was believed to correlate with the Neotyrrhenian, an interstadial during the Würmian glacial period (Debénath et al., 1986). As recently as 2007, the 20-40 ka chronology led to the exclusion of Aterian *Homo sapiens* fossils from a review of early modern human morphology:

> "Two other samples of Late Pleistocene remains are sometimes considered relevant; they are not. The northwest African Aterian remains (principally from Dar-es-Soltane and Témara) are regional late archaic humans, who present a complex mosaic of archaic and possibly derived modern human characteristics and may be too recent to be pertinent (Trinkaus, 2005)" (Trinkaus, 2007: 7367).

Some concerns about stratigraphic integrity and sample contamination, however, had been expressed relatively early. In two syntheses of radiocarbon dates, Close (1980; 1984) highlighted several anomalously young dates for the Aterian in Egypt and Morocco. Based on a detailed study of carbonate samples from the Western desert, she concluded that only two of twelve samples returned accurate, infinite ages (Close, 1980). Similarly, she regarded infinite ages for the Algerian Aterian as probably more reliable than finite, and dates younger than 30 ka from the Moroccan Aterian as suspect. Anomalously young dates could result from contamination of samples by younger carbon, particularly for shell samples and bulk charcoal (Close, 1980; 1984).

## Trapped charge dating and U-series

The earliest application of other absolute dating techniques occurred in both Egypt and Morocco nearly simultaneously, but resulted in two significantly different outcomes. In Egypt, different methods were introduced as a direct result of the previously discussed concerns about the suitability of earlier radiocarbon dates. By 1987, the Combined Prehistoric Expedition had abandoned radiocarbon dating for the Aterian of Egypt, stating:

> "The dating of the Middle Palaeolithic at Bir Tarfawi is more difficult. We know from earlier work that the entire sequence lies beyond the range of radiocarbon dating (F. Wendorf and Schild, 1980), and we are attempting to obtain chronometric dates from a suite of new, and still experimental, techniques. These include thermoluminescence dating of the sediments; uranium-series dating of ostrich eggshell, bone, tooth-enamel, carbonates and snail-shells; and electron-spin resonance and racemization dating of ostrich eggshell and tooth-enamel" (Wendorf et al., 1987: 62).

Indeed, two U-series dates on eggshell and an ESR date on tooth enamel placed the top of the palaeolake sequence (fifth and youngest cycle) at about 90 ka and the base of the fourth lake event beyond 125 ka. Aterian lithics had been found associated with even lower lake sediments. Therefore, Aterian samples were clearly much older than the radiocarbon dating limit, ~ 50-60 ka, which is imposed by the half-life of $^{14}C$. Not only was the 20-40 ka chronology extremely inaccurate, but other, more appropriate dating methods were necessary.

The first applications of TL and OSL in Morocco, however, seemed to support Debénath's chronology. The Aterian open-air sites, Chaperon Rouge I and II (CR I/II), are approximately 1 km apart on a plateau south of Rabat and share a similar stratigraphy. A burnt flint from the Aterian level at Chaperon Rouge I was dated directly by TL to 28.2 ± 3.3 ka (Texier et al., 1988). OSL ages from both sites bracket the Aterian presence: an age of 41.1 ± 6.1 ka was obtained for underlying sediment at CR II, and ages of 25.8 + 2.8/-3.3 ka (CR I) and 26.6 ± 2.9 ka (CR II) for overlying sediment (Rhodes, 1990). Similar ages were obtained at El Harhoura, namely a TL date of 41,460 ± 3500 BP and a gamma TL date of 32,150 ± 4800 BP (Debénath et al., 1986). Such ages fit nicely within the standard Aterian chronological framework (Debénath et al., 1986; Texier et al., 1988).

Due to these results, an intellectual schism of sorts formed. Radiocarbon dating continued to be the preferred methodology for the study of the Aterian in Morocco and Algeria throughout the 1990's, but it was completely abandoned for the Middle Palaeolithic in Egypt. Furthermore, the Egyptian evidence was compelling enough so that teams working in Libya also adopted TL and OSL dating strategies early. Thus dates from the cave sites of Uan Afuda and Uan Tabu in Libya support the existence of probable Aterian phases between 60,000 and 90,000 years ago (Cremaschi et al., 1998). In light of the dates from Egypt and Libya, and the likelihood of obtaining anomalous radiocarbon dates from material beyond the dating limit, all radiocarbon data for the Aterian in Morocco must be considered suspect.

Redating efforts in Morocco due to the accumulating evidence for the Aterian's antiquity have only recently begun. It seems, however, that the TL and OSL dates from Chaperon Rouge are not representative of the antiquity of the Aterian. ESR dates are available for four ungulate teeth from El Aliya, two of which derive from Aterian levels (Wrinn and Rink, 2003). Balancing various assumptions, including uranium uptake models and moisture contents, the authors proposed an age of between 35,000 and 60,000 years for Aterian levels. Similarly, a TL and OSL study of Rhafas cave placed the transition from Mousterian to Aterian between 60 and 80 ka, more likely between 70 and 80 ka (Mercier et al., 2007). At Taforalt, newer dating of the Aterian indicated ages of around 82 ka (Bouzouggar et al., 2007b), though as this thesis will show, earlier ages are more likely. Similarly, initial work at Dar es-Soltan I suggested an MIS 5 age for the earliest Aterian (Barton et al., 2009).

### 2.1.10 Implications and requirement for further research

The significance of Aterian sites for the early evolution of modern humans is a relatively recent idea (McBrearty and Brooks, 2000), largely because the dated sites had been considered much too young to be relevant. However, developments in absolute dating and fossil morphology have combined with more careful excavation strategies and a rethinking of the available evidence to suggest that not only may anatomically and behaviorally modern humans have produced the Aterian, but that this technocomplex may have mirrored a similarly early spread of anatomically modern humans into the Levant.

The precise behavioral characteristics that indicate "modernity" and even the utility of such a label are disputed, but it is clear from the previously discussed archaeological evidence that several important behavioral innovations appear during the Aterian. Pigment and bead use, which may point to the development of complex symbolism, both occur for the first time in Africa (d'Errico et al., 2009). Changing lithic styles and occupational patterns may be attributable to the emergence of more rigid types of socialization. McBrearty and Brooks (2000) have argued that the development of various stone point types corresponds with the

proliferation of regional styles in the Middle Stone Age. Increase in raw material quality occurs at many sites, and bone is used as a supplementary material. Moreover, as discussed previously, the development of a tang may also signal rising technological complexity with its implication for the use of hafting. The construction of hearths and other artificial stone features may indicate both features of permanence and the solidification of social boundaries, and are rarely, though sometimes (Hublin, 1992), found in Mousterian levels. Finally, there is some evidence to show that Aterian resource use, subsistence, and settlement patterns imply an increasingly sophisticated and efficient use of their natural environment (Garcea, 2004).

Defining the Aterian and placing it within the context of modern human evolution is hampered by the lack of secure dates, particularly in the key region of the Maghreb. A robust chronology is necessary to understand relationships between Aterian sites and the exploitation of the prehistoric environment, the relationship between the Aterian and the Mousterian, and the patterns and mechanisms of development for both anatomical and behavioral modernity.

## 2.2. Luminescence dating

When the theory and practice of luminescence dating are considered, the great value of OSL studies for Aterian chronology becomes apparent. It also becomes clear, however, that the next logical stage in development requires a step change in measurement and analysis techniques. This section first discusses the physical principles underlying luminescence dating, then describes the assumptions inherent in obtaining an age from laboratory measurements, and finally introduces a new approach to equivalent dose measurement.

### 2.2.1 Fundamental principles

Optically stimulated luminescence (OSL) and thermo-luminescence (TL) studies exploit the ubiquity of natural, solid-state dosimeters—quartz and feldspar crystals—for a variety of purposes. OSL and TL chronologies depend upon the measurement of absorbed dose from mineral crystals, from which age can be calculated if the average environmental dose rate is known. The basic relationship is then absorbed dose (‘equivalent dose’) divided by average dose

rate. Dating studies can be used to determine when a sediment was last exposed to sunlight, thereby providing chronological constraints for archaeological and geomorphological studies spanning the last 300,000 years or more (Aitken, 1998).

#### *2.2.1.1 Signal build-up*

To function as dosimeters for the natural world, quartz and feldspar crystals must begin in some base state, be physically modified by impinging radiation, and maintain the altered state crystals, however, have a variety of local and regional atomic defects that perturb this ordered structure and produce allowable energy levels within this range.

It is this band structure that provides a viable system for dosimetry via OSL or TL (Aitken, 1985; 1998). When energy is deposited in a natural crystal, electrons are ionized and enter the conduction band (Fig. 2-7, stage (i)). Some proportion of these electrons will lose just enough

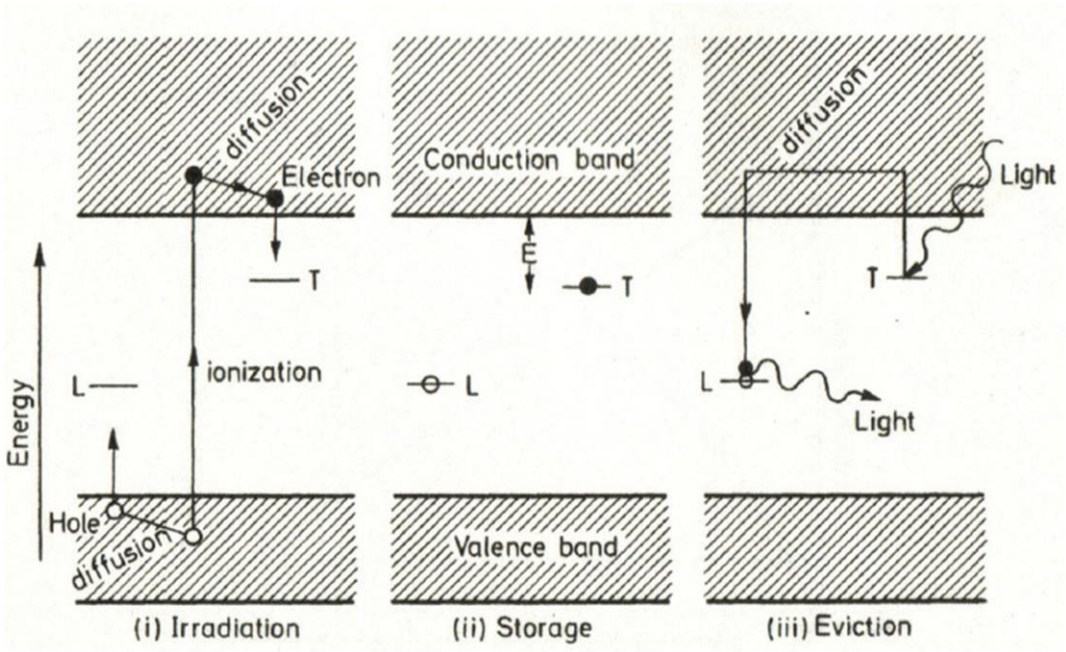


**FIG. 2-7.** Schematic of OSL process. Three stages (irradiation, storage, and eviction) are shown (after Aitken, 1998: 14).

energy to occupy energy levels ('traps') within the band gap. Once trapped, electrons must gain energy to re-enter the conduction band; the amount of energy required depends on the trap's position within the band gap. If the trap is deep enough, it may be difficult for an electron to obtain enough energy to be released. Hence such electrons are considered to be stored (Fig. 2-7, stage (ii)). When a crystal with trapped electrons is finally exposed to a source of such energy, however, these electrons will again enter the conduction band (Fig. 2-7, stage (iii)). Some of the evicted electrons will recombine at 'centers' in the band gap, releasing excess energy via photon emission ('luminescence'). The magnitude of the luminescence signal can then be used to determine the amount of radiation absorbed by the crystal.

Natural quartz and feldspar crystals have a relatively wide band gap, and certain characteristic traps and centers (Poolton et al., 1994; Preusser et al., 2009). Therefore, luminescence measurements on these minerals have been used to calculate absorbed energy (and therefore age) for a variety of archaeological and geological applications. Two of the most common uses of OSL and TL measurements are calculating the burial age of sediments (Murray and Roberts, 1997; Rhodes et al., 2006) and determining the time of firing of burned lithics (Wintle and Aitken, 1977; Richter et al., 2010; 2012) or pottery (Fleming, 1979; Zacharias et al., 2007). In both cases, background environmental radiation (described further in the next section) provides the energy source for electron ionization. For sediments, the luminescence signal in the crystals is reset by exposure to sunlight during erosion and transport ('bleaching'). After the mineral grains are buried, electrons are trapped and stored. If the sediment is collected without exposure to sunlight, these grains can be optically stimulated in a laboratory and the resultant luminescence signal used in age calculations (Aitken, 1998). Similarly, electrons are released by high heat in the case of burned lithics or fired pottery, thereby resetting the luminescence signal. Over time, electrons are trapped and stored, until the material is again exposed to temperatures on the order of hundreds of degrees (Aitken, 1985). Alternately, light can again be used to stimulate and evict these electrons (Thomas et al., 2008).

### *2.2.1.2 Ionizing radiation in the environment*

Luminescence dating requires knowledge of the average absorbed energy due to ionizing radiation per unit time. This dose rate is usually reported in units of Gray per millennium (Gy $ka^{-1}$, equivalent to milligray per year, mGy $a^{-1}$), where one Gray is an absorbed dose of one joule per kilogram of material (Rhodes, 2011). This unit does not include a biological effectiveness weighting. A typical median value is on the order of ~1 Gy $ka^{-1}$.

Four types of ionizing radiation occur in nature: alpha particles, beta particles, gamma rays, and cosmic rays (Attix and Roesch, 1968). The components and characteristics of each form of radiation are summarized in Table 2-2. Alpha, beta, and gamma radiation are produced by the decay of radioisotopes, predominantly those present in naturally occurring uranium, thorium, and potassium. Both thorium and uranium have decay chains that include a number of daughters, and emit all three types of radiation, whereas potassium decays directly to one of several stable daughters, and emits only beta and gamma radiation (Heath, 1997). Rubidium is chemically similar to potassium and also produces beta emissions, but natural amounts are typically negligible and so it is usually ignored in luminescence studies (Aitken, 1985). Each radioisotope produces a typical decay chain, with parents decaying into daughters via well-known patterns resulting in characteristic energy emission functions. An excess or deficiency of either a parent or daughter is termed disequilibrium and will result in a different and more complex, time-dependent energy function (see Section 4.3.2.3 for further discussion).

The relative importance of each type of radiation depends on the site. In general, however, for coarse (i.e. 90-300 μm diameter), etched quartz, absorbed dose is predominantly due to beta and gamma emissions (Aitken, 1998). Potassium usually contributes the majority of this environmental dose rate (Fig. 2-8). The cosmic ray dose may become significant when unusually low radioisotope concentrations are present, or if the sample has been close to the surface (e.g. within 30 cm) for most of its burial history.

**TABLE 2-2.** Types of ionizing radiation in the environment.

| Type | Description | Range (sediment) | Occurrence (decay or decay chain) |
|---|---|---|---|
| *Alpha* | Two protons + two neutrons (helium nucleus) | Several tens of micrometers in sediment | Th, U |
| *Beta* | Electron | Several millimeters | Th, U, K, Rb |
| *Gamma* | High energy electromagnetic radiation | Several tenths of a meter | Th, U, K, Rb |
| *Cosmic Rays* | Protons, alpha particles, electrons, gamma rays and other nuclei (in order of predominance) from sun and other sources; Interactions in atmosphere lead to the production of neutrinos (soft component) and muons (hard component) | Soft component: ~half meter<br>Hard component: Decreases exponentially with depth | --- |

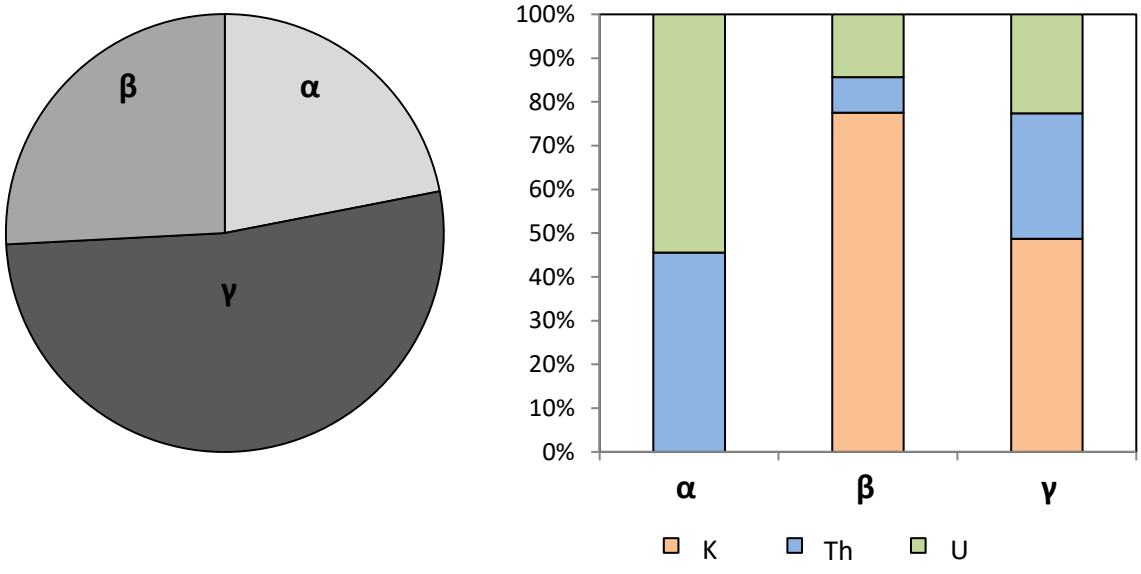


**FIG. 2-8.** Relative dose rate components for a typical soil with 1% potassium (K), 3 ppm thorium (Th), and 1 ppm uranium (U). a) Proportion of total dose rate, 1.93 Gy $ka^{-1}$, by radiation type (excluding cosmic dose). Alpha dose rate is usually negligible due to HF etching. b) Proportion of each radiation type by radioisotope. Values used are given in Table 2.1 (Aitken, 1998: 44).

The effective range of each type of radiation is controlled by how it interacts with matter and the emission energy (Attix and Roesch, 1968). These ranges have various implications for dose rate calculations. Both alpha and beta particles have short enough ranges that radiation calculations tend to be made from bulk radioisotope concentration measurements (Aitken et al., 1985; Brennan and Lyons, 1989). Additionally, attenuation in mineral crystals must be considered during dose rate calculation (Mejdahl, 1979). Alpha particles in particular have such a short range that entire alpha tracks can be absorbed by mineral grains greater than a few tens of micrometers in diameter ('coarse grains'). Therefore, a grain in sediment or a solid matrix (pottery or rock) absorbs energy from alpha particles due to both internal and external sources (Brennan et al., 1991). External alpha particles may contribute a significant dose, however, only the outer rind of the grain will be so affected and this may be mostly removed during sample preparation by hydrofluoric acid (HF) etching. The much longer range of gamma radiation means that all sources within a sphere ~30 cm in diameter around a luminescence sample must be considered for accurate dose rates. Therefore, direct measurement via on-site gamma spectrometry is generally preferred to calculation (Guérin and Mercier, 2012). Finally, the range of cosmic rays is so large that the only calculation requirement is attenuation through overburden over the sample.

The cosmic ray dose rate depends on the geomagnetic latitude and altitude of the site, and the thickness and average density of the sample's overburden (Prescott and Stephan, 1982; Barbouti and Rastin, 1983; Prescott and Hutton, 1994). Both hard and soft components may be calculated, though the relatively quickly-attenuated soft component is often negligible for buried samples. The penetrating hard component, though, will usually contribute at least a few percent of the dose rate. The difference in attenuation of the two components is immediately apparent when component dose rates are calculated as a function of depth over a range of densities (Fig.

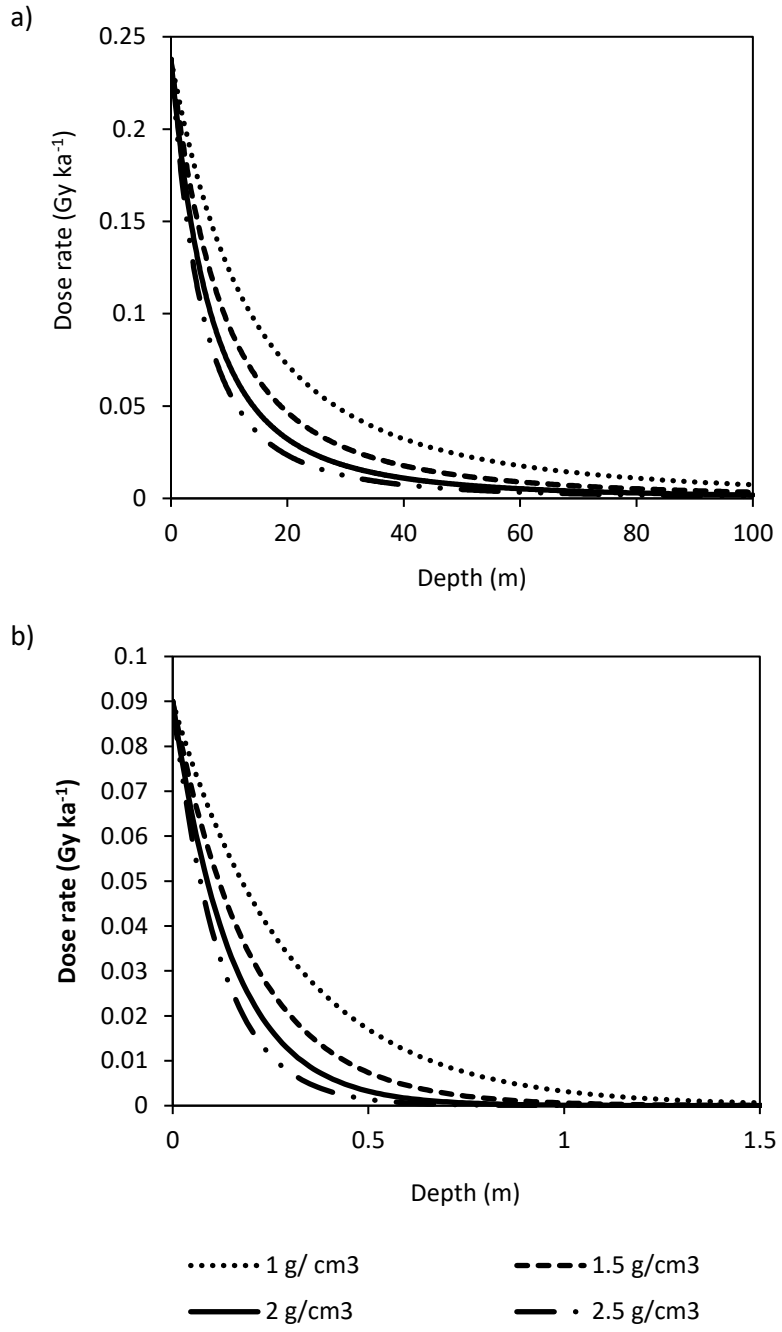


**FIG. 2-9.** Attenuation of cosmic rays with depth, both hard (a) and soft (b) components for a variety of sediment densities. These calculations were made in accordance with the methods described in Chapter 4.

2-9; see Section 4.3.1.4 for equations used to generate values). At the surface, the soft component contributes 30.0% of the total cosmic dose (0.328 Gy $ka^{-1}$), but by 1 m deep in very low density sediment (1 g $cm^{-3}$), the total cosmic dose rate has dropped to 0.225 Gy $ka^{-1}$ (68.6% of the surface dose rate), and the soft component contributes only 1.61%. One meter of rock (2.25 g $cm^{-3}$) sees the total cosmic dose rate fall to 0.203 Gy $ka^{-1}$ (62.0% of the surface rate), with the soft component negligible at 0.0277% of the total.

### 2.2.2 Factors affecting equivalent dose OSL ages

Via technological advances (see Section 2.2.2.1) and theoretical developments (Sections 2.2.2.2 and 2.2.2.3) in OSL dating, it is now clear that a number of factors influence the measured equivalent dose distribution of mineral grains in sediments. These include intrinsic physical processes in the crystal (Thomsen et al., 2012), experimental variation during laboratory measurements (Thomsen et al., 2005), microdosimetry in the sediment (Kalchgruber et al., 2003; Nathan et al., 2003), physical mixing by processes such as bioturbation (Bateman at al., 2007a; 2007b), and partial bleaching during deposition (Singarayer et al., 2005; Prescott et al., 2007).

Therefore, though the fundamental age equation is still essentially correct, that is:

$$Age = \frac{D_e}{\dot{D}}$$

where $D_e$ is the equivalent dose and $\dot{D}$ is the average dose rate for the sample, the essential value $D_e$ may not be related to the measured equivalent dose distribution in a completely straightforward manner. A number of recent publications (see Section 2.2.2.2) have documented equivalent dose distributions that arise from particular sedimentological or dosimetric processes, but multiple processes (with very different implications for the final OSL age) may yield nearly identical distributions. This can be a major roadblock for luminescence studies, as determination of burial age is sometimes dependent upon correcting for a number of confounding factors.

This section will describe the equivalent dose measurement advances that enabled the discovery of sediment complexity, factors that affect equivalent dose distributions and therefore

dating, and statistical models that are used to correct for some of these influences. Finally, a new research direction (Sr-OSL) is suggested that may help resolve some of these issues.

#### *2.2.2.1 Methodological developments*

It is primarily the increasingly detailed measurement of equivalent dose that has driven most recent OSL advances, by revealing the complexities of natural sediment. Individual mineral crystals can vary not only in intrinsic brightness and radiation sensitivity, but also in absorbed dose. The first luminescence dating methods were multiple aliquot techniques, which involved measuring several dozen subsamples ('aliquots') to obtain a single equivalent dose (Zimmerman, 1971). These methods circumvented the minerals' tendency to change dose sensitivity during measurement, as each aliquot was stimulated and irradiated only once. However, the intrinsic variation between aliquots led to high scatter and imprecise equivalent doses (Murray and Olley, 2002). The more recent development of the now standard Single Aliquot Regeneration (SAR technique) measurement protocol has enabled the calculation of equivalent doses from single aliquots and even single grains (Murray and Wintle, 2000). The primary innovation of the SAR technique is a normalization method that corrects emission intensity for sensitivity changes, by interpolating repeated irradiations into the measurement cycle. The advent of SAR allowed luminescence practitioners to more accurately gauge the absorbed dose distributions in sediment, and gave rise to new types of study in which the effects of aliquot size on equivalent dose were investigated (see review by Murray and Olley, 2002).

At approximately the same time as the development of SAR, attachments specifically dedicated to single grain measurement were developed (Duller et al., 1999). With laser spot illumination, one hundred individual grains could be measured in essentially the same amount of time as a single 'multigrain' aliquot could be measured. Though in practice only a few percent of measured grains may be sensitive enough to yield equivalent doses, this equipment dramatically increased data collection capabilities. A single grain study of a single sample may now generate hundreds of equivalent dose estimates (Jacobs et al., 2011; 2012). The practical effect of such

detailed studies has been to emphasize the complexity of the record left by natural sedimentary processes. Over a decade has passed since the first published study to utilize single grain measurements, and much of the intervening research has attempted to define the various factors that may offset or change the distribution shape of the absorbed dose distribution.

#### *2.2.2.2 Controlling variables for equivalent dose distribution*

While absorbed dose distributions can be reported for either single grain or multigrain studies, multigrain aliquot distributions convolve dose response curve shape and grain brightness so that determining the underlying single grain dose distribution may be very difficult. Even if only a few tens of grains are measured at a time, 'phantom' dose components may emerge in the distribution (Arnold et al., 2012), thereby making it difficult to determine the absorbed dose distribution arising from a suggested influence.

If one therefore considers single grain studies only, equivalent dose populations are often described with several of the following values:

1. Minimum or central tendency values, for assumed single or multimodal populations: These values are calculated via several statistical models described more fully in section 4.2.3.3.
2. Overdispersion: a measurement of equivalent dose scatter beyond that which can be explained by error values (see section 4.2.3.3).
3. Skewness (or weighted skewness),
4. Kurtosis (or weighted kurtosis).

Any given distribution is the convolution of a number of factors, each of which will affect some of these distribution parameters to a greater or lesser degree. The known laboratory-induced, intrinsic crystalline, and natural sedimentary processes that lead to these characteristic distributions are summarized here.

The basic processes of measurement and calculation of equivalent dose themselves may affect several distribution characteristics, primarily overdispersion but also calculations of

skewness and multi-modality. Thomsen et al. (2005) estimate that nearly 9% of overdispersion in a conventionally-measured single grain equivalent dose distribution is due to minor experimental variations, including spatial heterogeneity of beta sources, grain movement between measurement cycles, illumination power, and variations in timed processes. A number of other published relative overdispersion values for single grain measurements of γ-irradiated samples, collated by Thomsen et al. (2012), range from 7% to 12%. The sensitivity of individual PMT's has also been related to increased overdispersion values for single grains and single aliquots (Adamiec et al., 2012). The authors of this study caution that not correcting for such effects may yield incorrect component groupings when using statistical models such as the finite mixture model (see Section 2.2.2.3), and the combination of measurements from various machines may introduce patterns in the measured data that are not present in the underlying absorbed dose distribution (Adamiec et al., 2012). Finally, equivalent dose error tends to increase with equivalent dose, as the decreasing slope of the dose response curve results in a larger range of possible equivalent doses for a given relative signal error. Galbraith (2003) notes that a simple statistical implication of this tendency is that the larger values of equivalent dose will therefore tend to scatter more. Therefore a simple histogram of equivalent dose values will tend to be positively skewed, even in the absence of other effects.

As yet undetermined physical properties of the measured crystals also seem to control measured distribution parameters. Thomsen et al. (2012) found that distributions of recovered dose values from γ- and β-irradiated grains were positively skewed (weighted skewness), with statistical significance controlled by the value of the weights used. Their experiments indicate that relative overdispersion values are dependent upon a sample's thermal history, grain brightness, and absorbed dose. Indeed, they suggest that the magnitude of these effects may be sufficient to explain the full range of overdispersion values determined from well-bleached, homogeneous natural samples.

Natural sedimentary processes including partial bleaching, bioturbation, and microdosimetric effects may create skewed distributions with high overdispersion. Partially bleached grains are those deposited and covered by further sediment before the trapped electron signal from a previous burial history can be completely reset. If these grains are then dated, the obtained age will be older than the 'true' age. Partial bleaching may occur in light-restricted depositional regimes, such as fluvial environments ( Singarayer et al., 2005; Fiebig and Preusser, 2007) or caves and rock shelters (Roberts et al., 1999; Prescott et al., 2007). Deposits thought to have been partially bleached are highly skewed with multiple high dose grains and large overdispersion values (Olley et al., 1999; Bailey and Arnold, 2006; Ballarini et al., 2007).

Even if all grains have been fully bleached at burial, mixing processes can complicate equivalent dose interpretation. Bioturbation involves the transport of grains by biological means including animal or molluscan burrowing and root growth. Though vertical transport of grains can occur in either an upward or downward direction (Bateman et al., 2007a), bioturbation is often marked by the incorporation of younger grains. Where known bioturbation has occurred, equivalent dose distributions often include zero-dose grains (in sedimentary layers near the present surface), have overdispersion values of up to 200%, and are likely to be skewed and/or multimodal (Bateman et al., 2007b).

Finally, the heterogeneity of natural radiation fields can be reflected in complex distributions. The range of beta radiation (several millimeters) is short enough that grains within a suitably heterogeneous sample may experience variable dose rates. This effect is known as "microdosimetry," and multiple studies have theorized about its role in producing anomalous equivalent dose distributions ( Murray and Roberts, 1997; Lomax et al., 2007; Jacobs et al., 2008b). Standard methods for calculating beta dose rates in OSL, however, are not suitable for determining the presence or degree of microdosimetry (see section 4.3.1.2).

Only a handful of studies have either physically tested or modeled the equivalent dose distribution effects of microdosimetry in sediments. Kalchgruber et al. (2003) was a limited

study in which grains of a synthetic dosimeter, aluminum oxide, were distributed within loess to directly measure microdosimetric variation. Results suggested that scatter equivalent to 18% of the absorbed dose could be attributed to such variations, mostly due to the high carbonate content (25%) of the loess. Nathan et al. (2003) implemented a wide-ranging study involving both numerical modeling and experimental verification of results, via the creation of artificial sediments with a range of heterogeneous compositions. Both Monte Carlo models and measurements of absorbed dose from aluminum oxide grains proved that mean absorbed dose varied significantly with sediment geometry, and the distribution of doses to individual grains could be highly asymmetric. These results led the authors to warn against simplistic and commonly applied equivalent dose models in which high or low dose grains are excluded from analysis. Interestingly, though a number of luminescence studies have attributed multi-modal equivalent dose populations to microdosimetry, Nathan et al. (2003) could not reproduce such effects. Mayya et al. (2006) and Guérin et al. (2012) also reported asymmetric distributions in quartz grains resulting from the presence of potassium feldspar grains in a matrix. Therefore, the minimal evidence available so far indicates that equivalent dose distributions may be both shifted and skewed by various beta dose microdosimetry, in some cases significantly.

#### *2.2.2.3 Dating studies: Equivalent dose interpretation and influence on ages*

It is evident that a number of different effects can produce the same equivalent dose distribution in a sample. As it is not possible to deconvolve sedimentary and laboratory processes from distribution characteristics, OSL practitioners must rely on a hierarchy of possibilities and analyze each site individually, e.g. Jacobs et al. (2008).

Current OSL practice requires that a particular dose component is extracted from the distribution. Three primary statistical models have been widely adopted for this purpose, namely the central and minimum age models (Galbraith et al., 1999), and the finite mixture model (Galbraith and Green, 1990; Roberts et al., 2000). The mathematical description of each model is given in section 4.2.3.3. For this discussion, it is relevant simply that the central age

model assumes the equivalent doses correspond to a log-normal distribution with a desired central equivalent dose value, the minimum age model assumes a log-normal (or normal) distribution truncated at some minimum point and extracts this truncation value, and the finite mixture model determines central values for a number of mixed grain populations.

Model choice is an extremely important part of the analysis, as application of each model usually results in considerable differences to the final date. Though various model decision trees have been suggested (Bailey and Arnold, 2006; Arnold et al., 2007), the individuality of each site and sample is such that choice of the most appropriate age model for a site is controlled by the investigator's interpretation (Galbraith and Roberts, 2012). It can easily be seen that if a model is chosen which does not correspond to the correct physical process, a precise but inaccurate OSL age may be obtained. For example, a simple case would be the sampling of a cave sediment that returns a highly skewed, high overdispersion, single grain population. It is likely in this scenario that partial bleaching might be suspected, and therefore the minimum age model would be used. If, however, the distribution is actually the result of microdosimetry or bioturbation, the resultant OSL age would underestimate the true age significantly. With standard OSL techniques, it would be extremely difficult to determine that such an error had occurred. Though this stage in the analysis may introduce the largest uncertainty into current OSL ages, there is no satisfactory suggestion for formally incorporating these unknowns.

#### *2.2.2.4 The impetus for methodological research (SR-OSL)*

Therefore, though a number of studies have shown OSL ages to be accurate within uncertainties when compared to independent dating techniques (Olley et al., 2004a; Magee et al., 2009), it is clear that in some circumstances OSL ages can be inaccurate for reasons that are difficult to prove unambiguously (Almond et al, 2007; Owen et al., 2007; Lowick et al., 2010). Moreover, identifying how mineral grains are situated in the microstructure of sediments is likely to help improve both the accuracy and precision of OSL ages in a number of environments,

as shown in van Mourik et al.'s (2010) study of an interstratified soil and sand section in the Netherlands.

Currently, any causation suggested for an observed equivalent dose distribution *in nature* must remain a hypothesis. Each potential factor for a scattered distribution must be discussed, and while site characteristics may point towards certain causes, there are no standard OSL techniques that can definitively prove which contribute to nearly ubiquitous overdispersion. Much of this problem is due to standard sample preparation, in which sieving and chemical treatments result in a physically homogeneous mineral extract. Any data relating to the physical location of a particular grain within its sedimentary fabric is irretrievably lost. To the contrary, if one made equivalent dose measurements upon a consolidated sample and identified luminescence emitting grains, one might construct microdosimetry models, identify bioturbated grains within small burrows or root casts, avoid suspected partially bleached grains within weathering rinds, or investigate any number of relationships between luminescence and the sample's microfabric. Such extra information about samples may allow OSL ages to become both more accurate and more precise.

Spatially resolved OSL (SR-OSL) involves the use of a scanning or imaging system to record luminescence emissions from known sources within a sample (Fig. 2-10). Combined with appropriate sampling methods, SR-OSL may help increase the precision and accuracy of OSL dating. With recent improvements in scientific imaging technology, SR-OSL is potentially feasible for the first time.

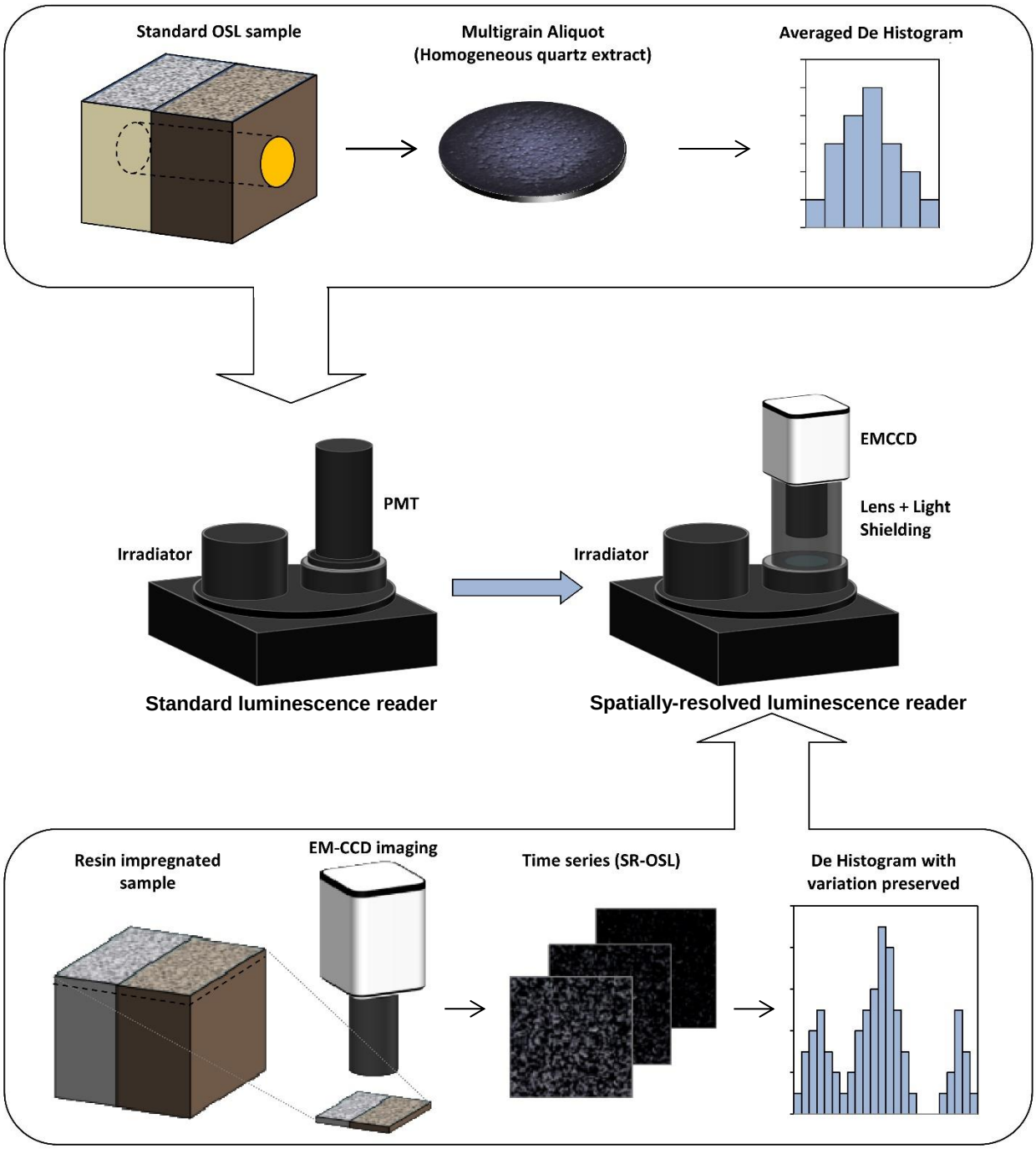


**FIG. 2-10.** Comparison of a standard luminescence reader (e.g. Risø machine) and an SR-OSL system. The standard reader on the left requires the extraction of homogeneous quartz from a sample (often a cylinder of sediment), which is then mounted on a disc (top center). The measurement of many tens or hundreds of grains simultaneously gives an averaged equivalent dose measurement for the sample (top right). An SR-OSL system replaces the PMT with equipment that can image luminescence from a thin section or polished surface of a sample over time (bottom). This will allow measurement of the innate variation in equivalent dose, which can then be compared to modeled microdosimetry to produce more accurate and precise dates.

# Chapter Three

## *SITES AND SAMPLING*

Samples for luminescence dating have been obtained and dated from four sites, the locations of which are shown in Fig. 3-1. Several tens of samples were collected from two cave sites, 30 from Dar es-Soltan I (Atlantic Coast) and 43 from Taforalt (Atlas Mountains). These samples span and bracket the Aterian occupation of the caves. Two further sites have been investigated in a more limited way. First, a sample from the open air site of Chaperon Rouge (Atlantic Coast) has been re-analyzed via modern OSL measurement techniques. This site provided one of the first OSL ages obtained in Morocco (Texier et al., 1988; Rhodes, 1990), and the sample underlies a rare open-air Aterian artifact layer. Second, sediment from within a possibly Aterian femur fragment found at Rhafas Cave has been dated. Due to the relatively small number of post-cranial remains from early *Homo sapiens*, the age of this sample is a high priority issue.

The first section of this chapter introduces the typical sampling procedures used in this project; atypical methods used for the Rhafas and Chaperon Rouge samples are described in the site-specific subsections. The second section provides site and sampling details for each study

location in the order they have been introduced here. Detailed background information is presented for each site, including geographical and environmental information, excavation history, sedimentological information, and any existing absolute dating information. Next, the overall sampling strategy for each site is described, and specific sampling locations and any non-standard procedures are summarized.

## 3.1 Sample types and guidelines

### 3.1.1 Location

Standard OSL sampling techniques are based on the premise that the most reliable dates will be obtained from samples taken within homogeneous bodies of sediment. Due to the range of gamma rays in sediment, an ideal sample would be obtained from within a sphere of homogeneous sediment with a ~30 cm radius. This is often impossible within an archaeological site, as archaeologically significant layers tend to contain a high density of lithics, hearths, and faunal remains. Additionally, the dating of sedimentary or occupational hiatuses may be of interest, and these are best constrained by samples taken near sedimentary boundaries.

For this project, a number of samples were collected near visible sedimentological boundaries and within complex archaeological layers. These locations were chosen to maximize the precision of the archaeological information obtained via age estimates. Dose rate calculation methods, including on-site gamma spectrometry and planar boundary modeling (see section 4.3.2.2), have been chosen to accommodate this strategy.

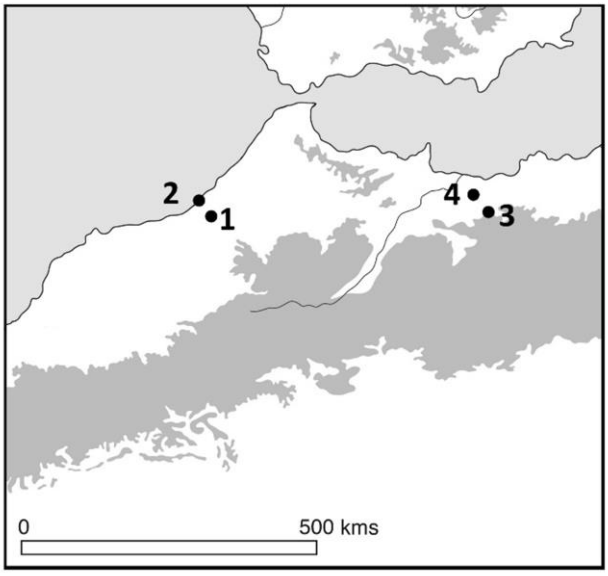


**FIG. 3-1.** Sampling locations: Chaperon Rouge (1), Dar es-Soltan I (2), Rhafas (3), and Taforalt (4).

### 3.1.2 Collection

#### *3.1.2.1 Standard samples*

Standard OSL sample collection uses cylinders cut from either opaque PVC or metal pipes (Aitken, 1998). In the Oxford Luminescence Laboratory, these usually range in size from 4 to 6 cm in diameter and 10 to 15 cm in length. When a sample location has been selected, the exterior face of the sediment is cut back several centimeters with a trowel (particularly if a sample is being taken from a face that has been exposed for several weeks, months, or years). This creates a flat, secure platform for the sample tube and limits the incorporation of weathered or bleached material in the ensuing sample. One end of the tube is placed snugly against the sediment, and a metal cap is placed on the other end. Using a hammer, the tube is driven into the sediment until it is flush with the surface. It is then removed from the face and capped. If the tube is not completely filled with sediment, the remaining space is filled with aluminum foil to prevent mixing. The sample is then wrapped tightly in cling film, and sealed with tape. It may also be wrapped with aluminum foil to ensure that it is protected from light. The sample is given a field code, described, and labeled.

Measurements and samples used for dosimetry are then taken. The depth of the overlying sediment and rock (e.g. a cave roof) is measured, and corrected for suspected overburden loss. Water content samples (several tens of grams of sediment) are collected from the interior of the empty sample hole, so that the measured moisture content is less affected by evaporation from the sediment face. Each water content sample is sealed in two clean, laboratory sample bags and labeled. Another sediment sample can be taken for ICP measurements. Finally, if possible, the sample hole is augered to a size and depth that allows the insertion of the gamma spectrometer probe and the gamma dose rate is measured (see section 4.3.1.3).


**FIG. 3-2.** Standard OSL sample (3 on left) and microsample (far right) containers.

### *3.1.2.2 Microsamples*

Substantially smaller sediment cores ('microsamples') were also obtained (Fig. 3-2). Microsamples allow high density sampling strategies, which may produce higher precision ages when combined with Bayesian modelling techniques. They also allow close constraint of sedimentary boundaries, and should produce less of a 'time average' in compacted cave sediments as a smaller sediment volume is collected. Each sampling container measured between 5 and 8 cm long, with a 1 to 2 cm diameter. These were cut from hollow aluminum piping of the desired diameter, and filed to a sharp edge on one end to facilitate insertion into sediment.

Microsamples were obtained in a similar fashion to standard sampling. Each section of pipe was capped on the blunt end with either cork or thick pads of aluminum foil, and the filed end was placed against the cleaned sediment face. A hammer was used to drive the tube into the face. If the sediment was indurated, a small block of wood was interposed between the

hammer and aluminum cylinder so that it was not deformed. The sample was then removed from the sediment, wrapped in cling-film and aluminum foil, and labeled with the sample number and date. A small black mark was used to indicate the end of the tube that contained sediment from the exterior of the face. Separate water content and dosimetry samples were also taken. Gamma spectrometer measurements were either made at the sample position by enlarging the sample hole with an auger, or one gamma spectrometer measurement was made at the center of a group of samples.

#### *3.1.2.3 Heated cobbles*

Like more commonly applied TL methods, OSL can also be used to date heated material (Mejdahl and Bøtter-Jensen, 1997). Therefore heated cobbles were collected from hearth features and heat-processing areas. Color (either reddish-orange or charred black) and surface texture (cracking and powdery surface) were considered to be evidence of heat exposure. Samples were also chosen to be as nearly as possible spherical, due to the difficulty of assessing gamma dosimetry for irregular shapes. Cobbles of between ~4 and 8 cm in diameter (or longest dimension) were obtained, in order to balance the likelihood of complete resetting and the ease of removing the exterior during sample preparation.

Once an appropriate burned stone sample had been identified, its position was noted, and it was removed from the sediment, bagged, and labeled. If the stone was fractured or friable, it was also wrapped in several layers of aluminum foil. Samples of surrounding sediment were obtained for water content and ICP measurement. If possible, a gamma spectrometer measurement was made.

## 3.2 Sites

### 3.2.1 Taforalt (Grotte des Pigeons)

Grotte des Pigeons, commonly known as Taforalt after a nearby village, is located in the Beni Snassen range of the Atlas Mountains (34°48’38” N, 2°24’30” W). It is situated at 720 m

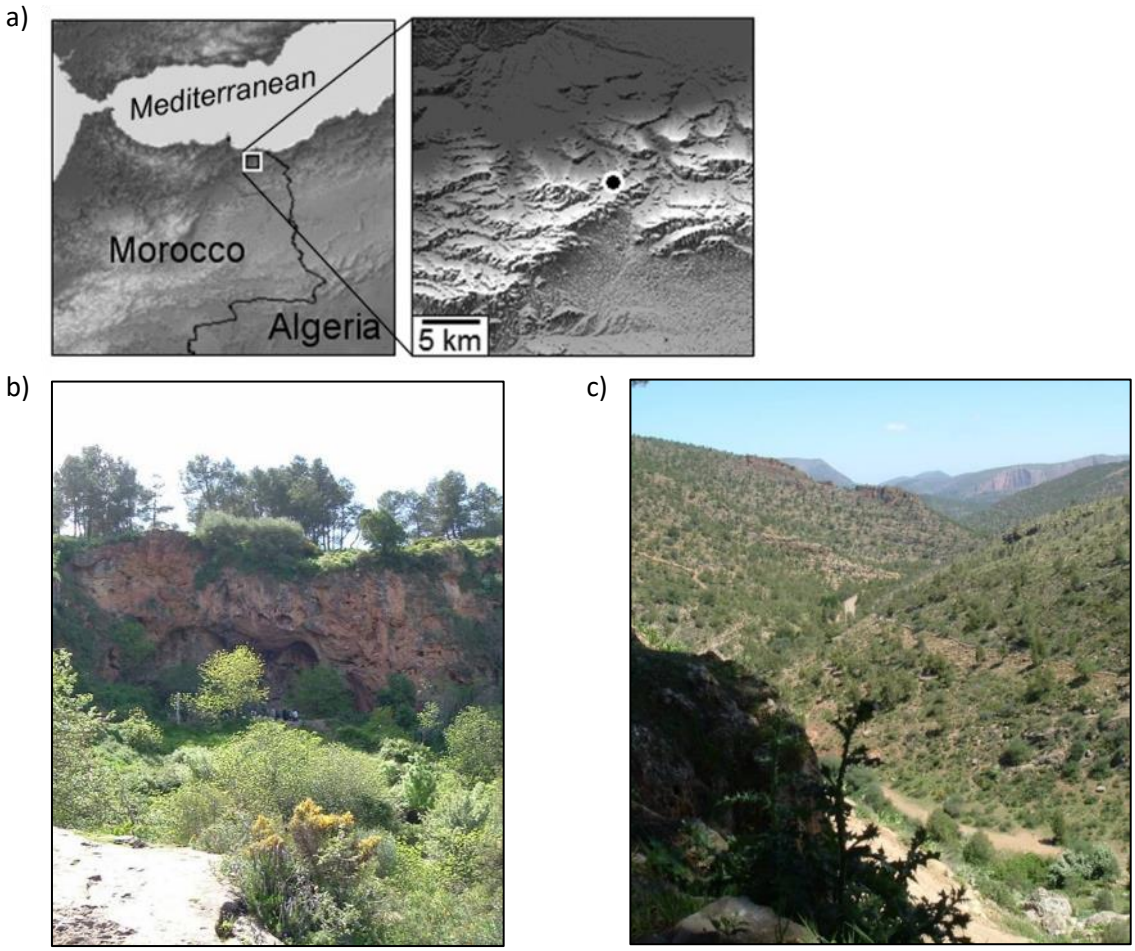


**FIG. 3-3.** Location and environment of Grotte des Pigeons (Taforalt). a) Map showing location of Taforalt in Eastern Morocco. b) Exterior view of cave. c) View from above the cave looking down the valley.

**FIG. 3-4.** View into cave from near the top of the Grey Series. The scale of the excavations is apparent.

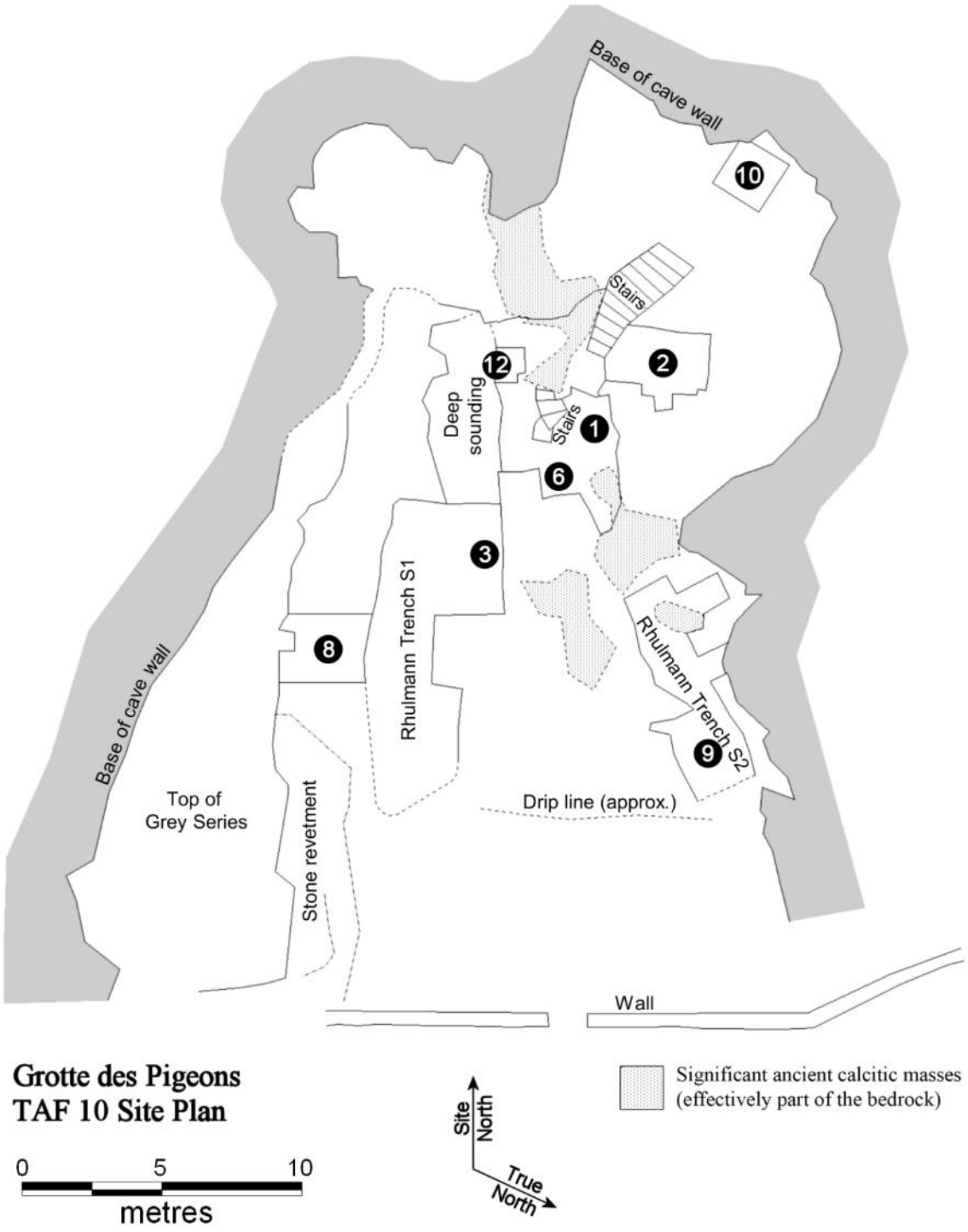


**FIG. 3-5.** Site plan for Taforalt indicating current sector identifications.

a.s.l., in the side of a small hill overlooking a valley (Fig. 3-3). The present cave is approximately 20 m wide at the entrance and 25 m deep, with an interior area of >400 $m^2$ (Figs. 3-4, 3-5). It was formed by rekarstification of an earlier karstic deposit comprising travertine and fluvial conglomerates. Local bedrock is a Permo-Triassic dolomitic limestone (Bouzouggar et al., 2007b), which is covered by a thick bed of red calcareous soil (Courty et al., 1989).

The modern local environment is characterized as 'thermo-Mediterranean,' a biozone found in low altitude areas of the Mediterranean with average minimum temperatures between 5°C and 7°C (Blondel and Aronson, 1999). The nearby weather station at Oujda (34.8°N, 1.9°W, 470 m a.s.l.) has a mean maximum temperature of ~33°C in August, and minimum of <4°C in January. Mean yearly rainfall is only ~350 mm, with maximum rainfall occurring in April (Hong Kong Observatory, 2012). This environment supports primarily evergreen oak, *Tetraclinus articulata* and *Pinus halepensis* (Bouzouggar et al., 2007b).

#### *3.2.1.1 Excavation history and archaeology*

Nearly 10 m of extant sediment are currently exposed, though large segments of the deposits were removed during previous excavations. These have occurred frequently since the cave's discovery in 1908 (Bouzouggar et al., 2007b). The first excavations were directed by A. Ruhlmann from 1944 to 1947, by J. Roche from 1951 to 1955 (Roche, 1972) and in the early 1970's (Humphrey et al., 2012), and Roche and J.-P. Raynal in the 1980's (Raynal, 1980). From 2003 to 2011, excavations have been undertaken under the co-direction of A. Bouzouggar (Institut National des Sciences de l'Archéologie et du Patrimoine Morocco) and R.N.E. Barton (University of Oxford).

Roche identified eight major archaeological levels: three Iberomaurusian (A, B, C), three Aterian (D, E, F), a possible Mousterian (G), and a problematic level (H) (Roche, 1953). Level H yielded few lithics, among which there were no pedunculates but several bifacial foliates. It is suggested that the culture in H may correspond to a local transition between the Mousterian and Aterian (Roche, 1967). In general, the Aterian in Taforalt is characterized by relatively low

frequencies of pedunculates. Bifacial foliates also occur infrequently in the early Aterian, but they become more important over time and eventually become more common than pedunculates. Aterian development is also recognizable in the ratio of endscrapers to sidescrapers, which increases over time (Roche, 1967; Roche, 1969).

Micromorphological studies were also conducted on cave sediments extending from the Iberomaurusian into the Aterian levels (Courty et al., 1989; Courty and Vallverdu, 2001). Courty and Vallerdu (2001) identified a number of rapid climatic alterations in the micromorphological record, and suggested that two discontinuities—one at the Aterian/Iberomaurusian transition and one during Iberomaurusian occupation—may be related to Dansgaard-Oeschger and/or Heinrich events. These conclusions relied on the early and inaccurate chronology for Taforalt cave and are now disputed (N.Barton, pers. comm.).

The most recent excavations defined five major sedimentological groups from the upper > 6 m of cave infill. From oldest to youngest, these are the Calcareous Group, Lower Laminated Group, Pink Group, Upper Laminated Group, and Grey Series (Fig. 3-6). Sediments slope downwards towards the cave entrance and overlie a large calcitic dome. Therefore older sediments are found towards the back of the cave, and thin towards the front, eventually disappearing. The Grey Series accounts for the top 4 m, and it is primarily composed of ashy material and fire-cracked rock derived from human activity (see detailed description below). The lower ~2.5 m of sediment comprise the other four groups, which have a much higher proportion of 'natural' sediment that the Grey Series but still contain hearth-related material. Excluding the human-activity related ash, cave sediment is believed to derive primarily from aeolian transport, with a relatively small proportion likely to be introduced by water-borne (i.e. via the cave mouth or through cracks in the bedrock) transport (S. Collcutt, pers. comm.). The relative influence of each process (aeolian transport, water-based transport, and human hearth building) on final sediment characteristics has altered through time, due to both climatic drivers and human population pressure (Oh, 2012).

Here, the sedimentology, archaeology, and available absolute dates for each Group are described. Sediments exposed in the 'Deep Sounding' (Fig. 3-5) have not been rigorously characterized or re-excavated, nor have sediments in Sector 9. Correspondences to Raynal 'niveaux' are given in square brackets (Bouzouggar et al., 2007b).

Calcareous [R24-R32?]

Laterally variable deposits include flowstones (both dense and porous), carbonate nodules, stalagmite mounds, and silty to sandy loams (Clark-Balzan et al., 2012). MSA archaeology of an Aterian facies is present, with characteristic pedunculates, bifacial foliates, and small Levallois cores (Bouzouggar and Barton, 2012). Two OSL ages (85.5 ± 8.1 ka and 103.8 ± 9.1 ka) and two uranium-series ages (94.8 ± 0.9 ka and 93.9 ± 0.8 ka) have previously been obtained (Bouzouggar et al., 2007b).

Lower Laminated [R16-R23]

This group is dark grey with coarsely laminated silty to sandy loams and high ash content (Clark-Balzan et al., 2012). Archaeological finds comprise characteristic MSA side scrapers, small radial Levallois cores, bifacial foliates, and *Nassarius gibbosulus* shells (R21) with ochre pigment and evidence of bead stringing. Cedar charcoals dominate, and faunal remains include equids, hares, and various shrews and gerbils. These flora and fauna suggest a relatively cool, arid, and open environment with patchy woodland. Previously reported OSL ages on sediment range from 60.1 ± 3.9 ka to 84.5 ± 4.4 ka, and TL ages on burnt flints range from 70.3 ± 2.8 ka to 108.7 ± 5.1 ka (Bouzouggar et al., 2007b).

Pink [R12-R15]

Pink Group sediments are stony loams with some cementation, and slight speleothem formation at the top. Scour features indicate the periodic presence of free-flowing water. Similar MSA artifacts are found as with the Lower Laminated group, excluding shell beads. Existing OSL ages range from 44.3 ± 3.7 ka to 54.9 ± 4.6 ka (Bouzouggar et al., 2007b).

Upper Laminated [R1-R11]

a)

**Grey Series**

**Upper Laminated Group**

b)

**Upper Laminated Group**

**Pink Group**

**Lower Laminated Group**

**Calcareous Group**

**FIG. 3-6.** Visible distinctions between major sedimentological Groups. a) View of southern cave wall, showing the Grey Series and Upper Laminated Sediments. The sloping nature of the sediment fill is apparent. At the left of the image, the Grey Series is ~ 4 m thick. b) Sector 1 (east), with Groups indicated.

Sediments are fine, laminated silty to sandy loams with some coarser beds, comprising discontinuous lower (Sectors 1 and 2) and upper sub-groups (Sectors 3 and 8). MSA artifacts are present in the lower and basal upper sub-groups. It seems that the Levallois-based Aterian is succeeded by a non-Levallois MSA flake industry, followed by three technologically distinct Iberomaurusian phases (R.N.E. Barton, J. Hogue, pers. comm.). This is in contrast to the direct progression from Aterian to Iberomaurusian suggested for the Maghreb (Camps, 1975). A radiocarbon date for charcoal from the top of the sequence returned 16,567.5 ± 377.5 Cal BP, while OSL and TL ages further down in the sediments ranged from 19.0 ± 1.1 ka to 37.4 ± 1.8 ka (Bouzouggar et al., 2007b).

Grey Series [NA]

This deposit is composed of fine, ashy, grey sediment, much of which has been removed by previous excavations. A significant concentration still remains along the south wall of the cave. There is also a remnant on the west side of the cave which includes evidence of up to 40 Iberomaurusian adult and juvenile burials (Mariotti et al., 2009). Some buried human remains have cut marks, ochre staining, and accompanying horn cores (Roche 1953; Ferembach 1959; Humphrey et al., 2012). Elsewhere in the cave, the Grey Series contains significant numbers of burned cobbles, faunal remains, lithics, and snail shells dispersed throughout. Some interior bedding is discernible. Lithic artifacts are of LSA types (Iberomaurusian), with microlithic backed bladelets retouched into a variety of shapes (Roche, 1963; Bouzouggar et al., 2007b). The micropalaeontology and botanical remains for these layers are still under study but initial results suggest that the Grey Series accumulated during broadly warm, humid conditions. Some hint of drier, cooler periods near the base and top of the sediments is indicated by the presence of Barbary ground squirrel (*Atlantoxerus getulus*) and cedar (*Cedrus*) (R.N.E. Barton, pers. comm.). Land snail numbers, size, and the restricted species composition suggest intentional human collection, possibly for consumption (Taylor et al., 2011). According to radiocarbon dating of charcoals, the Grey series was deposited between 15,057-14,201 Cal BP and 12,942-12,649 Cal

BP (Bouzouggar et al., 2008). Published OSL and TL dates are approximately 5000 years older (Bouzouggar et al., 2007b).

#### *3.2.1.2 OSL samples*

The scale of the excavations at Taforalt allowed an intensive sampling strategy in which high numbers of OSL samples were taken throughout the volume of the cave infill. Numerous samples were obtained not only from each of the main sedimentary groups in the overall stratigraphy, but also from the same sediment series in various exposures distributed around the cave. OSL accuracy tests were considered during sampling. In almost all cases, a vertical sequence of directly associated samples was obtained in each dated sector. This technique allows internal consistency checks on the OSL dates. Additionally, efforts were made to take OSL samples in close proximity to samples dated by independent chronological methods such as radiocarbon and uranium-series dating. Finally, microsamples and standard samples were grouped together in several locations to test whether the combination of dense, small samples and VSA data would yield accurate and more precise ages.

Samples were collected during field seasons in 2008, 2009, and 2010. Several were collected by one of the author's advisors (Dr. Jean-Luc Schwenninger) during April 2008, and the author collected samples during 2009 and 2010 field seasons. A full sample list is given in Table 3-1, which comprises 46 samples within and bracketing Aterian layers. Approximately half of the samples taken were standard, and half were microsamples. Due to the complexity of the Taforalt stratigraphy, detailed sample descriptions are presented by sector.

Sector 1

Two standard samples for OSL dating were collected from sandy-silt units within the Calcareous Group at the base of Sector 1: TAF08-01 from unit R29 and TAF08-02 from R27 (Fig. 3-7). These samples directly bracket the flowstone/cave pearl unit R28 and provide a *terminus ante quem* for the R30 flowstone. A gamma-spectrometer measurement was made for TAF08-02, but the gap between the flowstones was not wide enough to obtain one for TAF08-01. A sample of

**TABLE 3-1.** Samples collected from Taforalt, ordered by field code.

| Field Code | Lab Code | Sector | Group (see below) | Raynal Niveau | Sample Type (see below) |
|---|---|---|---|---|---|
| TAF08-01 | X3350 | 1 | C | R27e | S |
| TAF08-02 | X3351 | 1 | C | R29 | S |
| TAF08-03 | X3352 | 8 | UL | -- | S |
| TAF08-04 | X3353 | 8 | UL | -- | S |
| TAF08-05 | X3354 | 8 | UL | -- | S |
| TAF08-06 | X3355 | 8 | UL | -- | S |
| TAF08-08 | X3357 | Backfill | | -- | S |
| TAF08-10 | X3359 | 3 | UL | -- | S |
| TAF08-11 | X3360 | 3 | UL | -- | S |
| TAF08-12 | X3361 | 3 | UL | -- | S |
| TAF08-13 | X3362 | 3 | UL | -- | S |
| TAF08-14 | X3363 | 8 | UL | -- | S |
| TAF08-15 | X3364 | 8 | UL | -- | S |
| TAF08-16 | X3365 | 8 | UL | -- | S |
| TAF08-17 | X3366 | N/A | Grey | -- | S |
| TAF09-01 | X3653 | 3 | UL | -- | S |
| TAF09-08 | X3660 | 8 | UL | -- | S |
| TAF09-20 | X3672 | 9 | -- | -- | S |
| TAF09-21 | X3673 | 9 | -- | -- | S |
| TAF09-22 | X3674 | 9 | -- | -- | S |
| TAF09-23 | X3675 | 9 | -- | -- | S |
| TAF09-24 | X3676 | 8 | Grey | -- | S |
| TAF09-25 | X3677 | 8 | Grey | -- | S |
| TAF09-26 | X3678 | 2 | LL | R19 or R21 | S |
| TAF09-27 | X3679 | 2 | C | -- | S |
| TAF09-34 | X3686 | 12 | -- | -- | S |
| TAF09-35 | X3687 | 2 | P | R14 | M |
| TAF09-36 | X3688 | 2 | LL | R16 | M |
| TAF09-37 | X3689 | 2 | LL | Base R17 | M |
| TAF09-38 | X3690 | 2 | LL | Base R19 | M |
| TAF09-39 | X3691 | 2 | LL | R21 | M |
| TAF09-40 | X3692 | 2 | C | -- | M |
| TAF10-01 | X3964 | Deep Sounding | -- | -- | S |
| TAF10-02 | X3965 | 3 | UL | -- | M |
| TAF10-05 | X3968 | 3 | UL | -- | M |
| TAF10-06 | X3969 | 3 | UL | -- | M |
| TAF10-07 | X3970 | 3 | UL | -- | M |
| TAF10-10 | X3973 | 8 | UL | -- | M |
| TAF10-11 | X3974 | 8 | UL | -- | M |
| TAF10-14 | X3977 | 8 | UL | -- | M |
| TAF10-16 | X3979 | 9 | -- | -- | S |
| TAF10-17 | X3980 | 2 | C | R23d/e | S |
| TAF10-18 | X3981 | 2 | C | Base R23g | M |
| TAF-COB-01* | X3680 | 2 | LL | -- | Cobble |
| TAF-COB-02 | X3700 | 8 | Grey | -- | Cobble |
| TAF-EXP-01 | X3695 | Exterior | Weathered Bedrock | -- | S |

*Removed from auger hole for sample TAF09-26.

Calcareous Group (C) Upper Laminated (UL) Standard Sample (S)
Lower Laminated (LL) Grey (G) Microsample (M)
Pink (P)

the flowstone between the two OSL samples (R28) was collected for ICP-MS analysis. Five U-series dates in Sector 1 (three samples from R28, and two from R30) provide direct age comparisons.

Sector 2

Sector 2 comprises sediments from the Calcareous Group through the lower part of the Upper Laminated Group. A modern porcupine burrow cuts through upper deposits, but samples were taken well away from the burrow and the visibly bioturbated area. Finely laminated hearth lenses are present throughout the sampling locations. Three standard samples and seven microsamples were collected, spanning deposits from the Calcareous Group to the base of the Pink Group (Figs. 3-8, -9, -10). In addition, a heated cobble was obtained from fill removed while augering for a gamma spectrometer measurement (Fig. 3-11).

Microsamples (TAF09-35--TAF09-40) were collected in the sector both to test the technique by comparison with standard tube samples, and to give accurate deposition dates for sediments on either side of the group boundaries. TAF09-38 was intended to replicate the standard sample TAF09-26. Boundaries were bracketed by sample pairs TAF09-40 and -39 (CG/LL) and TAF09-36 and -35 (LL/PG). Another microsample was collected from Calcareous Group sediments in the adjacent face (Fig. 3-10). These samples can be linked stratigraphically by a flowstone running through Sector 2, however, this sample has not been securely linked to either of those that appear in Sector 1.

Sector 3

Sector 3 is located nearer the entrance of the cave and opposite Sector 8. These sediments belong to the Upper Laminated Group, though in this section they are sometimes referred to as the Yellow Series. The sediments overlie a rising calcite dome. It is difficult to determine whether any remnant of the Pink Group remains between the calcite and yellow-orange, Upper Laminated sediments. Distinct, charcoal-rich horizons can be traced horizontally through the sector, and root casts are visible in some of the pink-orange horizons.

a)

b)

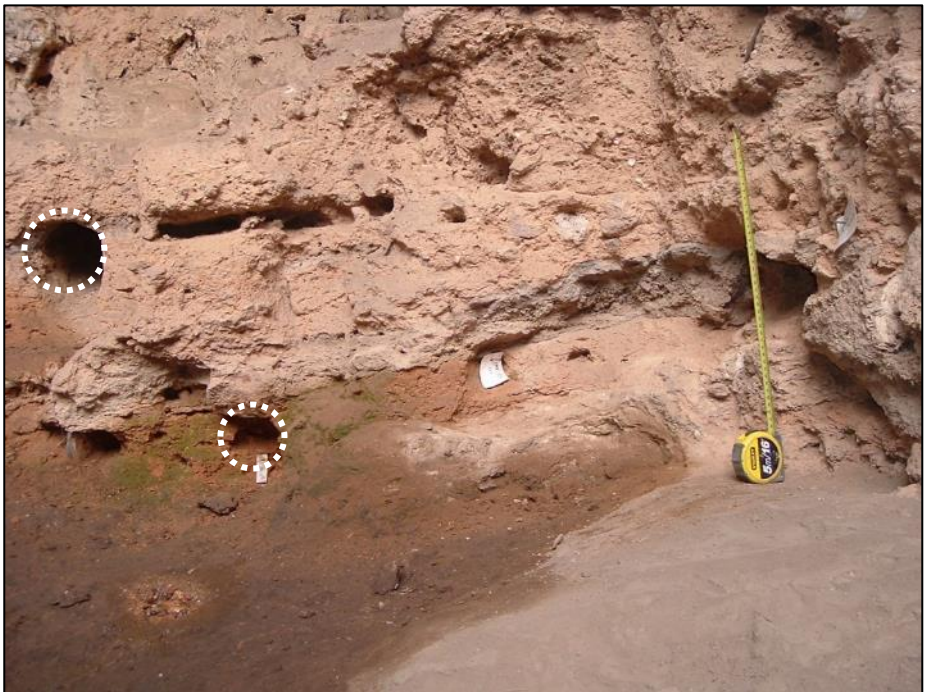

**FIG. 3-7.** General view of Sector 1 (a). Photograph courtesy of I. Cartwright. Earlier OSL sample locations are evident (Bouzouggar et al., 2007). The box and arrow indicate the direction of the photograph in (b), which shows the OSL samples collected for this project.

a)


b)

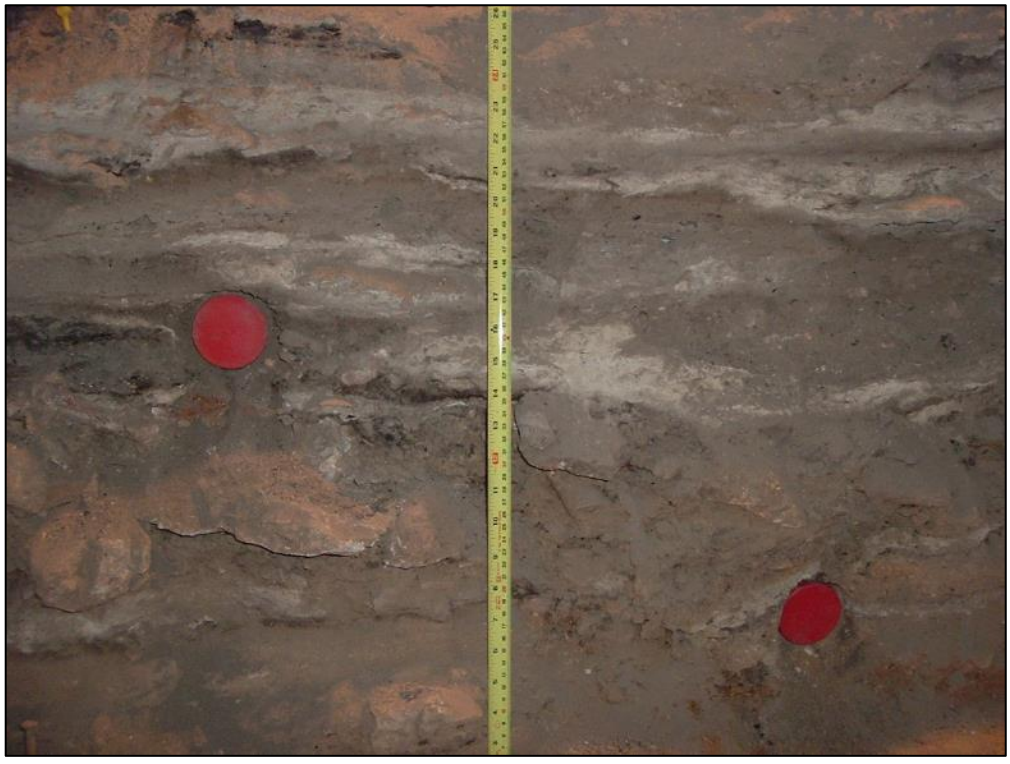


**FIG. 3-8.** General view of Sector 2 with image locations indicated (a). Photograph courtesy of I. Cartwright. b) Two standard samples collected from subsection A.

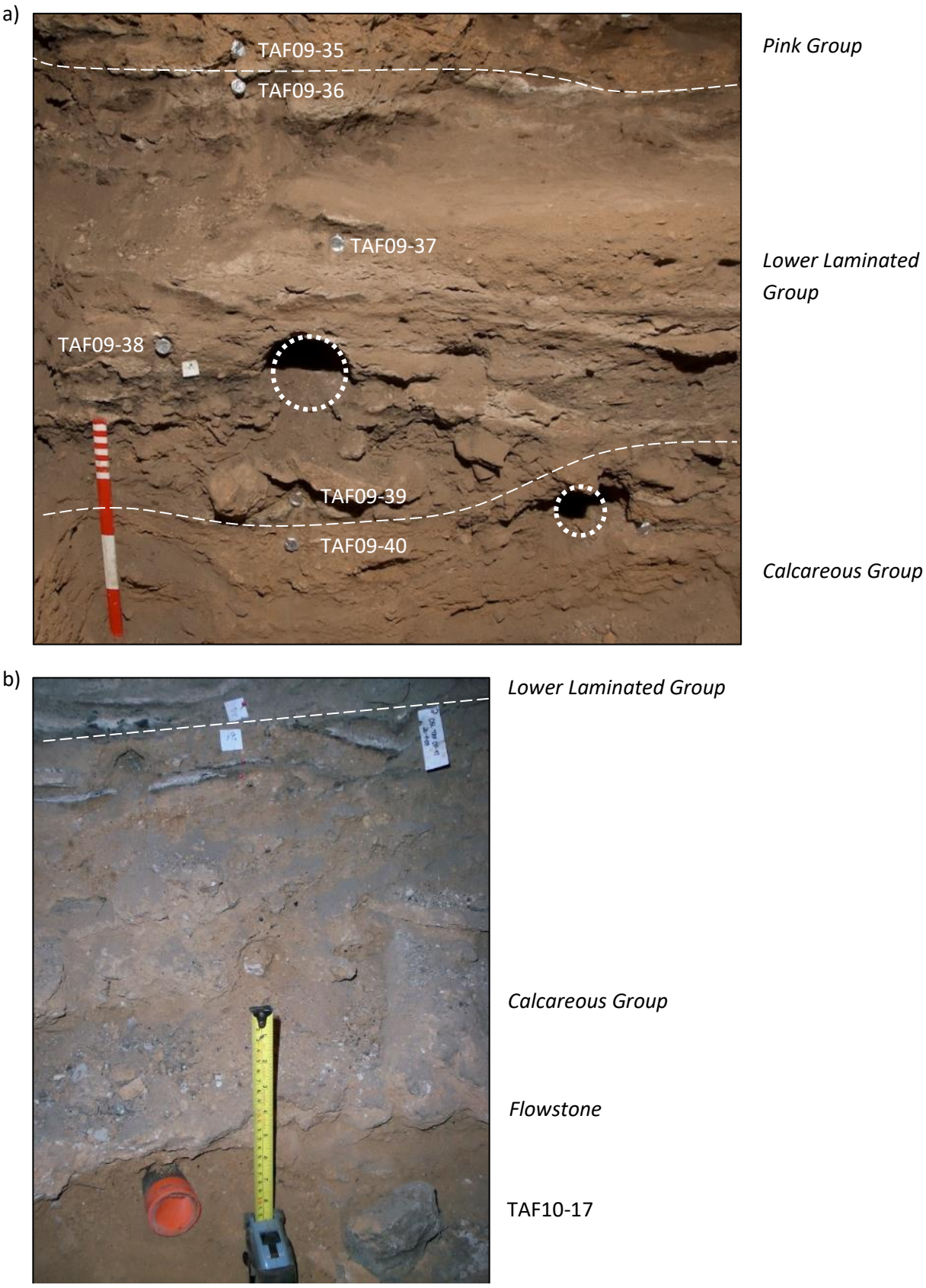


**FIG. 3-9.** Images of Sector 2, section A (see previous figure). a) Microtube locations and sediment Groups, with sample locations shown in Fig. 3-8b) indicated. Photograph courtesy of I. Cartwright. b) A sample collected from lower in the same section.


**FIG. 3-10.** Calcareous Group microsample collected from below the burrow in subsection B of Sector 2 (see Fig. 3-8). The marked flowstone is the same as that noted in Fig. 3-9b).

**FIG. 3-11.** TAF-COB-01, a heated cobble obtained during augering for gamma spectrometry measurement for sample TAF09-26.

Five standard samples were collected from this section (Fig. 3-12). The lowest sample (TAF09-01) was collected within ten centimeters of the flowstone and may incorporate some Pink Group sediments. About 1 m further along the section, a high density collection of microsamples was taken. Eight samples (TAF10-02 – TAF10-09) were located in a generally vertical line down the section, one every five centimeters. A marker horizon ('Y5') is bracketed by TAF10-06 and TAF10-07; though there are no radiocarbon dates for this sector, Y5 has been securely dated in nearby Sector 8 (see Fig. 3-5 for sector locations).

Sector 8

Sector 8 contains both Upper Laminated and Grey Series deposits, and a number of angular boulders that are presumed to be roof fall. Distinct charcoal horizons are not readily apparent, though some horizons can be correlated with those in Sector 3. Generally horizontal beds can be traced through the Sector, but this becomes more difficult towards the base as boulders interrupt the sequence. Thirteen sediment samples, three from the Grey and 10 from the Upper Laminated, and one heated cobble (Grey) were collected for dating (Figs. 3-13, -14, -15). One sample (TAF08-08) was also collected from a deposit at the base of Sector 8, which incorporated backfill and storm-runoff (Fig. 3-14b). This deposit is at most a few decades in age. It is finely laminated with bands of grey and pinkish-orange sediment, which is derived from the cave sediments around the trench.

The unconsolidated nature of the Grey Series necessitated a slightly adapted collection technique for the standard sample, TAF09-24. To alleviate the danger of face collapse, it was decided that the tube would be inserted into the sediment several centimeters under the current level of an archaeological cut. Before sampling, a layer of foil was placed on the base of the cut so that it would shade the sample from sunlight if the ashy sediment shifted slightly during collection. The sample tube was then slowly inserted into the face. Excavation proceeded until the tube had been cleared, after which it was retrieved and sealed as usual.

a)

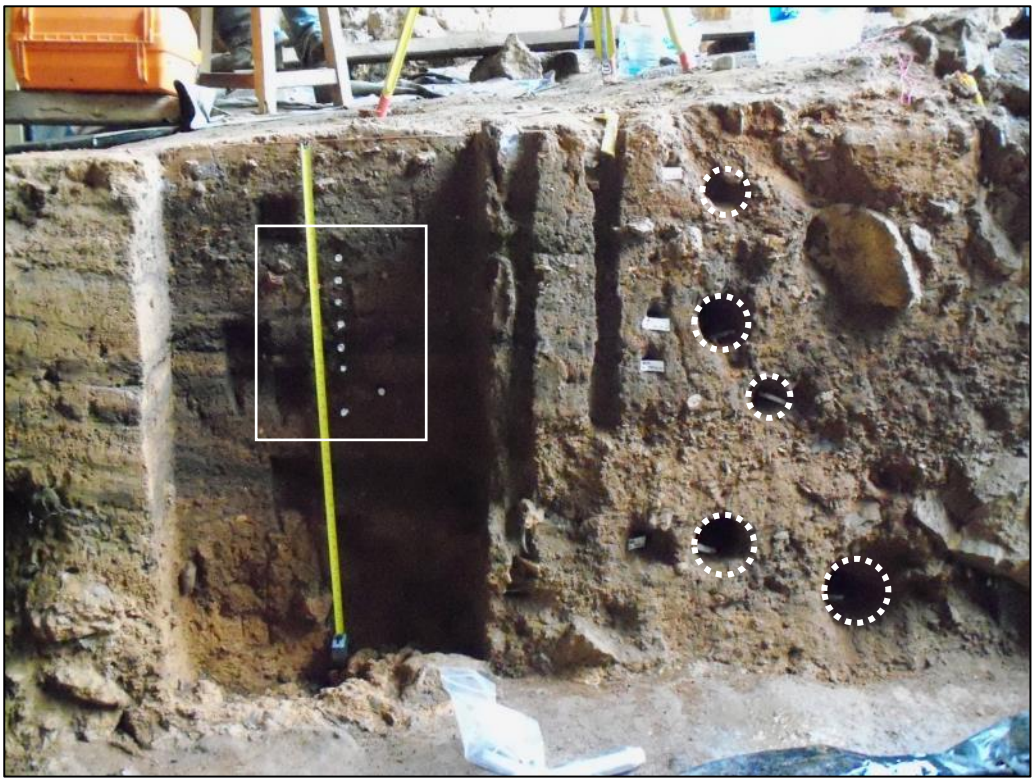


b)


**FIG. 3-12.** General view of Sector 3. Standard tube samples collected (a), and white box indicates Microtubes collected area shown in (b).

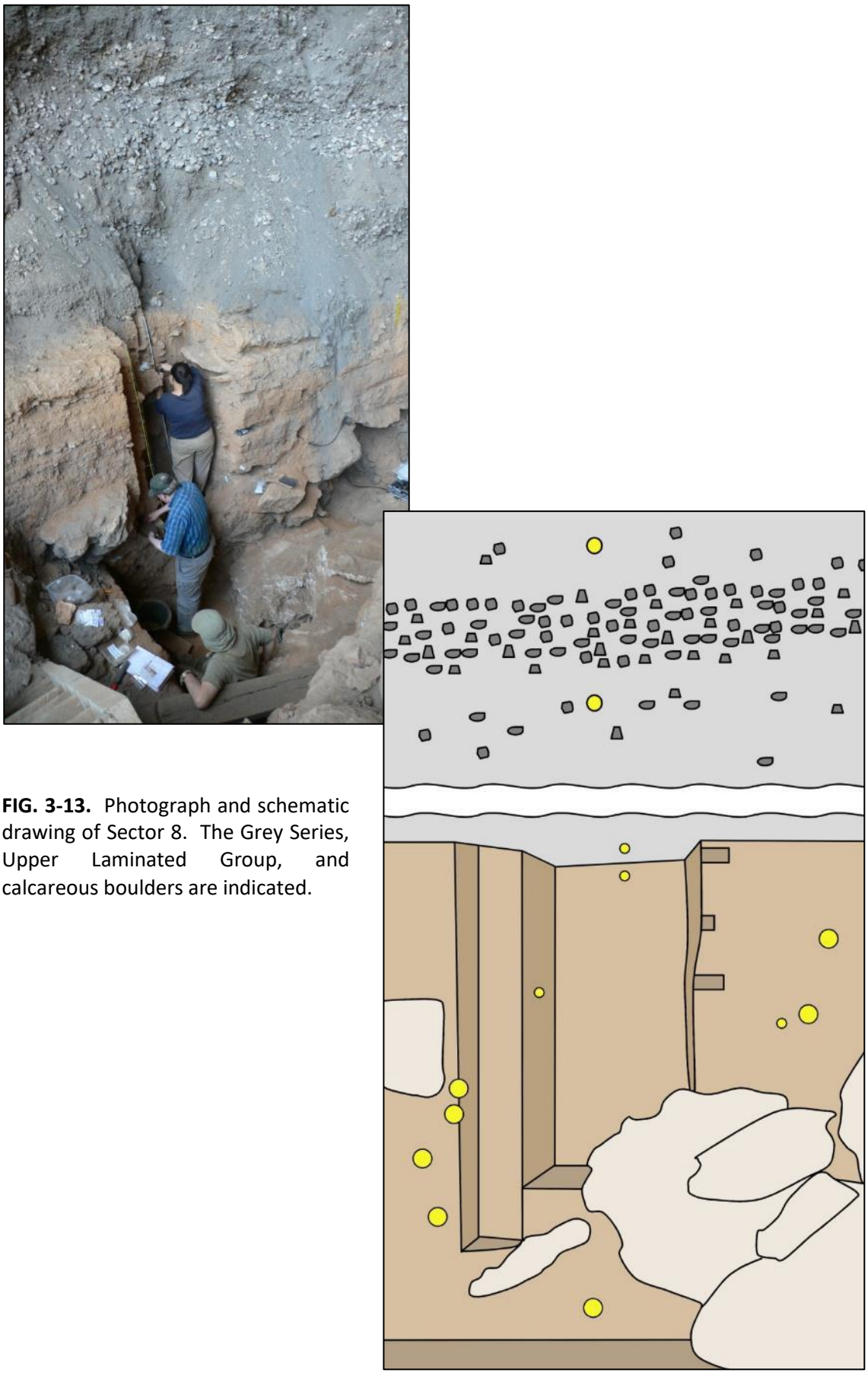

**FIG. 3-13.** Photograph and schematic drawing of Sector 8. The Grey Series, Upper Laminated Group, and calcareous boulders are indicated.

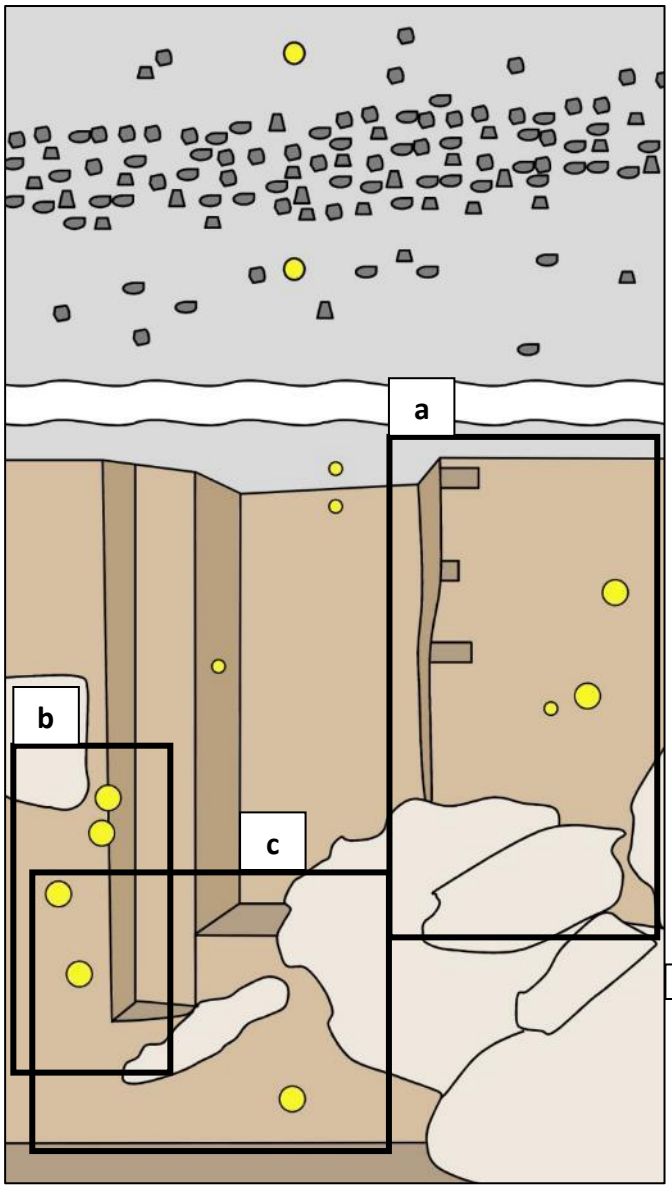



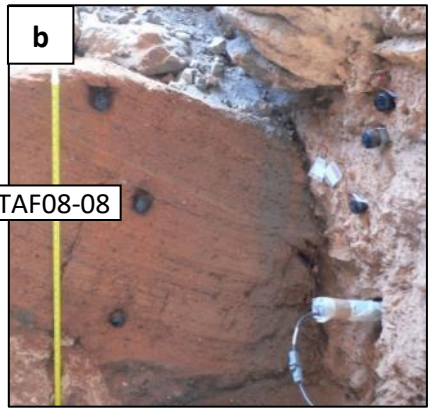


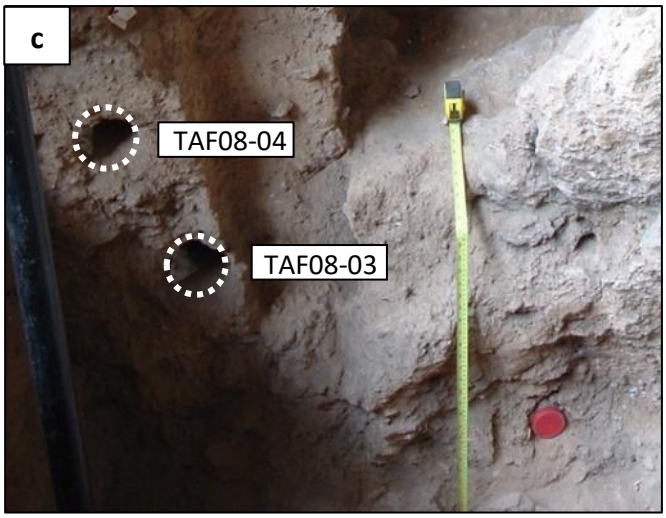


**FIG. 3-14.** Photographs of sample locations. Photograph positions are indicated on the section drawing. a) and c) face towards the section wall; b) is taken facing towards the mouth of the cave, and shows the modern backfill as well.

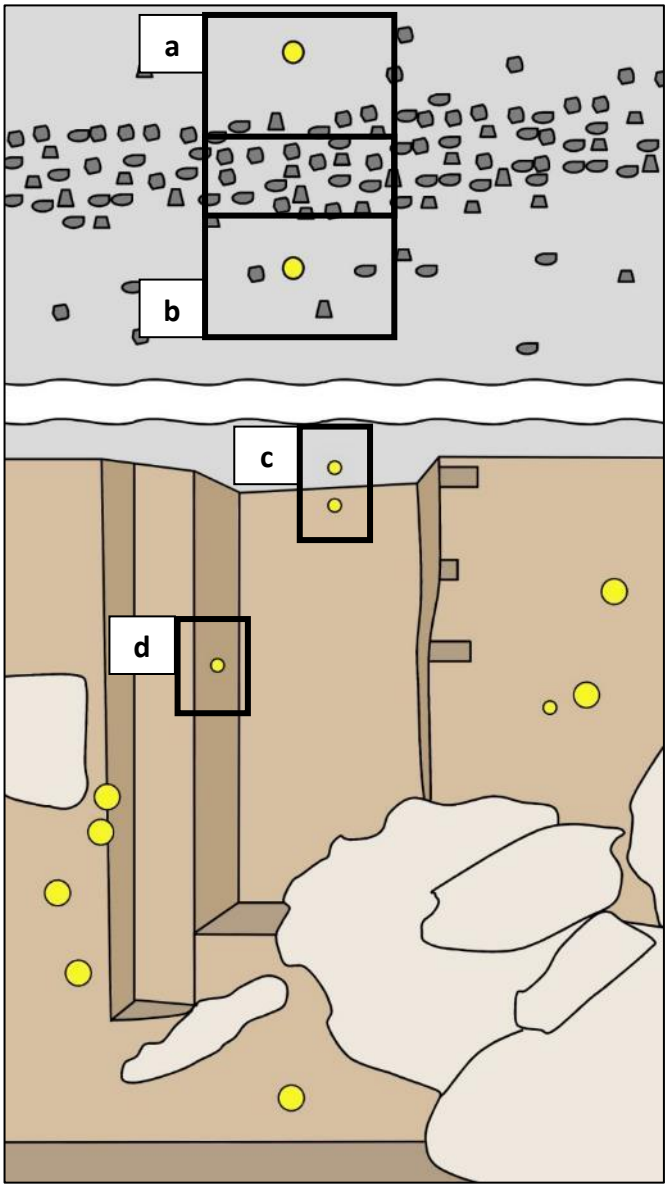


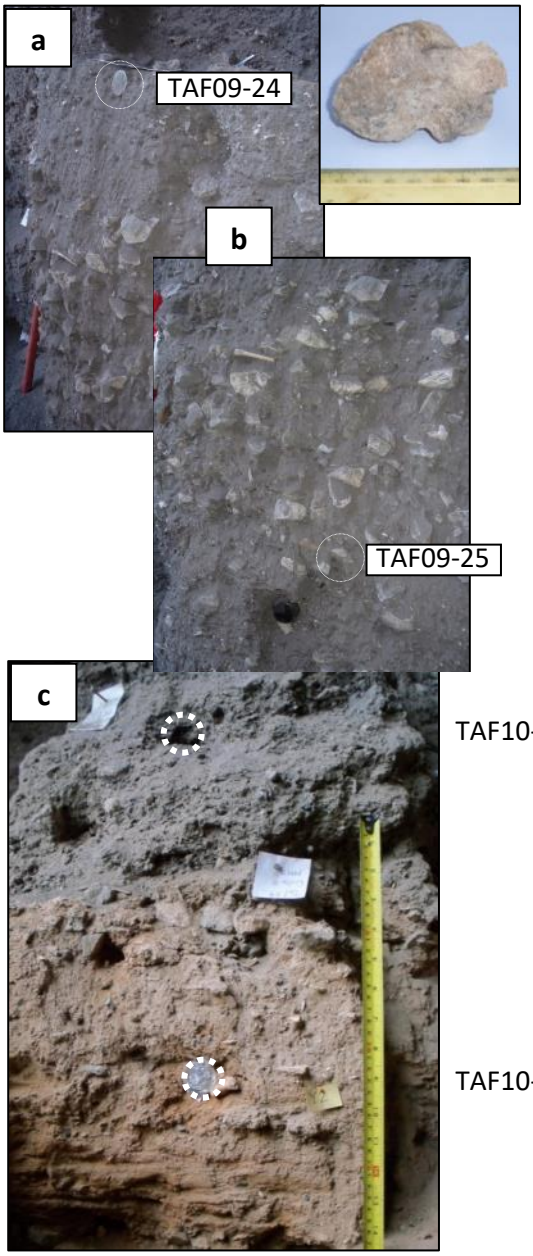


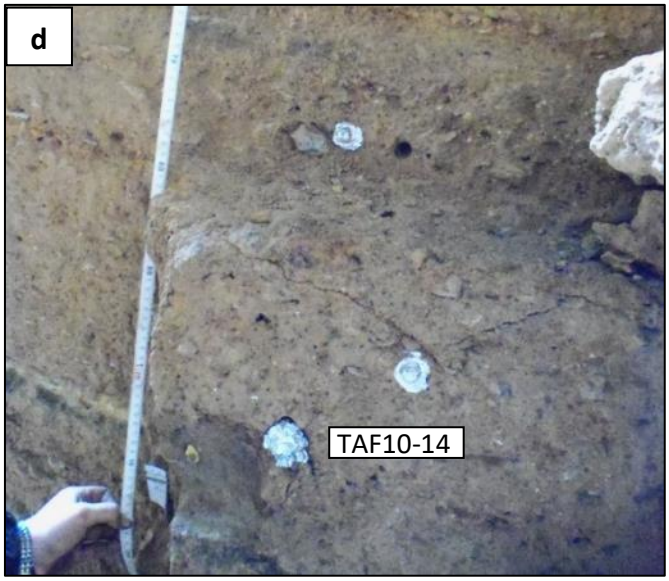


**FIG. 3-15.** Photographs of sample locations. Photograph positions are indicated on the section drawing. a, b, c) face towards the section wall; d) is taken facing towards the mouth of the cave. The inset image of the cobble with is sample TAF-COB-02, a typical Grey Series component.

Sector 9

Sector 9 denotes a previously excavated section (dug by Ruhlmann), which comprises primarily pinkish-orange sediment with discrete, charcoal-rich bands ~5 cm thick. Calcite blocks form a barrier at the base of the section, covering well-bedded, hearth deposits similar to those noted in Sectors 1 and 2. The origin of the blocks is unclear, as there is not yet enough evidence to connect them to any feature excavated within the cave. Four standard samples were collected from the orange-yellow sediments above the blocks, and one from the laminated hearth deposits underneath (Fig. 3-16).

Sector 12

Sector 12 comprises deep sediments, which have not been studied in detail but from which rich microfaunal samples have been obtained. It is composed of blocky and rounded cobbles and small to large boulders, with pockets of fine pinkish sediment. Some bedding is visible, with sediments dipping towards the cave's exterior. The sector has not been excavated to the bedrock. One standard sample (TAF09-34) was collected at the base of the section from a small sediment pocket (Fig. 3-17).

Deep Sounding

Like Sector 12, the Deep Sounding has not been extensively studied or excavated to bedrock. Sediments here incorporate significantly more grey, ashy material than Sector 12, and there are fewer boulders. Layers dip towards the east. A sample (TAF10-01) was collected near the base of the Deep Sounding, approximately 3.7 m deeper than the base of Sector 3 (Fig. 3-18).

Interior Grey

After a small exploratory pit was dug into the Grey Series near the back of the cave, a tube sample was taken from the ashy material. A gamma spectrometer measurement was also made by digging a vertical hole into the sediment and lowering the gamma spectrometer in. This is the only on-site gamma ray measurement to have been made for the Grey Series.

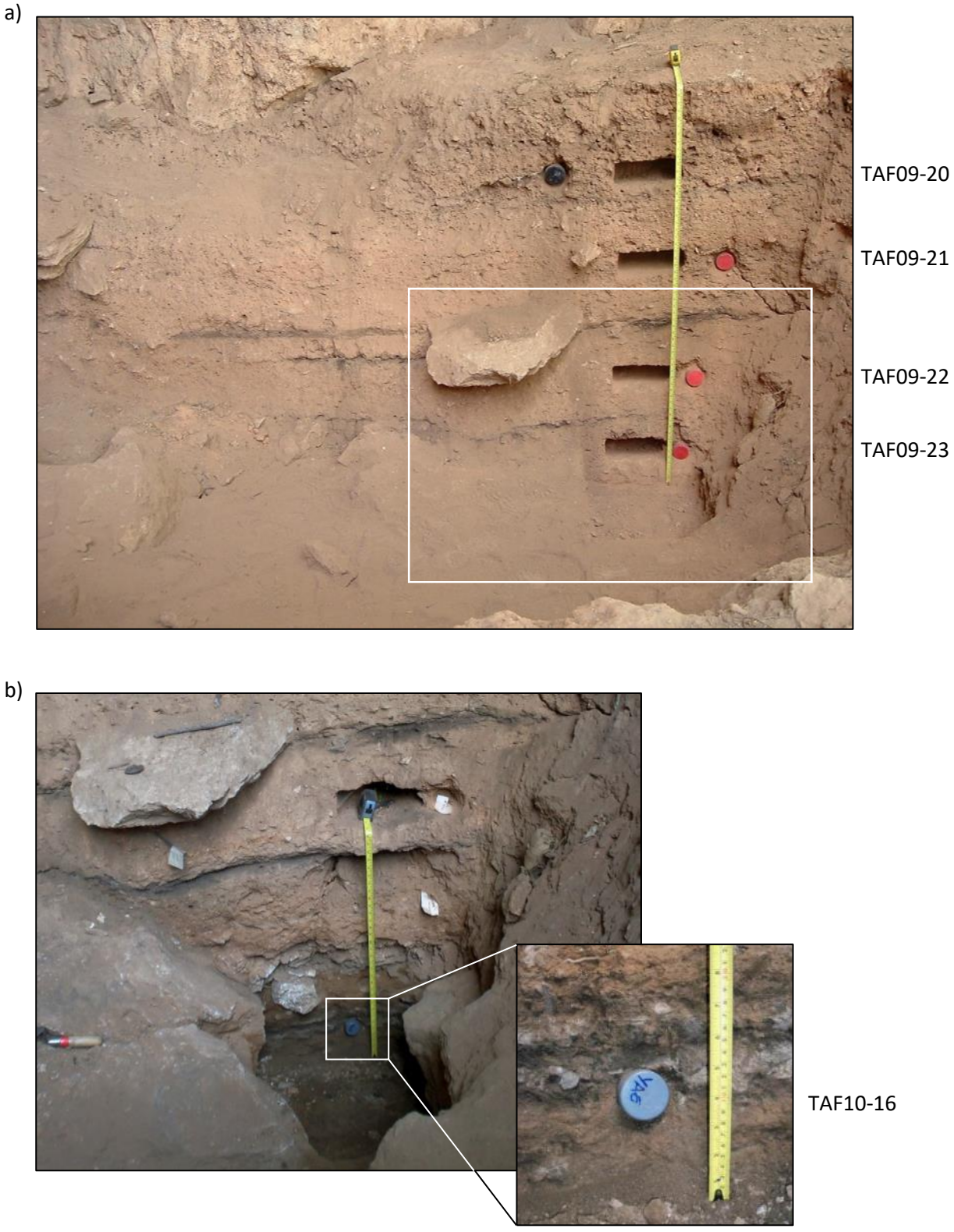


**FIG. 3-16.** General view of Sector 9 (towards 'Site East'). a) Samples collected in 2009, with white box indicating position of image shown in (b). b) Sample collected in 2010 from laminated hearth deposits.

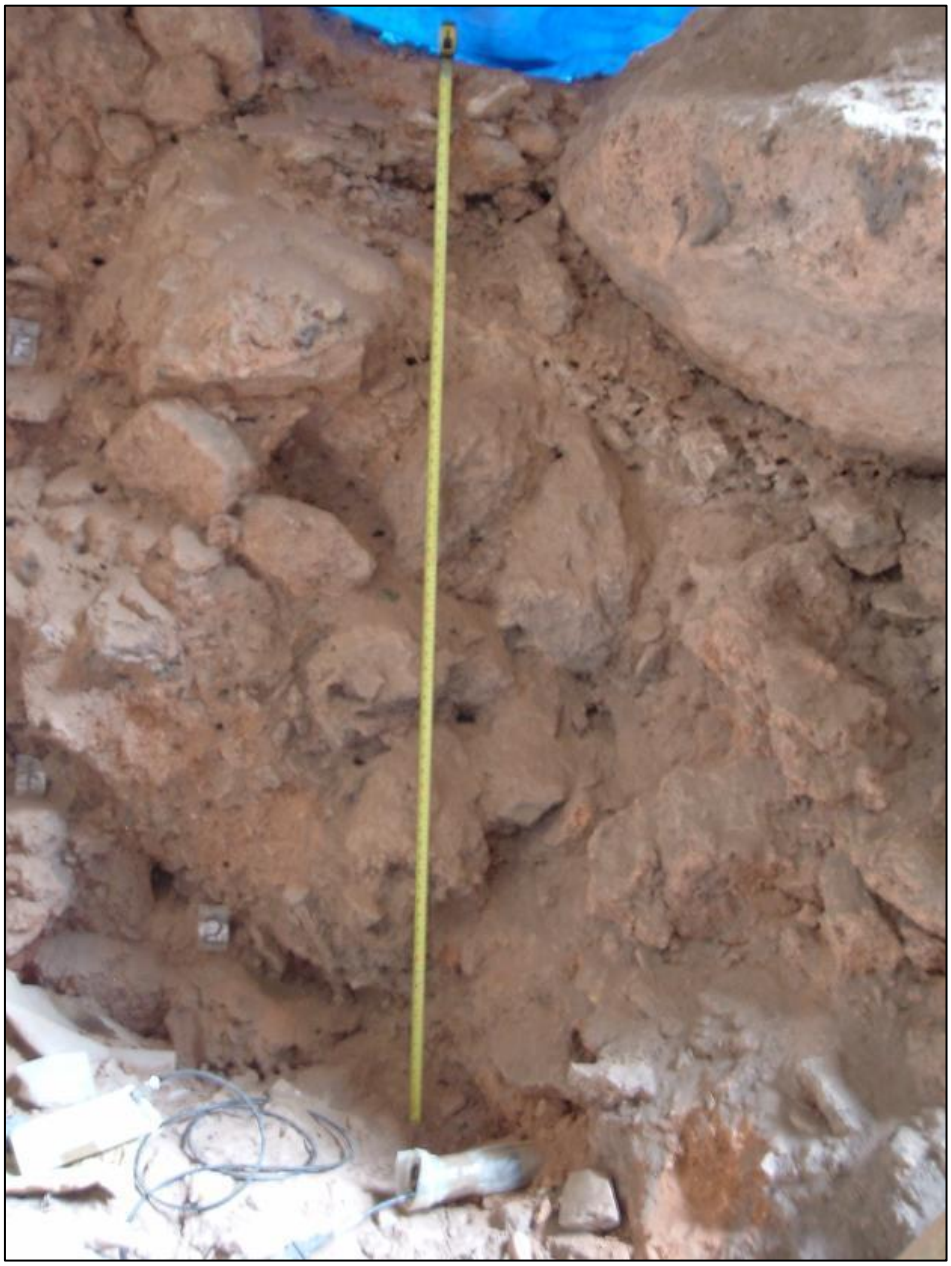

**FIG. 3-17.** TAF09-34 location (gamma spectrometer) at the base of Sector 12; photograph taken towards 'Site East.'


**FIG. 3-18.** A composite image showing TAF10-01 collected at the base of the Deep Sounding. The inset cave plan shows the direction of the photograph (towards 'Site South').

Weathered Bedrock

A standard sample (TAF-EXP-01) was collected from the hillside above the cave. The sampled sediment was extremely weathered limestone, which may have served as a source of material for the cave if transported by water through fractures in the bedrock.

### 3.2.2 Dar es-Soltan I

Dar es-Soltan I (33˚58'44" N, 6˚53'51" W) is a cave eroded from a calcarenite cliff on the Atlantic coast of Morocco, near Rabat (Fig. 3-19). It lies approximately 260 m from the modern shoreline, with the exterior oriented towards the sea (heading 300˚). The cave has not been fully excavated, nor has bedrock been found at the bottom of the interior deposits, but it is at least 43 m deep, 6 m wide, and contains more than 8 m of deposits (Figs. 3-20, -21). It is one of a series of nearby caves, which include Dar es-Soltan II and the recently discovered Kehf Ayrod (Barton et al., 2009).

Dar es-Soltan I lies in the infra-Mediterranean biozone. It is more temperate than the interior of Morocco, with an average maximum temperature of ~27°C in August and an average minimum of 8°C in January. The Rabat area typically receives over 550 mm of rain per year, with heaviest rainfall in November and December (Hong Kong Observatory, 2012).

The original and most extensive excavations in Dar es-Soltan I occurred in 1937 and 1938, led by Dr. Armand Ruhlmann from the *Inspection des Antiquités du Maroc*. His excavation notes, published posthumously in 1951 as 'La Grotte Préhistorique de Dar es-Soltan,' identified the cave as an important Aterian site. No further work was conducted until recently. In June 2005 and November 2008, a combined expedition from the Institut National des Sciences de l'Archaélogie et du Patrimoine (Morocco) and the University of Oxford reappraised the site, analyzed Ruhlmann's excavation collections, and collected samples for dating and palaeo-environmental analysis.

a)

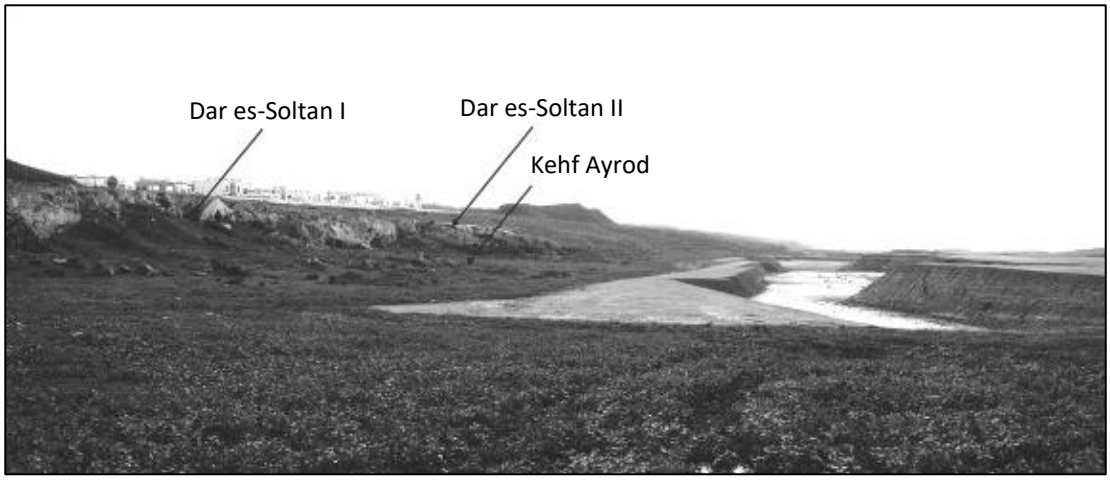


b)

**FIG. 3-19.** Exterior views of Dar es-Soltan I. a) This view of the sea front shows Dar es-Soltan I in relation to Dar es-Soltan II and the newly discovered Kehf Ayrod. Extensive recent landscaping is visible in the image, adapted from Barton et al. (2009: 1916). b) The mouth of Dar es-Soltan I is shown in the calcarenite ridge, with modern development behind.

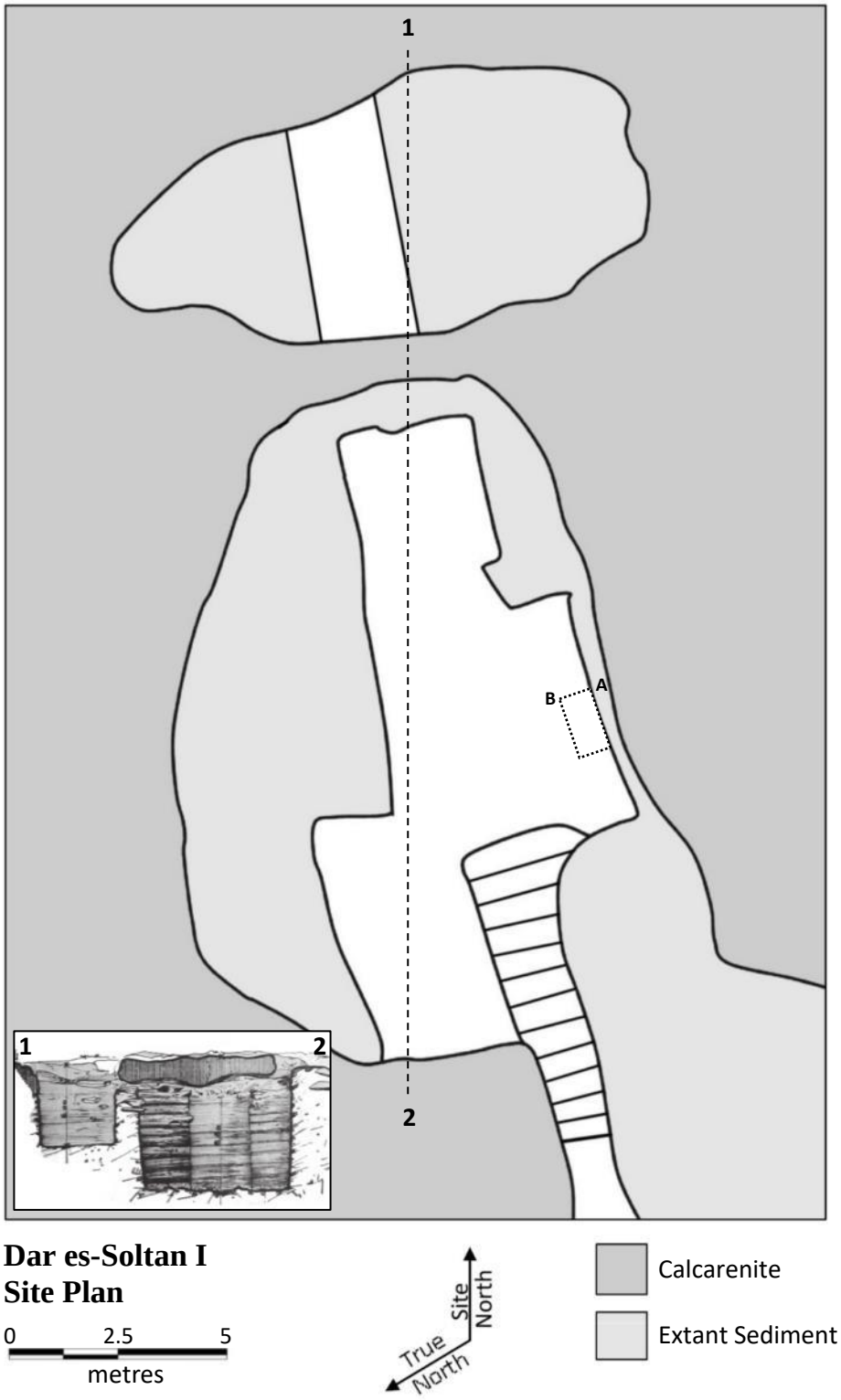


**FIG. 3-20.** Site plan for Dar es-Soltan I (redrawn from Ruhlmann, 1951: 19) and inset section along dashed transect (after Ruhlmann, 1951: 21). A hole in the cave roof is apparent in the plan and section (near point 1). A deeper excavation is outlined by the dotted line. Letters give sample image reference points.

**FIG. 3-21.** A view of the eastern face (site East) taken from the cave entrance. Groups 1 (base) through 5 (top) are visible. Photograph courtesy of J.-L. Schwenninger.

Archaeological analyses are available from Ruhlmann's monograph, and two studies have been conducted upon his collection at the Archaeological Museum in Rabat (Roche, 1956; Barton et al., 2009). Ruhlmann's section was studied by Simon Collcutt in 2005 and 2008, but no further excavation took place. Therefore, all analyses are constrained by Ruhlmann's archaeological understanding. As a consequence, rather than integrating the sedimentological and archaeological information, each is treated separately.

#### *3.2.2.1 Stratigraphy and sedimentology*

The cave infill has been described by Collcutt and divided into five geological groups (starting at the base). Descriptions, chronology, and correlations with Ruhlmann's 'Niveaux' follow the detailed analysis published by Barton et al. (2009) (Fig. 3-22).

Group 1 [Niveaux K-M]

Group 1 sediments are marine-deposited at the base, but aeolian by the top. There is a basal layer of coarse, typically well-bedded shelly sands (>1 m), likely produced by low energy wave action over a long period; the intersection of this layer with the bedrock has not been found. Overlying these sands is a section of reworked coarse sands and some beach rock (0.6 m). The top 0.6 m of Group 1 is composed of alternating strong bands of cemented/concreted sandy clay loams and carbonates, truncated by a cemented angular unconformity. The presence of manganese in this banded series strongly suggests post-depositional chemical alteration. Although Ruhlmann did not identify archaeological finds in this Group, the combined Moroccan/UK team found an undiagnostic, unrolled flake in the basal sands of Group 1 thus demonstrating human presence. OSL ages from this Group are scattered, but Bayesian modeling suggests it was deposited between 123.5 ± 5.4 ka and 144.2 ± 9.1 ka (Barton et al., 2009).

Group 2 [Niveaux G-8]

This group is composed of banded sediments, primarily sandy to silty loams, of slightly over 1 m in depth. Carbonate lenses, small speleothems, and small calcareous growth fallen

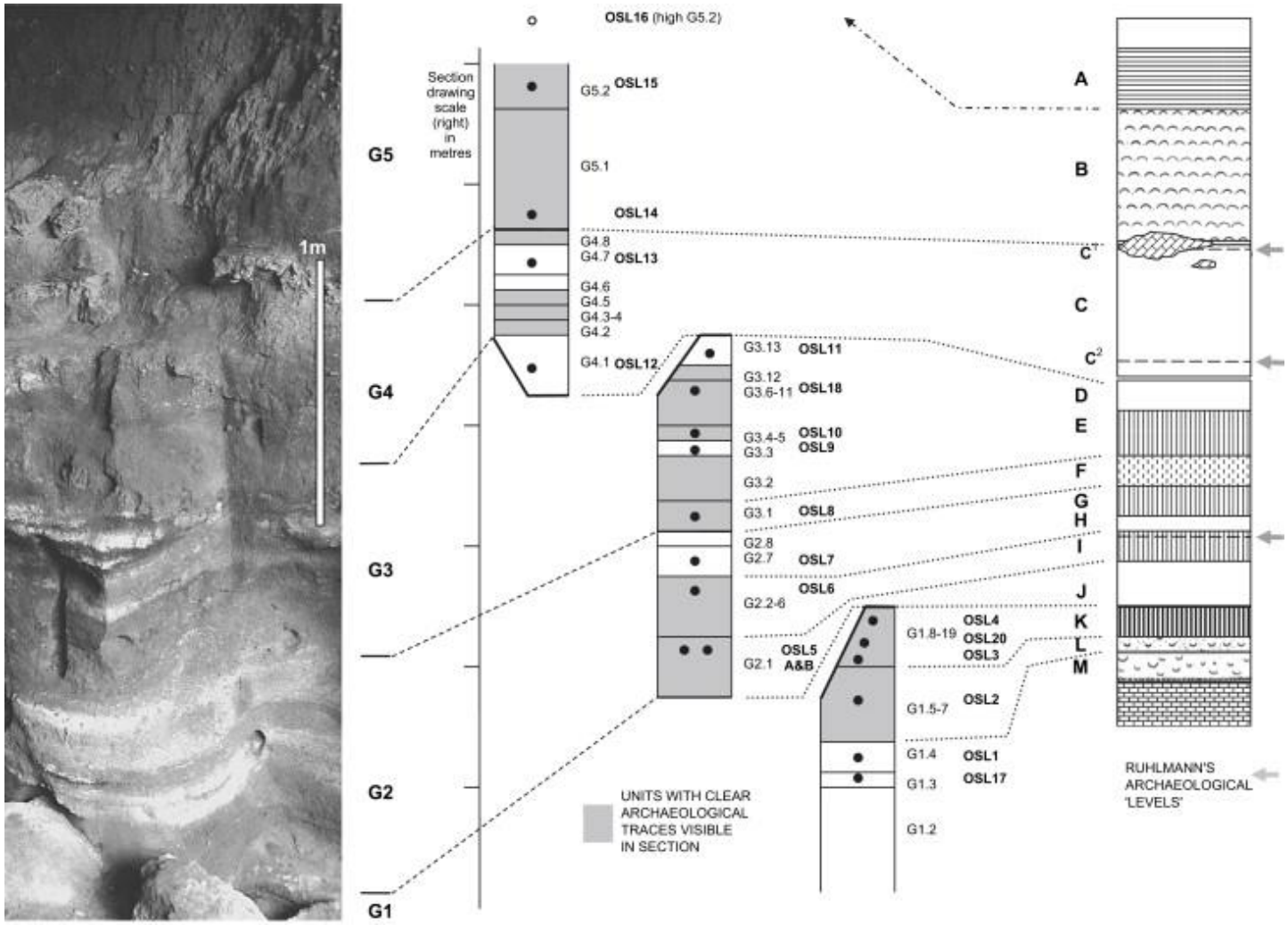


**FIG. 3-22.** Correlation between stratigraphic Groups defined by the recent joint project and Rulmann's (1951) schematic, after (Barton et al., 2009: 1916). Arrows indicate Ruhlmann's archaeological levels, while the grey shading shows locations of archaeological activity noted recently.

from the cave roof are present. Ruhlmann's 'Atérian inférieur' (Niveau I) is found within these sediments. Modeled ages range from 106.0 ± 7.4 ka to 119.1 ± 6.4 ka (Barton et al., 2009).

Group 3 [Niveaux D-F]

Sediments (~1.7 m) are strongly anthropogenic, with repeated burning events, typically cycling through (from the base) brown mineral layers, black charcoal, pink fired material, and creamy ash or carbonate at the top. Bioturbation is clearly present. Modeled OSL ages span 68.4 ± 4.3 ka to 87.9 ± 4.6 ka (Barton et al., 2009).

Group 4 [Niveau C]

The deposit comprises red-brown silty/powdery loams with fine sand and significant erosion troughs. Large blocks of the cave roof, up to nearly half a meter thick and over a meter long, occur frequently near the eastern end of the cave decreasing toward cave entrance. This Group contains both Ruhlmann's 'Atérian supérieur' (C2) and 'Moustérien decadent' (C1). Two OSL samples were obtained, and modeled and raw OSL ages are essentially identical: 51.2 ± 4.0 ka and 52.7 ± 3.1 ka (Barton et al., 2009).

Group 5 [Niveaux A-B]

Near the base of Group 5 is fine, loamy orange sand, with progressively more marine shell towards the top (nearly 1 m). An ashy midden with significant shell components overlies this (>1.5 m). Several pits are dug from this point down into underlying layers, reaching into Group 4 near the cave entrance. The top half meter is grey and stony, but has not been well-studied. This group was deposited over a significant period of time with a high rate of sediment deposition towards the end. Modeled and original OSL ages are again essentially identical. A basal OSL age of 33.0 ± 2.4 ka is obtained approximately 1 m lower than an age of 7.7 ± 0.5 ka, but another >1 m of material accumulated by 6.8 ± 0.4 ka (Barton et al., 2009).

Formation

Analysis of the lithostratigraphy at Dar es-Soltan I suggests that the cave formed via dissolution of previously lithified aeolian sand dunes (Collcutt in Barton et al., 2009), rather than

via wave action as originally suggested (Ruhlmann, 1951). A marine high-stand deposited the basal Group 1 sediments, but sediment deposition during this interval shifted towards more terrestrial sources and aeolian transport. Groups 2-5 are terrestrial and primarily aeolian. Both Groups 2 and 3 show characteristics of a reasonably stable humid and 'biologically-active' environment, with some erosion due to especially wet conditions. Group 4 sediments, by contrast, show less biological activity, more characteristics of aeolian deposition, and significant erosive troughs suggesting repeated water flow; the environment may be more unstable at this time.

#### *3.2.2.2 Archaeology*

Ruhlmann identified four distinct archaeological levels within Dar es-Soltan I: the 'Atérian inférieur' (Foyer I), 'Atérian supérieur' (Foyer C2), 'Moustérien decadent' (Foyer C1), and 'Néolithique ancien' (Foyer B). After these occupations, the cave was abandoned due to a significant rock fall. Based on prevailing archaeological theory at the time, Ruhlmann suggested all identified industries were Upper Palaeolithic; this is now known to be false. The current state of knowledge for each of these is described briefly below, based on the four available sources (Ruhlmann, 1951; Roche, 1956; Barton et al., 2009; Bouzouggar and Barton, 2012).

Aterien inférieur

255 objects were excavated from a 30 cm thick layer (I). The lithic collection has a high frequency of characteristic Aterian points and pedunculate tools (Ruhlmann, 1951), and contains two bifacial foliates and small discoidal cores (Barton et al., 2009). More than 90% of the lithics were produced from flint, with the rest approximately evenly split between sandstone, quartzite, and metamorphic rocks (e.g. diorite). The Levallois technique was used primarily on fine-grained flints (Barton et al., 2009). One flake was produced in hematite, and Ruhlmann recognized two ivory objects. Roche (1956), however, suggested the ivory fragments were produced by natural processes rather than by human activity. The presence of *Rhinoceros sp.* and *Hippopotamus amphibious* in levels G and I indicates the presence of nearby bodies of water

during the Upper Pleistocene (Ruhlmann, 1951). Though Ruhlmann characterized this level as lower Aterian, based on comparison with the next younger industry, Roche (1956) classified it as a middle Aterian (Antoine's Aterian II or III). It is now clear that comparisons of archaeological 'sophistication' are not appropriate chronological or even developmental guides.

Atérian supérieur

This industry is situated 1.65 m above the last, approximately 20 to 30 cm within Niveau C. It comprises 185 objects, which were produced from a more limited range of raw materials than those in Foyer I (Ruhlmann, 1051). Aterian points and pedunculates are still present in high numbers. Bouzouggar and Barton (2012) calculate over 30% of lithics are pedunculates, and this category includes more tool types than previously (Barton et al., 2009). New tools include the 'pointe marocaine,' foliates, and blades. The burins noted by Ruhlmann (1951) are thought to be the product of accidental *siret* fractures (Barton et al., 2009).

Moustérien decadent

This industry comprises 95 objects excavated from the contact surface between Niveaux B and C. It incorporates both new forms (e.g. geometric microliths) and more ancient Mousterian tools. Ruhlmann (1951) believed that this industry corresponded to a local development near the end of Moustero-Aterian evolution, which might explain the lack of a typical Iberomaurusian at the site. Based on a visual assessment of sedimentary residues on tools, Roche (1956) proposed instead that this collection resulted from mixing due to bioturbation (i.e. rodent burrowing). However, Barton et al. (2009) note that the lithics such as bladelet cores are not necessarily intrusive archaeology.

Néolithique ancien

Niveau B is ~2.5 m in depth, and rich in characteristic lithics and pottery. Human remains are present. It is suggested that this is a 'Neolithique de tradition Iberomaurusian.' Faunal remains (e.g. *Rhinoceros simus*) suggest an early Holocene date.

**TABLE 3-2.** Samples collected from Dar es-Soltan I, ordered by field code. The Group and Subgroup are based on recent reanalysis of the lithostratigraphy (Barton et al., 2009), and these have been correlated to Ruhlmann's Niveaux where possible.

| Field Code | Lab Code | Group/Subgroup | Ruhlmann Niveau |
|---|---|---|---|
| DES08-21 | X3469 | 1.4 | M |
| DES08-22 | X3470 | 1.3 | M |
| DES08-24 | X3472 | 1.2 | M |
| DES08-31 | X3479 | 3.2 | D/E |
| DES08-32 | X3480 | 2.7 | G/H |
| DES08-33 | X3481 | 2.6 | I |
| DES08-34 | X3482 | 2.1 | J |
| DES08-35 | X3483 | 2.1 | J |
| SOL1-05-01 | X2376 | 1.4 | M |
| SOL1-05-02 | X2377 | 1.7 | L |
| SOL1-05-03 | X2378 | 1.8 | K |
| SOL1-05-04 | X2379 | 1.16 | K |
| SOL1-05-05A | X2380 | 2.1 | J |
| SOL1-05-05B | X2381 | 2.1 | J |
| SOL1-05-06 | X2382 | 2.6 | I |
| SOL1-05-07 | X2383 | 2.7 | G/H |
| SOL1-05-08 | X2384 | 3.1 | F |
| SOL1-05-09 | X2385 | 3.3 | D/E |
| SOL1-05-10 | X2386 | 3.4 | D/E |
| SOL1-05-11 | X2387 | 3.13 | D/E |
| SOL1-05-12 | X2388 | 4.1 | C |
| SOL1-05-13 | X2389 | 4.7 | C |
| SOL1-05-14 | X2390 | 5.1 | B |
| SOL1-05-15 | X2391 | 5.2 | B |
| SOL1-05-16 | X2392 | 5.2 | B |
| SOL1-05-17 | X2393 | 1.3 | M |
| SOL1-05-18 | X2394 | 3.11 | D/E |
| SOL1-05-19 | X2395* | 4 (no subgroup) | -- |
| SOL1-05-20 | X2396 | 1.10 | K |
| SOL1-05-21 | X2397 | Calcarenite Bedrock | -- |

* Sample collected from weathered portion of fallen calcarenite boulder.


**FIG. 3-23.** Samples collected from Group 1 and base of Group 2 (separated by dotted line). The white outline in (b) shows the location of image (c). Photographs courtesy of J.-L. Schwenninger.

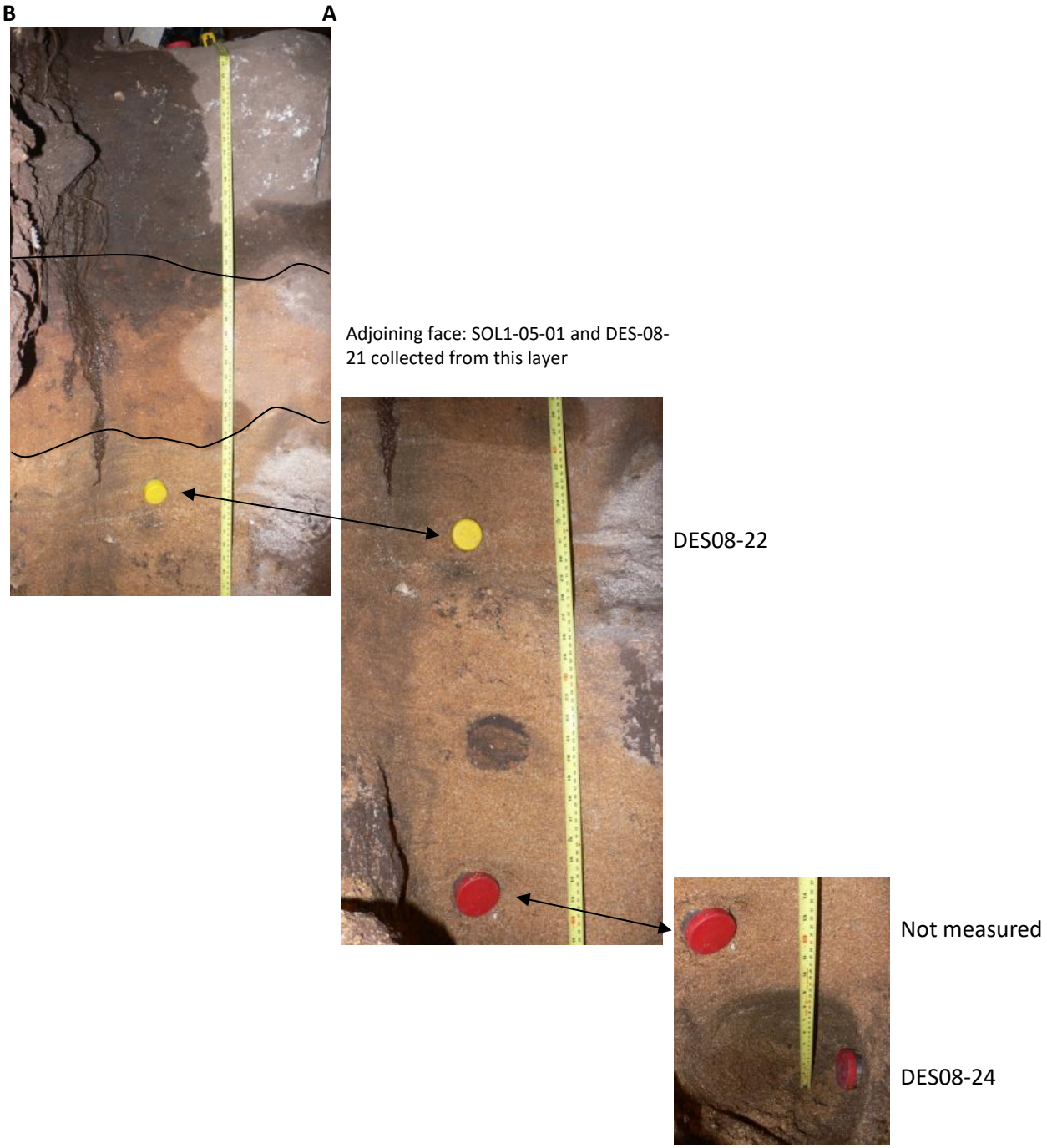


**FIG. 3-24.** Further samples from Group 1. These images show the north (site) face of the trench into Group 1 sediments; transect A-B is shown on the site plan (Fig. 3-20). Photographs courtesy of J.-L. Schwenninger.

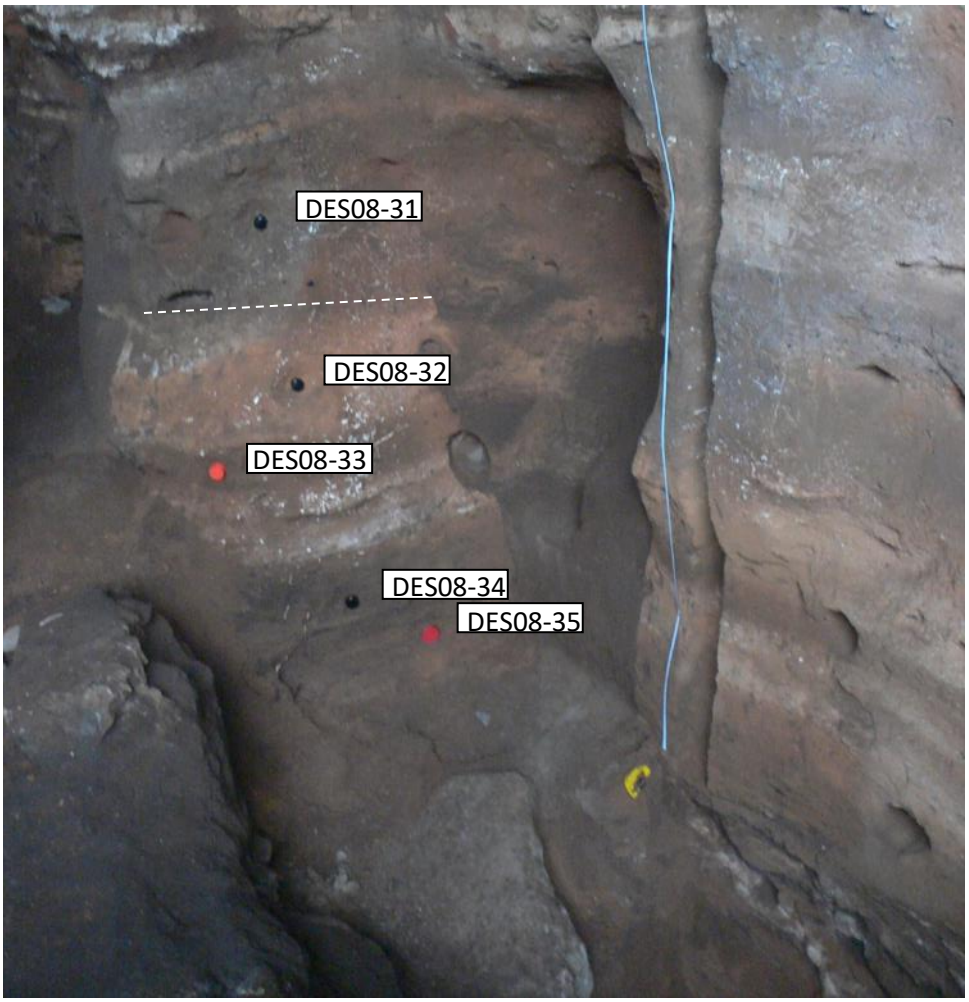


**FIG. 3-25.** Group 2 and 3 samples (separated by dotted line). Photograph courtesy of J.-L. Schwenninger.

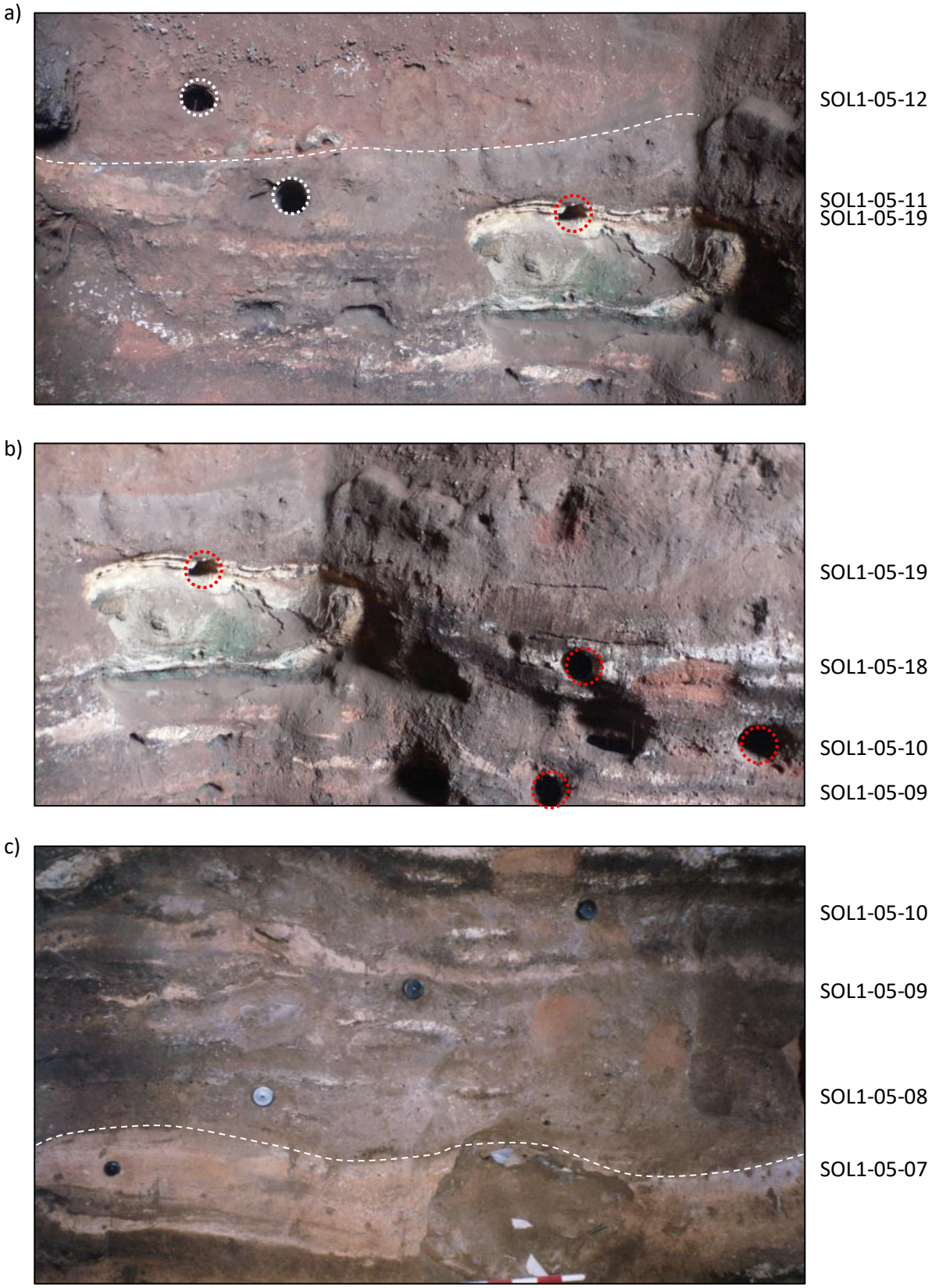


**FIG. 3-26.** Groups 2, 3, and 4 samples shown in overlapping images (a-c). White dotted lines indicate Group boundaries. Photographs courtesy of J.-L. Schwenninger.

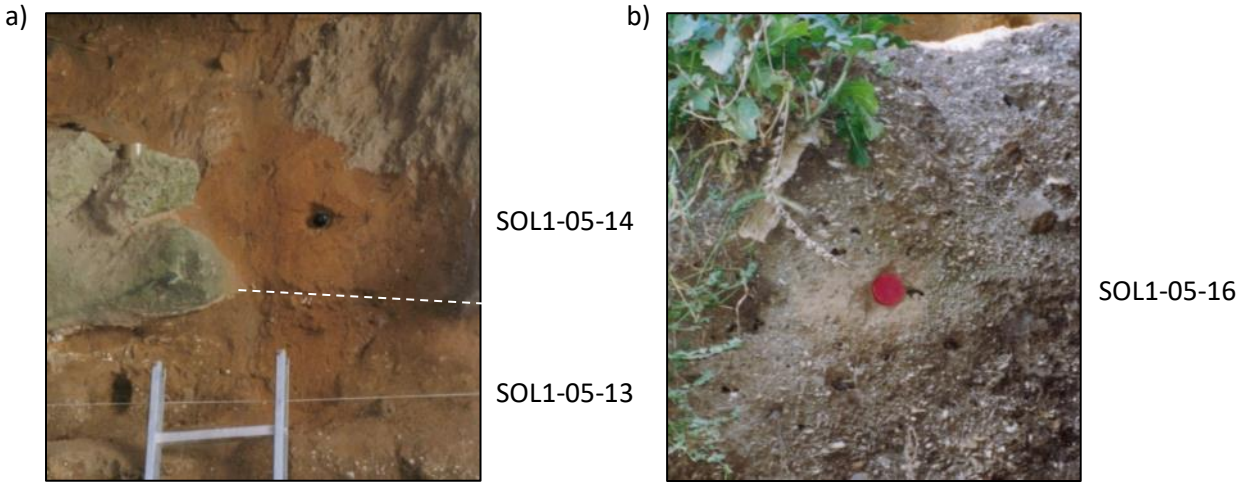


**FIG. 3-27.** Group 4 and 5 samples. a) Cave interior: Top of Group 4 and base of Group 5 (separated by dotted white line). b) Upper Group 5, from western (site) midden at cave entrance. Photographs courtesy of J.-L. Schwenninger.

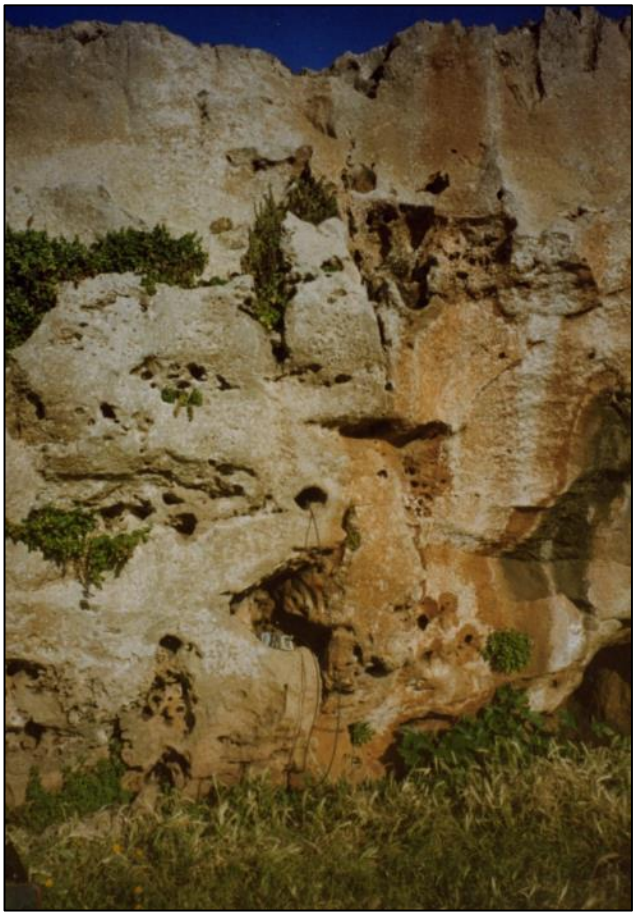

**FIG. 3-28.** Calcarenite bedrock, from which SOL1-05-21 was collected.

#### *3.2.2.3 Sampling*

Dar es-Soltan I was sampled in 2005 and 2008 by Jean-Luc Schwenninger, and a total of 30 samples have been collected (Table 3-2). Standard OSL samples were collected primarily from the southern face of the site. A number of samples were collected from each of the major sedimentary Groups, in order to provide a chronological framework spanning the cave's existence. Stratigraphic layers are clearly visible across the length of the face, so that samples taken in various locations and from both field seasons can be easily associated. Figures 3-23 through 3-28 show sample collection locations.

Prior to this dissertation, twenty samples were collected and analysed with multigrain techniques (Barton et al., 2009), and single grain measurements were made on eight of these (Clark-Balzan, 2007). For this project, previously-obtained equivalent dose data were re-analysed via the automated fitting system coded by the author (see Section 4.2.3), and new multigrain and single grain analyses were performed. Dose rates have also been recalculated for all samples in order to standardize the results.

### 3.2.3 Rhafas

Rhafas Cave is located in the Oujda mountains, within the local dolomitic limestone. It is situated at an altitude of 900 m, overlooking a wide, shallow valley (Fig. 3-29). Its climate is similar to Taforalt, though the increased altitude causes it to be somewhat cooler and more arid. Extensive excavations were carried out by L. Wengler in the 1980's and 1990's (Mercier et al., 2007; Wengler, 1990). Excavations since 2007 have occurred under the auspices of A. Bouzouggar (Institut National des Sciences de l'Archéologie et du Patrimoine Morocco) and the Max Planck Institute.

More than 4 m of sediment fills the ~6 x 10 m site (Fig. 3-30). Wengler (1990; Mercier et al., 2007) has identified four stratigraphic units comprising 72 levels, of which 36 contain archaeological finds. Significantly, the cave contains both Mousterian and Aterian archaeology. Mousterian occupation 'floors' are common until Unit II, level 3a, in which a Proto-Aterian is

found (Mercier et al., 2007). This Proto-Aterian is indistinguishable from the Mousterian except for the presence of tanged lithics; it is only later that the Aterian 'acquires the characteristics of a prehistoric culture in the archaeological sense' (Mercier et al., 2007: 310). The frequency of pedunculates rises in Unit II, level 2, and this is identified as 'Old Aterian.' Five *Nassarius* shell beads have been found at Rhafas, one of which has been excavated from a secure context in the Proto-Aterian level 3a (d'Errico et al., 2009).

A large selection of raw materials is found in all layers, but green quartzite, green schist, and Triassic chalcedony occur most often. Finer-grained material tends to increase over time, but it seems that patterns of selection and transport were generally similar in both the Mousterian and Aterian (Wengler, 1990). Wengler (1993) linked episodes of aridity and humidity to changes in lithic technology, but this should be investigated further in the light of recent chronological data (Mercier et al., 2007; Dörschner et al., 2012).

Two limited OSL/TL dating studies have been carried out at Rhafas. Mercier et al. (2007) dated twelve heated chalcedony lithics from Mousterian and Aterian levels using TL. Most of these TL ages ranged between 60 and 90 ka, and an OSL age of 107 ± 12 ka was also obtained for a sandy loam (level 6d, top of Unit III). The authors suggest that the Mousterian/Proto-Aterian transition occurred at some point between 60 and 80 ka, most probably between 70 and 80 ka, based on these data. More recently, an OSL age of 74 ± 3.6 ka was calculated for the earliest Aterian level (Level 3a) by Dörschner et al. (2012), which supports this chronology.

Dr. Schwenninger also collected several samples from the Aterian levels of the cave infill (J.-L. Schwenninger, Pers. comm.). These have not been dated as part of this project, but two of the samples (RHA-05-01 and RHA-05-02) have been used for preheat plateau tests (see Section 5.3.1). These samples are believed to adequately represent cave sediment characteristics for experimental purposes.

a)

b)

**FIG. 3-29.** Local environment of Rhafas Cave. a) View towards the cave, with arrow indicating cave entrance. b) View from the cave.

a)

b)

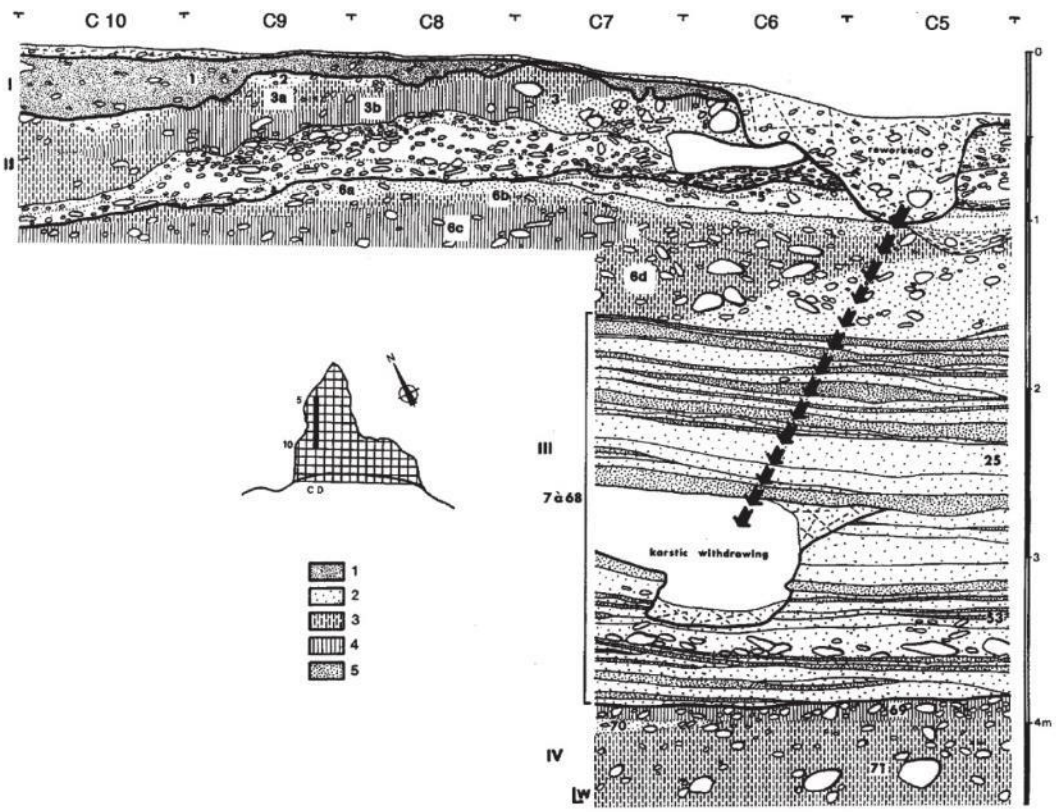


**FIG. 3-30.** Interior of Rhafas Cave from the entrance (a) and site plan (b), after Mercier et al. (2007: 311). The location of the section drawing within the cave is shown in the small inset plan, though that fill has now been removed from the cave as is evident in (a).

#### *3.2.3.1 Rhafas femur fragment*

A fragment of a human femur was discovered during sieving of excavated sediment, therefore its original burial location is unknown. Once found, the femur was cleaned of internal and external sediment and submitted for X-radiography. These X-rays showed a core of remaining sediment within the femur fragment, which was sampled for OSL dating by J.-L. Schwenninger. Though problematic for a number of reasons, OSL dating of the sediment offered the only means of providing a minimum age for the femur via non-destructive techniques. The original burial location may have been re-discovered recently, but further work is necessary to confirm this and analyze the associated stratigraphy (P. Ditchfield, pers. comm.).

Anatomical study is ongoing, but some description is available from a preliminary assessment (L. Humphrey, C. Stringer, pers. comm.). The fragment is a proximal portion of a left femur, measuring approximately 125 mm long (Fig 3-31). It was broken at the base of the lesser trochanter and above the midline (Fig. 3-32). Several chips of bone have been removed at various times in the fragment's history. Overall, the bone fragment presents a polished appearance.

Sampling

The interior sediment plug of the Rhafas femur was sampled by J.-L. Schwenninger during the April 2009 Taforalt field season. Sampling took place within a small interior room with no windows. Opaque, black plastic sheeting was taped around the edges of the door frame to block all exterior light, and working illumination was provided by an amber LED torch (590 nm).

The sediment plug was consolidated, so subsamples could be taken and analyzed separately (Fig. 3-33). To obtain each subsample, a wooden probe was scraped gently over the surface of the sediment. The femur fragment was then tilted, and the dislodged sediment tipped onto a clean piece of aluminum foil. Eight such subsamples were taken: two from the proximal end (A, B), four from the distal end (D, E, F, G), and then the remaining core was


**FIG. 3-31.** Photographs of Rhafas femur fragment. The large pores of the interior trabecular bone are visible in (b). Images courtesy of A. Bouzouggar.

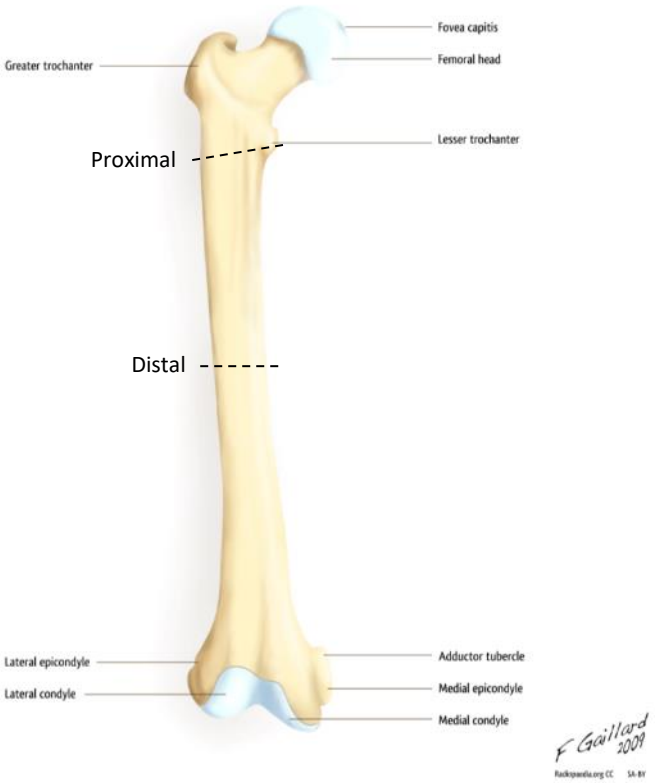


**FIG. 3-32.** Anatomy of a femur (Gaillard, 2009), with (approximate) portion corresponding to Rhafas femur fragment indicated via dotted lines. Proximal and distal ends are labeled.

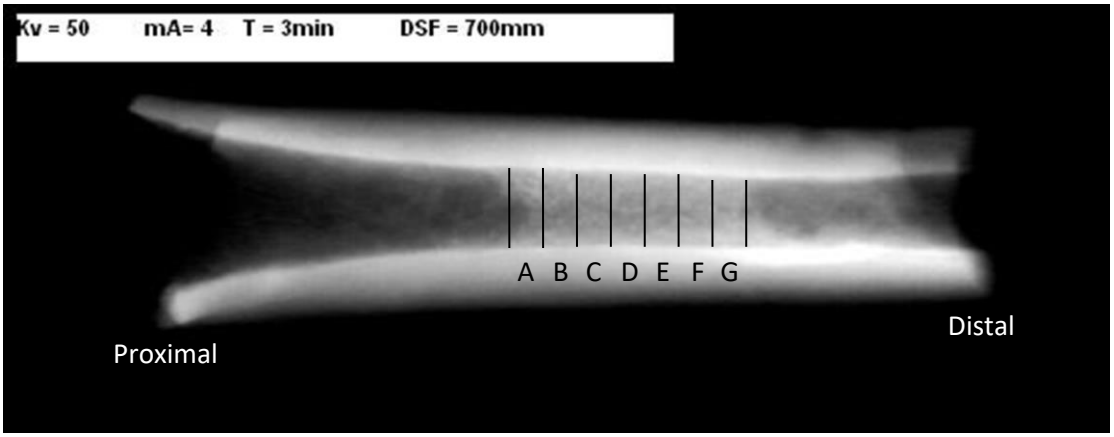


**FIG. 3-33.** X-radiograph of Rhafas femur fragment and sediment plug, with approximate subsample positions indicated. X-ray courtesy of A. Bouzouggar.

dislodged (C). All subsamples were labeled, bagged in opaque plastic, and sealed into an OSL sampling tube for transport.

### 3.2.4 Chaperon Rouge II

Chaperon Rouge I and II are open-air sites, 1 km apart, located approximately 7 km south of Rabat on a small plateau. A 'sandy, pedogenized formation of aeolian origin' at each site yields Aterian artifacts at the base and Ibero-Maurusian artifacts within the layer (Rhodes, 1990: 123). Underneath, brown sandy silts occur at both Chaperon Rouge I and II, though the stratigraphy diverges below (Rhodes, 1990). The climate is temperate, similar to that of Dar es-Soltan I.

Chaperon Rouge I and II were included in two early luminescence dating studies. As part of Rhodes' D.Phil. research on OSL dating, samples were collected at both sites in cooperation with J.-P. Raynal, J.-P. Texier, J-.P. Daugas, and A. Ballouche. These samples were used to test the accuracy of the newly developed OSL technique for sediment dating. Sample locations are displayed in Fig 3-34. At Chaperon Rouge I, the OSL age from sediments 10 cm above the Aterian layer (24,000 +3,050/-4800 ka) and a TL age on heated flint (28,200 ± 3,300 ka) were congruent (Texier et al., 1988). These ages seemed to support the radiocarbon chronology for Aterian sites, as discussed in Section 2.1.9.2.

The Chaperon Rouge locations are the only open-air sites dated in Morocco, and the age of the Aterian seems anomalously young in light of recent chronological studies. Therefore, some of the remaining sediment from sample CR 724 b1 was prepared and measured via modern methods. This sample was collected from the brown silt underlying the Aterian, either via sediment excavation at night or by standard tube collection processes (Rhodes, 1990).

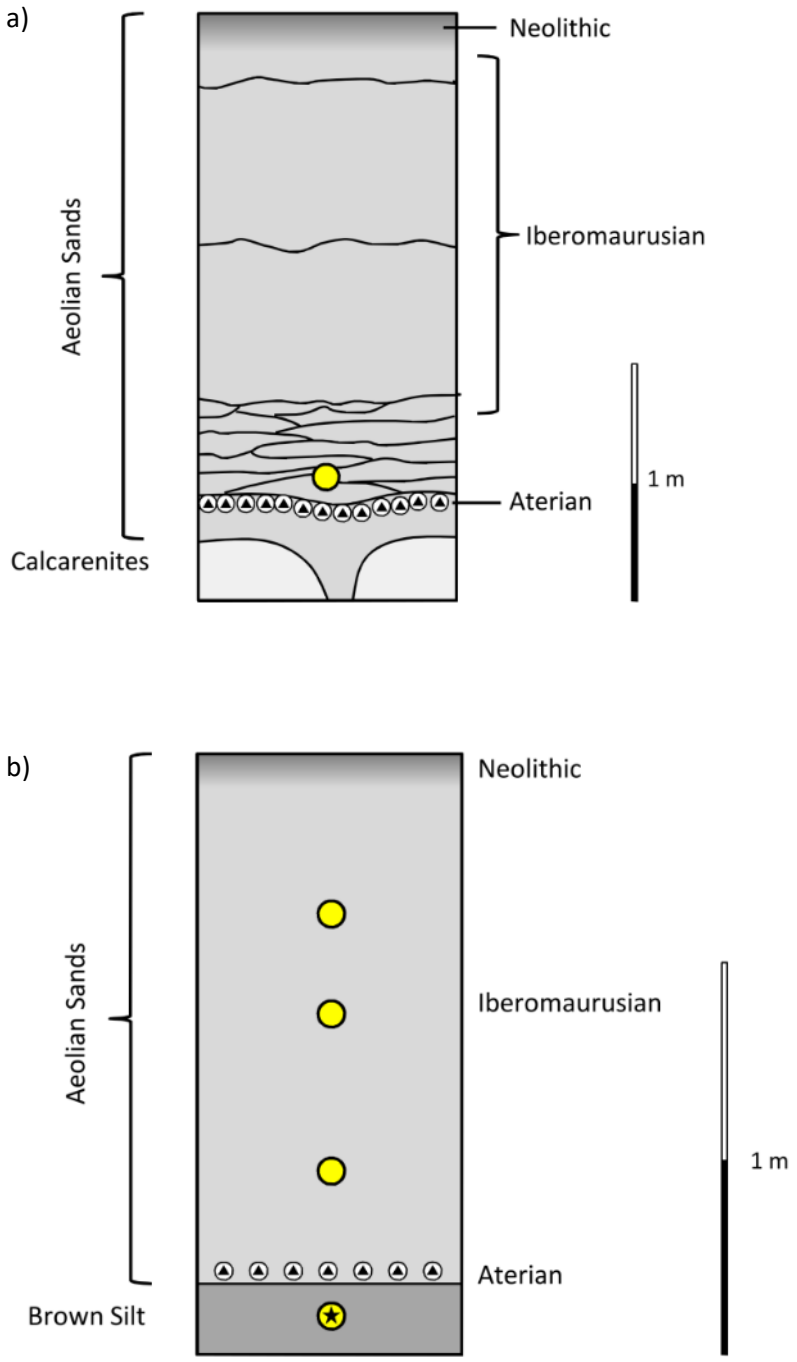


**FIG. 3-34.** Section drawings for Chaperon Rouge I (a) and II (b). Redrawn from Rhodes (1990: 123-124). Yellow circles indicate the location of OSL samples, and the starred circle is CR 724 b1.

# Chapter Four

## *Standard OSL Methods*

This chapter describes the laboratory methods and calculations used to obtain the equivalent dose and dose rate estimates required for OSL dating. Sample preparation procedures, equivalent dose measurement, dose rate calculations, and the creation of Bayesian models for obtaining final ages are discussed in turn.

## 4.1 Sample preparation

After collection, samples were taken to the Oxford Luminescence Dating Laboratory for preparation. The laboratory is illuminated with both yellow-orange and red light sources, comprising filtered sodium lamps (588 nm), LED lights (590 nm), and red-filtered fluorescent lights. All light sources have been thoroughly tested to ensure minimal sample bleaching (M. Telfer, pers. comm.), and light exposure was minimized whenever possible. Between processing steps, samples were kept double-sealed in opaque black plastic bags, and samples undergoing long chemical treatments were shielded from direct light.

### 4.1.1 Sample opening

First, potentially bleached material must be removed from the bulk of the sample. Standard samples, microsamples, and heated cobbles require slightly different approaches.

Before opening, tube samples were weighed. Next, any wrapping (typically cling film or aluminum foil) and end caps (if present) were removed and weighed. The condition of the sample container and interior sediment was noted, including the proportion filled by the sample, evidence for sediment compaction, and any damage to the sample container. The ends of the sample, which may have been bleached during collection, were then removed. A layer of sediment approximately 2 cm deep was removed from either end of the sample tube and set aside. Any loose grains were removed from the tube walls before the core sediment was removed. If a sample was not well-consolidated, one end was removed first. Then a clean scoop was used to remove the bulk of the sample from the tube, leaving the other 'end' in the bottom of the sample tube. Microsamples were processed in the same manner, though less sediment was removed from the ends (~1 cm). To lessen the risk of analyzing partially bleached grains, a slightly thicker layer of sediment (2 cm) was removed from the exterior-facing end, which had been marked in the field. Sample ends were used for dosimetry calculations (see Section 4.3).

For heated cobbles, one must remove the entire outer surface to a depth of several millimeters. This step eliminates bleached material and simplifies dosimetric calculations. Chosen cobbles were coated with black spray paint. After the paint was dry, each cobble was wrapped in several layers of heavy aluminum foil and crushed in a hydraulic press. Fragments with traces of paint were set aside, and the remaining material was retained for dating. If necessary, large chunks were crushed and sorted again. A portion of the removed exterior was washed with acetone to remove the paint, and then ground with an agate mortar and pestle to obtain a subsample for dosimetry purposes.

### 4.1.2 Obtaining mineral extracts

#### *4.1.2.1 Coarse grains*

A combination of physical and chemical treatments were used to obtain mineral extracts of the desired size fraction. These techniques and their purpose are described below, and optional steps are indicated. Unless noted in the results, 180-255 µm grains were used for multigrain and single grain measurements, while 125-180 µm grains were used for 'very small aliquots' (see Section 4.1.3.3).

1. Wet sieving: The sample was wet sieved into five size fractions: 90-125 µm, 125-180 µm, 180-255 µm, 255-355 µm, and >355 µm.

2. Dissolution of carbonates: The desired size fraction was treated with hydrochloric acid (HCl, 10%) to dissolve carbonates, with acid added as necessary until any visible or audible reaction ceased. The acid was then decanted.

3. Grain etching: Hydrofluoric acid (HF, 40%) was used to etch mineral grains. Treatment time depended upon the chosen size fraction: 45, 60, and 90 minutes for 90-125 µm, 125-180 µm, and > 180 µm size fractions, respectively. During treatment, mineral extracts were vibrated on a mechanical shaker to ensure isotropic etching. Post-treatment, the HF was decanted and the extracts were rinsed with deionized water four times.

4. Dissolution of fluoride precipitates: The mineral extract was again treated with HCl to dissolve any fluoride precipitates. It was then rinsed with deionized water, methanol, and acetone, and oven-dried.

5. Dry Sieving: The extract was dry sieved (same mesh size as Step 1) to remove any fractured grain fragments.

Handling microsamples, including both Taforalt samples and the Rhafas femur sample, entailed slight changes to the procedure due to the small amounts of material available. Tube microsamples typically yielded between two and three grams of un-bleached, core sediment for OSL processing. For these, dry rather than wet sieving was used in the first step, in order to

minimize grain loss, and they were etched for 45 minutes in 40% HF. No other changes to the standard procedure were made. The Rhafas femur subsamples were significantly smaller, yielding between 0.03 g and 0.15 g. These were also dry rather than wet sieved, and, after step 2, grains were kept wet in covered, small beakers, so that they were easier to manipulate and transfer between containers. The Rhafas subsamples were etched for only 15-20 minutes with 40% HF, in order to preserve grains. Finally, the samples were not second sieved, as only a few tens of grains or fewer were available for measurement; it was feared that second sieving would lead to the loss of this material. Because alpha dose rates are calculate to be average values between etching end-points (see Section 4.3.1.1.) with large error margins, shortened HF etching times will not affect the final dose rates and OSL ages.

#### *4.1.2.2 Fine grains*

Fine grain extraction was necessary only for the heated cobbles, as all other samples yielded adequate numbers of coarse grains. After removal of the bleached exterior, a small piece of each cobble was tested with hydrochloric acid to determine appropriate treatment. All reacted strongly, therefore, these samples were left to react with 10% HCl until all carbonates had been dissolved. After the cessation of reaction, the resultant material was wet sieved with the standard five mesh sizes mentioned previously, plus a 60 μm mesh. Fine grains, i.e. those grains with diameters <60 μm, were also retained.

The fine fraction was further separated by Stokes' Law settling. All fines were emptied into a beaker, topped with water to 88 mm depth, and then stirred. The mixture was left to settle for two minutes. Then the supernatant (including <29 μm grains) was decanted into another beaker and the sediment left in the bottom (29-60 μm) was labeled and oven-dried for storage. The decanted liquid was left to settle for another 20 minutes, then the supernatant (<9 μm) was poured off and retained for storage. The sediment left in the beaker (9-29 μm) was reserved to make fine grain discs. These grains are larger than those typically used for fine grain analysis (<15 μm), which size fraction is chosen so that the alpha dose attenuation is negligible

within the grain (Zimmerman, 1967). For the grains separated here, dose rate estimation would have required alpha dose attenuation modelling. The two minute settle was performed twice, and the twenty minute settle three times (water added each time) to improve separation. No further chemical preparation was necessary for this polymineral size fraction.

### 4.1.3 Aliquot preparation

#### *4.1.3.1 Multigrain*

Coarse grains

Sample aliquots were prepared by covering the central portion of a thin, flat aluminum disc with a small amount of silicone oil, and inverting the disc onto a small pile of quartz grains. The disc was then tapped on the counter to dislodge any loose grains. This procedure created a monolayer of quartz grains for OSL/TL measurement. Depending on the size of the aliquot (given in mm diameter) and the grain size, a single measurement might combine the emissions from several tens to several thousands of grains. Aliquots measured during this study were generally 1-2 mm in diameter (30-70 grains), but previously prepared aliquots could be larger (e.g. some of the Dar es-Soltan I samples).

Once used, the aluminum discs were cleaned thoroughly for repeat use. Each disc was wiped across clean paper towels to remove adhering grains and then agitated in hot, soapy water. The water was decanted, and the discs were rinsed several times. Deionized water was used for the last rinse. Discs were air-dried, and then inspected in light to ensure no grains or oil residue remained.

Fine grains

A custom sample holder was used to create fine grain discs, comprising a base plate and thick block of aluminum with holes drilled through it. The block was tightly screwed onto the base plate to create wells 1 cm in diameter and 3 cm tall. One aluminum sample disc was placed in each well. A small amount of the 4-11 µm grains was added to deionized water to make a barely cloudy suspension of approximately 1 mg $mL^{-1}$. A pipette with disposable tips was used to

add 1 mL of this suspension to each well. The sample holder was placed into an oven for several days, until dry. The pieces were then unscrewed, and the discs removed for measurement. Both pieces of the block holder were carefully cleaned before reuse, and the aluminum discs were used only once.

#### *4.1.3.2 Single grain*

Special aluminum discs (9.7 mm diameter, 1 mm thick) were required for use with the Risø single grain attachment (Fig. 4-1). These discs comprise a ten by ten grid of pits (300 μm in diameter, 300 μm deep) that hold single coarse grains, and three larger 'location holes' (500 μm wide) for laser positioning. To load a single grain disc, quartz grains were tipped onto the surface of a clean disc. A thinly bristled brush was used to sweep the grains lightly across the surface of the disc, so that some were captured in the pits and the rest were brushed off. Location holes must be kept free of grains. Risø recommends that 180-250 μm grains are used with standard single grain discs (Risø DTU, 2009).

For cleaning, single grain discs were placed on a silver mesh and immersed in a small container of acetone, which was then placed in an ultrasonic cleaner filled with water. After five to ten minutes, the discs were removed and inspected under a microscope. If any grains remained in the holes, the disc was returned to the ultrasonic cleaner. Occasionally a grain could not be removed from one of the grain positions. Such cases were noted, and the equivalent dose measurements made for that position were discarded during data processing.

#### *4.1.3.3 'Very small aliquots'*

For samples with limited quartz, some equivalent dose measurements were made with 'very small aliquots' (VSA's). In this procedure, standard single grain discs were loaded with quartz grains 125-180 μm in size. Grain packing calculations for this size fraction suggest that each 300 μm coarse grain pit could include between four and 12 grains (Arnold et al., 2012), although this will strongly depend on grain shape. Equivalent dose measurements were

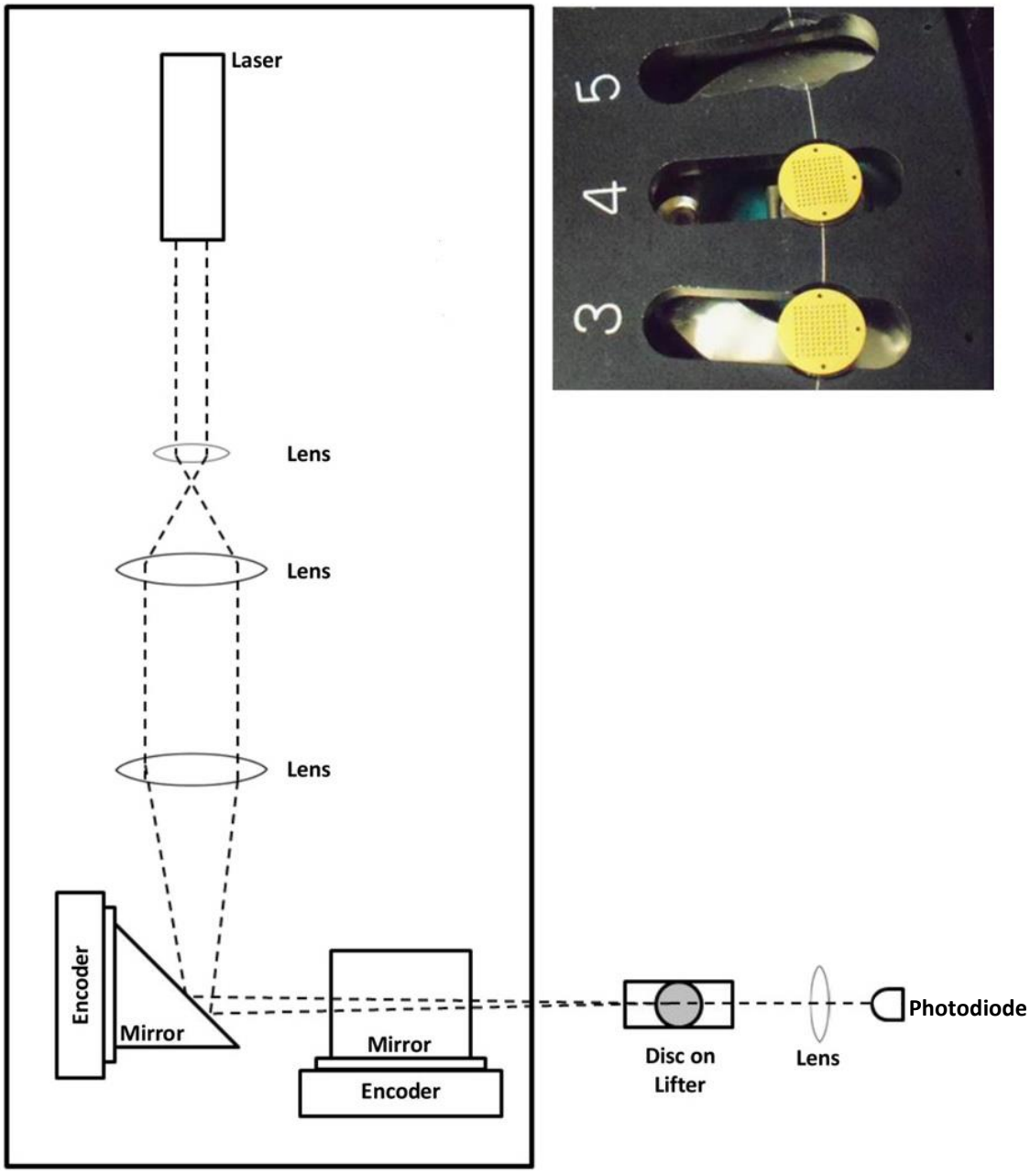


**FIG. 4-1.** Single grain attachment, adapted from Bøtter-Jensen *et al.* (2000) and (Risø DTU, 2009). Two empty single grain discs are shown in the sample carousel, with the lift mechanism (underneath pos. 4) retracted.

obtained via the single grain laser attachment, but these data must be considered as multigrain equivalent doses for the purposes of age model choice (Arnold et al., 2012). Calibration must also be considered separately, which will be discussed in Section 4.2.1.2.

## 4.2 Equivalent dose determination

### 4.2.1 Equipment

#### *4.2.1.1 Specifications*

Equivalent doses were measured with Risø TL/OSL Mini-sys readers. Each reader has facilities for movement, stimulation, irradiation, and emission detection. Once the machine has been programmed with a sequence of movements and measurement parameters (Sequence Editor: TL/OSL for Windows), measurements cycles are automated. The following information is provided from the Risø reader manual (Risø DTU, 2008) or the single grain attachment manual (Risø DTU, 2009), except where noted.

A sample carousel can hold up to 48 aliquots in machined slots, though aliquots were loaded only in alternate positions due to potentially significant cross-talk effects (Bray et al., 2002). Aliquots cycle between two main stations, irradiation and stimulation. A $^{90}Sr/^{90}Y$ beta source provides irradiation (maximum particle energy 2.27 MeV, from $^{90}Y$ decay) at a rate of less than 0.1 Gy $s^{-1}$. Precise irradiation rates depend on the individual source characteristics and the source-sample distance, which can be changed via a lift on some machines. The stimulation station provides both optical and thermal stimulation. Sample discs are lifted into position by a Kanthal strip that also serves as a heater (maximum 700˚C, up to 10 K $s^{-1}$). A thermocouple mounted on the underside of the strip monitors temperature and provides feedback for current regulation. Once lifted, the aliquot is about 25 mm distant from the stimulation LEDs and 55mm from the PMT cathode. It is separated from the emission/detection unit by a clear quartz window, which protects the PMT from aerosolized silicone oil. Specifications for machines used in the project depend on the age of the equipment (see Table 4-1). The emission/detection unit

**Table 4-1.** Equipment specifications for TL/OSL readers used during this project (see text for more details). A 7.5 mm U-340 filter was used to separate stimulation light from OSL/IR emissions for all systems.

| Machine Name | Risø Model | OSL stimulation | IR stimulation | PMT model # (EMI Electronics) |
|---|---|---|---|---|
| Risø 2 | TL-DA-10 | Blue LEDs | Laser diode | 9235/0158/19747.0020 |
| Risø 3 | TL-DA-12 | Filtered halogen lamp | IR LEDs | 9635/0158/17703.0020 |
| Risø 4 | TL-DA-15 | Blue LEDs; Single grain green laser | IR LEDs | 9235/0158/19747.0020 |
| Atlas | TL-DA-15 | Blue LEDs | IR LEDs | 9635/0158/17703.0020 |
| Bacchus | TL-DA-15 | Blue LEDs | IR LEDs | 9235/0158/1498 |
| Cyclops | TL-DA-15 | Blue LEDs; Single grain system laser (green) | IR LEDs; Single grain system laser | 9235/0158/1498 |
| Delphi | TL-DA-15 | Blue LEDs | IR LEDs | 9235/0158/19747.0020 |

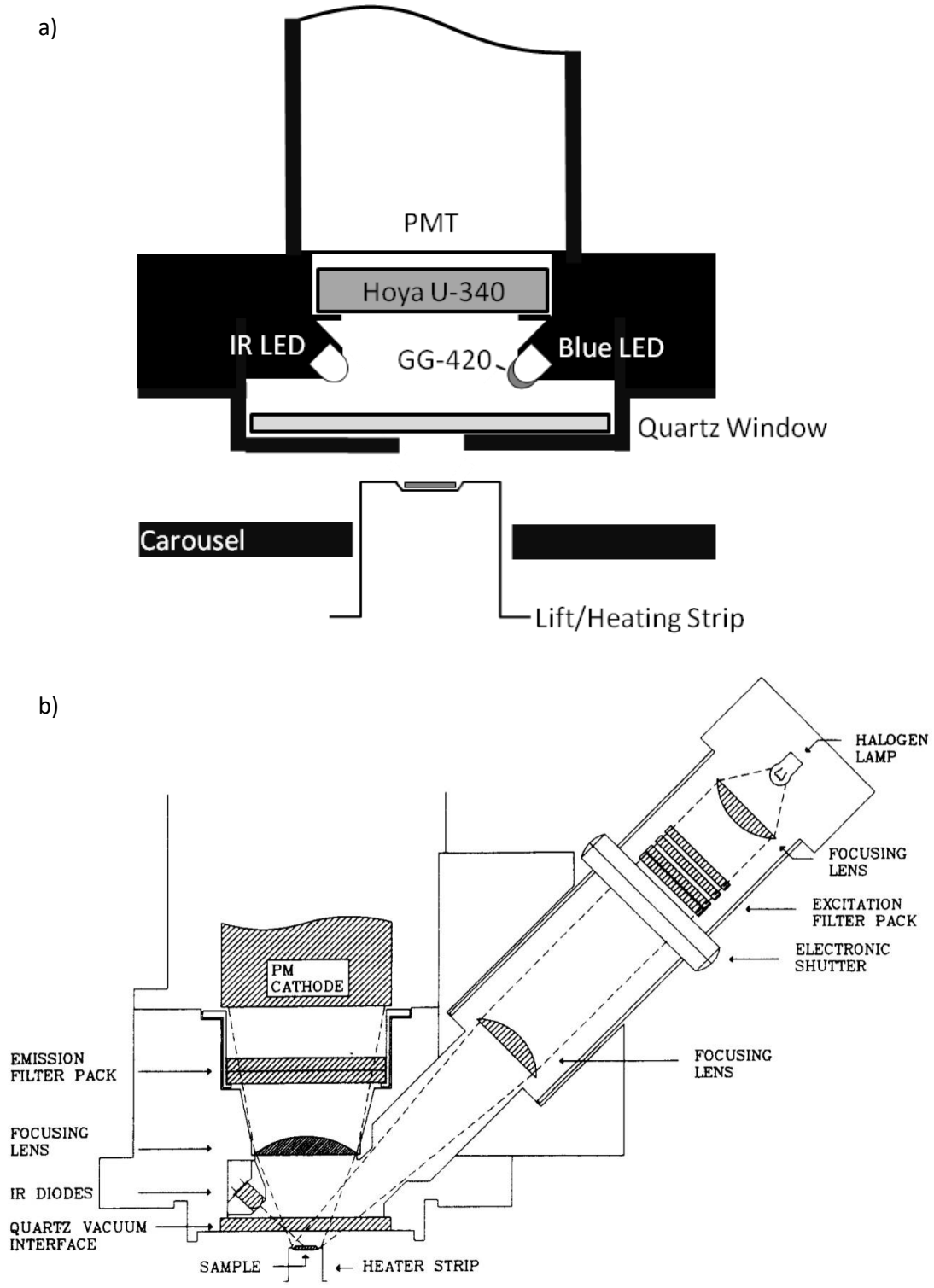


**FIG. 4-2.** Schematic of two types of emission/detection unit. a) Filtered halogen lamp stimulation unit (figure from Bøtter-Jensen and Duller, 1992: 550). B) LED stimulation unit (Bøtter-Jensen et al., 2000; Bøtter-Jensen et al., 2003): clusters (blue and IR) are distributed evenly around the sample. The path of the single grain laser is not shown.

comprises either a filtered halogen lamp (Bøtter-Jensen and Duller, 1992) or a ring of blue and IR LEDs (Bøtter-Jensen et al., 2000; Bøtter-Jensen et al., 2003), filter basket, and photomultiplier tube (PMT) (Fig 4-2). NISHIA blue LEDs (NSPB-500S, 470Δ20 nm) are organized into four clusters of seven diodes, and these provide approximately 35 $mWcm^{-2}$ to the sample. IR stimulation is provided by either a solid-state IR laser diode (830 nm, 200 to 400 $mWcm^{-2}$) or three clusters of seven IR LEDs (875 nm, 135 $mWcm^{-2}$), depending on the age of the machine (Bøtter-Jensen et al., 2000; Bøtter-Jensen et al., 2003). Both blue and IR LEDs are stabilized with a feedback loop during stimulation. A bialkali EMI 9235QB photomultiplier tube (PMT) detects luminescence. Quantum efficiency is highest for this PMT over a range of wavelengths that covers the emission spectrum of ultraviolet OSL and IRSL (Fig. 4-3). Mean dark noise is typically several tens of counts per second.

Appropriate filtering is essential, as it is estimated that the stimulation light is around $10^{18}$ times more intense than the measured emissions (Fig. 4-3) (Risø DTU, 2008). Quartz emission spectra tend to be broad peaks in the ultraviolet centered around 360-380 nm, and feldspars also emit some photons in the near UV. The main filter in the system is a 7.5 mm Hoya U-340 bandpass filter, which blocks blue and IR wavelengths while passing ultraviolet. Maximum transmission is around 75% at 340 nm. Blue LEDs emit a small amount of light in this spectral window, so an additional green long pass filter (GG-420) is inserted in front of each LED cluster.

Two machines have single grain attachments, which include one or more stimulation lasers, lenses, and motorized mirrors for beam positioning (Fig. 4-1) (Duller et al., 1999). Single grain discs have already been described (Section 4.1.3.2). By monitoring reflectance as the stimulation laser makes transects across the disc's positioning holes, the laser can reposition itself with less than 3 μm error in either horizontal direction (Risø DTU, 2009). Stimulation accuracy across samples is controlled by variations in machined discs, which have been reported to have mean standard deviation of 35 μm in x and y directions (Bøtter-Jensen et al., 2000). The

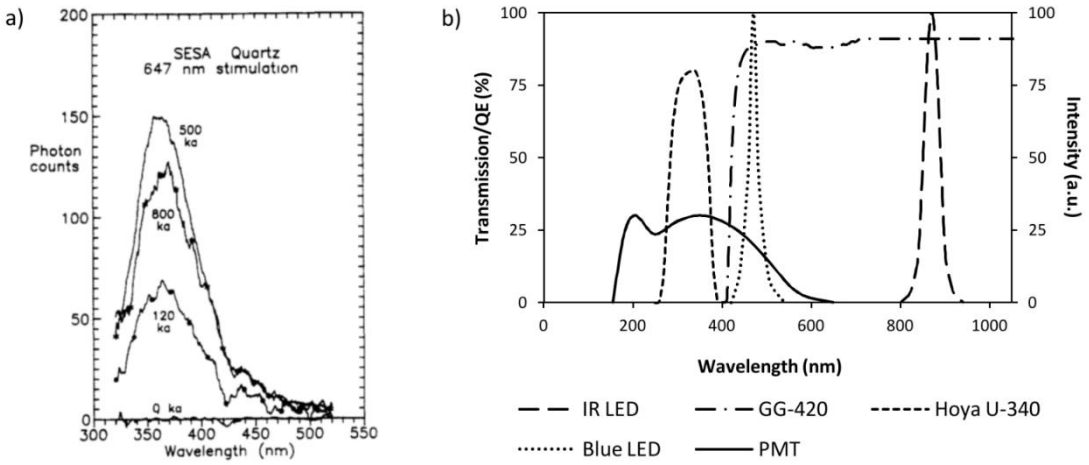


**FIG. 4-3.** Risø specifications: filter transmissions, stimulation light spectra, and PMT quantum efficiency curve. For comparison, typical quartz emission spectra from Huntley et al. (1991: 128) are also shown.

OSL stimulation laser is a green (532 nm) solid state, diode-pumped laser (10 mW, Nd:$YVO_4$), that produces a maximum power density of 50 $Wcm^{-2}$ at the disc. Though the beam is gaussian in density, the optics focus 90% of the power to a 20 µm "spot". The beam is presumed to reflect evenly within each (much larger) grain holding pit, therefore the small errors in a properly functioning single grain system should not significantly affect the final results. One of the single grain attachments also includes an IR (830 nm) single grain laser (150 mW), which uses the same optical focusing and alignment system as the green laser. Maximum energy fluence at the disc is 500 $Wcm^{-2}$. The quartz window below the stimulation unit is removed during single grain measurements.

#### *4.2.1.2 Calibration*

Irradiation sources are calibrated by measuring equivalent doses from aliquots of known-dose quartz ('calibration quartz'). The ratio of the known, given dose to the recovered dose is the dose rate of that machine's source (Gy $s^{-1}$) at the time of calibration. If dose rate $\dot{D}_0$ is measured at time $t = 0$, then the dose rate $\dot{D}$ at time $t$ is given by:

$$\dot{D} = \dot{D}_0 e^{-t \ln 2 / T_{1/2}}$$

where $T_{1/2} = 28.90$ a is the half-life of $^{90}$Sr. Multigrain, single grain, and VSA measurements must be calibrated independently, due to the differing geometries of source and sample. In addition, single grain and VSA data may need calibration factors for each grain position. Because grains are spread across the face of a nearly 1 cm wide disc, relatively small variations in dose can lead to significant systematic differences in equivalent dose (Veronese et al., 2007).

The automated readers used in this study have been calibrated with gamma-dosed, annealed quartz, certified by either the Risø DTU National Laboratory (Denmark) or the National Physical Laboratory (UK). Irradiation source calibrations are kept up to date for each reader in the Oxford Luminescence Laboratory, with new calibrations conducted after a source is replaced or after any refurbishment or alteration to the reader that may alter the source-sample distance. Additionally, the author re-calibrated three Risø readers for multigrain measurements and both single grain attachments (for single grain and VSA measurements). All equivalent doses were generated by the same automated fitting procedures and rejection criteria used for age samples.

For single grain and VSA calibrations, the calibration quartz was first sieved to the appropriate size fraction (180-255 µm and 125-180 µm, respectively), then single grain discs or VSA's were prepared as described above. Equivalent doses were measured and grain position values accepted according to standard rejection criteria. The common age model was used to calculate an equivalent dose (seconds of irradiation) for each single grain disc position, after which raw calibration factors were calculated (known dose of the sample divided by the measured equivalent dose). Finally, the raw calibration factors were fitted with three models:

1. A position-independent central age model
2. A power law relationship suggested by Veronese et al. (2007), with the addition that the maximum dose rate position was allowed to vary across the disc:

$$\dot{D} = \dot{D}_0 \left[1 - a\left(600 * 0.0001 * \sqrt{(x - x_0)^2 + (y - y_0)^2}\right)^b\right]$$

Here, $x$ and y coordinates are schematic, running from 1 to 10, $x_0$ and $y_0$ are the coordinates of the maximum dose rate position, and distances are converted to centimeters.

3. A Gaussian distribution plus planar variability, in order to account for build-up of dose near the center of the source, as well as a highly heterogeneous pattern noted in earlier calibrations.

Residuals from each model were calculated and examined for spatial patterning. The model with the lowest and most random residuals was then chosen in order to calculate final calibration factors.

Single grain calibration measurements have been made for single grain and VSA data on the reader known as Risø 4. The spatial variation of the dose should be similar for the two grain size fractions, though the overall magnitude will be different due to differential scattering and geometry effects. Three single grain discs were measured in March 2008. In addition to the standard rejection criteria, data from one disc of the March 2008 set was rejected due to concerns about anomalous dose responses for a number of cycles. The other two discs of standard grains yielded one hundred thirty accepted measurements, such that nine disc positions had zero measurements, 52 had 1 measurement, and 39 had 2 measurements. Six VSA's were measured in March 2010, of which 386 equivalent dose values were accepted (between one and six values per position).

Median and standard deviation of residuals were similar for all models, but skewness of the residuals was lower for the 'Flat' calibration and there was no particular dependence on disc position. Hence the position independent calibration (model 1) was chosen, and spatial heterogeneity of the source does not seem to be an issue. The standard single grain calibration (March 2008) yielded a calibration factor of 53.642 mGy $s^{-1}$. By accounting for decay rate over the intervening time, this dose rate can be compared to the VSA dose rate measured in March 2010. Coarse single grains are irradiated at a rate 3.5% higher than VSA's.

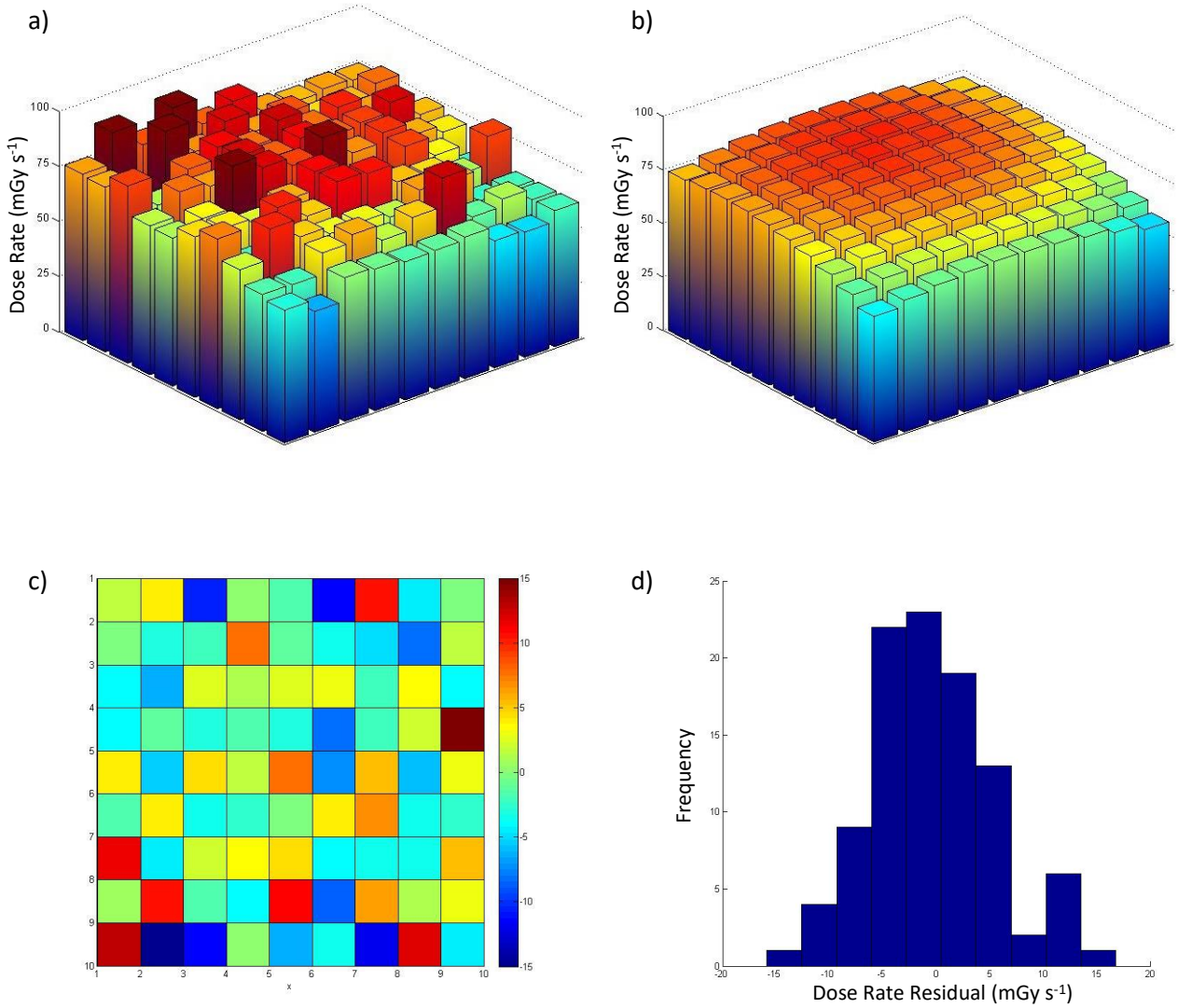


**FIG. 4-4.** Single grain calibration for Risø reader with significant irradiation source heterogeneity ('Cyclops'). Each column indicates a grain position. a) Measured calibration factors, calculated via the common age model. b) Estimated fit (gaussian plus plane). c) Residuals (mGy $s^{-1}$): no spatial pattern is apparent. d) Histogram of residuals.

The other single grain reader ('Cyclops') was calibrated with fifteen discs of standard single grain calibration quartz (180-255 µm) in September 2011. Four hundred fifty-three equivalent dose measurements were accepted, giving between two and nine values per grain position. Results indicated strong spatial patterning in the dose rate, and residuals were smallest for the chosen model 3. The raw calibration factors, model fit, and residuals are shown in Fig. 4-4. Spatial heterogeneity is more pronounced for this source.

### 4.2.2 Measurement fundamentals

#### *4.2.2.1 Single aliquot regeneration*

The current standard procedure for calculating equivalent dose is known as single aliquot regeneration (SAR), in which a unique dose response curve is produced for each aliquot by means of a sensitivity correction (Murray and Wintle, 2000). SAR involves repeated cycles of irradiation and measurement that create a dose response curve with points bracketing the natural signal intensity (Fig. 4-5). The natural signal can then be interpolated onto the curve to calculate that aliquot's equivalent dose. This technique is possible because of the use of a sensitivity correction, in which a small, constant dose ('test dose') is applied and measured after each regeneration dose. The test dose response serves as a normalization factor for each regenerated dose measurement. Thus each point on the dose response curve is the result of a two-part measurement cycle, with the regenerated dose intensity ($L_X$) divided by the following test dose intensity ($T_X$).

In addition to ensuring that the regeneration doses bracket the equivalent dose, two types of dose point are included to test fundamental assumptions of the SAR protocol: the zero-dose and recycled dose points. The zero-dose point is a standard measurement cycle, but with no regenerative irradiation. The $L_X$ / $T_X$ ratio for this point should be near zero, as the traps have not been refilled by ionizing radiation. If the ratio is much greater than zero, then 'thermal recuperation' has occurred, i.e. charge has been transferred from unbleachable traps into bleachable traps by heat. Such an effect cannot be accounted for with SAR normalization and

thus the aliquot results must be disregarded. The recycled dose is another test of suitability, in which at least one regeneration dose is repeated. If the ratio of the normalized intensities ('recycling ratio') for this dose point is near unity, then the test dose correction is succeeding. If not, a fundamental assumption of the SAR protocol is invalid, and the aliquot should be disregarded. These tests form a part of the widely adopted rejection criteria, which will be discussed in more detail in Section 4.2.3.1.

In order that OSL signals from regenerated dose points can be compared with the natural signal, stimulated traps must be stable for periods longer than the sample's age. Preheats and infrared stimulation are used before each OSL measurement (either natural or regeneration) to strip out or identify any unstable components of the signal. Preheating an aliquot involves heating the disc and grains to a specified temperature, usually between 160˚C and 280˚C. This causes shallow traps to release their charge; one such shallow trap may create a '110˚C peak' in the TL signal. This charge population spontaneously decays in slightly over an hour at room temperature (Polymeris et al., 2009). Infrared stimulation, on the other hand, empties traps in quartz at an insignificant rate at typical measurement temperatures (125$^{o}$C) and stimulation power (Spooner, 1994; Jain et al., 2005), but it strongly bleaches feldspars (Huntley et al., 1991). The emitted signal is known as infrared-stimulated luminescence (IRSL). Because feldspars tend to be much brighter than quartz, most of the measured signal from an aliquot incorporating both minerals might be emitted by the feldspar (Jain and Singhvi, 2001). Feldspar signals can fade over time (Wintle, 1973), so this is not ideal. Hence, incorporating an IRSL step before OSL measurement ('post-IR blue/green stimulation'; Banerjee et al., 2001) allows the identification and removal of mixed aliquots (identified by IRSL emission) from subsequent analysis.

For a schematic of the full measurement protocol used in this study, including standard measurement times and temperatures for a multigrain run, see Fig. 4-5. For machines with LEDs run at ~60% of full intensity (due to electrical difficulties), OSL stimulation time was extended to

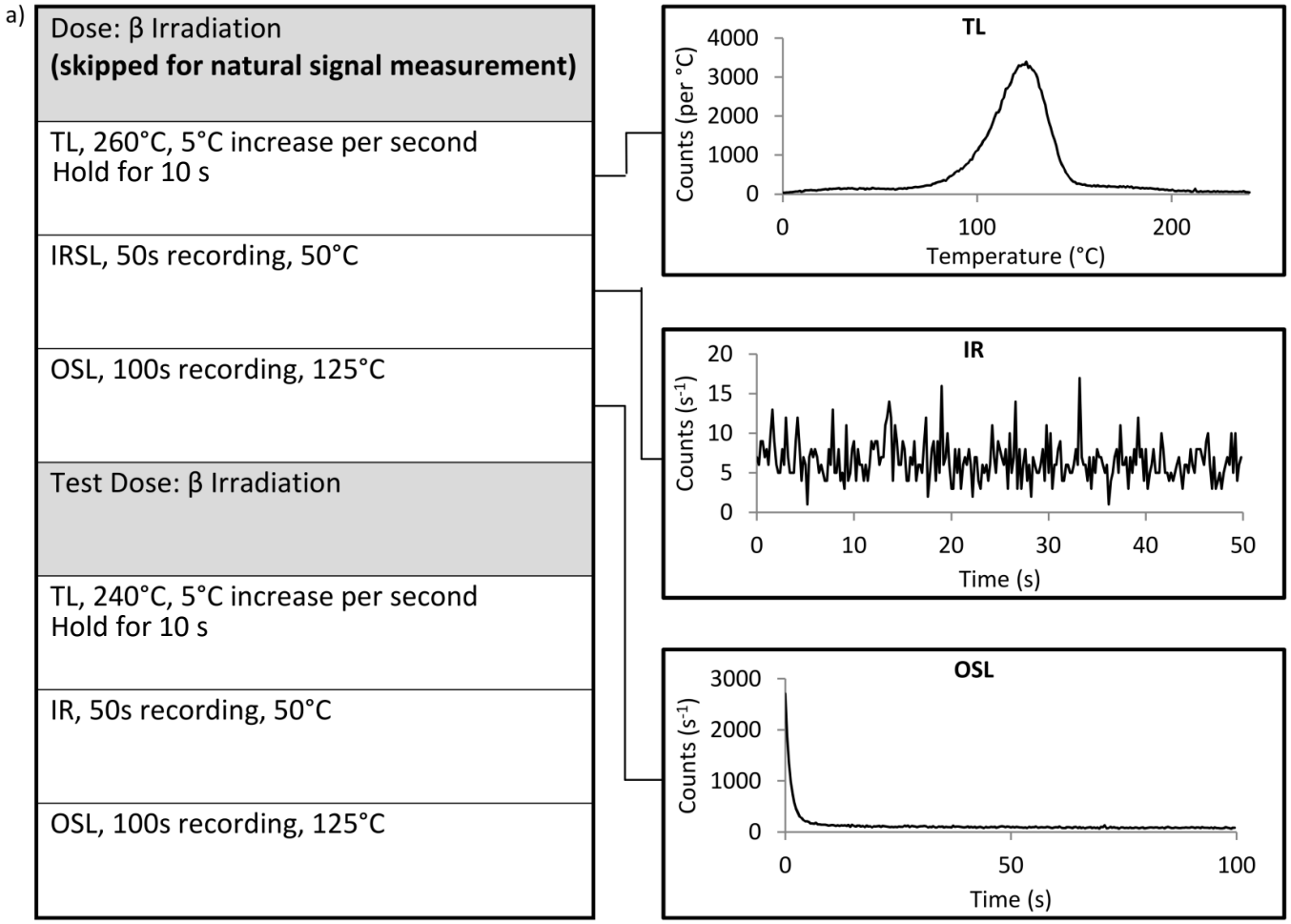


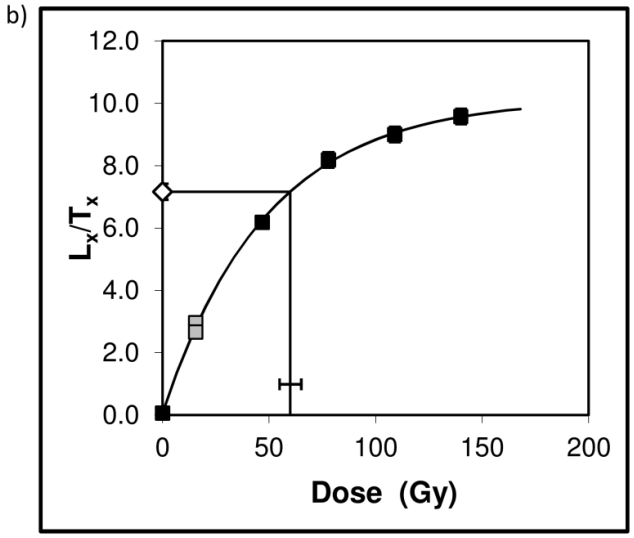


**FIG. 4-5.** OSL measurement schematic (multigrain aliquot). a) The measurement cycle for a single dose point. Typical response curves for TL, IR (feldspar-free sample), and OSL are shown. The OSL intensity (minus the background) after a dose is divided by the intensity after a constant test dose (Lx/Tx), giving the OSL response to a laboratory dose. b) The natural signal is compared to the laboratory dose response (growth curve) to solve for the equivalent dose (i.e., the dose in the burial environment giving rise to the observed natural signal). The recycled dose is shown in light grey. The recycling ratio and zero dose for this aliquot are well within rejection criteria limits.

ensure that similar signal components were analyzed. Single grain runs differed from multigrain runs in preheat temperatures (typically 240˚C for regenerated doses, 220˚C for test doses) and stimulation time (1 s). All other parameters were identical. TL, IRSL, and OSL measurements comprise 250 'data channels,' i.e. measurements made at 250 points equally distributed over the duration of stimulation. Laser OSL measurements are only 60 channel data strings, due to the shorter stimulation period.

#### *4.2.2.2 SAR suitability experiments*

Dose recovery

Dose recovery tests were conducted on representative samples for each site, to ensure that given laboratory doses could be recovered by the SAR protocol. Between six and twelve multigrain aliquots (1-2 mm diameter) or several single grain discs were prepared, then bleached at room temperature (outside) or 25°C (Minisys) for several hundred seconds. Either the Minisys blue LED stimulation unit (typical OSL measurement power) or sunlight was used for bleaching; bleaching times and methods for each experiment are given in Chapter 5. Aliquots were then irradiated with a dose of approximately the same magnitude (i.e. within several Gy) as the sample's measured equivalent dose (central age model value) at that stage in the project. This given dose was recovered using a standard SAR protocol ($260^{o}$ preheat for 10 s on regenerative dose steps and $240^{o}$ preheat for 10 s on test doses), unless specifically noted in the results text. Recovered dose estimates were calculated with the central age model, and these were considered to be acceptable when overlapping a range of 1.0 ± 0.1% at one sigma (similar to the 10% criteria suggested by Murray and Wintle, 2000; 2003).

Preheat plateau

Dose recovery preheat plateau tests were also conducted. Multigrain aliquots were prepared, bleached, and dosed as for dose recovery experiments. Aliquots were then grouped into sets, and each set was measured with a different preheat temperature (between 160°C and

280°C) during dose regenerations. Three or more aliquots comprised each set. A low preheat temperature, e.g. 200°C, was used for all test dose preheats.

### 4.2.3 Data analysis

An automated procedure for equivalent dose calculation was written in MATLAB (Appendix A). It was felt that reducing user input into the fitting procedure was important to improve the reproducibility of results. The automated fitting results were checked for all data by comparing MATLAB-derived results with those obtained via 'Analyst' version 3.24 (Duller, 2007) and an Excel-based fitting program written by Richard Bailey. Regenerative dose point calculation, decay curve form, and growth curve fits were also verified manually for several tens of randomly chosen aliquots during program testing.

During each sequence, the Risø software produced a binary file that contained all recorded measurements (Duller, 2007). These values were read into data structures in MATLAB. Each OSL decay provided a signal and background value. Typically, the first 0.8 s of stimulation comprised the signal, and the last 10 s was used as the background for multigrain measurements (first 0.04 s and last 0.1 s for single grain measurements). Mean background per channel was calculated from the chosen background interval. Net signal intensity was calculated by subtracting the mean background value per signal channel and then integrating over the desired interval. Dose points were obtained by normalizing the natural or regeneration intensity by that of the following test dose ($L_x/T_x$). The relative standard error for the luminescence signal measurement itself was found according to Galbraith (2002):

$$rse(\hat{\mu}_S) = \sqrt{1 + \frac{\hat{\sigma}^2}{\bar{Y}}} \text{ x } \sqrt{\frac{Y_0 + \bar{Y}/k}{Y_0 - \bar{Y}}}$$

$\bar{Y}$ is mean background (over $m$ channels), $Y_0$ is total signal (over $n$ channels), $k = m/n$, and $\hat{\sigma}^2$ is:

$$\hat{\sigma}^2 = s_Y^2 - \bar{Y}$$

where $s_Y^2$ is the variance of the background counts. This equation assumes that there is overdispersion in measured counts that cannot be attributed completely to Poisson processes. To account for random uncertainties occurring during each measurement cycle (e.g. fluctuations in LED power, final sample temperature, and aliquot position during irradiation), 2% error is also added in quadrature for each regenerative dose point.

#### *4.2.3.1 Rejection criteria*

Five rejection criteria were used to assess each grain or aliquot: maximum test dose error, signal size, zero ratio, recycling ratio, and IR response (Fig. 4-6). The first two criteria are related to the brightness of the signal. For maximum test dose error, an aliquot passed if the largest relative error value for the natural test dose was less than 20% of the net test dose signal. The signal size criterion required that the mean of the net natural signal be greater than three standard deviations above the mean background level. Zero ratio, defined as the ratio of the normalized zero dose signal to the normalized natural signal, was required to be either less than 5% or within two standard deviations of zero. Similarly, the recycling ratio is the ratio of the normalized, repeated dose point intensities, and was required to be either within 10% of unity or two standard deviations of unity. The rationale for the recycling and zero dose ratios has been discussed previously. These criteria and values are typical for OSL analysis (Jacobs et al., 2003).

A fifth rejection criterion was used to detect aliquots or grains that had a significant IR response. Multigrain aliquots were considered to have a measureable IRSL signal during the natural measurement cycle if the mean of the net IRSL signal was greater than three standard deviations above the mean background level. Elimination of these aliquots depended upon the sample characteristics, and is discussed further in Chapter 5. For single grain runs in which grains were stimulated individually with the IR laser, this criterion could not be used as some of the brightest IRSL emitters did not significantly decay during the measurement. It was clear, however, that this signal was not due to cross-talk, as the emissions were orders of magnitude

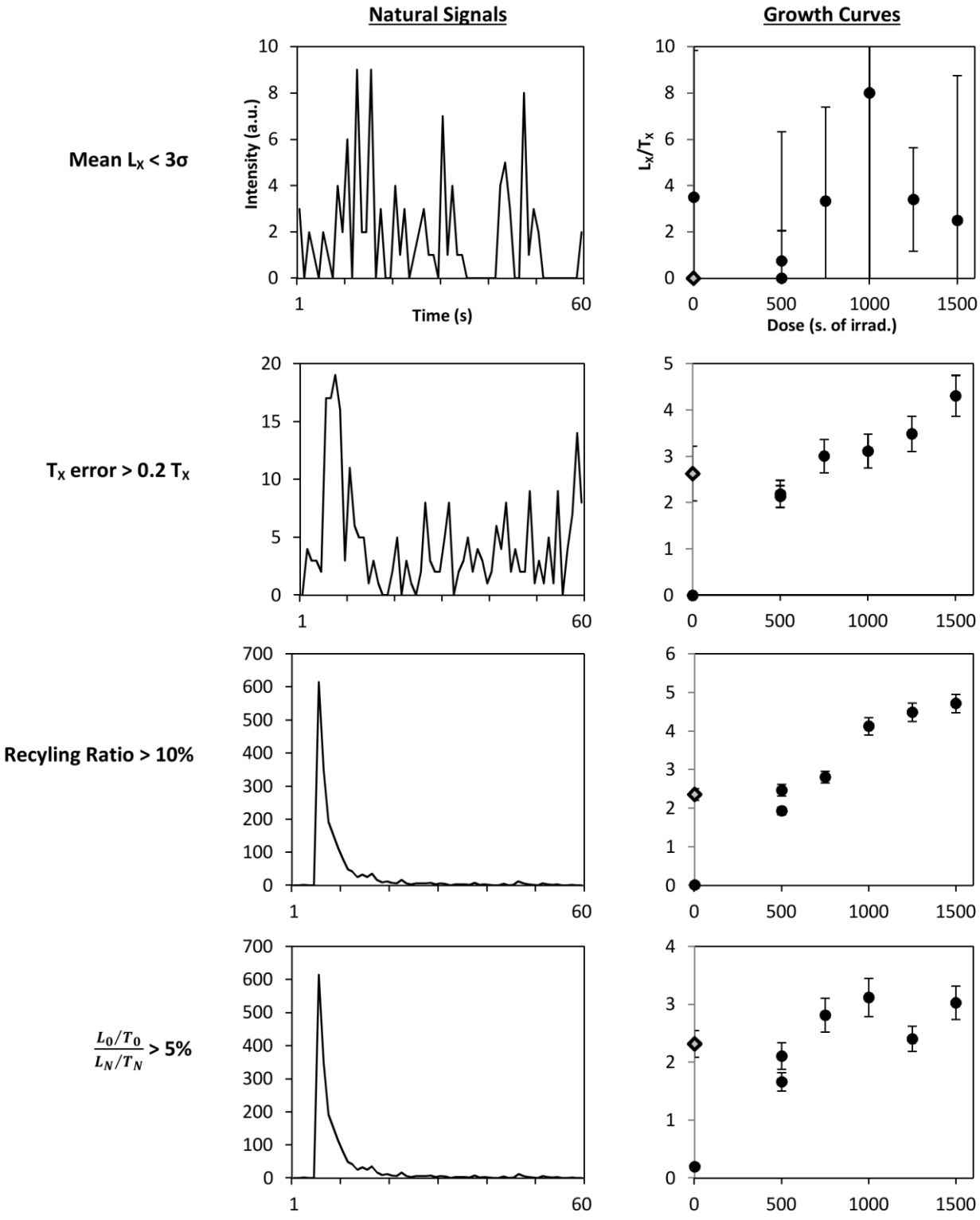


**FIG. 4-6.** Examples of natural signals and growth curves for single grains failing various rejection criteria. The natural data point is the grey diamond, and the recycled dose point is 500 s.

greater than those reported by Duller (2012a) from a systematic cross-talk experiment. A signal threshold value of 50 counts was therefore used to detect emitting grains during IR laser stimulation. Otherwise, if the full single grain disc was stimulated with IR LEDs, IRSL response was noted for analysis. Single grains could not be excluded, however, as it was not known which supplied the IRSL signal.

Grain or aliquot saturation, a state in which all available traps were filled at some point during a sample's burial history, functions implicitly as a rejection criterion in many studies. A disc or grain has reached saturation when the dose response curve no longer rises with increasing dose. A grain or aliquot may be considered in saturation when the normalized intensity of the natural dose response is approximately at the same level as the laboratory dose curve plateau. There is no agreed definition of saturation in luminescence literature, though naturally saturated aliquots or grains are usually discarded. See the next section for descriptions of saturation criteria used in this study.

#### *4.2.3.2 Curve fitting*

Grains/aliquots that passed all rejection criteria were automatically fitted to find equivalent dose ($D_e$) values. First, each dose response curve was fitted with three equations that have been suggested to describe this behavior ('fit-type'): linear, exponential, and exponential plus linear (see Table 4-2). Curve fitting proceeded by chi-square minimization. For calculated regeneration points $y_1 \dots y_n$ with errors $\sigma_1 \dots \sigma_n$ and fit estimates $f(x_1) \dots f(x_n)$, this is:

$$\chi^2 = \sum_{i=1}^{n} \left( \frac{y_i - f(x_i)}{\sigma_i} \right)^2$$

MATLAB's 'fminsearch', which is an unconstrained nonlinear optimization function that implements a Nelder-Mead simplex direct search, was used to perform this fitting. The fit-type with the minimum summed, weighted residuals was then used to calculate the central equivalent dose.

**Table 4-2.** Equations used for curve-fitting of growth curves.

| **Fit-Type** | **Equation** |
|---|---|
| Linear | $Y = ax + b$ |
| Exponential | $Y = a\left(1 - e^{-bx}\right) + c$ |
| Exponential + Linear | $Y = a\left(1 - e^{-bx}\right) + cx + d$ |

A Monte Carlo approach was implemented to determine the error in $D_e$ values. For each cycle, natural and regenerated dose points were randomly chosen from a normal population with mean equal to the calculated $L_X/T_X$ value and sigma equal to the measurement error. The derived dose response curve was fit by minimizing un-weighted residuals, using the Levenberg-Marquardt algorithm implemented in 'lsqcurvefit.' The equivalent dose was then either calculated directly using the solution parameters (linear and exponential fit-types) or by finding the zero of the equation ($f(x = 0) - L_n/T_n = 0$). MATLAB's 'fzero,' which is based upon an algorithm proposed by T. Dekker, was used for this purpose. If the natural signal level never intersected the growth curve, the equivalent dose was recorded as infinite. The error was calculated as the standard deviation of equivalent doses obtained from two thousand such Monte Carlo cycles.

Saturation criteria were developed for dose response curves fit with exponential and exponential plus linear fits. Dose curves fit with a linear equation cannot be saturated since any $L_n/T_n$ value can be mapped to some equivalent dose. Exponential plus linear curves (assuming b>0) will also have no saturation values as long as parameter 'c' in the fitting equation is greater than 0. If c<0, then there will be some maximum intensity point $(x_{max}, L_{max}/T_{max})$, which can be determined. If $L_n/T_n$ is within one sigma of $L_{max}/T_{max}$, the aliquot is saturated, and the natural dose to this aliquot is $(\geq x_{max})$. Similarly, for an exponentially fit curve (b>0):

$$\lim_{x\to\infty}\left(a - ae^{-bx} + c\right) = a + c$$

An aliquot with $L_n/T_n$ within one sigma of $(a + c)$ is saturated, and its equivalent dose can be thought of as $(\geq x')$, where $x'$ is a threshold value such that for $x \geq x'$, $f(x)$is within a given percentage of the asymptotic limit. For this study, 5% was used. These saturation criteria were used as rejection criteria.

In some cases, $L_n/T_n$ was significantly greater than the signal level reached by the aliquot or grain in saturation (according to visual inspection), but shallow exponential plus linear (*c* near 0) curves were fit to the growth curve data. This combination yielded unlikely, high equivalent dose values that visual inspections of these growth curves did not support. These grains or aliquots have been called 'unbracketed' (by the given regeneration doses), and excluded from analysis. They are grouped with saturated and supersaturated types in rejection criteria summaries.

#### *4.2.3.3 Equivalent dose population*

Standard OSL methodology requires that the population of measured $D_e$'s are winnowed down to one value per sample, calculated according to certain assumptions concerning the shape of the underlying distribution (Fig. 4-7). Certain statistical models, such as the common age and central age models, are appropriate for the averaging effects of a multigrain aliquot or VSA data, and others, such as the minimum age and finite mixture models, should only be applied to single grain data. Model choice is an important part of the analysis, as disagreement about the most appropriate model will usually result in considerable differences to the final date. The mathematics underlying each model will be discussed first, followed by discussion of the procedure by which various models were applied to the samples in this dating study.


**FIG. 4-7.** Assumed equivalent dose populations for central age, minimum age, and finite mixture models. The desired equivalent dose is given by either $\delta$ or $\gamma$. See text for futher details.

Common age model

The common age model, introduced by Galbraith et al. (1999), assumes that the logged equivalent dose value ($\hat{\delta}_i$) measured for the $i$th grain/aliquot is equal to the sum of some 'true' value ($\delta$) and an error term. The equivalent dose, $\delta$, is common to all measured grains or aliquots, and individual relative errors ($s_i$) are randomly chosen from a normally distributed population with mean 0 and variance equal to the square of the measurement's relative standard error. By maximum likelihood:

$$\delta = \frac{\sum_{i=1}^{n} w_i \hat{\delta}_i}{\sum_{i=1}^{n} w_i}$$

where $w_i = {}^{1}/_{s_i^2}$ , and the relative standard error is $(\sum w_i)^{-0.5}$. Final $D_e$ and error values are thus $e^{\delta}$ and $s_i e^{\delta}$, respectively. Common age parameters were found via MATLAB software written by the author.

Central age model

The central age model (CAM), also introduced by Galbraith et al. (1999), is similar to the above but assumes that each grain or aliquot may have a different 'true' equivalent dose (e.g. due to microdosimetric effects). These 'true' values are drawn from a normally distributed

underlying population with mean $\delta$ and standard deviation $\sigma$. Maximum likelihood estimation shows that $\delta$ and $\sigma$ must satisfy:

$$\delta = \frac{\sum_{i=1}^{n} w_i \hat{\delta}_i}{\sum_{i=1}^{n} w_i}$$

$$\sum_{i=1}^{n} w_i^2 \left(\hat{\delta}_i - \delta\right)^2 = \sum_{i=1}^{n} w_i$$

where $w_i = 1/\left(\sigma^2 + s_i^2\right)$. Relative standard errors for $\delta$ and $\sigma$ are then:

$$\delta_{Err} = \left(\sum_{i=1}^{n} w_i\right)^{-\frac{1}{2}}$$

$$\sigma_{Err} = \left(2\sigma^2 \sum_{i=1}^{n} w_i^2\right)^{-\frac{1}{2}}$$

The central age model value $\delta$ is understood to be the mean of the logged, true equivalent doses, and is put into the age equation as the sample's $D_e$. The value $\sigma$ is known as the overdispersion, and relates to the amount of scatter in the equivalent dose measurements that cannot be explained by the instrumental error. Final $D_e$ and error values are calculated as for the common age model. CAM calculations for this study were conducted with an Excel spreadsheet created by Richard Bailey.

Minimum age model

The minimum age model (MAM) begins with the same model of true and measured equivalent doses as the central age model, but the underlying distribution of true equivalent doses has a different form (Galbraith et al., 1999). They are assumed to be drawn from a truncated normal distribution, with the point of truncation $\gamma$ giving the minimum equivalent dose of the population. The shape of the distribution is also determined by the parameters $\mu$ and $\sigma$, which can be thought of as the mean and standard deviation of the untruncated normal distribution that is the basis of the model. The final parameter necessary to describe the model

is the proportion ($p$) of grains that have received the minimum equivalent dose. To calculate these values, one must maximize the log likelihood ($L$), given by

$$L = \sum_{i=1}^{n} \ln f_i(\hat{\delta}_i)$$

where $f_i$ is the probability density function of the measured $\hat{\delta}_i$:

$$f_i(z) = \frac{p}{\sqrt{2\pi s_i^2}} e^{-(z-\gamma)^2/2s_i^2} + \frac{(1-p)\left[1-\Phi\left(\frac{\gamma-\mu_0}{\sigma_0}\right)\right]}{\sqrt{2\pi(\sigma^2+s_i^2)}\left[1-\Phi\left(\frac{\gamma-\mu}{\sigma}\right)\right]} e^{-(z-\mu)^2/2(\sigma^2+s_i^2)}$$

$$\mu_0 = \frac{\mu/\sigma^2 + z/s_i^2}{1/\sigma^2 + 1/s_i^2}$$

$$\sigma_0 = \frac{1}{\sqrt{1/\sigma^2 + 1/s_i^2}}$$

and $\Phi$ is the cumulative distribution function of a normal distribution. One may either estimate all four parameters describing the truncated distribution ('four-parameter MAM'), or assume that the truncation point occurs at the 'mean' ($\gamma = \mu$) for the three-parameter MAM. S-PLUS software written by Rex Galbraith was used for this study. Again, the population $D_e$ and error is calculated from these parameters as for the common age model.

Finite mixture model

The finite mixture model is a logical extension of the central age model, in that it assumes the true equivalent dose distribution is drawn from a mixture of several normally distributed populations (Galbraith and Green, 1990; Roberts et al., 2000). Each component population contributes a different proportion of grains and has a different mean value ($\delta_i$), however, all share a common overdispersion value ($\sigma$). The overdispersion value is chosen by the luminescence practitioner. Component calculation is carried out for various numbers of mixed populations, and the maximum log likelihood is used to choose the best fit. The mathematics used in the calculation of the various parameters has not been presented here because of its length and complexity, but see Galbraith and Green (1990) for details.

For a chosen sample, S-PLUS software developed by Rex Galbraith was used to calculate model parameters for two to five components. The best fit was chosen according to the criterion suggested by Roberts et al. (2000), i.e. that the addition of another component had to increase maximum log likelihood by at least two or the model was overfit. Components were analysed in light of site characteristics such as potential for bioturbation, partial bleaching, and microdosimetry (see Chapter 5 for discussion by site). In general, the component with the highest proportion of grains was used as the equivalent dose value for age calculations, as is common in other single grain studies that use the FMM to analyse data from similar environments (Jacobs et al., 2006; Bateman et al., 2007b; Jacobs et al., 2008b). This was considered the most parsimonious approach, as factors that might have created discrete components within the equivalent dose distribution were in general not considered prevalent enough to affect the majority of grains in the studied sediments. The FMM was run twice for each sample, assuming overdispersion values of 20%, as suggested for well-bleached, relatively homogeneous samples (Olley et al., 2004a; 2004b), and 30%, to allow for higher overdispersion due to microdosimetry effects.

Model choice

Each of the models that has been presented assumes that the measured $D_E$ distribution has certain characteristics, and yields different descriptive quantities based on this underlying structure. The common age model, which assumes that all measured grains or aliquots have received the same absorbed dose (subject to analytical error), is unlikely to represent the physical sediment well. Therefore, this model has been used only for laboratory calibration calculations. Of the other models, the central age model imposes the least bias onto the data, and it is typically used for equivalent dose distributions (multigrain, single grain, or VSA) that are not thought to be significantly affected by partial bleaching or bioturbation. The minimum age model, which is strongly biased towards the lowest equivalent dose values, is used to account for suspected cases of partial bleaching (Arnold et al., 2007; Brill et al., 2012). Though the

minimum age model will sometimes yield appropriate results if used on multigrain data (Arnold and Roberts, 2009), the central limit theorem means that multigrain measurements on partially bleached single grain populations will tend to yield normal distributions that overestimate the minimum equivalent dose. Finally, the components calculated according to the finite mixture model have been attributed in some studies to partial bleaching, physical mixing and microdosimetric effects (Jacobs et al., 2006; Jacobs et al., 2011). For many samples, though, it may be difficult if not impossible to attribute individual components to particular on site processes. Moreover, the limited data available on microdosimetry in sediments suggests that these processes are not likely to result in separable equivalent dose components (Nathan et al., 2003).

Model choice therefore depends significantly on site characteristics and which of several sedimentary processes is thought to dominate the measured equivalent dose distribution. As discussed in Chapter 2, no rule for model choice has been found to yield accurate results in multiple settings. Therefore, each site must be evaluated carefully for possible factors including partial bleaching, bioturbation, and microdosimetry, and the results of this analysis used to guide the choice of the most appropriate age model. This study has chosen to use the central age model whenever possible, as it imposes the fewest restrictions upon the data. Nevertheless, other age models are also sometimes applied to the data when deemed necessary. Site analyses and age model results are discussed for each site in turn in Chapter 5.

## 4.3 Dosimetry

Dose rates can either be measured directly for OSL samples or calculated based on information such as elemental concentration in the sediment. When no evidence to the contrary exists, these calculations are made under the assumption that the sample is taken from a homogeneous matrix in which current, measurable conditions mimic the burial history of the sample. This may be termed the ‘standard model’ of luminescence dosimetry. However, this

assumption is one that requires careful consideration and some experimental validation, as dose rate estimation can be a major limiting factor in OSL accuracy and precision.

Standard model derivations of alpha, beta, gamma, and cosmic dose rates are presented first. Corrections to this simplistic assumption, including the presence of spatial dose gradients and time-dependent changes in radioisotope concentration, are discussed next. In each subsection, both physical/chemical laboratory methods and necessary mathematical calculations are provided. It should be noted that the following information does not include calculations for fine grain dosimetry. Fine grain calculations have been excluded because no equivalent dose measurements were obtained from prepared discs (see Chapter 5).

### 4.3.1 Standard model (coarse grains)

#### *4.3.1.1 Alpha dose*

It is possible for alpha particle sources to occur both externally and internally to a quartz grain, though radionuclide concentrations in these two locations generally differ by several orders of magnitude. Due to the short penetration depth of alpha particles in quartz, which ranges from single microns to several tens of microns, dose from external alpha sources is primarily confined to a grain's outer shell. Typically, luminescence studies using coarse grains therefore assume that a standard etching procedure will essentially remove the irradiated portions (Aitken, 1998). Internal sources are likewise often also considered negligible due to the assumed purity of quartz grains. However, these assumptions may not always be warranted.

This study adopts a more cautious approach to alpha dose rate calculation. Alpha dose rate for a quartz grain of a given size was calculated by:

$$\dot{D}_\alpha = \dot{D'}_{Th}\left[w_{Th,ext} \cdot \varphi(d_o, d_e)_{Th} + w_{Th,int} \cdot (1 - \varphi(d_o, d_e)_{Th})\right] + \dot{D'}_{U}\left[w_{U,ext} \cdot \varphi(d_o, d_e)_{U} + w_{U,int} \cdot (1 - \varphi(d_o, d_e)_{U})\right]$$

where $D'$ is the effective alpha dose rate for Th or natural U (Gy/ka$^{-1}$ppm$^{-1}$), $w$ is the measured concentration (ppm) of internal or external Th or U, and $\varphi(d_o, d_e)$ is an attenuation factor dependent upon both the original grain size and the etched size. Full series effective alpha dose

rates were obtained from Adamiec and Aitken (1998: Table 7), which are based upon deposited alpha track length and take into account alpha particles' lower efficiency of OSL production (a=0.1). For internal dose, this study adopts the average values measured by Vandenberghe et al. (2008) for uranium (0.08 ± 0.02 ppm) and thorium (0.18 ± 0.03 ppm). This gives an infinite matrix dose rate of 0.0284 ± 0.0015 Gy $ka^{-1}$, which is larger than that suggested by Vandenberghe et al. (due to their use of a lower a-value) but similar to values chosen by other OSL dating studies (Jacobs et al., 2006; Jacobs et al., 2013). External radioisotope concentrations are based upon ICP-MS measurements. Dependence of alpha dose rate upon etching is shown for both internal and external sources in Fig. 4-8.

Grain attenuation factors for Th and U were calculated according to deposited track length in a spherical quartz grain (Brennan et al., 1991), with alpha particle ranges dependent upon energy (Brennan and Lyons, 1989). This approach assumes spherical grains and isotropic etching, but the authors emphasize that the dose rate results are insensitive to non-sphericity. However, isotropic etching is unlikely (Bell and Zimmerman, 1978) and may significantly affect the average alpha irradiation factor of the etched grain (R. Nathan, pers. comm.). This uncertainty was taken into account by finding attenuation factors for etching end-points, from significant etching to no etching. That is, for grains in the size fraction 180-255 µm *prior* to HF etching that are then second sieved, there are two possible end points:

1) Most alpha-irradiated quartz remaining: no etching, smallest grain size (180 µm →180 µm)

2) Least alpha-irradiated quartz remaining: largest grain etched to smallest grain size (255 µm →180 µm).

The mean of these two values was used as the attenuation factor for all grains in that size fraction, with an error chosen to include both endpoints (see Table 4-3 for boundary case calculations).

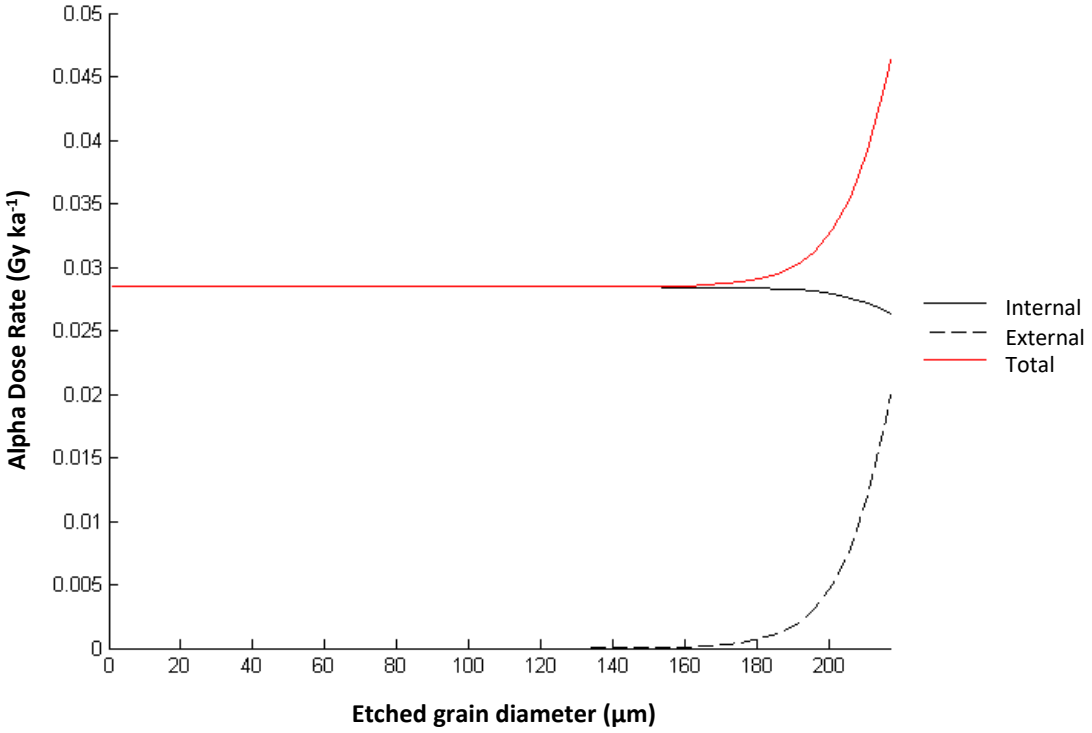


**FIG. 4-8.** The dependence of alpha dose rate values upon grain etching, for a grain with an original diameter of 217.5 µm diameter (average value for 180-255 µm sieved size fraction). Radioisotope concentrations external (1 ppm U, 1 ppm Th) and internal (0.08 ppm U, 0.18 ppm Th) to the grain have been assumed. Removal of the grain's outer 10-20 µm shell excludes nearly all external alpha dose rate.

**TABLE 4-3.** The effect of HF etching on the importance of external alpha dose rate sources. As explained in the text, two etching scenarios (minimum and maximum end-points) exist for a given grain size fraction, assuming first and second sieving with the same mesh sizes. The values in the last two columns give the factor (%) that is multiplied by the infinite matrix external alpha dose rate in order to calculate the external alpha dose rate to the grain. This factor depends on the original and etched diameters of the grains.

| Sieved size fraction (µm) | Original→Etched Diameter (µm) | Th Series (% Inf. Dose) | U Series (% Inf. Dose) |
|---|---|---|---|
| 90-125 | 125→90 | 1.259 | 0.537 |
| | 90→90 | 19.836 | 16.867 |
| 125-180 | 180→125 | 0.139 | 0.026 |
| | 125→125 | 14.398 | 12.212 |
| 180-255 | 255→180 | 0.004 | 0.000 |
| | 180→180 | 10.044 | 8.506 |

#### *4.3.1.2 Beta dose*

Beta dose rates were calculated from radioisotope concentrations using infinite matrix dose assumptions. As all samples were collected at least a centimeter away from visible sedimentary boundaries, this calculation should be valid.

Radioisotope concentration: ICP-MS

Several grams from the light-exposed portion of each sample were retained for ICP-MS analysis. For sediment samples, a portion of the oven-dried ends was used. ICP-MS measurements for the Rhafas femur were made on the outermost layers of the sediment plug. For heated cobbles, chips of the paint-coated exterior were used, after removal of the paint with an acetone rinse. These chips were ground with an agate mortar and pestle.

Elemental concentrations for each sample were obtained through lithium metaborate fusion inductively-coupled plasma mass spectrometry (ICP-MS). This technique involves introduction of a small amount of each sample into a high temperature plasma, which dissociates molecular bonds in the sample and ionizes the constituent atoms. The atoms are then directed into a mass spectrometer, which returns the elemental makeup of the sample. As the University of Oxford Luminescence Lab does not have the necessary facilities, samples were sent to one of three labs: Activation Laboratories, LTD (Canada), the IsoProbe MC-ICP-MS Laboratory at Royal Holloway, or the Scottish Universities Environmental Research Centre at East Kilbride. In calculations, a standard fractional error (5%) is applied to ICP-MS concentrations. Replicate samples and known sediment standards tested over a number of years have suggested that this error limit is appropriate (R. Bailey, pers. comm.).

Conversion of concentration to dose

Assuming that a sample is taken from a region of reasonably homogeneous sediment with a volume much larger than the range of radiation under consideration, this region can be modeled as an 'infinite matrix.' Within this infinite matrix, conservation of energy requires that all energy released by radioactive decay is absorbed. Therefore, energy release is equivalent to

energy absorption, which simplifies calculations. Furthermore, if the matrix is isotropic in both energy release and absorption, one can calculate absorption per unit mass. The steps of calculation of dose rate (alpha, beta, or gamma) from a particular parent radioisotope (Th-232, U-235, U-238, or K-40) are then:

1. Calculate specific activity (Bq $kg^{-1}$)
2. Multiply by amount of energy released of type in decay chain in equilibrium
3. Consider attenuation effects.

Each of these steps is considered in turn, following the discussion of Aitken (1985).

First, it is useful to calculate the dose emitted by a unit mass proportion of each radioisotope. The specific activity, that is, decays per second per kilogram sample (Becquerel per kg, Bq $kg^{-1}$), must be found. The decay constant, $\lambda$ (a $^{-1}$), gives the probability of decay per year for a quantity of isotope:

$$\lambda = \frac{\ln 2}{t_{1/2}}$$

where $t_{1/2}$ is the half-life (a). For one part parent element per million parts sample (ppm, Th or U), the specific activity of the parent is then:

$$SA_{ppm} = \frac{\lambda \alpha N_A}{A_r}(3.17\text{x}10^{-11})$$

in Bq $kg^{-1}$, where $\alpha$ is the isotope's natural abundance, $N_A$ is Avogadro's number, $A_r$ is the isotope's atomic weight and the constant is a unit conversion. Potassium concentration is usually reported by percent mass: 1% is equivalent to 10,000 ppm.

For a decay chain in equilibrium, the decay rate of the parent isotope per kilogram of sample ($SA$) is equal to the decay rate of its daughters. Thus the dose rate due to 1 ppm of parent element is

$$\dot{D} = E_{Tot}\left(SA_{ppm}\right)(5.05\text{x}10^{-3})$$

in Gy $ka^{-1}$, where $E_{Tot}$ is the total energy (MeV) released as radiation of the desired type by all steps in a particular decay chain in equilibrium. Again, this can be adjusted for concentrations

given as percentages. Determining the infinite matrix dose rate is then a simple matter of multiplying the dose rate per unit concentration by the total concentration in the sample. The dose rate conversion values published by Adamiec and Aitken (1998) were used in this study.

Beta radiation from sediment is attenuated as it travels through a grain. The beta attenuation factor, and therefore the proportion of the infinite matrix dose rate actually deposited within the grain, depends on the grain's size. That is,

$$\dot{D}_{\beta} = (1 - \varphi(d))\, \dot{D}$$

where $\varphi(D)$ is the absorbed beta-dose fraction in a spherical region of diameter $d$. A table of $\varphi(d)$ values at selected diameters was published by Mejdahl (1979). To determine values at other grain sizes, the MATLAB function 'spline' was used to interpolate Mejdahl's values for a desired average grain diameter. For a measured sample, the average diameter was calculated as the average of the maximum and minimum mesh sizes used to obtain that size fraction. A standard error of 5% was used for the attenuation values. Error was propagated through the conversion equations in the standard manner.

#### *4.3.1.3 Gamma dose*

Making an infinite matrix assumption to calculate gamma dose requires a homogeneous sphere of sediment around the sample with a radius of about 30 cm. This is rare, particularly within an archaeological site or cave system. Therefore on site gamma spectrometer measurements were made for each sample whenever possible. A scintillation spectrometer of the type used in this study comprises a scintillation crystal and PMT. Incoming gamma rays interact with the crystal, producing photons of various energies centered around a peak corresponding to a particular radioisotope. Gamma rays from $^{40}$K are measured directly, but daughters $^{214}$Bi and $^{208}$Tl serve as proxies for the uranium and thorium series, respectively (Aitken, 1985). This approach assumes radioactive equilibrium.

A multi-channel Ortec MicroNOMAD gamma spectrometer with a three-inch, thallium-doped sodium iodide (NaI(Tl)) crystal was used on site. This spectrometer has been calibrated

against known parent concentrations in the Oxford concrete blocks (Rhodes and Schwenninger, 2007). After each OSL sample was collected, an auger was used to excavate a hole approximately 10 cm in diameter, and more than 30cm long (4π geometry). If the gamma spectrometer could only be inserted between 15 and 25 cm into the sediment face, this was noted. Because the crystal head would not be inserted to the correct distance, the gamma dose measured would not accurately measure the infinite matrix dose. The gamma spectrometer was then left in counting mode for at least half an hour. Each measured spectrum was analyzed by a program written by E. Rhodes, which returns the total gamma dose rate. A standard error of 5% was applied.

Sometimes it was not possible to obtain a gamma spectrometer measurement. This was usually due either to difficulties of physically augering the hole (presence of indurated sediment, large rocks, or flowstone) or because several samples were taken in particularly rich and archaeologically important material which could not be disturbed. One of two methods of calculating the gamma dose was used in these cases. First, a nearby measurement or an average of nearby measurements from similar sediment could be used. Only measurements made within 30 cm, in sediments with similar elemental concentrations (such that their calculated gamma doses from ICP-MS were within 20% of each other) were considered for 'borrowing' or 'averaging'. Qualitative similarity, e.g. the presence of nearby flowstones and boulders, was also considered. Second, the gamma dose rate could be derived from ICP-MS results in the same manner as the beta dose, excluding grain attenuation (see previous subsection). If the surrounding environment was heterogeneous, this spatial variation was accounted for in the calculations (see Section 4.3.2).

#### *4.3.1.4 Cosmic ray dose*

The cosmic ray dose to a sample depends on the geomagnetic latitude and altitude of the site, and the thickness and average density of the sample's overburden. Cosmic dose

calculations follow the steps suggested by Prescott and Hutton (1994), though extra calculations have been included to allow for the soft component.

First, the total cosmic dose ($C_0$) was calculated for the equivalent burial depth at sea level, 55˚ geomagnetic latitude. The hard component contribution was calculated with the Barbouti and Rastin (1983) expression reproduced by Prescott and Hutton (1994):

$$C_{H,0} = \frac{6072e^{-0.00055x\rho}}{((x\rho + 11.6)^{1.68} + 75)(x\rho + 212)}$$

where $C_{H,0}$ is the hard component dose rate (mGy $a^{-1}$) , $x$ is depth (m), and $\rho$ is overburden density (g $cm^{-3}$).

An equation for the soft component was determined from Prescott and Hutton's (1988) Figure 1. Depth and total cosmic dose rate values for each data point were first estimated from the figure. The magnitude of the soft component was determined by subtracting the expected hard component at 50° geomagnetic latitude found via the Barbouti and Rastin (1983) relationship and the appropriate correction values (see below). An exponential relationship was fitted to the remaining soft component, and converted back to the standard 55˚ geomagnetic latitude values. This procedure gives:

$$C_{S,0} = 0.0814 * e^{-2.262\,x\rho}$$

where $C_{s,0}$ is the soft component dose rate (mGy $a^{-1}$) , $x$ is depth (m), and $\rho$ is overburden density (g $cm^{-3}$).

The geographic latitude and longitude of each site were converted to geomagnetic latitude (R. Bailey, pers. comm.):

$$\lambda = \sin^{-1}\left[.203\cos\left(\frac{\pi}{180}\Theta\right)\cos\left(\frac{\pi}{180}(\phi - 291)\right) + 0.979\sin\left(\frac{\pi}{180}\Theta\right)\right] \Big/ \frac{\pi}{180}$$

where $\lambda$ is geomagnetic latitude (degrees), $\Theta$ is geographic latitude (north positive, degrees) and $\phi$ is geographic longitude (east positive, degrees). Finally, the total cosmic dose was corrected for latitude and altitude:

$$C_\lambda = C_0(F + Je^{\frac{h}{H}})$$

where *h* is altitude (km) and *F*, *J*, and *H* are equations for correction parameters based on values provided by Prescott and Hutton (1994) in Figure 2. Equations approximating these parameters were fitted by Richard Bailey:

$$F = (1.347\text{x}10^{-11})\lambda^6 - (2.926\text{x}10^{-9})\lambda^5 + (1.772\text{x}10^{-7})\lambda^4 + (1.106\text{x}10^{-6})\lambda^3$$
$$- (3.319\text{x}10^{-4})\lambda^2 + (2.485\text{x}10^{-3})\lambda + 0.3968$$

$$J = -(1.921\text{x}10^{-11})\lambda^6 + (4.153\text{x}10^{-9})\lambda^5 - (2.492\text{x}10^{-7})\lambda^4 - (1.704\text{x}10^{-6})\lambda^3$$
$$+ (4.714\text{x}10^{-4})\lambda^2 - (3.284\text{x}10^{-3})\lambda + 0.5252$$

$$H = (3.520\text{x}10^{-11})\lambda^6 - (8.412\text{x}10^{-9})\lambda^5 + (6.636\text{x}10^{-7})\lambda^4 - (1.593\text{x}10^{-5})\lambda^3$$
$$- (1.532\text{x}10^{-4})\lambda^2 - (7.488\text{x}10^{-3})\lambda + 4.394$$

The original publication including the F, J, and H values (Prescott and Stephan, 1982) indicated that these were derived for the hard component of the cosmic ray dose. Figure 1 in the same paper demonstrates that the hard and soft components do not share an identical altitude dependence, therefore it might be considered incorrect to apply the F, J, and H correction values to the total dose rather than to the hard component only. Later analyses, however, state that the total measured cosmic ray dose at shallow depths have been corrected with these factors (Prescott and Hutton 1988: pg. 224), therefore this is the approach chosen for this study. Temporal corrections for systematic variation in cosmic dose intensity were not applied for any sites considered in this thesis, as all had geomagnetic latitudes greater than the cutoff of 35° suggested by Prescott and Hutton (1994).

The overburden depth in the previous formulas corresponds to an infinite planar layer of depth $x$ and average density $\rho$, whereas a cave roof of depth $d$ does not shield all samples within the cave evenly. Full calculations of the effect are complicated by cosmic ray path length variation and zenith angle intensity variation, but the overall situation was approximated in this study by applying a skyview ($S$) correction. In this approximation, the total cosmic dose comprised two portions. The first was the proportion that was attributable to cosmic rays

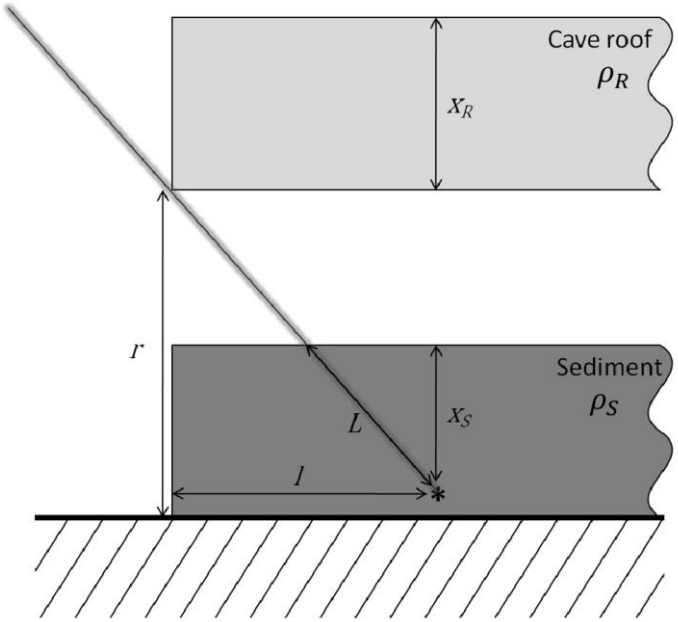


**FIG. 4-9.** Measurements used to calculate shielding correction for cosmic ray dose in caves. The shortest unshielded cosmic ray path is illustrated by the shaded, grey line.

entering through the mouth of the cave (weighted by $S$, the proportion of the sky that was unshielded). Both hard and soft components were calculated for this proportion. The second was that attenuated by both the cave roof and the sediment overlying the sample within the cave (weighted by $(1 - S)$). The soft component is completely negligible for this proportion, so only the hard component was calculated.

For this procedure, the skyview of the sample must first be found. All lengths and depths are given in meters. The cave entrance can be approximated by a half cone with basal radius ($r$) equal to the cave height, and length ($l$) equal to the distance between the sample and the cave entrance (Fig. 4-9). Then the solid angle subtended by the half cone is:

$$\Omega = \pi\left(1 - \frac{l}{\sqrt{l^2 + r^2}}\right)$$

and the skyview of the sample is

$$S = \frac{\Omega}{2\pi}$$

The minimum path-length through ash or sediment ($L_{A,S}$) for a cosmic ray that reaches the sample through the cave mouth is

$$L_{A,S} = \frac{x_{A,S}}{\sin\varphi}$$

where $x_{A,S}$ is ash or sediment depth (m) and $\varphi = \tan^{-1}\left(\frac{r}{l}\right)$. Assuming immediate burial to current depth, the final equation for cosmic dose rate during burial is

$$C_{Tot} = S\left[C_{H,\lambda}(L,\rho_S) + C_S(L,\rho_S)\right] + (1-S)\left[C_{H,\lambda}\left(x_R + x_S, \left(\frac{x_R}{x_R+x_S}\right)\rho_R + \left(\frac{x_S}{x_R+x_S}\right)\rho_S\right)\right]$$

in mGy a$^{-1}$, where the depth and average density ($\rho_S$, density of sediment, and $\rho_R$, density of the cave roof) must be substituted into the cosmic ray component equations. This equation gives a slight overestimation due to the decreasing intensity of muon flux with increasing zenith angle (Bogdanova et al., 2006), but it is serviceable as an approximation.

Errors were calculated via Monte Carlo techniques (5000 cycles). The following standard errors were assumed for model inputs: 5 m for altitude, 5 m for cave roof thickness, 1 m for estimates of distance to the entrance, 0.25 m for estimates of sediment overburden, and 0.2 g cm$^{-3}$ for density measurements.

### 4.3.2 Corrections to the standard model

Real sediment does not completely correspond to the approximations of homogeneity discussed previously. The most common correction factor involves the water content of the sediment, a value that is factored into the standard dose rate equation for every sample. However, there are many other types of spatial and temporal variations in dose rate that may also lead to significant errors in the final age. One's ability to correct for these factors depends first on being able to detect them and second on building a reliable, robust model to account for their effects. Or, conversely, one might show that any effects caused are so insignificant as to be safely ignored in the final analysis. This section will discuss water content corrections, spatial heterogeneity, and temporal variations in sediment.

#### *4.3.2.1 Water content*

The presence of pore water in sediment unbalances the assumption that a mineral grain in a matrix absorbs the same dose (subject to attenuation) from the matrix as the dose that is emitted by the matrix. If one calculates or measures the 'dry' dose rate, a correction factor can be applied to approximate the dose rate at a certain soil saturation level. For alpha, beta, or gamma radiation, the wet corrected dose rate becomes (Aitken, 1985):

$$\dot{D}_{\alpha\beta\gamma} = \frac{\dot{D}_{\alpha\beta\gamma,Dry}}{1 + H_{\alpha\beta\gamma}(WF)}$$

where $(WF)$ is the weight of the water in the sample divided by the sample's dry weight (referred to as 'water content'), and $H_{\alpha\beta\gamma}$ is the particular correction factor for the type of radiation. The correction values used for calculations are the original given in Aitken (1985), though it has been suggested that further analysis may lead to the revision of these factors (Aitken and Xie, 1990; Nathan, pers. comm.).

For determining gamma dose rates, the $(WF)$ value should be an appropriate value for the ~30cm radius sphere surrounding the sample. If on-site gamma spectrometry was used to measure the gamma dose for a sample, then the measured dose rate has already been attenuated by any water present in the environment. If this water content is not near the average value used in the corrections for the beta dose, then the measured gamma dose must be corrected as follows:

$$\dot{D}^{\gamma}_{avg} = \frac{\dot{D}^{\gamma}_{meas}[1 + 1.14(WF)_{meas}]}{1 + 1.14(WF)_{avg}}$$

where $\dot{D}^{\gamma}_{meas}$ is the spectrometer-measured dose rate, $(WF)_{meas}$ is the water content in the sediment during measurement, and $(WF)_{avg}$ is the time-averaged, estimated water content for the sample.

Present-day water content of the sampled sediment is measured by comparing original sediment weight with oven-dried sediment weight. The weight lost due to evaporation is expressed as a percentage of the original sediment weight. Two portions of sediment may be

used for this procedure, the light-exposed ends of the samples or the water content samples taken on site. Most of the samples in this study have corresponding water content samples; where the sample ends were used, this is noted in the results. In several cases, water content or tube samples were taken from the same sedimentary layer in consecutive years. Some of these samples were taken in the drip line, from sectors of the cave that were covered with tarpaulin one year and not the next. These samples were used to estimate 'dry' and 'saturated' water content end points.

In general, water content estimation is more accurate when the water content samples are used, as these have been wrapped to prevent moisture loss. However, this still only provides a single measurement of a potentially highly variable parameter, with significant seasonal and general climatic-based swings. Hence, in most cases a mid-range value with large errors was chosen as the average water content over the burial history of the sample.

#### *4.3.2.2 Spatial variation of dose*

Conversion of radioisotope concentrations to dose rate is complicated by the inhomogeneous nature of a real sedimentary matrix. While variation in the emission and absorption of radiation on the scale of microns may significantly affect the final date via alpha emission heterogeneity or beta dose microdosimetry, evaluation of these effects is beyond the scope of the current study. This section concerns larger scale variation, as microsamples were used to closely bracket boundaries between variable sediment types. Most of the boundary scenarios relevant to this study can be approximated by a simple set of equations relating to planar geometries, which are presented first. More complicated situations, such as that presented by the Rhafas femur, have been modeled via N-Particle Transport codes written by R. Nathan. Each approach will be discussed in this section.

*Planar variation*

The equations governing dosimetric gradients in a variety of planar geometries can be derived from one basic scenario: that of an active sediment (A) next to an inert sediment (B) (Fig

4-10) (Aitken, 1985: Appendix H). The dose at a distance *z* from the boundary (into the active sediment) increases as a proportion of the infinite matrix dose $D_a$, according to an empirical relationship $f(z)$:

$$D(z) = f(z) \cdot D_a$$

By definition, the sediment at depth $z$ would be exposed to the infinite matrix dose $D_a$ if the inert sediment were instead replaced by sediment A. The 'missing' proportion of the dose at depth z is therefore given by:

$$D'(z) = [1 - f(z)] \cdot D_a$$

which must also be the contribution of region A to the sediment at an equivalent depth *x* (*x = z*) in the inert sediment B. Superposition of these relationships can be used to derive the dose for any number of layered sediments. A selection of dosimetry models relevant to this project has been derived by solving for dose rates to infinitesimal planar layers in horizontal cylinders equivalent to tube samples, then integrating to find the average dose rate to the sample. These three models are illustrated in Figure 4-11. Cases two and three are geometrically symmetric for samples above and below the sedimentary features in the static case, but this symmetry is broken when burial history is considered; the temporal dependence of dose rates will be discussed below.

The function f(z) has been derived from measurements of the complementary function (*1 - f(z)*) for both beta and gamma gradients. The behavior of a beta particle with maximum energy *E* (Mev) depends on *z* as:

$$[1 - f(z)] = 0.5e^{-\mu z}$$

where $\mu$ ($cm^{-1}$), the linear attenuation coefficient in the sediment, is given by:

$$\mu = 3.3P^{-1}$$

$$P = \frac{0.0825}{\rho}[(1 + 22.4E^2)^{0.5} - 1]$$

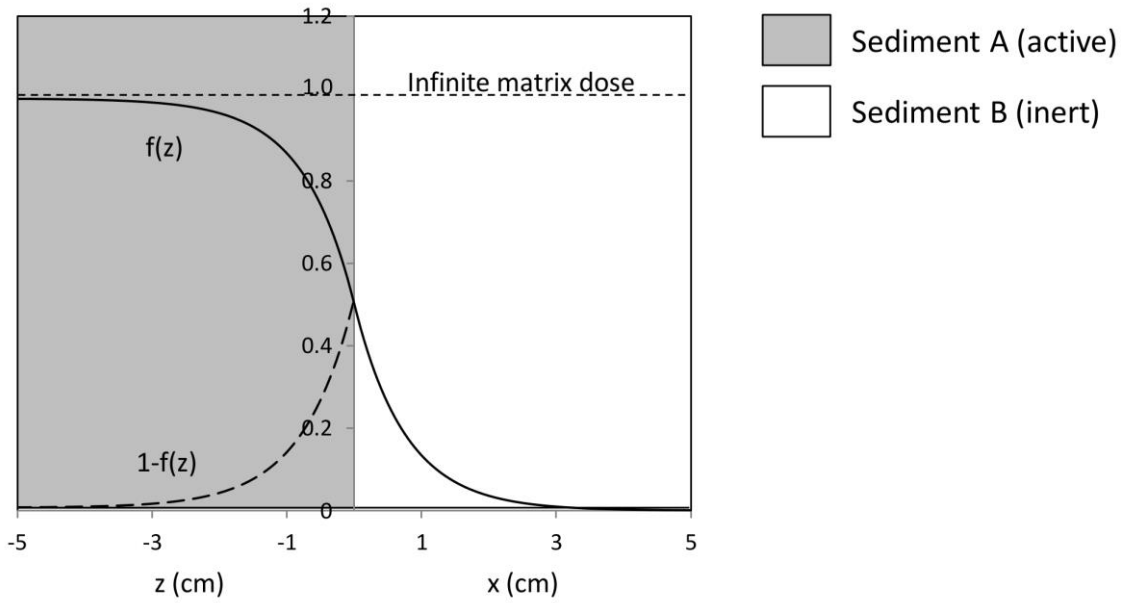


**FIG. 4-10.** Beta dose attenuation in an inert sediment next to an active sediment (see text for details), redrawn from Aitken (1985: Appendix H). The calculated relationship is for the Th decay series in sediment with a density of 2 g $cm^{-3}$.

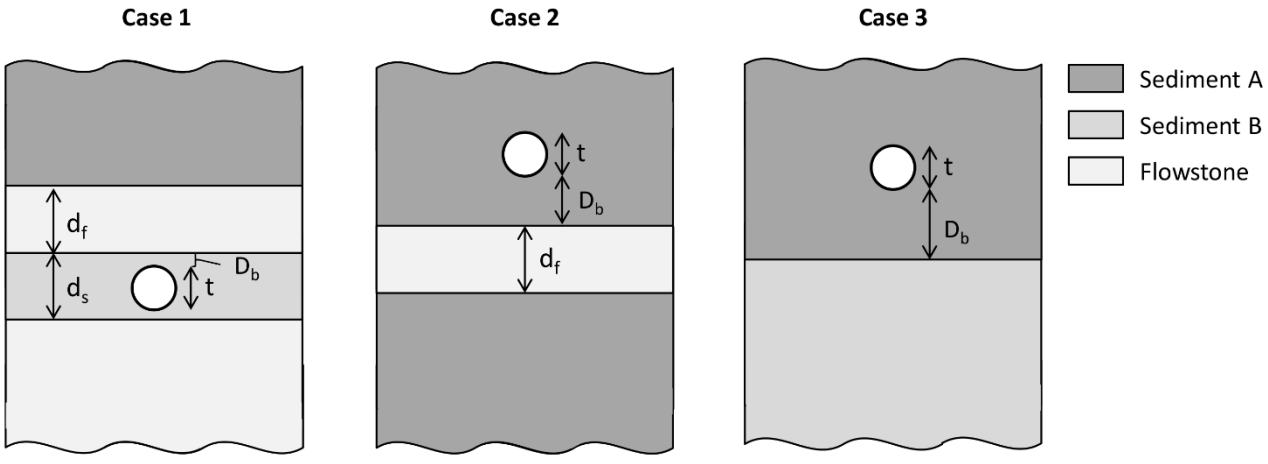


Parameter Definitions:

$D_b$=Distance from tube edge to boundary (cm)
$d_f$ = Flowstone thickness (cm)
$d_s$ = Sediment thickness (cm)
t = Tube diameter (cm)

**FIG. 4-11.** Three planar boundary models and input parameters for calculation of gamma dose rates to OSL samples near sedimentary boundaries.

and $\rho$ is density (g cm$^{-3}$) (Grün, 1986). According to Grün, this equation for $\mu$ gives results similar to the values reported for U and Th beta attenuation by Aitken et al. (1985). Because beta penetration in sediment is on the order of millimeters, any sample that is taken more than a centimeter from a boundary has a beta dose that has been emitted almost entirely from within the sample layer itself. For this reason, beta variation was not considered for any samples in this project.

Gamma dose attenuation has been calculated in two ways, depending on the scale of the distances involved. The first solution derives from a table of fractional gamma doses for K, Th, and U at varying depths in an active medium next to an inert medium (i.e. $f(z)$ in Fig. 4-10). These values, computed by L. Løvborg and reported by Aitken (1985: 290), were fitted by means of least squares using the MATLAB algorithm 'fminsearch.' Though a single saturating exponential was tried first, this did not fit the published data well. Two exponentials were used for the final fits, giving the following equations:

$$f(z)_K = 1 - 0.3915e^{-0.1112z} - 0.1053e^{-0.5937z}$$

$$f(z)_U = 1 - 0.3738e^{-0.1201z} - 0.1224e^{-0.5740z}$$

$$f(z)_{Th} = 1 - 0.3595e^{-0.1091z} - 0.1357e^{-0.4857z}$$

To account for variability in sediment density, the value *z* is multiplied by $2\rho^{-1}$ where $\rho$ is wet density (g cm$^{-3}$). For cases in which components have very different densities (i.e. flowstone and sediment), calculations used an approximate density, weighted by relative amounts. Errors were calculated via Monte Carlo methods (5000 repeats).

Temporal dependence

Dose gradients in a cave environment may be thought of as static, effectively static, or dynamic over a sample's burial history. For instance, samples taken near but above sedimentary boundaries are essentially in a static environment, in which they will have been exposed to approximately the same dosimetry gradient for their whole burial history. This does not take into account sedimentary compaction, however, error ranges can be increased to allow for such

changes. Samples below such boundaries will of course have been exposed to dosimetric variation during burial and possibly post-burial formation of alteration layers. In most cases, there will not be any indication of the precise date for such formations, but there may be evidence to support the usual supposition that the sediments attained their present-day state relatively quickly compared to a sample's burial age. Due to the lack of evidence, these scenarios are also treated as static during dosimetry calculations or by allowing the use of present-day gamma-spectrometer measurements. However, for a sample within a few centimeters of an unconformity, there may have been a period of many thousands of years before the unconformity was created depending on the amount of sediment that has been removed. By closely bracketing the unconformity with OSL samples, this scenario can be modeled as a dynamic process through time.

If the top sample (sample $S_A$ in sediment A) and bottom sample ($S_B$ in sediment B) bracket the unconformity, the dose rate for sample $S_A$ and relative proportions due to sediments A and B will have been constant during its burial history (assuming no disequilibrium and nearly instantaneous deposition of overlying sediment). Therefore, once the age for sample $S_A$ has been derived, this information can be used to calculate the age of the underlying sample $S_B$. A simple model assumes that the material in sample B was effectively instantaneously covered to a depth of several tens of centimeters by sediment B, thereby producing an infinite matrix gamma dose $\dot{D}_{B,1}$ for the first, unknown number of years. Following this, much of this material was washed away, producing the visible unconformity, and sediment A was laid down at a time $T_A$ years ago. In this geometry, sample B received dose rate $\dot{D}_{B,2}$. Thus the age of sample B, $T_B$, can be expressed as:

$$T_B = \frac{De_B}{\left(1 - \frac{T_A}{T_B}\right)\dot{D}_{B,1} + \left(\frac{T_A}{T_B}\right)\dot{D}_{B,2}}$$

which reduces to

$$T_B = \frac{De_B + T_A\left(\dot{D}_{B,1} - \dot{D}_{B,2}\right)}{\dot{D}_{B,1}}$$

Alternatively, the dose rate can be calculated according to the present-day geometry. For age calculations in this study, if the above equations indicated only a short hiatus in deposition (i.e. only a few thousand years), then the modern sample geometry was used for final age calculations.

Complex geometries

Monte Carlo N-particle transport models (MCNP5) have been created and analysed by R. Nathan for two sets of samples, TAF08-01 and TAF08-02 as well as the Rhafas femur. The model for samples TAF08-01 and 08-02 evaluated only gamma dose, and was based upon a simplified geometric representation of the sample locations. The results will be discussed later, as a comparison for the simpler dosimetry approximation made using the planar equations.

By contrast, the dosimetric effect of the Rhafas femur fragment was modeled in detail for beta and gamma doses. After the interior sediment was sampled, femur shape was analysed via computerized tomography (CT) scanning at the Max Planck Institue for Evolutionary Biology in Leipzig (courtesy J.-J. Hublin). The data from these scans was used to create an accurate three-dimensional model of the bone geometry, with volumetric pixels ('voxels') of 0.5 mm for the beta model and slightly larger ones for the gamma model. The position of the sediment core in this model was determined according to visible remnants of the sediment core in the CT scans (post-OSL sampling) and the X-ray images taken prior to sampling. The uranium content of the bone is unknown and the effect of this will be discussed in the results; a given concentration is modeled as having been present throughout the sample's burial history. All decay chains are assumed to be in equilibrium, including any radioisotopes in the bone. MCNP model results, i.e. geometric effects on dose rate, were used to calculate the average beta and gamma dose rate to sediment subsamples and the total sediment core based on measured elemental

concentrations. The uncertainty was chosen as the error. Attenuation factors were based on 5 μm of grain etching during HF treatment.

#### *4.3.2.3 Chemical changes over time*

Deposition or leaching of sedimentary constituents may prevent present day measurements from accurately reflecting the average sample condition during burial. Radioisotopes may be leached from or deposited into the system, and the significance of such effects depends both upon the magnitude of the dose rate shift and the date of the alteration. Some processes, such as potassium content shifts due to diagenetic alteration of ashy sediments, cannot be directly measured for an OSL sample.

By contrast, concentration changes resulting in disequilibrium in radioisotope decay chains (U or Th) is sometimes detectable in sedimentary samples. Disequilibrium occurs when the leaching or deposition of a radioisotope disturbs the chemical equilibrium between parent and daughter elements. Equilibrium is defined to be when decay and production rates are balanced according to:

$$\lambda_1 N_1 = \lambda_2 N_2 = \cdots$$

where $\lambda_i$ is the half life of the $i$th component and $N_i$ is the number of atoms of that component. Any excess (or deficiency) of a radioisotope will decay (or build up) over time until equilibrium is restored. The amount of time necessary is determined by both the half-life of the isotopes and the magnitude of the initial shift. If there is still an excess or deficiency at the time of sampling, which is far more likely for the uranium than for the thorium series (Olley et al., 1996), this is best detected by a combination of alpha and high resolution gamma spectrometry, in order to compare concentrations of parents and daughters (Krbetschek et al., 1994). Causes of disequilibrium include carbonate deposition (thorium deficiency), water-borne uranium mobility, scavenging of radioisotopes by iron or manganese-rich sediments (Murray and Funder, 2003), and escape of radon gas (Aitken, 1985). Various studies have reported disequilibrium in OSL-dated sediments (Olley et al., 1997; Zander et al., 2007; Guibert et al., 2009). However, a

survey of Australian fluvial sediments indicated that, though disequilibrium was common, the effects produced on dose rate were typically bracketed by the 5-10% errors of standard OSL dates (Olley et al., 1996).

The samples taken during this study did not yield enough material for disequilibrium measurements. The primary method for dealing with the possibility of disequilibrium was to use what were felt to be realistic, broad error ranges for dosimetry evaluations. It is sometimes suggested that on site gamma spectrometer measurements are compared with ICP-MS results from the same samples in order to provide a first approximation of disequilibrium likelihood (S. Burrough, pers. comm.). Any useful information in this comparison is due to the differing methods of calculating radioisotope concentration utilized by the techniques: ICP-MS counts parent isotopes directly, while gamma spectrometry measures late chain daughters as a proxy for parents. Practically, however, it is nearly impossible to relate discrepancies in these values to disequilibrium, as the measurement scales are not comparable (~$10^5$ $cm^3$ for the gamma spectrometer opposed to a few cubic centimeters for ICP-MS).

## 4.4 Bayesian modeling

OxCal 4.1 (Bronk Ramsey, 2009a) was used to construct age models for Taforalt and Dar es-Soltan I (Appendix B). To investigate the sensitivity of the final results, models were created that included various stratigraphic assumptions and methods of data input to reflect varying levels of confidence in the OSL ages. All presented models, unless stated otherwise, include all measured and accepted data. Central age model equivalent dose estimates were used. Sample ages were entered via the "Age" command, with parametrization of the equivalent dose estimate, dry dose rate, and water content estimates: parameters were assumed to have normal distributions. Independence was assumed for all parameters, excepting water content at Taforalt. Due to the extreme sediment difference in Taforalt between the ash and other cave infill, two parameters were used in these models. For samples with more than one measurement type (according to grain size or aliquot type), likelihoods were entered as

"combined" probabilities; that is, the probabilities were constrained to apply to the same dated event. OSL ages were then grouped into sequences or phases as appropriate, based on the stratigraphy of the site (see results for each site for details).

Sample ages thought to be less reliable, due to the presence of OSL-related anomalies (e.g. dose recovery problems), evidence of bioturbation, or extreme age inversions were either assigned higher outlier probability or excluded from the model (where noted). Outlier analysis used the "General" model, which assumes the samples are outliers in time with a student T distribution (5 degrees of freedom; see Bronk Ramsey, 2009 for details). Samples were allowed between 10 and 10,000 years offset. Where outlier analysis was used, samples were assigned an initial outlier probability of either 0.05 or 0.5; this is discussed further in the next chapter. Final models were run at a resolution of 200 years.

# Chapter Five

## *STANDARD OSL RESULTS*

Experimental results and calculations leading to OSL ages are given in this chapter. These include equivalent dose measurements, dosimetry calculations, and Bayesian models of the final OSL ages. Results are organized by site: Taforalt, Dar es-Soltan I, Rhafas, and Chaperon Rouge II.

## 5.1 Taforalt

### 5.1.1 Dose recovery and preheat plateau

A number of OSL samples have already been dated at this site (Bouzouggar et al., 2007b), however, several dose recovery and preheat plateau experiments were conducted to validate equivalent dose measurement parameters.

#### *5.1.1.1 Dose recovery*

Dose recovery experiments (see Section 4.2.2.2 for methods) were performed on eleven samples, chosen to represent all five sedimentological Groups: three from the Calcareous Group

(Sectors 1 and 2), two from the Lower Laminated Group (Sector 2), one from the Pink Group (Sector 2), two from the Upper Laminated Group (Sector 8), one from the Grey Series (Sector 8), and two from uncharacterized sediment (Sector 9). LED bleaching was used for all samples, except for the TAF09-27 preheat plateau experiment, in which half of the aliquots were bleached with sunlight and half with LEDs. Table 5-1 gives details of the bleaching times and given doses used in each experiment.

Results of these experiments are presented in Fig. 5-1, organized by Group for comparison. Box plots indicate the aliquot distribution for each sample (range, first and third quartiles, and median). Recovered dose, overdispersion, and skewness values are also displayed. Recovered doses for each sample are relatively consistent. All dose estimates have central values within 10% of unity, and all slightly underestimate the given dose. The mean recovered dose for all samples is 92.31% of the given dose, with a standard deviation of 2.58%.

Though the central tendency of each population is similar, intra-sample aliquot variability can be high and varies significantly between samples. Overdispersion values range from zero (TAF09-35, TAF08-02, TAF09-38, TAF09-24) to 11.30 ± 3.43% (TAF09-27). Such values are not unusual, as dose recovery tests on multiple grain aliquots have these are not unusual . Four samples are 'highly' skewed (>1), with weighted skewness greater than unity in either the positive or negative direction. Two more are 'moderately' positively skewed (0.5 to 1), and five are approximately symmetric (<0.5). Neither skewness nor overdispersion correlates with the accuracy of the central equivalent dose estimate. If these overdispersion and skewness values accurately reflect dose response differences in nature, this innate variation could be misinterpreted as absorbed dose variation or sediment mixing. Sample TAF08-01, in particular, would be at risk of misinterpretation. TAF08-01 and TAF09-27 (Calcareous Group) also yield aliquots with the worst given dose underestimates.

**TABLE 5-1.** Dose recovery measurement parameters and results using standard preheats (260°C/240°C).

| Sample | Bleaching Time (s) | Given Dose (Gy) | No. accepted aliquots | Recycling Ratio (μ ± 1σ) | Zero Ratio (μ ± 1σ) | Normalized Recovered Dose |
|---|---|---|---|---|---|---|
| TAF08-01* | 500/300 | 115.4 ± 2.3/ 124.1 ± 2.5 | 7 | 1.03 ± 0.05 | 0.00 ± 0.00 | 0.91 ± 0.04 |
| TAF08-02 | 300 | 98.0 ± 2.0 | 4 | 1.02 ± 0.03 | 0.00 ± 0.00 | 0.96 ± 0.03 |
| TAF08-16 | 300 | 33.9 ± 0.7 | 10 | 1.05 ± 0.02 | 0.01 ± 0.00 | 0.96 ± 0.02 |
| TAF09-08 | 300 | 42.4 ± 0.8 | 11 | 1.02 ± 0.03 | 0.00 ± 0.00 | 0.97 ± 0.01 |
| TAF09-22 | 300 | 42.5 ± 0.8 | 11 | 1.03 ± 0.04 | 0.00 ± 0.00 | 0.92 ± 0.03 |
| TAF09-24 | 300 | 14.5 ± 0.3 | 10 | 1.04 ± 0.06 | 0.00 ± 0.00 | 0.96 ± 0.02 |
| TAF09-27 | 500 | 73.2 ± 1.5 | 13 | 1.02 ± 0.04 | 0.01 ± 0.01 | 0.90 ± 0.04 |
| TAF09-35 | 300 | 42.5 ± 0.9 | 5 | 1.01 ± 0.07 | 0.00 ± 0.00 | 0.91 ± 0.03 |
| TAF09-37 | 300 | 58.8 ± 1.18 | 5 | 1.02 ± 0.05 | 0.01 ± 0.01 | 0.96 ± 0.04 |
| TAF09-38 | 300 | 58.8 ± 1.2 | 7 | 1.01 ± 0.02 | 0.01 ± 0.00 | 0.93 ± 0.02 |
| TAF10-16 | 300 | 42.5 ± 0.8 | 11 | 1.03 ± 0.04 | 0.01 ± 0.00 | 0.92 ± 0.02 |

*Data was indistinguishable for two sets of bleaching/dosing parameters, so aliquots have been analyzed together.

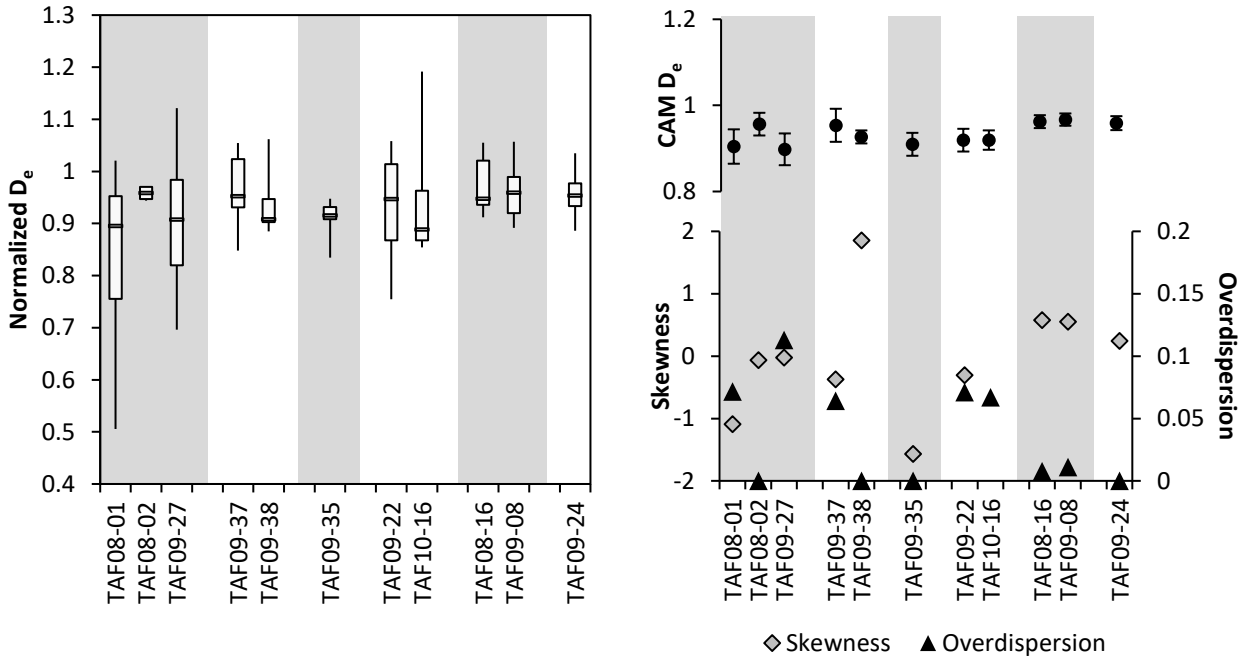


**FIG. 5-1.** Normalized recovered doses for Taforalt dose recovery experiments (standard preheat), grouped by sediment type. From left to right, Calcareous, Lower Laminated, Pink, Sector 9, Upper Laminated, and Grey. a) Box plots of accepted aliquots. b) Recovered dose estimates (common and central age models) skewness, and overdispersion values.

It is difficult to associate dose recovery performance with sediment type as recovered dose accuracy, skewness, and overdispersion values are not wholly consistent within Groups. Due to the significant underestimates from several Calcareous Group aliquots, though, preheat plateau experiments were conducted for Calcareous samples. Similar underestimates of recovered dose have been noted and resolved by tweaking thermal treatment regimes (Murray and Wintle, 2003; Tribolo and Stokes, 2006), and it was hoped that this approach would yield more accurate dose recoveries for these Taforalt samples.

#### *5.1.1.2 Preheat plateau*

The preheat regime used for most equivalent dose measurements (regenerative: 260˚C, test: 240˚C/220˚C for 10 s) was similar to that used successfully for previous OSL samples in Taforalt, including samples from the Calcareous Group (regenerative: 260˚C, test: 220˚C for 10 s in Bouzouggar et al., 2007b). Due to the preceding results, though, a series of preheat experiments was initiated. Two kinds of preheat plateau experiment were conducted on Calcareous group samples, utilizing dose recovery and natural equivalent dose measurements.

A dose recovery preheat plateau test was conducted on representative sample TAF09-27, in which regenerative dose step preheats were varied between 160$^{o}$C and 280$^{o}$C; the test dose preheat temperature was kept constant at 200$^{o}$C. Four aliquots were measured for each preheat temperature. Two Risø readers were used due to constraints on availability, so the given dose and dose steps were adjusted according to each machine's calibration factor. There seems to be no systematic offset between data from the two machines: two preheat temperatures (240$^{o}$ C and 260$^{o}$C) have data from both machines, and there is good agreement between them. No aliquots were rejected from analysis.

Fig. 5-2 shows the mean and standard deviation of recovered doses, recycling ratio, and zero ratio as a function of preheat temperature. A correlation between recovered dose and preheat temperature is apparent, such that the 'standard' preheat of 260$^{o}$C causes slight dose underestimation. Aliquots preheated to both 220$^{o}$C and 240$^{o}$C were more successful at

recovering a given dose. No trend in recycling ratio is apparent, but thermal transfer seems to increase with preheats higher than 240°C. Based on consideration of both recovered doses and thermal transfer values, a 220°C preheat ('low') was chosen for further testing.

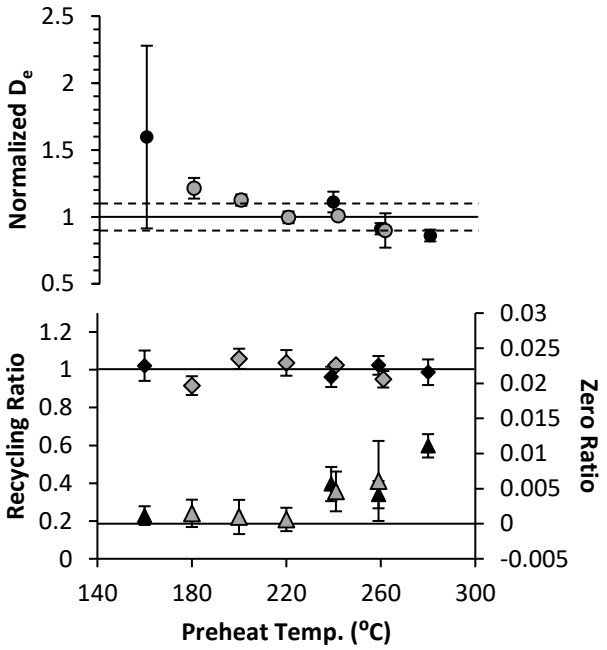


**FIG. 5-2.** Preheat plateau experiment for TAF09-27. Mean and standard deviation shown for normalized recovered doses, recycling ratios, and zero ratios at each temperature (four aliquots each). Filled symbols (black or grey) indicate groups measured on two different machines. Solid lines indicate desired values, and dotted lines show 10% boundaries for $D_e$.

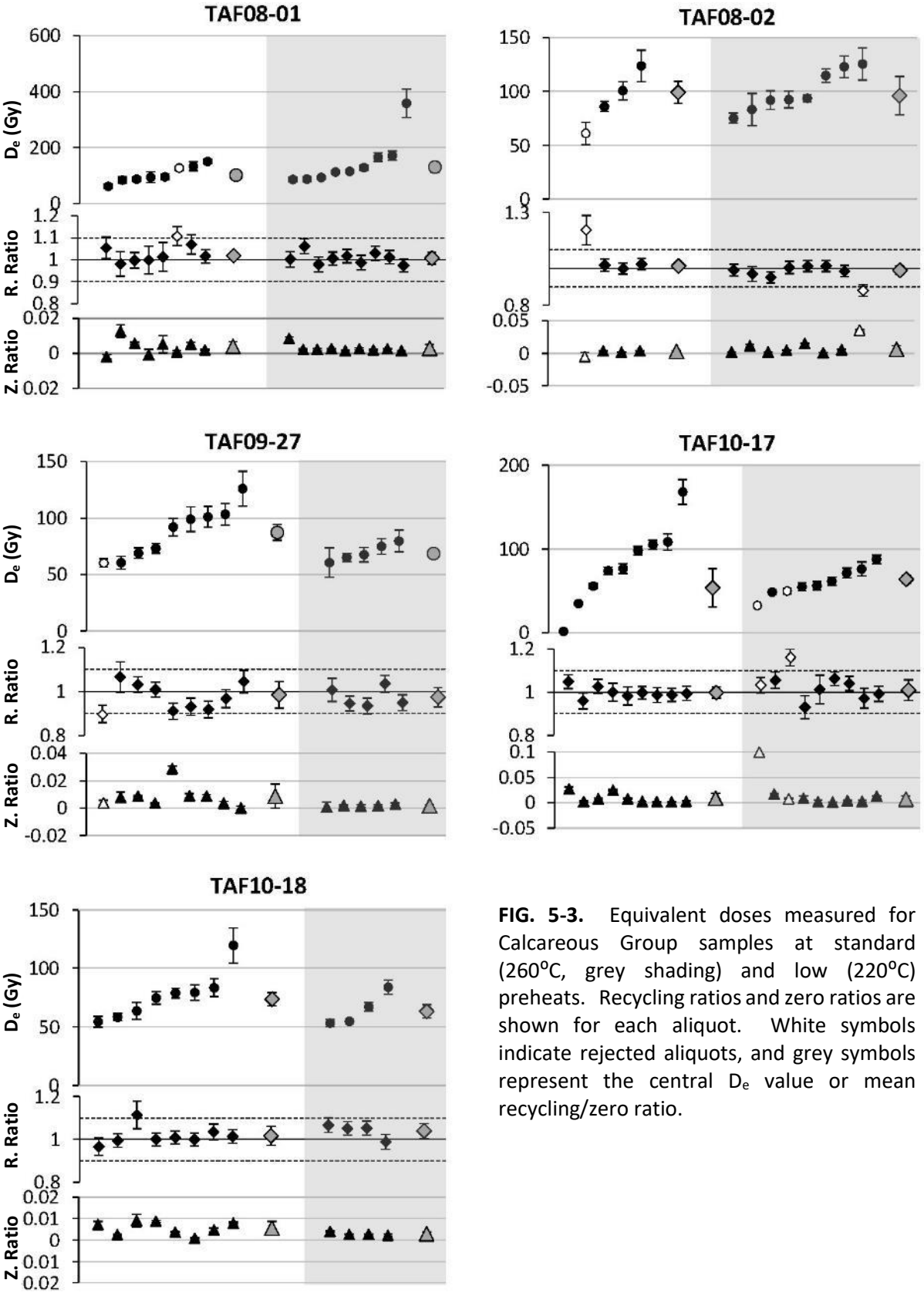


**FIG. 5-3.** Equivalent doses measured for Calcareous Group samples at standard (260°C, grey shading) and low (220°C) preheats. Recycling ratios and zero ratios are shown for each aliquot. White symbols indicate rejected aliquots, and grey symbols represent the central $D_e$ value or mean recycling/zero ratio.

In order to preserve limited sample material, equivalent doses were measured at both the standard (260°C regen./240°C test) and low (220°C regen./200°C test) preheat regimes rather than conducting further dose recovery experiments. Multigrain aliquots from all five Calcareous Group samples (TAF08-01, -02, 09-27, 10-17, and 10-18) were measured with a 220°C preheat. Equivalent doses, recycling ratios, and zero ratios measured for multigrain aliquots at the two preheat regimes are compared in Fig. 5-3. Aliquots with an IR response were rejected from the analysis, while those failing zero and recycling ratio criteria are plotted but were excluded from the central age model calculations.

Altering the preheat regime increased measured equivalent dose for both TAF10-18 and TAF09-27, but it did not produce systematic effects in all samples. For sample TAF08-01, the measured equivalent dose at 220°C (102.09 ± 10.20 Gy) is lower and distinguishable at 1σ from the 260°C degree equivalent dose (130.88 ± 17.74 Gy). However, this difference is due primarily to the inclusion of a single high equivalent dose aliquot (~350 Gy) in the 260°C measurements. The set measured at the lower preheat also had a high dose aliquot, but it was saturated and therefore excluded from analysis. If the high aliquot is also excluded from the 260°C set, the central equivalent dose becomes 116.34 ± 9.92 Gy and the results become indistinguishable at 1σ. TAF08-02 also yielded essentially identical central estimates for both regimes. TAF10-17 is unusual as the range of the 220°C aliquots (not including two saturated aliquots) is more than three times that of the 260°C aliquots, yet recycling ratio and zero ratio values are more consistent for the 220°C aliquots. The reason for this is not known.

It is evident that grain behavior depends on preheat for several samples from Sector 2, but no significant changes are apparent for Sector 1 samples. Therefore the preheat plateau experiment was not successful in explaining the significant underestimate of recovered doses in sample TAF08-01. Accordingly, final ages for Calcareous Group samples in Sector 2 used the equivalent doses obtained with a 220˚C preheat. In Sector 1, results from both preheat regimes were combined.

### 5.1.2 Equivalent dose estimates

#### *5.1.2.1 Multigrain data*

Between 6 and 12 aliquots each were measured for 39 samples, depending on the amount of quartz available. Certain samples were only measured as single grains and will thus be introduced in the next section. Table 5-2 summarizes rejection criteria data for all measured multigrain aliquots. Two aliquots rejected for high test dose error, unusual in multigrain analyses, were due to sample quantity restriction. Zero ratio values were generally very good: only 2 of 407 aliquots were rejected for unacceptably high thermal transfer. Unacceptable recycling ratios and IR response were identified for aliquots from various samples throughout the cave, but overall levels of feldspar contamination were low (see Table 5-2).

Dose response curves were fit either by exponential or exponential plus linear functions. Fig. 5-4 displays a density map of fitted dose response curves for all measured aliquots, plotted as (Lx/Tx)*(Test dose) for comparison (Telfer et al., 2008). Various behaviors are apparent, with some aliquots saturating at relatively low doses and others continuing to grow steeply at high doses. Saturated, super-saturated, and unbracketed aliquots were present in a number of samples, including those constrained to be relatively young by cave stratigraphy (e.g. TAF08-11).

Table 5-3 summarizes calculated distribution parameters and age model results for accepted aliquots, according to preheat temperature and sample. All equivalent doses were calculated via the central age model (see Sections 5.1.2.3 and 5.1.2.4); three samples yield an overdispersion equal to 0%, in which case the central age model is equivalent to the common age model. Excluding these three samples, overdispersion ranges from 6.3 ± 3.4% to 39.7 ± 9.8%. In general, overdispersion is not particularly high: nearly 75% of the measured samples have less than 20% overdispersion. Overdispersion values correlate very weakly with assigned sediment type, probably due to the correlation between Group and age (Table 5-4, Fig. 5-5a). There is a weak positive correlation of overdispersion with equivalent dose estimate (0.40).

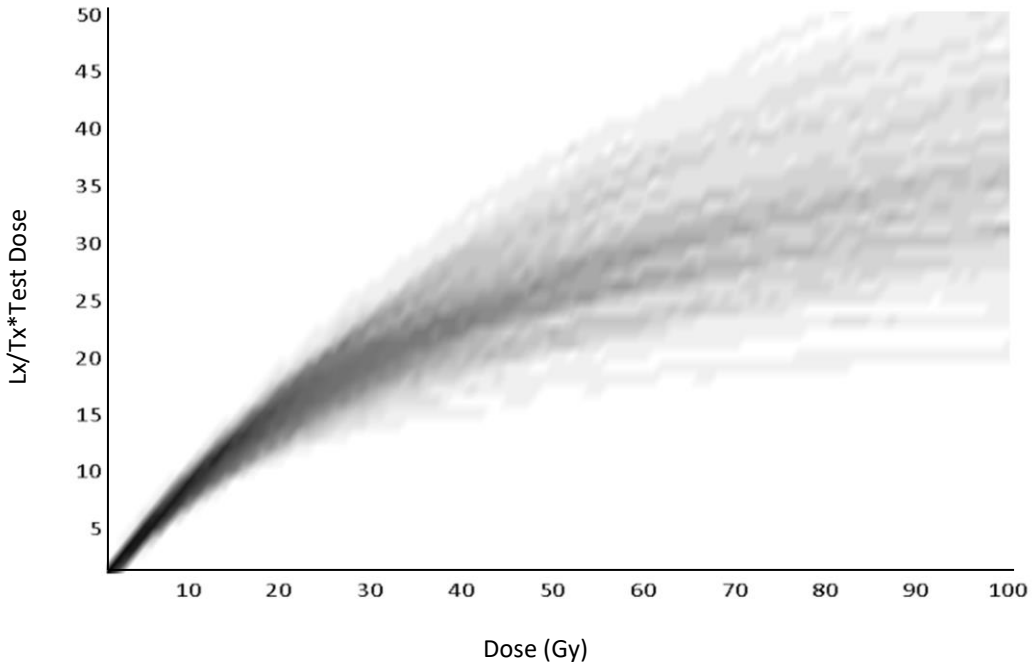


**FIG. 5-4.** Dose response curves for all accepted multigrain aliquots, shaded according to density. Growth curves have been standardized by multiplying Lx/Tx by test dose irradiation.

**TABLE 5-2.** Aliquots excluded according to rejection criteria.

| 220°C Preheat | | | | Non-exclusive | | | | | | | | | |
|---|---|---|---|---|---|---|---|---|---|---|---|---|---|
| **Sample** | **# Meas.** | **>3σ** | **Tx Err.** | **RR** | **IR** | **Zero** | **Sat.** | **Super-Sat.** | **Fit Err.** | **Neg. $D_e$** | **$D_e$ Err.** | **Not bracket** | **Accepted** |
| TAF08-01 | 12 | 0 | 0 | 1 | 3 | 1 | 0 | 0 | 0 | 0 | 0 | 1 | 7 |
| TAF08-02 | 6 | 0 | 1 | 1 | 1 | 0 | 0 | 0 | 0 | 0 | 0 | 0 | 3 |
| TAF09-27 | 12 | 0 | 0 | 2 | 1 | 0 | 0 | 0 | 0 | 0 | 1 | 0 | 8 |
| TAF10-17 | 12 | 0 | 0 | 0 | 0 | 1 | 0 | 0 | 0 | 0 | 0 | 2 | 9 |
| TAF10-18 | 12 | 0 | 0 | 0 | 4 | 0 | 0 | 0 | 0 | 0 | 0 | 0 | 8 |
| 260°C Preheat | | | | | | | | | | | | | |
| TAF08-01 | 12 | 0 | 0 | 0 | 3 | 0 | 0 | 0 | 0 | 0 | 0 | 0 | 9 |
| TAF08-02 | 12 | 0 | 0 | 1 | 4 | 0 | 0 | 0 | 0 | 0 | 0 | 0 | 7 |
| TAF08-03 | 12 | 0 | 0 | 1 | 1 | 0 | 0 | 0 | 0 | 0 | 0 | 0 | 10 |
| TAF08-04 | 12 | 0 | 0 | 1 | 0 | 0 | 0 | 0 | 0 | 0 | 2 | 0 | 9 |
| TAF08-05 | 12 | 0 | 0 | 1 | 1 | 0 | 0 | 0 | 0 | 0 | 0 | 0 | 10 |
| TAF08-06 | 12 | 0 | 0 | 0 | 2 | 0 | 0 | 0 | 0 | 0 | 0 | 0 | 10 |
| TAF08-08 | 12 | 0 | 0 | 0 | 1 | 0 | 0 | 0 | 0 | 0 | 2 | 0 | 9 |
| TAF08-10 | 12 | 0 | 0 | 0 | 1 | 0 | 0 | 0 | 0 | 0 | 0 | 0 | 11 |
| TAF08-11 | 12 | 0 | 0 | 0 | 0 | 0 | 1 | 0 | 0 | 0 | 0 | 0 | 11 |
| TAF08-12 | 12 | 0 | 0 | 0 | 0 | 0 | 0 | 0 | 0 | 0 | 0 | 0 | 12 |
| TAF08-13 | 12 | 0 | 0 | 0 | 0 | 0 | 0 | 0 | 0 | 0 | 0 | 0 | 12 |
| TAF08-14 | 12 | 0 | 0 | 1 | 0 | 0 | 0 | 0 | 0 | 0 | 0 | 0 | 11 |
| TAF08-15 | 7 | 0 | 0 | 1 | 0 | 0 | 0 | 1 | 0 | 0 | 1 | 0 | 4 |
| TAF08-16 | 7 | 0 | 0 | 0 | 1 | 0 | 0 | 0 | 0 | 0 | 0 | 0 | 6 |
| TAF08-17 | 9 | 0 | 0 | 4 | 2 | 0 | 0 | 0 | 0 | 0 | 0 | 0 | 5 |
| TAF09-01 | 12 | 0 | 0 | 1 | 1 | 0 | 0 | 0 | 0 | 0 | 0 | 0 | 10 |
| TAF09-08 | 12 | 0 | 0 | 1 | 0 | 0 | 0 | 0 | 0 | 0 | 0 | 0 | 11 |
| TAF09-20 | 12 | 0 | 0 | 0 | 2 | 0 | 0 | 0 | 0 | 0 | 0 | 0 | 10 |
| TAF09-21 | 12 | 0 | 0 | 1 | 1 | 0 | 0 | 0 | 0 | 0 | 0 | 0 | 10 |
| TAF09-22 | 12 | 0 | 0 | 1 | 0 | 0 | 0 | 0 | 0 | 0 | 0 | 0 | 11 |
| TAF09-23 | 12 | 0 | 1 | 2 | 0 | 0 | 0 | 0 | 0 | 0 | 1 | 0 | 8 |
| TAF09-24 | 6 | 0 | 0 | 1 | 0 | 0 | 0 | 0 | 0 | 0 | 0 | 0 | 5 |
| TAF09-25 | 6 | 0 | 0 | 2 | 0 | 0 | 0 | 0 | 0 | 0 | 0 | 0 | 4 |
| TAF09-26 | 6 | 0 | 0 | 2 | 0 | 0 | 0 | 0 | 0 | 0 | 0 | 0 | 4 |
| TAF09-27 | 6 | 0 | 0 | 0 | 0 | 0 | 1 | 0 | 0 | 0 | 0 | 0 | 5 |
| TAF09-34 | 8 | 0 | 0 | 1 | 2 | 0 | 0 | 0 | 0 | 0 | 3 | 0 | 2 |
| TAF09-37 | 6 | 0 | 0 | 0 | 0 | 0 | 0 | 2 | 0 | 0 | 0 | 0 | 4 |
| TAF09-40 | 6 | 0 | 0 | 0 | 0 | 0 | 1 | 1 | 0 | 0 | 0 | 0 | 4 |
| TAF10-01 | 12 | 0 | 0 | 2 | 0 | 0 | 0 | 0 | 0 | 0 | 2 | 2 | 6 |
| TAF10-02 | 10 | 0 | 0 | 0 | 0 | 0 | 0 | 0 | 0 | 0 | 0 | 0 | 10 |
| TAF10-05 | 12 | 0 | 0 | 0 | 3 | 1 | 0 | 0 | 0 | 0 | 0 | 0 | 9 |
| TAF10-06 | 12 | 0 | 0 | 0 | 0 | 0 | 0 | 0 | 0 | 0 | 0 | 0 | 12 |
| TAF10-07 | 12 | 0 | 0 | 0 | 1 | 0 | 0 | 0 | 0 | 0 | 0 | 0 | 11 |
| TAF10-10 | 12 | 0 | 0 | 4 | 0 | 0 | 0 | 0 | 0 | 0 | 0 | 0 | 8 |
| TAF10-11 | 12 | 0 | 0 | 0 | 0 | 0 | 0 | 0 | 0 | 0 | 0 | 0 | 12 |
| TAF10-14 | 12 | 0 | 0 | 0 | 1 | 0 | 0 | 0 | 0 | 0 | 0 | 0 | 11 |
| TAF10-16 | 12 | 0 | 0 | 1 | 1 | 1 | 0 | 0 | 0 | 0 | 0 | 0 | 9 |
| TAF10-17 | 12 | 0 | 0 | 1 | 4 | 0 | 0 | 0 | 0 | 0 | 0 | 0 | 7 |
| TAF10-18 | 6 | 0 | 0 | 0 | 2 | 0 | 0 | 0 | 0 | 0 | 0 | 0 | 4 |

**TABLE 5-3.** Distribution parameters for accepted multigrain aliquots by preheat, then sample. Starred samples indicate that these values were not used for final age estimates.

| Sample | Preheat (°C) | Overdisp. (%) | Wtd. Skew. | Wtd. Kurt. | $D_e$ (Gy) |
|---|---|---|---|---|---|
| TAF08-01* | 220 | 26.6 ± 8.5 | 1.04 | -0.24 | 98.4 ± 10.9 |
| TAF08-02* | 220 | 11.3 ± 7.0 | -0.10 | -- | 99.4 ± 8.1 |
| TAF09-27 | 220 | 20.7 ± 6.1 | -0.13 | -0.59 | 87.2 ± 7.0 |
| TAF10-17 | 220 | 0.0 | 0.08 | 0.71 | 61.5 ± 1.2 |
| TAF10-18 | 220 | 19.8 ± 5.9 | 0.43 | 2.68 | 73.8 ± 5.6 |
| TAF08-01* | 260 | 39.7 ± 9.8 | 0.77 | 5.79 | 130.8 ± 17.7 |
| TAF08-02* | 260 | 14.2 ± 5.0 | 0.36 | -0.52 | 96.2 ± 6.0 |
| TAF08-03 | 260 | 14.7 ± 4.4 | 0.85 | 0.85 | 59.1 ± 3.2 |
| TAF08-04 | 260 | 15.3 ± 4.2 | -0.03 | -1.35 | 51.7 ± 2.9 |
| TAF08-05 | 260 | 16.5 ± 4.3 | -0.19 | 1.09 | 56.4 ± 3.2 |
| TAF08-06 | 260 | 15.3 ± 4.4 | -0.07 | -0.73 | 44.0 ± 2.4 |
| TAF08-08 | 260 | 18.5 ± 5.3 | 0.26 | -1.79 | 40.9 ± 2.8 |
| TAF08-10 | 260 | 7.6 ± 2.5 | -0.05 | 1.14 | 61.0 ± 1.7 |
| TAF08-11 | 260 | 22.2 ± 5.1 | -0.17 | -1.34 | 45.3 ± 3.2 |
| TAF08-12 | 260 | 22.5 ± 4.8 | 0.34 | -0.96 | 42.5 ± 2.8 |
| TAF08-13 | 260 | 16.4 ± 3.6 | 0.45 | 0.90 | 32.8 ± 1.6 |
| TAF08-14 | 260 | 12.0 ± 3.3 | 0.41 | 2.53 | 40.4 ± 1.7 |
| TAF08-15 | 260 | 10.2 ± 5.2 | -0.06 | -2.09 | 44.1 ± 2.7 |
| TAF08-16 | 260 | 11.0 ± 4.0 | -0.25 | -1.60 | 37.3 ± 1.9 |
| TAF08-17 | 260 | 16.7 ± 5.8 | 0.58 | 3.57 | 13.7 ± 1.1 |
| TAF09-01 | 260 | 20.6 ± 5.4 | 0.43 | 4.81 | 46.6 ± 3.3 |
| TAF09-08 | 260 | 24.9 ± 6.1 | 0.25 | -0.18 | 47.1 ± 3.8 |
| TAF09-20 | 260 | 17.6 ± 4.5 | 0.18 | -0.09 | 34.9 ± 2.1 |
| TAF09-21 | 260 | 18.3 ± 5.0 | 0.16 | -0.64 | 36.3 ± 2.3 |
| TAF09-22 | 260 | 6.3 ± 3.4 | -0.02 | 0.11 | 45.8 ± 1.4 |
| TAF09-23 | 260 | 22.7 ± 6.5 | 1.01 | 3.30 | 45.3 ± 3.9 |
| TAF09-24 | 260 | 8.2 ± 3.2 | 0.17 | -3.05 | 14.8 ± 0.6 |
| TAF09-25 | 260 | 15.0 ± 5.8 | 0.24 | -0.64 | 19.3 ± 1.5 |
| TAF09-26 | 260 | 31.5 ± 11.9 | 0.11 | -1.57 | 65.7 ± 10.7 |
| TAF09-27* | 260 | 0.0 | 0.22 | -1.48 | 68.5 ± 2.7 |
| TAF09-34 | 260 | 0.0 | 0.05 | -- | 146.2 ± 6.0 |
| TAF09-37 | 260 | 18.1 ± 7.6 | -0.54 | 3.62 | 79.3 ± 7.8 |
| TAF09-40 | 260 | 8.6 ± 6.2 | 0.00 | -2.87 | 64.9 ± 4.1 |
| TAF10-01 | 260 | 21.2 ± 7.6 | 1.73 | 4.27 | 127.4 ± 12.4 |
| TAF10-02 | 260 | 20.7 ± 4.9 | 0.47 | 0.15 | 33.9 ± 2.3 |
| TAF10-05 | 260 | 24.8 ± 6.2 | -0.42 | -0.51 | 45.4 ± 3.9 |
| TAF10-06 | 260 | 14.3 ± 3.3 | -0.34 | 0.33 | 43.7 ± 1.9 |
| TAF10-07 | 260 | 19.4 ± 4.6 | 0.01 | -1.17 | 43.3 ± 2.7 |
| TAF10-10 | 260 | 12.9 ± 3.5 | 0.55 | 1.65 | 11.9 ± 0.6 |
| TAF10-11 | 260 | 14.5 ± 3.3 | -0.16 | -0.54 | 21.5 ± 1.0 |
| TAF10-14 | 260 | 11.8 ± 3.1 | 0.35 | 1.43 | 39.1 ± 1.6 |
| TAF10-16 | 260 | 18.1 ± 4.6 | 0.01 | 0.83 | 45.9 ± 2.9 |
| TAF10-17* | 260 | 18.2 ± 5.8 | 0.56 | -0.69 | 63.9 ± 4.8 |
| TAF10-18* | 260 | 16.9 ± 6.7 | 0.24 | -0.20 | 63.3 ± 5.7 |
| TAF08-01 | Comb. 220/260 | 37.0 ± 7.1 | 1.32 | 19.1 | 115.6 ± 11.1 |
| TAF08-02 | Comb. 220/260 | 13.5 ± 4.1 | 0.19 | -1.02 | 97.3 ± 4.9 |

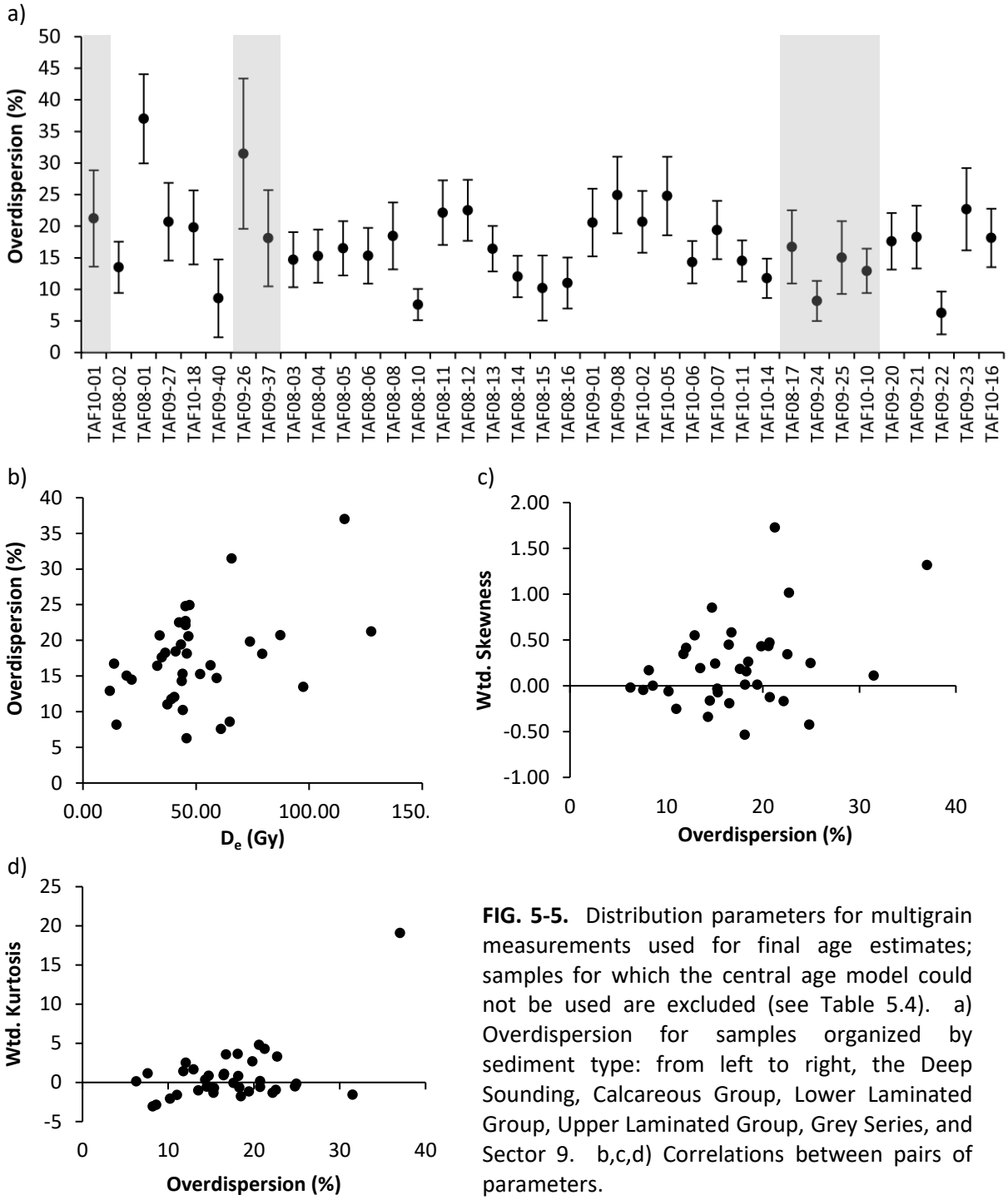


**FIG. 5-5.** Distribution parameters for multigrain measurements used for final age estimates; samples for which the central age model could not be used are excluded (see Table 5.4). a) Overdispersion for samples organized by sediment type: from left to right, the Deep Sounding, Calcareous Group, Lower Laminated Group, Upper Laminated Group, Grey Series, and Sector 9. b,c,d) Correlations between pairs of parameters.

**TABLE 5-4.** Correlation coefficients for multigrain distribution parameters (samples excluded as for Fig. 5-5).

| | $D_e$ (Gy) | Overdispersion | Wtd. Skewness | Wtd. Kurtosis |
|---|---|---|---|---|
| **De** | 1.00 | | | |
| **Overdispersion** | 0.40 | 1.00 | | |
| **Wtd. Skewness** | 0.34 | 0.34 | 1.00 | |
| **Wtd. Kurtosis** | 0.47 | 0.52 | 0.58 | 1.00 |

Weighted skewness and kurtosis are also weakly to moderately correlated with overdispersion and central $D_e$. These trends are shown in Fig. 5-5b-d.

#### *5.1.2.2 Single grain and VSA data*

Nineteen samples were analyzed via single grain, very small aliquots (VSA's), or both. Three types of sample were selected: those for which anomalous multigrain-based ages were obtained (i.e. samples with ages reversed with respect to stratigraphy: TAF08-01 and 08-02, 09-24 and 09-25, 09-26 and 09-27), microsamples, for which sample quantity was a limiting factor (TAF09-35 through 09-40), and "control" samples, for which multigrain results were coherent and likely to be reliable (TAF08-12 and 13).

Signal intensity

Variations in grains' natural signal intensities ('brightness' over first 0.04 s) were evaluated for all single grain data. VSA data was excluded due to possible averaging effects. Comparison of natural signals rather than test dose responses allows for the effect of very bright, super-saturated grains. The defining characteristic of these grains is that laboratory irradiation does not yield signals of an equal magnitude to the natural signal, therefore comparison of test dose intensities does not allow one to evaluate the effect of such signals on sample brightness. However, using natural signal levels convolves both intrinsic grain brightness and brightness differences due to equivalent dose variation, so this must be taken into account when considering results.

Light sums for each sample are displayed in Fig. 5-6. Samples with a shallower initial slope will tend to give less scattered multigrain equivalent doses than one with a steep rise, assuming similar equivalent dose variation. These plots indicate that multigrain results from TAF09-24 and TAF09-25 of the Grey Series should be most consistent.

Absolute natural signal intensity frequencies may also be compared between samples measured with the same PMT (to control for sensitivity and noise characteristics). By this measure, it is apparent that the Grey Series quartz (TAF09-24) is generally brighter than quartz

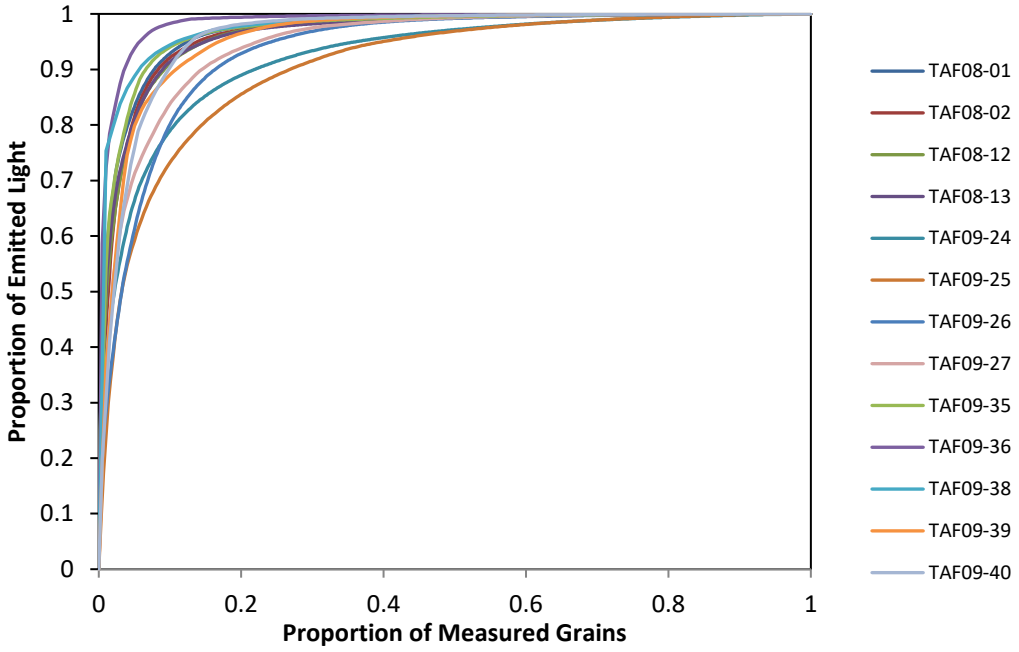


**FIG. 5-6.** Light sum graphs for measured single grains (natural signal, no background subtraction).

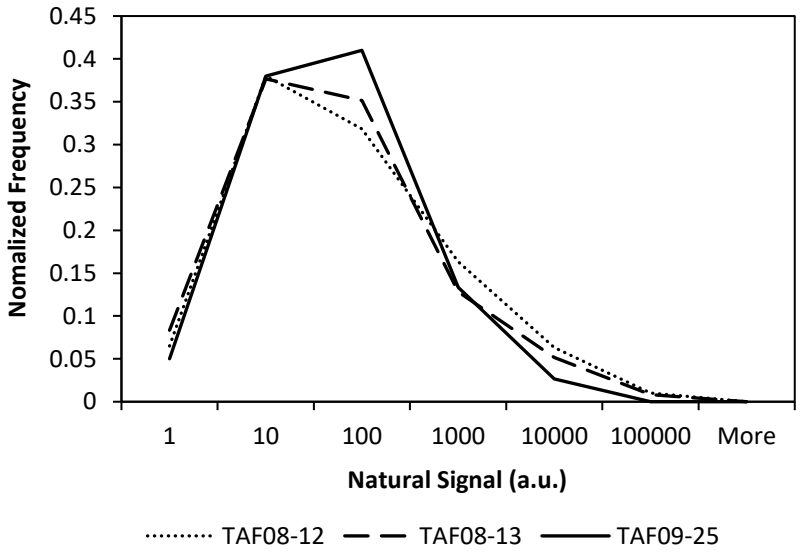


**FIG. 5-7.** Comparison between natural signal intensity frequencies (single grain) for nearby samples. The peak of Grey Series sample TAF09-25 is brighter than the nearby, higher equivalent dose samples (TAF08-12, -13). TAF09-25 is likely to have been sensitized by firing.

**TABLE 5-5.** Single grains (180-255 µm) excluded according to rejection criteria.

| 220°C Preheat | | | | Non-exclusive | | | | | | | | |
|---|---|---|---|---|---|---|---|---|---|---|---|---|
| **Sample** | **Meas. (#)** | **>3σ** | **Tx Err.** | **RR** | **Zero** | **Sat.** | **Super-Sat.** | **Fit Err.** | **Neg. $D_e$** | **$D_e$ Err.** | **Not bracket** | **Accepted (#)** |
| TAF08-01 | 197 | 106 | 44 | 12 | 4 | 4 | 2 | 0 | 2 | 10 | 4 | 8 |
| TAF09-27 | 197 | 83 | 53 | 20 | 18 | 1 | 0 | 0 | 1 | 14 | 2 | 10 |
| 260°C Preheat | | | | | | | | | | | | |
| TAF08-01 | 600 | 355 | 89 | 60 | 22 | 6 | 0 | 1 | 4 | 47 | 6 | 21 |
| TAF08-02 | 600 | 349 | 109 | 40 | 16 | 5 | 5 | 4 | 5 | 42 | 9 | 26 |
| TAF08-12 | 600 | 388 | 67 | 43 | 19 | 4 | 3 | 3 | 1 | 28 | 1 | 50 |
| TAF08-13 | 600 | 399 | 82 | 31 | 13 | 7 | 3 | 1 | 0 | 11 | 1 | 55 |
| TAF09-24 | 600 | 310 | 78 | 47 | 21 | 5 | 2 | 9 | 1 | 23 | 7 | 101 |
| TAF09-25 | 300 | 173 | 70 | 15 | 3 | 1 | 3 | 1 | 1 | 12 | 1 | 22 |
| TAF09-26 | 500 | 263 | 66 | 52 | 22 | 14 | 10 | 2 | 0 | 21 | 5 | 54 |
| TAF09-27 | 600 | 327 | 108 | 35 | 30 | 18 | 9 | 3 | 5 | 32 | 12 | 28 |
| TAF09-35 | 400 | 290 | 42 | 22 | 8 | 3 | 2 | 1 | 3 | 18 | 3 | 11 |
| TAF09-36 | 200 | 163 | 8 | 10 | 1 | 1 | 1 | 1 | 1 | 4 | 3 | 7 |
| TAF09-38 | 100 | 60 | 15 | 13 | 5 | 1 | 2 | 1 | 0 | 3 | 0 | 3 |
| TAF09-39 | 200 | 128 | 26 | 20 | 10 | 5 | 1 | 0 | 0 | 11 | 1 | 6 |
| TAF09-40 | 200 | 112 | 28 | 18 | 11 | 2 | 0 | 0 | 1 | 20 | 0 | 11 |

**TABLE 5-6.** Very small aliquots (125-180 µm) excluded according to rejection criteria.

| 240/260°C Preheat | | | | Non-exclusive | | | | | | | | |
|---|---|---|---|---|---|---|---|---|---|---|---|---|
| **Sample** | **Meas. (#)** | **>3σ** | **Tx Err.** | **RR** | **Zero** | **Sat.** | **Super-Sat.** | **Fit Err.** | **Neg. $D_e$** | **$D_e$ Err.** | **Not bracket** | **Accepted (#)** |
| TAF09-35 | 492 | 109 | 122 | 48 | 22 | 10 | 6 | 1 | 3 | 73 | 11 | 73 |
| TAF09-36 | 492 | 46 | 64 | 109 | 37 | 12 | 3 | 0 | 0 | 50 | 5 | 163 |
| TAF09-37 | 400 | 18 | 49 | 148 | 58 | 4 | 10 | 2 | 31 | 36 | 3 | 83 |
| TAF09-39 | 197 | 10 | 63 | 63 | 13 | 9 | 4 | 0 | 4 | 7 | 3 | 23 |

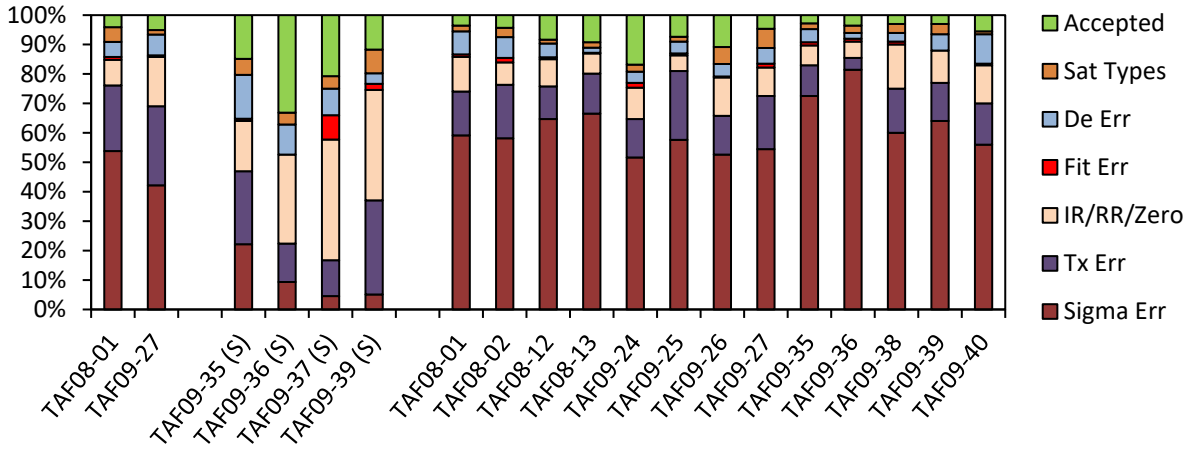


**FIG. 5-8.** Graphical comparison of proportion of grains/VSA's rejected by each criterion.

from the nearby Upper Laminated Series samples (TAF08-12 and -13), though it has half the absorbed dose (Fig. 5-7). It seems reasonable to assume that the Grey Series quartz has been sensitized by firing, while the more 'natural' sediments below are relatively dim.

Rejection criteria

Applied rejection criteria resulted in the exclusion of between 83.2% and 97.3% of measured single grains. Causes of rejection are summarized for each sample in Tables 5-5 and 5-6 and Fig. 5-8. Related values have been combined into categories for graphical presentation. Fitting errors include both negative De values and cases in which MATLAB was simply unable to solve the dose response system for a grain. These are primarily related to grains which have passed the rejection criteria and yet have no consistent dose response. Few grains (<1%) fall into this category. The number of accepted grains is strongly linked to the overall brightness of the sample, as reflected by the sigma error and test dose error criteria.

IRSL response of full single grain aliquots was also assessed. Not quite half of the measured single grain and VSA aliquots gave very weak IR signals, with net signals ranging from 1.1 times background to 7.6 times background. One VSA aliquot (TAF09-35) gave a substantial IR response of more than 33 times background. It was considered that this signal, due likely to a single feldspar grain, would not unduly bias the numerous accepted values from that aliquot so the data was retained. Recycling ratio rejections range from 5% to 13%, and zero ratio rejections from 0.5% to 5.5% for 260$^{o}$C preheats, rising to a high of 9.1% for the 220$^{o}$C preheat of TAF09-27. It should be noted that the high proportion of grains rejected for thermal transfer from the 220$^{o}$C data was surprising, as dose recovery experiments had suggested this preheat regime lowered thermal transfer.

All samples included some grains that met the criteria for saturation, and all but two had grains unbracketed by given doses. These are technically unclassifiable, but probably saturated or super-saturated when given doses are large. Fewer samples had clearly super-saturating grains (10 of 14 total), with samples TAF08-01, TAF09-24, 09-25, and 09-40 having none.

Distribution characteristics

Various distribution parameters (weighted skewness, weighted kurtosis, range, and overdispersion) and central age model equivalent doses are summarized for the analyzed samples in Table 5-7. Overdispersion values range from 22.4 ± 4.3% to 56.7 ± 4.6%. Calcareous Group samples produce the three highest values (~50% and over), while all other samples have overdispersion values less than 37%. Correlations between distribution parameters are not as strong as they were for multigrain data (Table 5-8, Fig. 5-9). As with the multigrain data, overdispersion values tend to increase with increasing CAM equivalent dose. This relationship is clear even for pairs of samples that may share similar microdosimetric and bioturbation effects, e.g. TAF08-12/13 and TAF09-24/25. In both cases, the sample with higher overdispersion has also received a higher burial dose. All grain populations are positively skewed, and there is a strong correlation between weighted kurtosis and weighted skewness.

Single grain and VSA data is graphically displayed for all samples via radial plots and equivalent dose histograms (Fig. 5-10). High equivalent dose 'tails' are common for Sector 1 and 2 samples. This is apparent even for VSA data, e.g. TAF09-37, which is likely to average out some of the underlying variation. Low equivalent dose grains are also present in these older samples and are particularly evident in sample TAF08-01. As expected from the analysis of overdispersion and equivalent dose, lower equivalent dose samples are visibly less scattered. Systematic input of partially bleached grains throughout the history of the cave seems unlikely, due to the relatively low overdispersion values apparent in single grain data from younger samples (e.g. TAF08-12, 08-13, 09-24, 09-25). Though it has been shown that VSA's or 'pseudo-single grains' cannot be analysed in the same way as true single grains due to averaging effects (Arnold et al., 2012; Russell and Armitage, 2012), the reported single grain distributions do not show evidence of mixing or partial-bleaching processes that would lead to the exclusion of the VSA data from consideration (see the next section for further discussion).

**TABLE 5-7.** Distribution parameters for accepted single grain and VSA data (indicated by †). Single grain and VSA data are presented, with preheat temperatures indicated. Starred samples indicate that these values were not used for final age estimates.

| Sample | Preheat (°C) | Overdisp. (%) | Wtd. Skew. | Wtd. Kurt. | $D_e$ (Gy) |
|---|---|---|---|---|---|
| TAF08-01* | 220 | 50.8 ± 13.6 | -- | -- | 118.3 ± 22.0 |
| TAF09-27 | 220 | 28.4 ± 7.6 | 0.30 | 0.27 | 86.8 ± 8.6 |
| TAF08-02 | 260 | 49.2 ± 7.5 | 1.34 | 12.25 | 74.8 ± 7.6 |
| TAF08-12 | 260 | 32.5 ± 3.9 | 0.82 | 1.87 | 37.5 ± 1.9 |
| TAF08-13 | 260 | 22.7 ± 2.9 | 0.39 | 0.03 | 29.9 ± 1.1 |
| TAF09-24 | 260 | 24.1 ± 2.2 | 0.63 | 0.29 | 14.1 ± 0.4 |
| TAF09-25 | 260 | 28.3 ± 5.7 | 0.39 | -0.81 | 18.3 ± 1.3 |
| TAF09-26 | 260 | 34.0 ± 3.8 | 1.52 | 4.32 | 54.3 ± 2.7 |
| TAF09-27* | 260 | 25.3 ± 4.7 | 0.52 | 1.05 | 58.9 ± 3.3 |
| TAF09-35 | 260 | 54.9 ± 12.5 | 0.11 | -0.08 | 48.5 ± 8.3 |
| TAF09-36 | 260 | 58.3 ± 16.2 | 1.20 | 0.67 | 74.2 ± 16.7 |
| TAF09-38 | 260 | 11.1 ± 8.6 | 0.01 | NaN | 41.7 ± 3.8 |
| TAF09-39 | 260 | 100.0 ± 29.9 | -0.42 | 0.70 | 44.5 ± 18.5 |
| TAF09-40 | 260 | 56.1 ± 12.5 | 2.03 | 9.36 | 71.6 ± 12.4 |
| TAF08-01 | Comb. 220/260 | 53.3 ± 8.9 | 2.39 | 8.84 | 91.2 ± 9.7 |
| TAF09-35† | 240, 260 | 36.6 ± 3.5 | 0.88 | 1.51 | 57.0 ± 2.6 |
| TAF09-36† | 240, 260 | 29.3 ± 1.9 | 2.32 | 40.85 | 55.5 ± 1.4 |
| TAF09-37† | 260 | 56.7 ± 4.6 | 2.04 | 5.70 | 81.9 ± 5.2 |
| TAF09-39† | 240 | 22.4 ± 4.3 | 0.61 | 2.10 | 76.6 ± 4.1 |

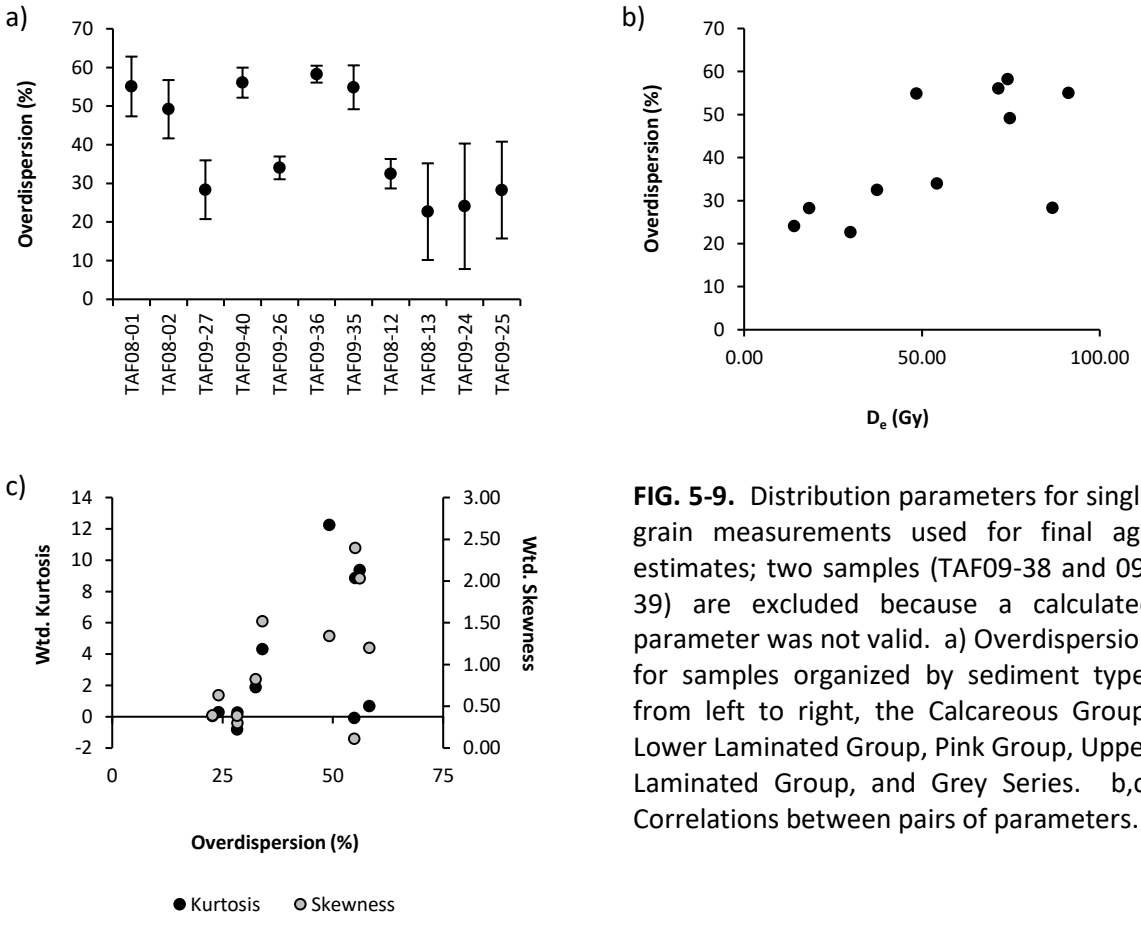


**FIG. 5-9.** Distribution parameters for single grain measurements used for final age estimates; two samples (TAF09-38 and 09-39) are excluded because a calculated parameter was not valid. a) Overdispersion for samples organized by sediment type: from left to right, the Calcareous Group, Lower Laminated Group, Pink Group, Upper Laminated Group, and Grey Series. b,c) Correlations between pairs of parameters.

**TABLE 5-8.** Correlation coefficients for single grain distribution parameters (same excluded as for Fig. 5-9).

| | De (Gy) | Overdispersion | Wtd. Skewness | Wtd. Kurtosis |
|---|---|---|---|---|
| **De** | 1.00 | | | |
| **Overdispersion** | 0.65 | 1.00 | | |
| **Wtd. Skewness** | 0.58 | 0.57 | 1.00 | |
| **Wtd. Kurtosis** | 0.58 | 0.54 | 0.81 | 1.00 |

The single grain sample characteristics found for this site are well within the range of parameters reported for other single grain studies of cave sediments. Single grain acceptance tends to be less than 20% due primarily to weak emission levels (Jacobs et al., 2011; Gliganic et al., 2012), though samples with much lower (<5%: Jacobs et al., 2003) and much higher acceptance rates (~50%: Jacobs et al., 2008a) have been reported. Absorbed dose distributions are also similar, with overdispersion levels of up to 37 ± 4% having been accepted as plausible values for well-bleached, non-mixed sediments (Tribolo et al., 2013). Even higher overdispersion values, up to 73 ± 6%, have been reported for Mumba rock shelter in Tanzania (Gliganic et al., 2012), and 'scattered' or 'mixed' cave sediment samples (according to the categories defined by Jacobs et al., 2008b) seem to be the dominant type (Dörschner et al., 2012; Gliganic et al., 2012; Jacobs et al., 2012). Examples of such single grain distributions from Sibudu Cave, South Africa (Jacobs et al., 2008b), and Mumba rockshelter, Tanzania (Gliganic et al., 2012), are shown in Fig. 5-11.

### *5.1.2.3 Equivalence of equivalent dose and burial dose*

Bioturbation

Taforalt sediments offer ample evidence for bioturbation on various scales (Fig. 5-12). Root casts are preserved in parts of the Upper Laminated sediments of Sector 3, tunneling bees have been observed to colonize various section faces, and a porcupine burrow disturbed large volumes of sediment near the extant surface of Sectors 1 and 2. However, it is believed that these effects are not likely to adversely affect the OSL ages of the collected samples. Careful

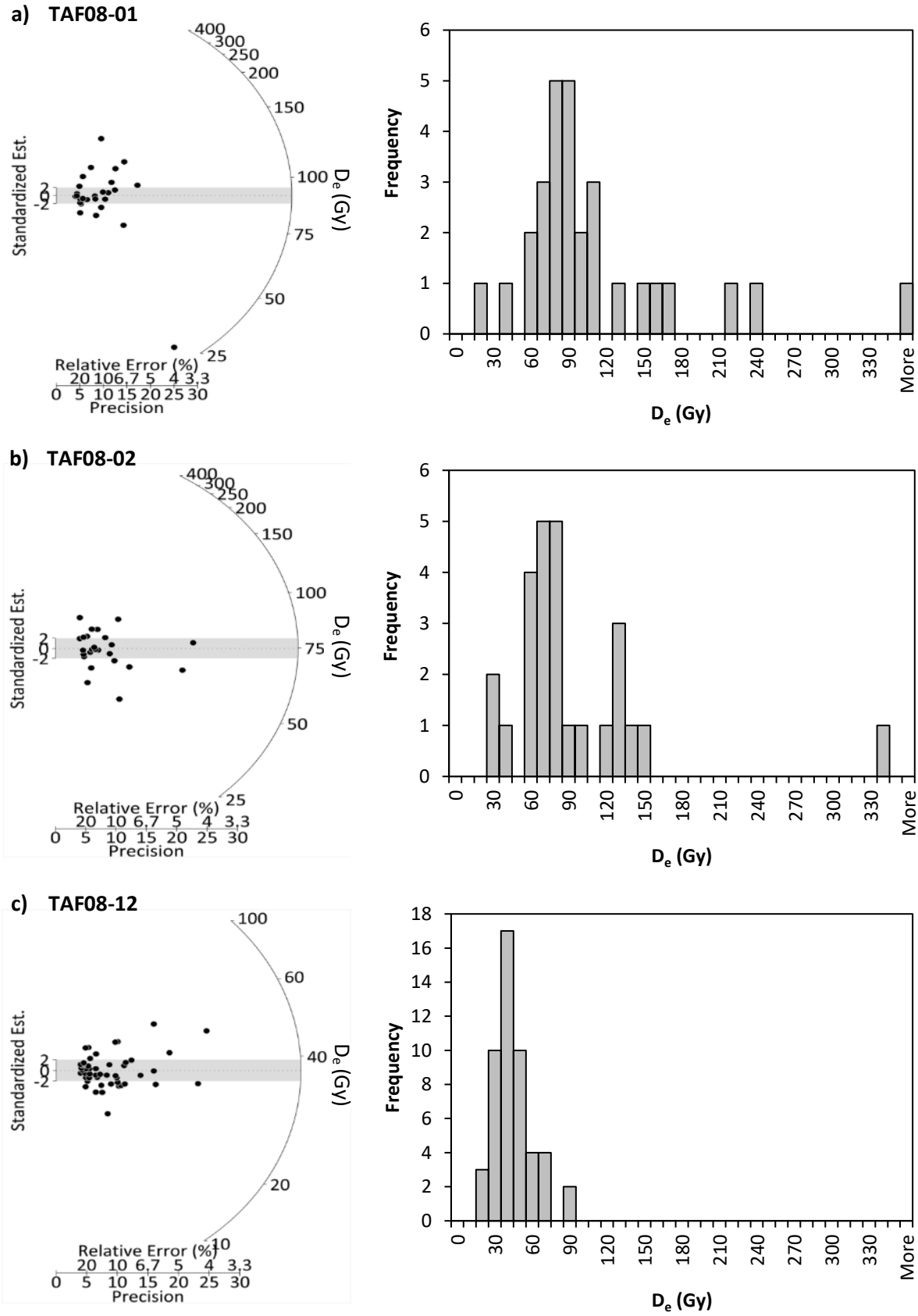


**FIG. 5-10.** Radial plots and histograms for single grain (a-j) and VSA (k-n) analyses. All samples are listed in order by field code. Radial plots are centered at CAM estimates; note scale changes for both radial plots and histograms.

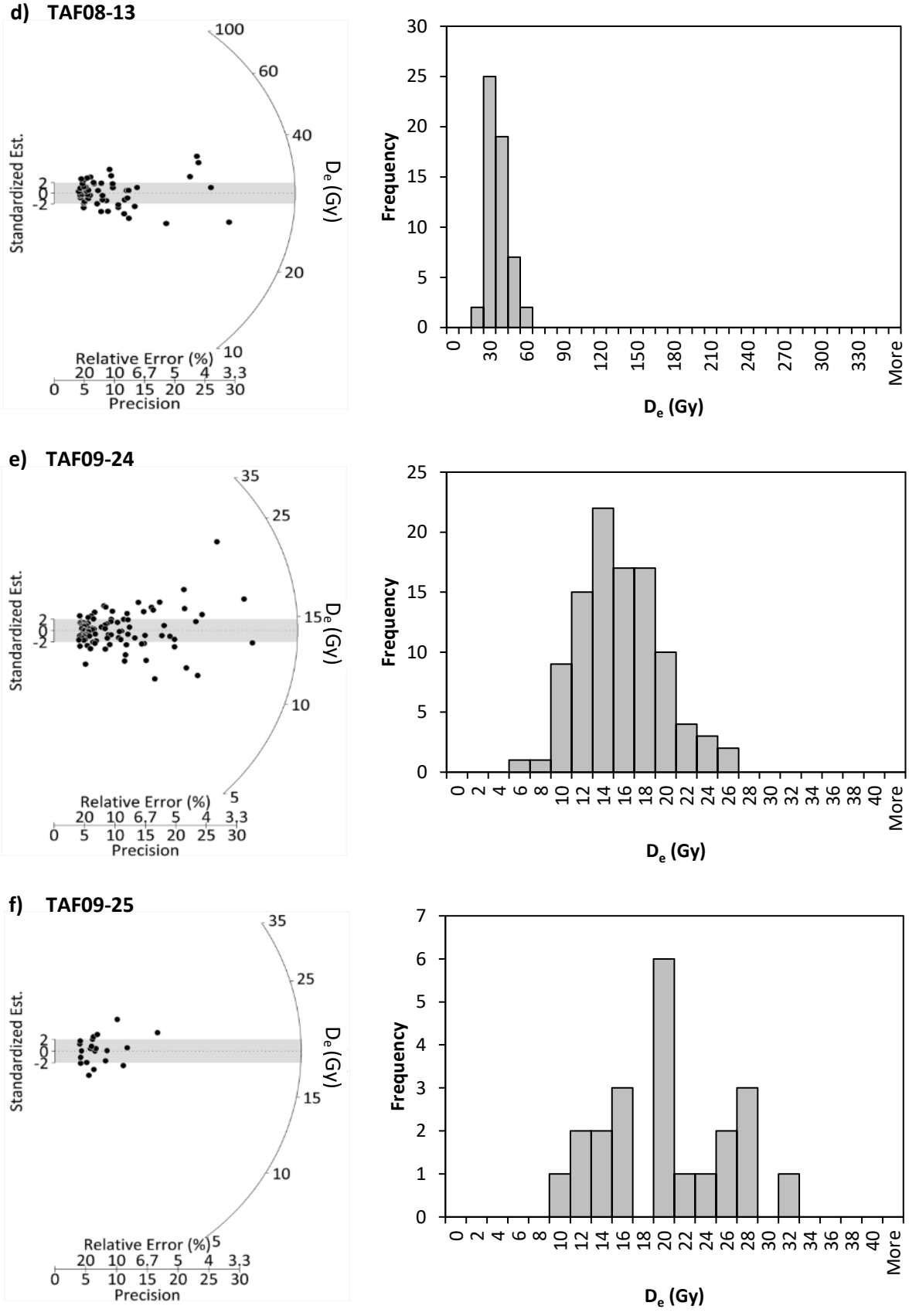


**FIG. 5-10.** (Continued)

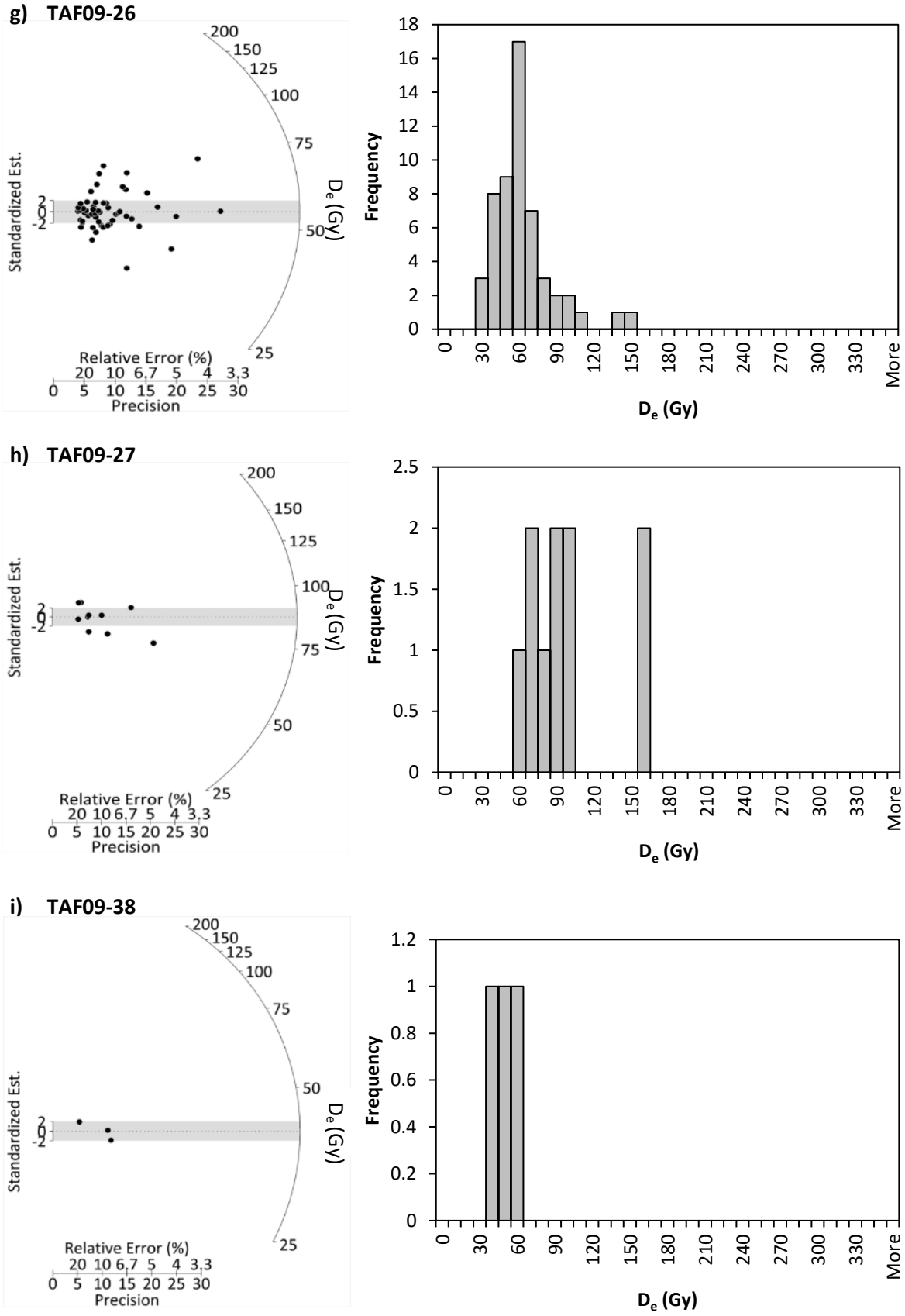


**FIG. 5-10.** (Continued)

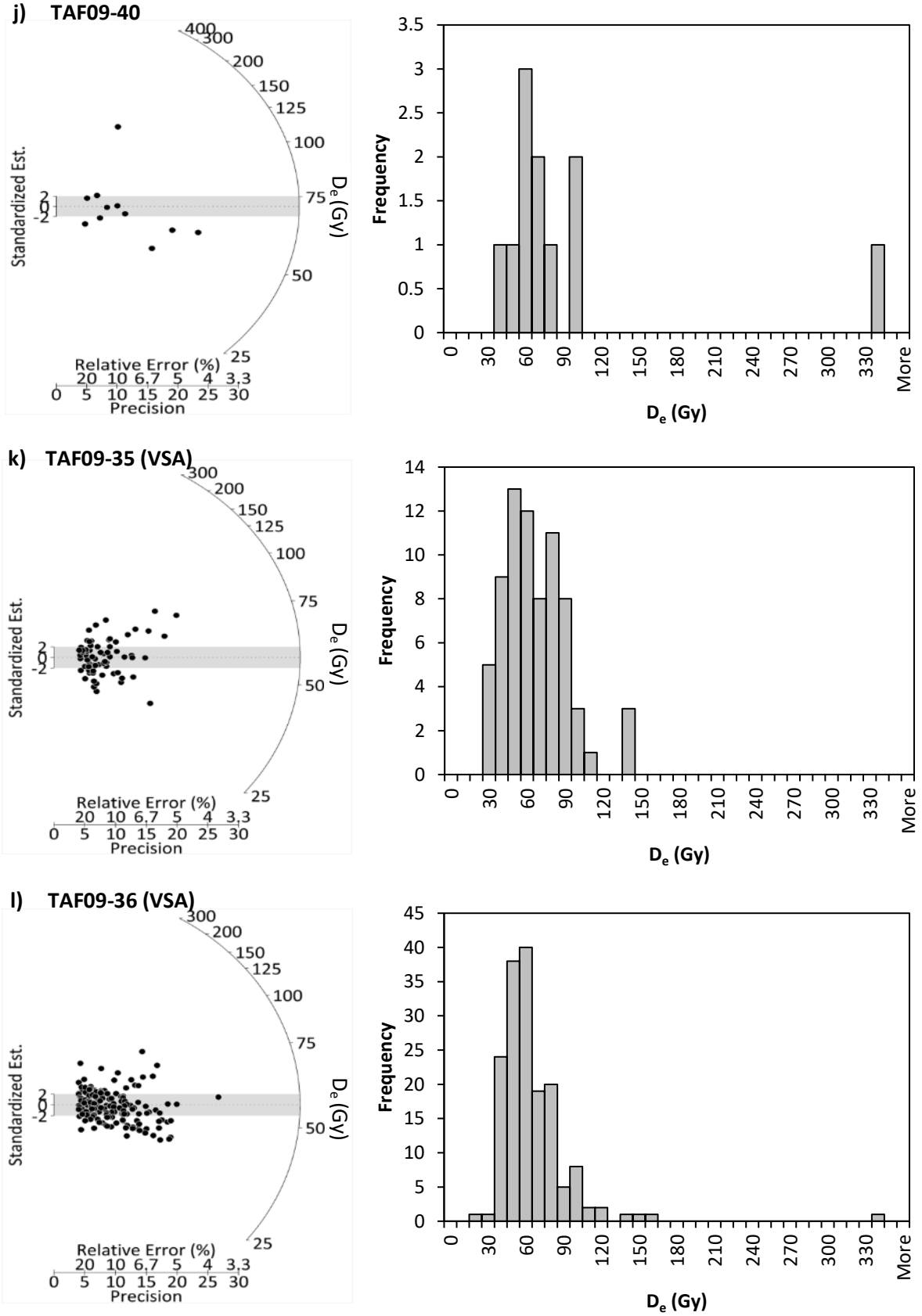


**FIG. 5-10.** (Continued)

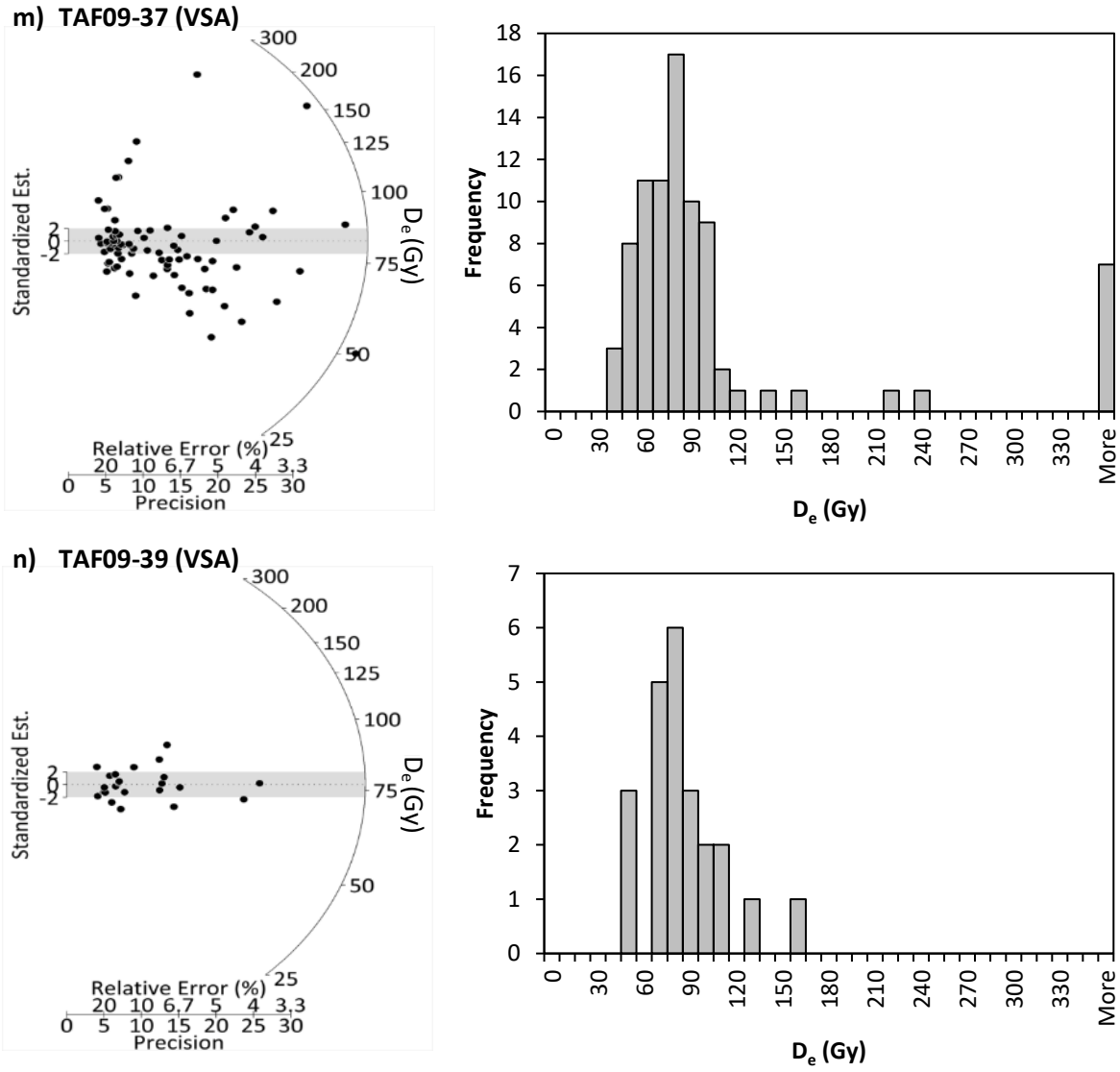


**FIG. 5-10.** (Continued)

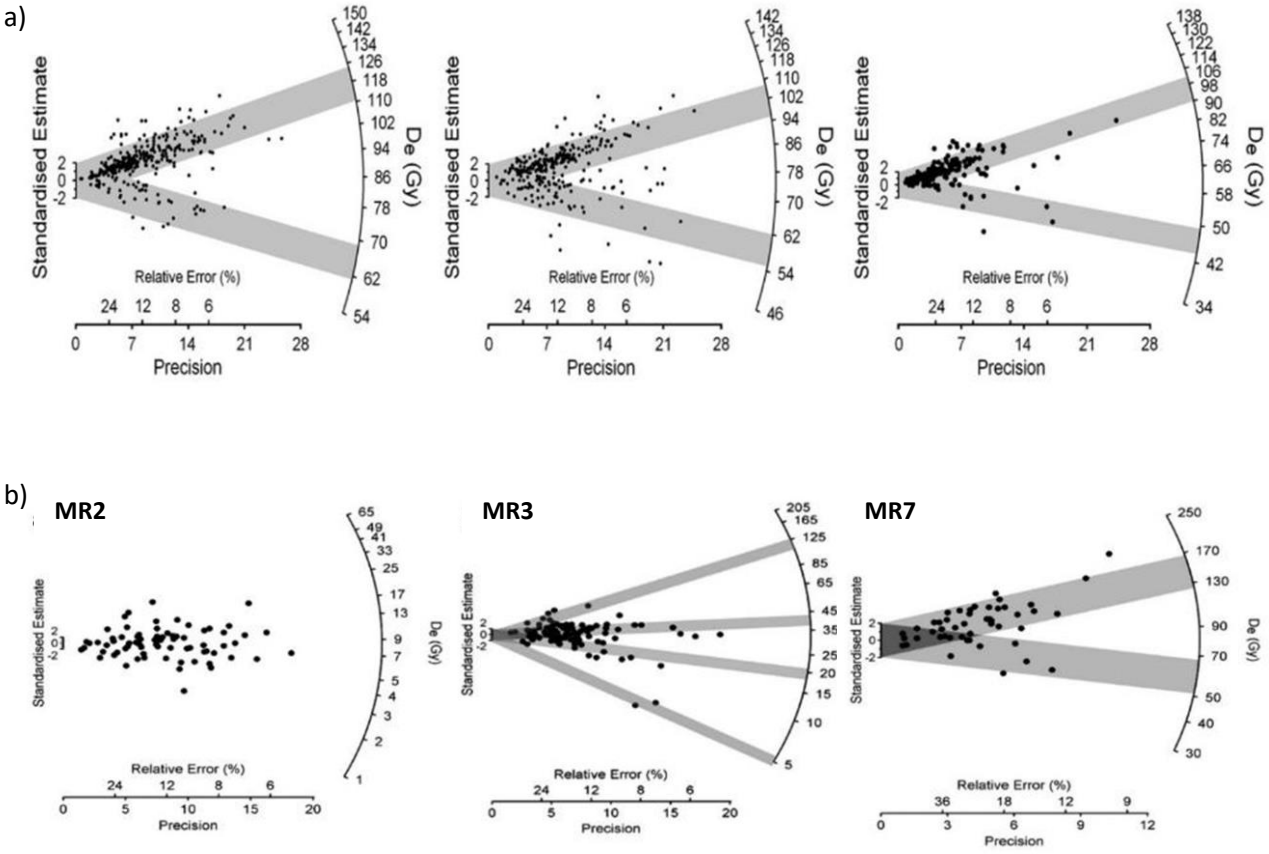


**FIG. 5-11.** Examples of single grain equivalent dose distributions from MSA cave sites, fit with the finite mixture model. a) 'Scattered' samples from Sibudu Cave, South Africa (from Jacobs et al., 2008b: 1813). b) Samples from Mumba Rock Shelter, Tanzania, with distributions identified by the authors as having no discrete dose components (MR2), having 'mixed' grains (MR3), and being 'scattered' (MR7) (from Gliganic et al., 2012: 542).

a)

b)

**FIG. 5-12.** Examples of bioturbation at Taforalt. a) Tunnels/burrows tunnels made by bees. Each hole is ~1-2 cm in diameter. b) Large burrow.

excavation delineated the extent of large-scale sediment mixing due to burrowing, and no samples were taken in this area. In addition, the stratigraphic integrity of most sampled sectors was apparent, as delicate sedimentary structures including hearth lenses were visibly preserved (particularly sectors 2 and 3). Exceptions to this were some regions of Sector 8, particularly near fallen boulders, and the base of Sector 12 and the Deep Sounding. Bioturbation in these areas may be present, but the magnitude of the effect is difficult to estimate.

Partial bleaching

In order to gauge the rapidity of quartz bleaching, aliquots used for the TAF09-27 preheat plateau experiment were bleached by either sunlight (partially cloudy English afternoon) for 500 s or blue LEDs for 300 s (25$^{o}$C). For each preheat temperature, two aliquots were bleached by each method. All accepted aliquots have been grouped by bleaching method, and box plots of the normalized recovered dose distributions are shown in Fig. 5-13a. It is apparent that the median for each group is very close to 1, and that neither bleaching method seems to leave a noticeable relict geological signal. The range of values is much larger for the LED bleached aliquots, which is primarily due to the inclusion of aliquots measured with a 160°C preheat. It is apparent that the OSL signal is essentially fully bleached in well under a minute (see Fig. 5-13b for a representative decay curve): signal emissions from 10 of 12 aliquots fell by more than 90% after 12 s of illumination. These results indicate that Taforalt quartz bleaches fully within several minutes in either sunlight or under restricted wavelengths (i.e., blue LEDs).

Partial bleaching is still possible, however, through the following mechanisms:

1. Quartz or feldspar grains may weather out of the limestone bedrock, either as roof spall, or from boulders incorporated into the infill
2. Disaggregation of cobbles due to heating by human activity, particularly in the Grey Series

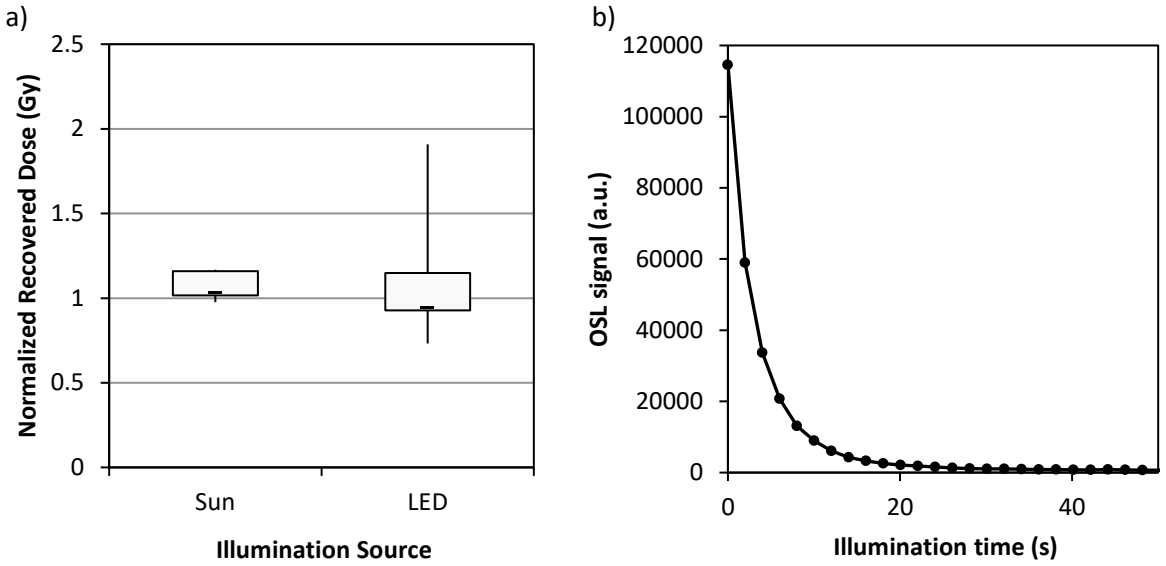


**FIG. 5-13.** Bleaching efficiency. a) Comparison of recovered doses from multigrain aliquots (TAF09-27) bleached either by sunlight or with LEDs at various preheats. Median values and interquartile ranges are similar, but total range is different due to scattered aliquots from the 160°C preheat (see Fig. 5-2). b) Typical natural signal bleaching with LEDs at 25°C.

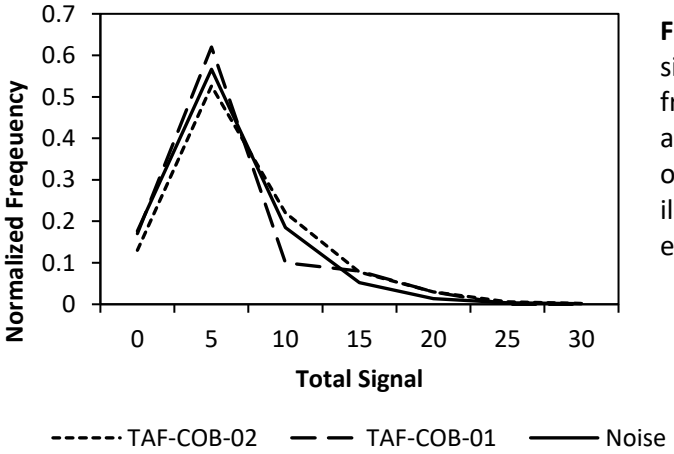


**FIG. 5-14.** Comparison of natural OSL signals for single grains disaggregated from limestone cobbles (TAF-COB-01,-02) and PMT noise characteristics (summed over the same amount of time but with no illumination). The populations are essentially indistinguishable.

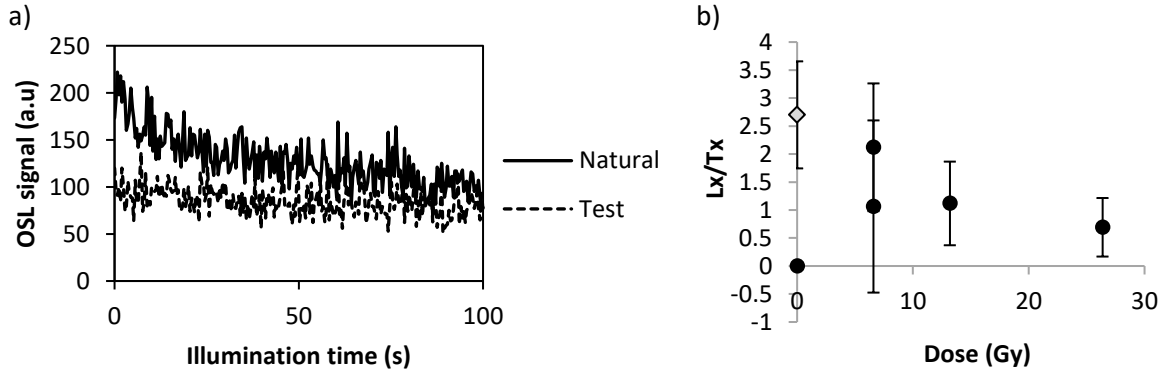


**FIG. 5-15.** Fine grain multigrain measurements (TAF-COB-02). a) Natural and test OSL emissions for one of a few aliquots to have a dim but apparent natural signal. Test dose signals, however, were never bright enough to pass the related rejection criterion. b) Dose response curve for this aliquot.

3. Unbleached grains may be transported by water into cracks in the limestone roof of the cave, reside there for an unknown length of time, then be released into the cave infill

4. Grains may be transported into the cave in a light-restricted environment, either at night, or during a large sediment influx caused by heavy rain.

In all cases, restricted light levels in the cave may not successfully bleach the grains before they are covered by other sediment. The magnitude of the likely relict signal is difficult to estimate, and would depend on the cause of partial bleaching and the grain's original signal.

Routes 1 through 3 were investigated by means of three relevant samples: a tube sample collected from extremely weathered limestone above the entrance of the cave, and burned cobbles from sectors 2 and 8. Based on ICP results (see Section 5.1.3.1), the sector 8 cobble is probably cave limestone, but the sector 2 cobble is not. After disaggregation in HCl and wet sieving, the number of coarse grains released was estimated. From 92.1 g of weathered bedrock, several tens of grains were obtained in the 60-90 μm and 180-255 μm size fractions, with perhaps 200 collected from the 125-180 μm fraction. Samples TAF-COB-02 (Sector 8) and TAF-COB-01 (Sector 2), released approximately 1 to 2 coarse grains (180-255 μm) per gram of original material.

Coarse grains collected from samples TAF-COB-01 (~20-30 grains) and TAF-COB-02 (~200-300) were then prepared as usual and analyzed via single grain techniques. The signals obtained were extremely dim, as is apparent in the histograms of integrated natural signal for both samples. For comparison, PMT noise values were summed over the same number of data channels (channels 58-60 of a 60 channel recording) for the whole measurement file to give ~9300 values. The signal frequencies recorded for both heated cobbles are indistinguishable from the recorded noise (Fig. 5-14). Fine grains were also prepared and investigated for sample TAF-COB-02. Very dim natural OSL decay curves were obtained from most aliquots, however,

signals were not bright enough to generate useable dose response curves (see Fig. 5-15 for representative OSL signal and dose response curves).

These results lead to the conclusion that none of the first three suggested routes are likely to significantly impact OSL ages. Not only are relatively low numbers of grains likely to enter the cave infill via routes 1 and 2 (route 3 may actually be a relatively high input), but the signals obtained will contribute noise rather than a coherent and systematic offset to equivalent dose measurements. Likelihood of the other two routes is more difficult to assess. It is known that heavy downpours occur during the modern wet season, as observed during excavation. Sediment transport at these times was not assessed. In the event, these routes are likely to activate sporadically, therefore one should not expect a systematic effect for all samples. The potential for grains with residual doses must be recalled during age evaluation, but there is no convincing evidence that a correction for partial bleaching (i.e., the minimum age model) should be systematically applied to the OSL equivalent dose estimates.

Microdosimetry

Microdosimetry may have a significant effect on some of the Taforalt sediments, though the evidence is not clear cut. Soil heterogeneity is present, predominantly in Lower Laminated, Calcareous, and Grey Series sediments. Carbonate concretions are common in the Calcareous Group, and shielding effects may account for some of the observed overdispersion. Localized areas of higher dose rate may be present in ash deposits, due to siliceous aggregates with high concentrations of potassium (Mercier, 1995; Jacobs et al., 2008b). Grey Series results, however, indicate these are not common in Taforalt ash. Based on ICP data, the Grey Series is very low in potassium, and analyzed single grain populations have low levels of overdispersion. Yet high concentrations of ash lenses in the Lower Laminated Group may still contribute to microdosimetric effects, due to differing attenuation constants and elemental concentrations between the ash and sediment. Replicate ICP results for Sector 3 samples also indicate the presence of highly variable soil components (see Section 5.1.3.1).

Saturation effects

Saturation characteristics of both single grain and multigrain data were investigated in order to screen Taforalt samples for effects that might adversely affect the calculation of equivalent doses. Both saturated and super-saturated grains have been reported from a variety of environments (Armitage et al., 2000; Yoshida et al., 2000; Feathers, 2003; Jacobs et al., 2003), and experimental data indicates that the presence of either type of grain can cause inaccuracy of the measured equivalent dose when multigrain or synthetic aliquots (those created by summing signals from some number of single grain measurements) are measured: underestimation due to saturated grains (Duller, 2012b) and overestimation due to super-saturated grains (Stone and Bailey, 2012). The magnitude of this effect will depend in large part on the relative signal intensity of the saturated/super-saturated grains, and it may be difficult to spot in the multigrain data due to signal averaging and convolution of growth curve shapes. Therefore, the Taforalt samples were examined to determine: 1) whether the presence of saturated/super-saturated grains determined via single grain analysis could be reliably detected in the multigrain data, and 2) whether equivalent dose could be used as a simple screening mechanism to identify samples that might be particularly affected by these issues.

The proportion of natural signal emissions attributed to saturated, supersaturated, or unbracketed single grains ranged from <5% to >20% (TAF08-02) for analysed samples (Fig. 5-16a). Saturated-type multiple aliquots were also apparent for some, though not all samples. For samples with data of both types, however, the amount of light emitted by saturated grains was not necessarily a good predictor of the ability to recognize saturation effects in multigrain data. Figure 5-16a shows the proportion (%) of the natural signal attributable to saturated grains (from single grain/VSA data) compared to the proportion of multiple grain aliquots in saturation for the same sample (where available). It can be seen that the relationship between recognized saturation in single grains and multigrain aliquots is not straightforward. Many of the samples have levels of single grain saturation not reflected in the multigrain data. In particular, it is

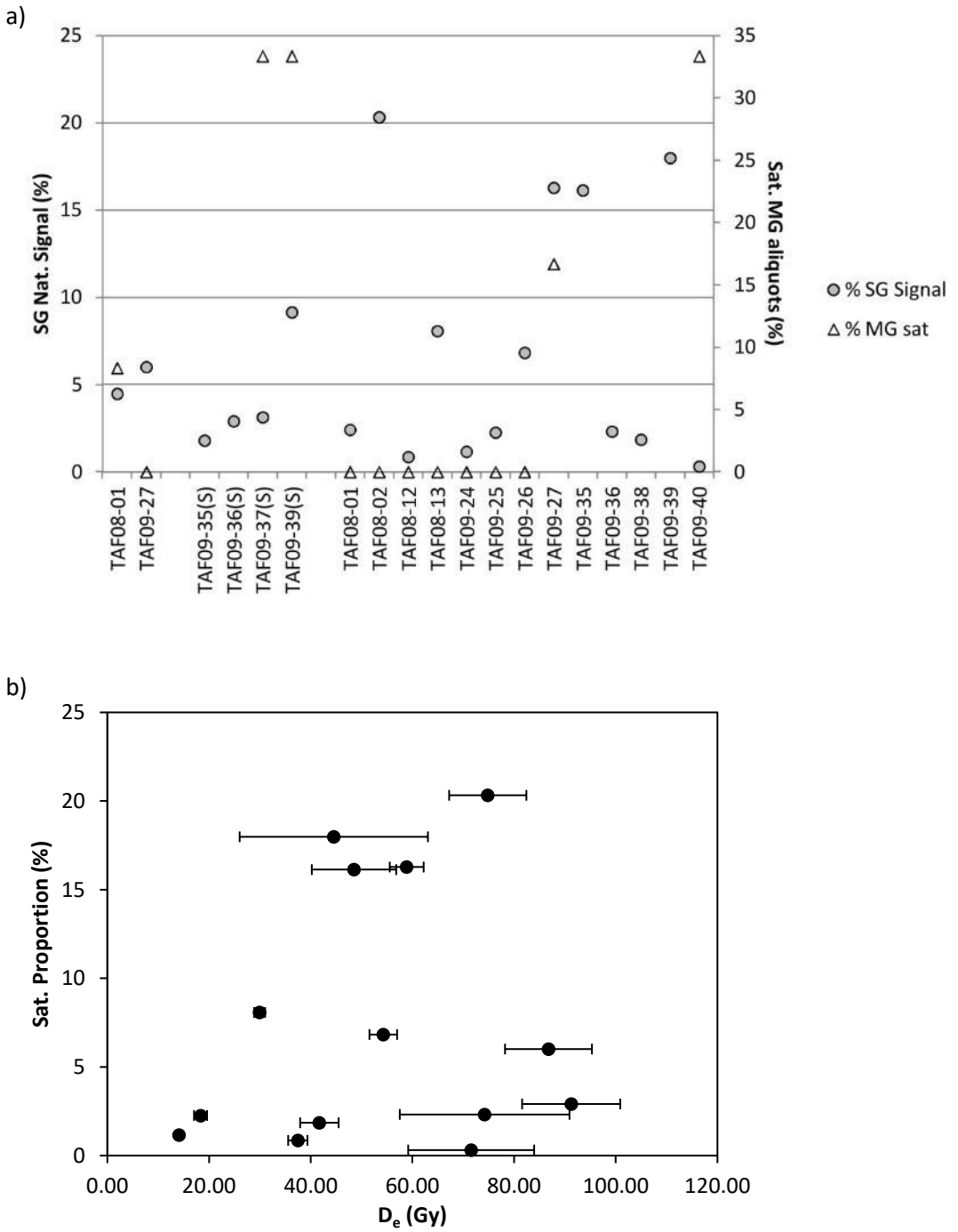


**FIG. 5-16.** Saturation analysis, including saturated, super-saturated, unbracketed grains. a) Proportion of natural signal emitted by saturated-type single grains compared to proportion of saturated multigrain aliquots for each sample. Measurements are grouped from left to right by 220°C preheat, VSA's, and 260°C preheat. b) Proportion of natural signal emitted by saturated grains versus equivalent dose.

concerning that multigrain results in no way indicated that a sample such as TAF08-02, which is likely to be the most affected, has a significant population of saturated grains.

Analysis of the saturated proportion of single grain natural signal versus equivalent dose (central age model value) did not yield a strong correlation. The samples with the highest proportion of saturated grain emission (>15%) tended to have median equivalent doses, while samples with higher equivalent doses had saturated grain emissions of ~5% or lower. It is clear from this data that equivalent dose cannot be used to determine samples that may have high proportions of signal derived from saturated-type grains.

Based on this data and the sources cited above, it seems likely that it may be safest to trust single grain data rather than multigrain for samples which either produce saturated/super-saturated multigrain aliquots, or have high proportions (perhaps > 10%) of light due to such grains. This finding has implications for the cave chronology, which will be discussed further in Section 5.1.4.

#### *5.1.2.4 Age model*

In light of the above analysis, the central age model is the most conservative and the most appropriate choice. Microdosimetry is probably the main cause of equivalent dose distribution scatter, with some influence from SAR effects such as anomalous underestimation of absorbed doses (TAF08-01) and super-saturation (TAF08-02) (see Sections 5.1.1.1, 5.1.1.2, and 5.1.2.3). Partial bleaching is likely to be infrequent and not systematic, therefore it is not possible to deconvolve from microdosimetry without making unsupported assumptions.

Single grain results also do not suggest the systematic input of grains with a common, high equivalent dose (i.e. completely unbleached grains from a nearby geological source), which might be expected if partial bleaching were a significant issue. The finite mixture model was used to investigate single grain distributions in three samples: TAF09-24 (101 grains), TAF09-26 (54 grains), and TAF08-13 (55 grains). These samples were chosen due to their low equivalent doses; if grains with high remnant geological doses are being partially bleached, they should be

TABLE 5-9. Finite mixture model calculations for samples TAF09-24, -26, and 08-13. The accepted model for each initial value (σ) is highlighted in grey, and its components and the maximum log likelihood values are given below.

| | TAF09-24 | | TAF09-26 | | TAF08-13 | |
|---|---|---|---|---|---|---|
| *k* | σ=0.2 | σ=0.3 | σ=0.2 | σ=0.3 | σ=0.2 | σ=0.3 |
| 1 | -260.1 | -260.4 | -136.9 | -135.2 | -115.6 | -117.0 |
| 2 | -259.3 | -260.4 | -134.4 | -135.2 | -115.3 | -117.0 |
| 3 | -518.5 | -520.7 | -268.8 | -270.5 | -230.6 | -234.1 |
| 4 | -777.7 | -781.1 | ------ | -405.7 | -345.9 | -351.1 |
| 5 | -1037.0 | -1041.5 | ------ | ------- | -461.2 | -468.2 |
| Comp. 1 | 14.10± 0.39 | 14.10± 0.39 | 49.36± 0.06 | 54.27± 2.72 | 29.94± 1.08 | 29.94± 1.08 |
| % grains | 100 | 100 | 84.71 | 100 | 100 | 100 |
| Comp. 2 | -- | -- | 83.12± 0.21 | -- | -- | -- |
| % grains | -- | -- | 15.29 | -- | -- | -- |

most visible in the equivalent dose distributions of these samples. The FMM fitted two of three samples (TAF09-24, TAF08-13) with one equivalent dose component for both tested overdispersion values, though assigned grain proportions varied between samples (Table 5-19). If 30% overdispersion was assumed, all samples reverted to a single population. Though overdispersion may be large and skewness high for some samples, there is no evidence for discrete, separable populations.

It is likely that over-interpretation of these results would be detrimental. Though various equivalent dose populations can be statistically extracted from single grain data via the finite mixture model, it is difficult to suggest criteria in this environment for determining the component most closely related to the sediment's burial age. With the lack of such concrete information, simply choosing one based on dominant grain proportion is not likely to provide a robust and accurate chronology (Rhodes et al., 2010; Reimann et al., 2012). Similarly, the minimum age model will cause systematic underestimation if the dominant factor is microdosimetry (Nathan et al., 2003; Mayya et al. 2006). While the central age model may not accurately reflect all underlying physical processes, at least it does not bias the results. It also corresponds more closely to the scale of analysis of standard dose rate measurements, which return only the average dose rate.

### 5.1.3 Dosimetry

#### *5.1.3.1 Sample parameters*

Water content

Water content measurements were made for 48 unique sample locations, 32 from ends and 37 from water content samples. There are also three repeated water content samples (TAF08-14—TAF08-16), taken in the same location in consecutive years because the moisture levels changed significantly. The following analysis takes into account only one measurement per unique sample location (water content sample when available), excepting samples TAF08-14—16 which have both 'dry' and 'wet' values included. Though values derived from water

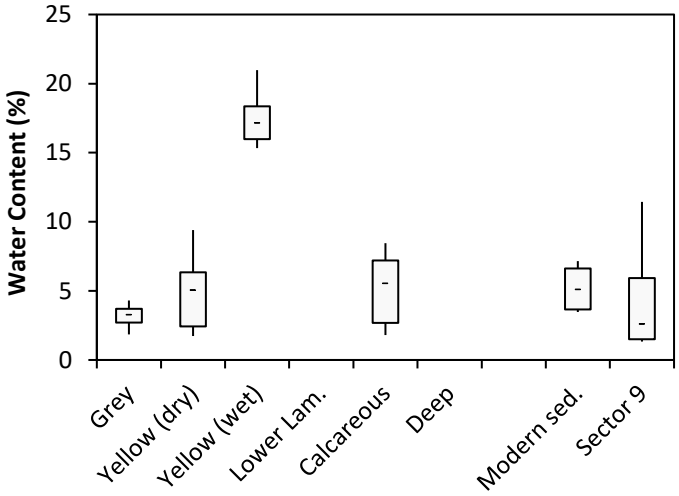


**FIG. 5-17.** Measured water content by sediment type. 'Yellow' sediment is the Upper Laminated Group in Sector 8.

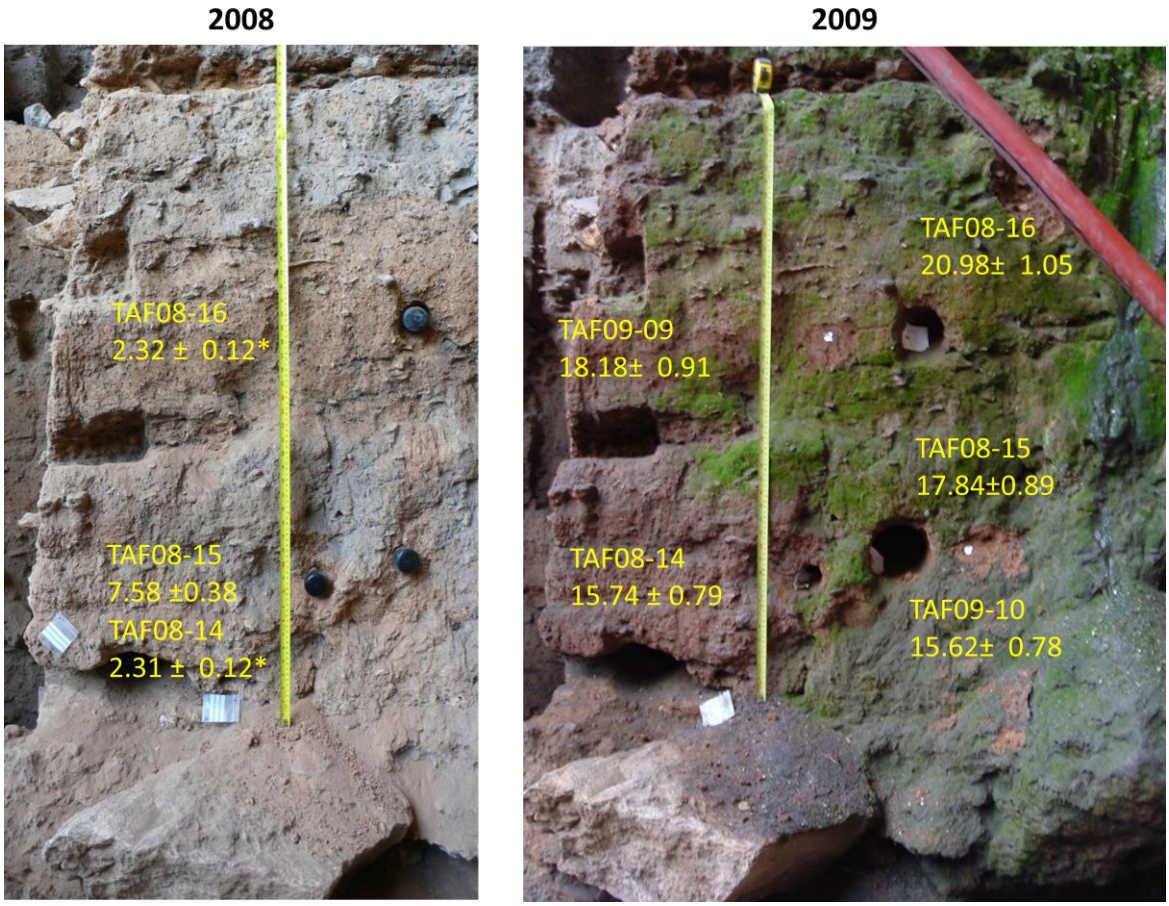


**FIG. 5-18.** 'End-point' water contents (%) measured in sequential years. This section is under the drip line of the cave; it was covered by a tarp prior to sampling in 2008, but left open to moisture during large storms in 2009. Starred measurements were obtained from sample ends rather than water content samples.

content samples are slightly higher than those from sample ends, this difference is not significant: the median shift between these values for the same sample locations (taken simultaneously) is only 1.56%.

Fig. 5-17 shows box plots for each major sediment type and further samples from the Deep Sounding, modern backfill, and Sector 9. Grey Series sediments have water content values between 1.85% and 4.30%. Values for other sediment types have a much larger range, with fairly consistent minima (1- 2%) but maxima that range from 6% to 18%. This is due to sample location. Samples taken from both Sectors 3 and 8 (Upper Laminated) fall into two distinct groups, here called "UL (wet)" and "UL (dry)." The 'wet' samples are located under the drip line of the cave, therefore the moisture of the sediment is expected to fluctuate significantly between seasons. Indeed, significant differences have been noted in soil condition in sequential sampling years (Fig. 5-18).

The excavation history of the cave may also have a significant influence. Water contents for Calcareous Group sediments in Sector 2 range from 5.17% to 8.46%, while those of Sector 1 are much lower at 1.80% and 1.87%. This is almost certainly due to the fact that Sector 1 was excavated several decades ago and has thus lost almost all moisture, while Sector 2 excavations occurred between 2007 and 2010. Likewise, exposed Sector 9 sediments range from 1.33% at the top to 5.9% (tube samples), and rise to 14.04% (water content sample) for the newly excavated (immediately before sampling) Laminated Hearth sediments at the bottom. For this reason, in situ water contents may not be considered reliable values for dose rate estimation.

For the Grey Series, a median value of 3.25 ± 1.5% was chosen to be representative of historical water content levels. Though there may have been periods of significantly higher water content, these are likely to have been brief due to the very porous nature of the sediment. The rest of the sediment is also given one value. The only values from freshly excavated samples within the cave are those of five from Sector 2 (1 Lower Laminated and 4 Calcareous). The median value is 7.63%. The high group of water content sample values from Sectors 3 and 8 can

serve as a high end point, and the median is 17.11%. An average historical value for OSL calculations was therefore chosen to be 12 ± 5%.

Density

An analysis of 32 OSL samples was conducted in order to determine the most appropriate density values for cosmic dose calculations. Density correlated weakly with moisture content ($R^2$=0.2018) and depth ($R^2$=0.142), but there was significant variation within sediment layers (Fig. 5-19a). Grey Series sediment is considerably less dense than other cave infill: median density values are 0.963 g $cm^{-3}$ (Grey) and 1.48 g $cm^{-3}$ (other infill) (Fig. 5-19b). Slightly higher estimates of 1.0 ± 0.1 g $cm^{-3}$ and 1.5 ± 0.2 g $cm^{-3}$ are considered suitable to cover the majority of measured values. Bedrock density, 2.25 ± 0.2 g $cm^{-3}$, was chosen to reflect a medium density limestone (Harrison, 1993).

Elemental concentration

Natural concentrations of U, Th, and K have been measured for 46 samples, comprising 43 sediment samples from the cave interior, two cobbles, and weathered bedrock from the cave exterior. Elemental biplots include all samples sorted by sedimentary Group (Fig. 5-20). It is clear that U, Th, and K are highly correlated in cave sediments.

Thorium values range from 1.4 to 8.22 ppm, uranium values from 0.49 to 2 ppm, and potassium values from 0.51 to 1.83%. The Sector 3 Upper Laminated sediments have the highest radioisotope concentrations. For unknown reasons, they seem to form a distinct group from the Sector 8 Upper Laminated sediments on the basis of the biplots. The Grey Series samples have some of the lowest concentrations in the cave. The Sector 8 cobble and weathered bedrock have by far the lowest elemental concentrations of K and Th, and are likely to derive from cave limestone. The Sector 2 cobble has K, Th, and U concentrations near the maximum of those found in the cave infill, and is clearly from a different source. Sediment samples from within the cave lie on a consistent trend-line, therefore, the main sediment supply for the cave has probably not changed significantly.

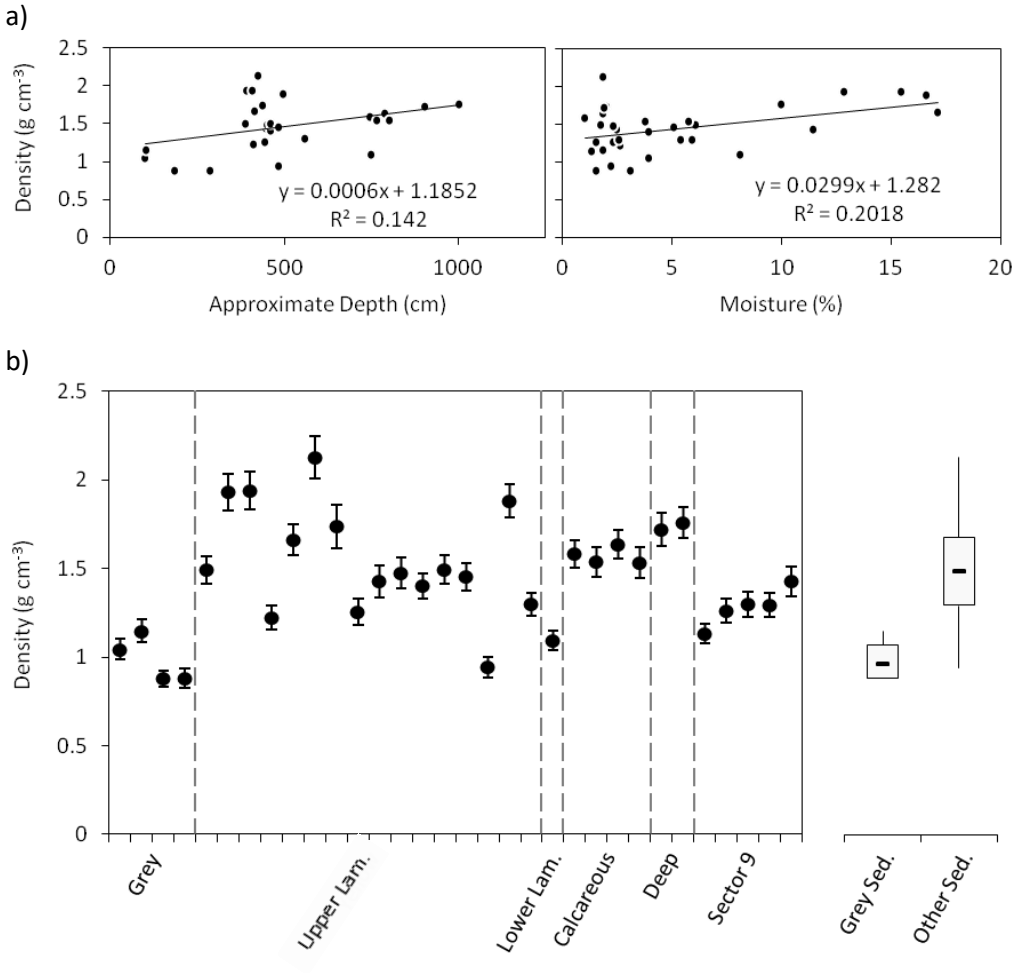


**FIG. 5-19.** Density measurements obtained from Taforalt standard OSL samples. a) Density correlations with depth and water content. b) Measured density by sediment type, all values and box plots.

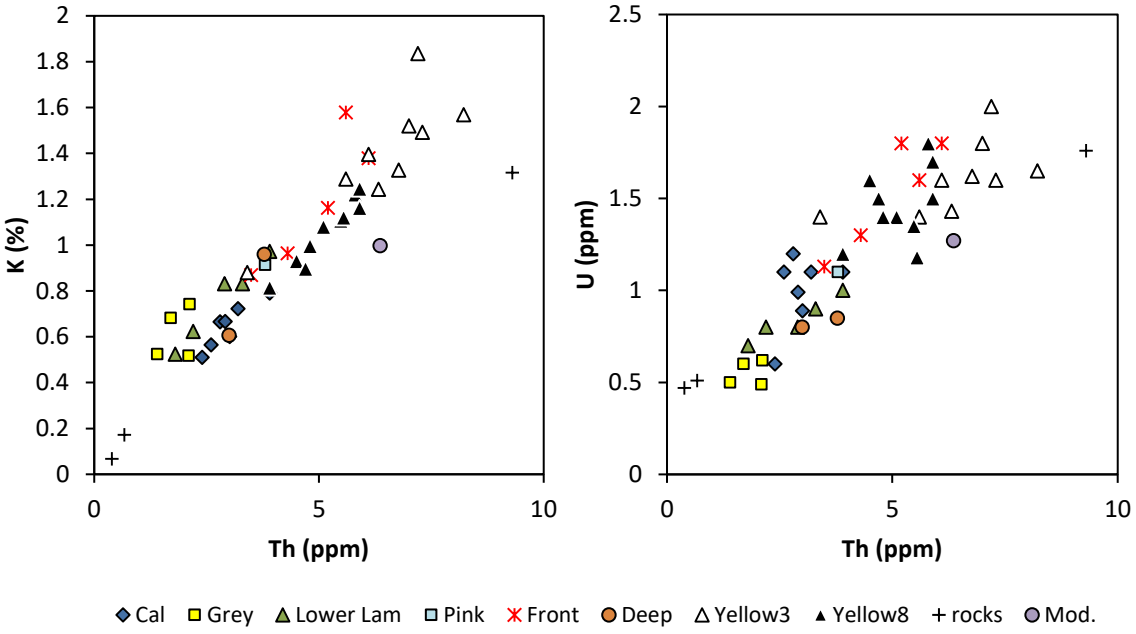


**FIG. 5-20.** Elemental biplots for measured samples (ICP-values) from all sectors. 'Yellow3' and 'Yellow8' indicate the Upper Laminated Group in Sectors 3 and 8, respectively.

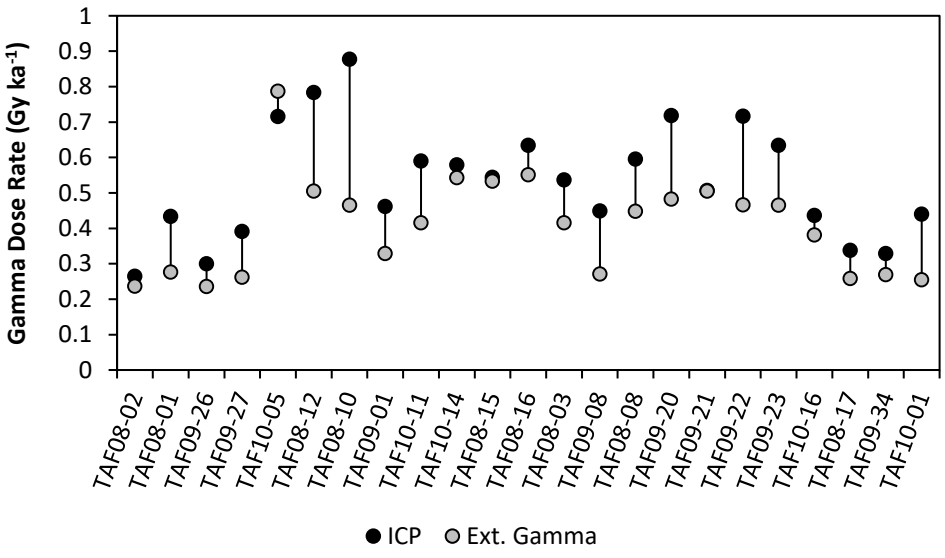


**FIG. 5-21.** Comparison between on-site gamma spectrometer measurements and gamma dose rates calculated from ICP-derived elemental concentrations. The lower dose rates typically measured on site are likely attributable to the presence of calcites and limestone boulders in the sediment.

Reproducibility of measured concentrations is thought to depend primarily on the variation within the sediment, rather than instrumental error. Four samples from Sector 3 (TAF08-10 through 08-13) were sent twice for ICP-MS analysis. Absolute differences in measured concentration ranged from 0 to 26%. Clearly, these cave sediments are highly heterogeneous, and such variations in measured radioisotope concentration could significantly affect the final age estimates.

#### *5.1.3.2 Dose rates*

Sample parameters and calculated dose rates are given in Table 5-12. Calculations for each type of radiation are summarized here.

Gamma dose rate

On-site gamma dose rate measurements were made for most standard tube samples and some microsamples in Taforalt. These values, which have been corrected for assumed average water content, are used in the final age calculation. TAF10-11 has additionally been corrected for its measurement position (only 10 cm into the face due to sediment instability) according to gamma dose attenuation factors given in Aitken (1985: 290): at a depth of 10 cm into the sediment, it will measure 85.61% of the infinite matrix dose rate (averaged K,Th, and U attenuation values). Fig. 5-21 compares these on-site measurements to gamma dose rates calculated from ICP-MS, with samples organized by sector, then depth. The external gamma measurements tended to yield slightly lower dose rates than those calculated from elemental concentrations. Differences are probably caused in most cases by the presence of nearby calcites or limestone boulders from the roof. Table 5-10 records the gamma dose rate and measurement or calculation method for each sample.

*Planar geometry*

Wet gamma dose rates for samples near a sedimentary boundary were calculated both with and without a planar model approximation to the local sediment geometry (Table 5-10). Values calculated without a geometry approximation simply assumed that the sample was

**TABLE 5-10.** Comparison of gamma dose rates: on site γ-spectrometer measurements, calculated from ICP (homogeneous sediment), and calculated from ICP (planar variation). The difference in dose rate when planar variation is taken into account is also given. Gamma dose rate values used in final age calculations are indicated by bold text.

| Sample | γ-spec. (Gy ka$^{-1}$) | Homogeneous Calc. (Gy ka$^{-1}$) | Planar Model (Gy ka$^{-1}$) | % Diff |
|---|---|---|---|---|
| TAF08-01 | -- | 0.43 ± 0.04 | **0.34 ± 0.02** | -22.63 |
| TAF08-02 | **0.27 ± 0.01** | 0.26 ± 0.02 | -- | -- |
| TAF08-03 | **0.43 ± 0.02** | 0.54 ± 0.05 | -- | -- |
| TAF08-04 | **0.43 ± 0.02**[a] | 0.53 ± 0.04 | -- | -- |
| TAF08-05 | -- | 0.67 ± 0.06 | -- | -- |
| TAF08-06 | -- | 0.67 ± 0.06 | -- | -- |
| TAF08-08 | **0.48 ± 0.02** | 0.60 ± 0.05 | -- | -- |
| TAF08-10 | **0.51 ± 0.03** | 0.81 ± 0.07 | -- | -- |
| TAF08-11 | **0.53 ± 0.03**[b] | 0.63 ± 0.05 | -- | -- |
| TAF08-12 | **0.56 ± 0.03** | 0.76 ± 0.06 | -- | -- |
| TAF08-13 | **0.56 ± 0.03**[c] | 0.65 ± 0.06 | -- | -- |
| TAF08-14 | **0.56 ± 0.03**[d] | 0.57 ± 0.05 | -- | -- |
| TAF08-15 | **0.56 ± 0.03** | 0.54 ± 0.05 | -- | -- |
| TAF08-16 | **0.49 ± 0.02** | 0.63 ± 0.05 | -- | -- |
| TAF08-17 | **0.26 ± 0.01** | 0.34 ± 0.02 | -- | -- |
| TAF09-01 | **0.31 ± 0.02** | 0.46 ± 0.04 | -- | -- |
| TAF09-08 | **0.28 ± 0.01** | 0.45 ± 0.04 | -- | -- |
| TAF09-20 | **0.55 ± 0.03** | 0.72 ± 0.06 | -- | -- |
| TAF09-21 | **0.57 ± 0.03** | 0.51 ± 0.04 | -- | -- |
| TAF09-22 | **0.52 ± 0.03** | 0.72 ± 0.06 | -- | -- |
| TAF09-23 | **0.50 ± 0.03** | 0.63 ± 0.05 | -- | -- |
| TAF09-24 | -- | 0.24 ± 0.01 | -- | -- |
| TAF09-25 | -- | 0.30 ± 0.02 | -- | -- |
| TAF09-26 | **0.24 ± 0.01** | 0.30 ± 0.03 | -- | -- |
| TAF09-27 | **0.27 ± 0.01** | 0.39 ± 0.03 | -- | -- |
| TAF09-34 | **0.30 ± 0.02** | 0.33 ± 0.03 | -- | -- |
| TAF09-35 | -- | 0.46 ± 0.04 | **0.43 ± 0.03** | -5.73 |
| TAF09-36 | -- | 0.37 ± 0.03 | **0.40 ± 0.02** | 6.99 |
| TAF09-37 | -- | 0.40 ± 0.03 | -- | -- |
| TAF09-38 | **0.24 ± 0.01** | 0.25 ± 0.02 | -- | -- |
| TAF09-39 | -- | 0.46 ± 0.04 | **0.42 ± 0.02** | -8.89 |
| TAF09-40 | -- | 0.33 ± 0.03 | **0.37 ± 0.02** | 12.30 |
| TAF10-01 | **0.25 ± 0.01** | 0.44 ± 0.04 | -- | -- |
| TAF10-02 | **0.75 ± 0.04** | 0.66 ± 0.06 | -- | -- |
| TAF10-05 | **0.75 ± 0.04** | 0.72 ± 0.06 | -- | -- |
| TAF10-06 | **0.75 ± 0.04** | 0.77 ± 0.07 | -- | -- |
| TAF10-07 | **0.75 ± 0.04** | 0.83 ± 0.07 | -- | -- |
| TAF10-10 | -- | 0.27 ± 0.01 | **0.29 ± 0.02** | 6.39 |
| TAF10-11 | **0.55 ± 0.03**[e] | 0.59 ± 0.05 | 0.59 ± 0.03 | 0.72 |
| TAF10-14 | **0.59 ± 0.03** | 0.58 ± 0.05 | -- | -- |
| TAF10-16 | **0.37 ± 0.02** | 0.44 ± 0.04 | -- | -- |
| TAF10-17 | -- | 0.34 ± 0.03 | **0.30 ± 0.02** | -10.50 |
| TAF10-18 | -- | 0.36 ± 0.03 | **0.31 ± 0.02** | -12.09 |

[a] Used TAF08-03 γ-spec.

[b] Mean TAF08-10 and 08-12 γ-spec.

[c] Used TAF08-12 γ-spec.

[d] Used TAF08-15 γ-spec.

[e]Corrected for measurement geometry (see text for details).

collected from an infinite matrix with ICP-derived radioisotope concentrations. By comparing these values (Table 5-10), it is apparent that modeling local geometry can significantly influence the local dose rate. While TAF10-11 remained almost unchanged, other samples' dose rates changed by anywhere from 5% to 20%. The direction of change was expected in nearly all cases, i.e. modeled gamma dose became higher for a sample in a low dose sediment next to a high dose sediment. The exception to this was TAF10-11, which was situated in the relatively high dose Upper Laminated Group near to the lower dose Grey Series. In this instance, the modeled gamma dose rate increased slightly, due to the interaction of water content and attenuation effects. It should be noted that average dose rates were calculated for both 'static' and 'sediment replacement' scenarios for samples underneath boundaries. However, in all cases, the length of the suggested time gap was short enough to make the replacement assumption seem unlikely, so static scenario values were used for final age calculations.

These calculations can be checked by cross-comparing them with independent values in two cases. The first, TAF08-01, was also modeled via Monte Carlo methods as outlined in Chapter 4. These calculations were performed assuming a 1.6 g $cm^{-3}$ sediment density, and all other values as given in previous sections. Assuming a matching sediment density for the moment, the planar model gives a dose rate of 0.364 ± 0.018 Gy $ka^{-1}$ (dry) and 0.338 ± 0.019 Gy $ka^{-1}$ (wet), while the Monte Carlo model yields 0.30 ± 0.05 Gy $ka^{-1}$. That is, the planar geometry dose rate is ~84% of the unmodeled dose rate, while the Monte Carlo dose rate is only 69.1%. Altering the sediment density to 1.5 g $cm^{-3}$, the density value chosen for this project, reduces the planar model's dose rate slightly to 0.362 ± 0.018 Gy $ka^{-1}$ (dry) and 0.336 ± 0.019 Gy $ka^{-1}$ (wet). In the second case, the calculated value for TAF10-11 can be compared with a (corrected) external gamma measurement. The measured value, 0.545 ± 0.027 Gy $ka^{-1}$, is 7.7% lower than the calculated gamma dose rate. Both gamma-spectrometer measurements and N-particle transport models are more reliable than the simplified calculations used in this thesis, and the

**TABLE 5-11.** Model parameters for planar variation calculations of gamma dose rates. Models have been described in Ch. 4. For models 1 and 2, flowstone ICP values were U: 0.30 ± 0.02 ppm, Th: 0.70 ± 0.04 ppm, and K: 0.15 ± 0.01%.

Parameter Definitions:

$D_b$=Distance from tube edge to boundary (cm)
$d_f$ = Flowstone thickness (cm)
$d_s$ = Sediment thickness (cm)
t = Tube diameter (cm)

a) Model 1

| **Sample (Sediment 1)** | **Sediment 2** | **t** | **$D_b$** | **$d_f$** | **$d_s$** |
|---|---|---|---|---|---|
| TAF08-01 | TAF08-02 | 5.5 | 3.5 | 13.0 | 12.5 |

b) Model 2

| **Sample (Sediment 1)** | **Sediment 2** | **t** | **$D_b$** | **$d_f$** |
|---|---|---|---|---|
| TAF10-17 | -- | 4.5 | 2.5 | 13.0 |
| TAF10-18 | -- | 2 | 3 | 13.0 |

c) Model 3

| **Sample (Sediment 1)** | **Sediment 2** | **t** | **$D_b$** |
|---|---|---|---|
| TAF09-35 | TAF09-36 | 2.0 | 2.0 |
| TAF09-36 | TAF09-35 | 2.0 | 2.0 |
| TAF09-39 | TAF09-40 | 2.0 | 2.0 |
| TAF09-40 | TAF09-39 | 2.0 | 2.0 |
| TAF10-10 | TAF10-11 | 2.0 | 18.0 |

results obtained disagree slightly. It is clear, though, that the planar approximations are more accurate than assuming a homogeneous sediment.

Cosmic dose rate

The skyview correction that has been used depends on the sample's distance from the entrance to the cave, which affects both the skyview proportion and the minimum path length through sediment for cosmic rays entering through the cave mouth. The effect of the skyview correction upon samples is demonstrated in Fig. 5-22. Three cases are considered: a sample in Taforalt's overlying ash layer 1 m from the surface (case 1), and samples in an underlying sediment layer 1 m and 5 m under the sediment/ash interface (cases 2 and 3, respectively). For all cases, the difference between the skyview-corrected and uncorrected values is significant at the cave entrance. The skyview-corrected values for the cases are between 3 and 4 times higher than the uncorrected values at the cave entrance, but only 1 to 1.5 times higher by the back of the cave (~20 m).

### 5.1.4 Age estimates

Table 5-13 compares ages calculated via all equivalent dose analyses (multigrain, single grain, and VSA). Single grain ages are systematically younger than those calculated from multigrain data. This is clearest in the Upper Laminated and Grey Series data: single grain ages are 10-14% younger in the Upper Laminated Sediments and ~5% in the Grey Series. Data from Sectors 1 and 2 are more variable, but the trend is still present. For all samples but TAF09-40, single grain ages are younger than multigrain; since only 11 grains were accepted from TAF09-40, this may not be an actual exception. In general, there is no reason to think that the younger, single grain ages are more reliable. Exceptions to this will be discussed below.

A schematic of Taforalt samples and their OSL ages is displayed in Fig. 5-23 (see Figs. 3-7 through 3-18 for photographs of sample locations). Preference has been given to VSA, multigrain, and single grain data in that order, based on the number of grains measured by each technique and given the lack of partial bleaching issues suggested by single grain analysis. The

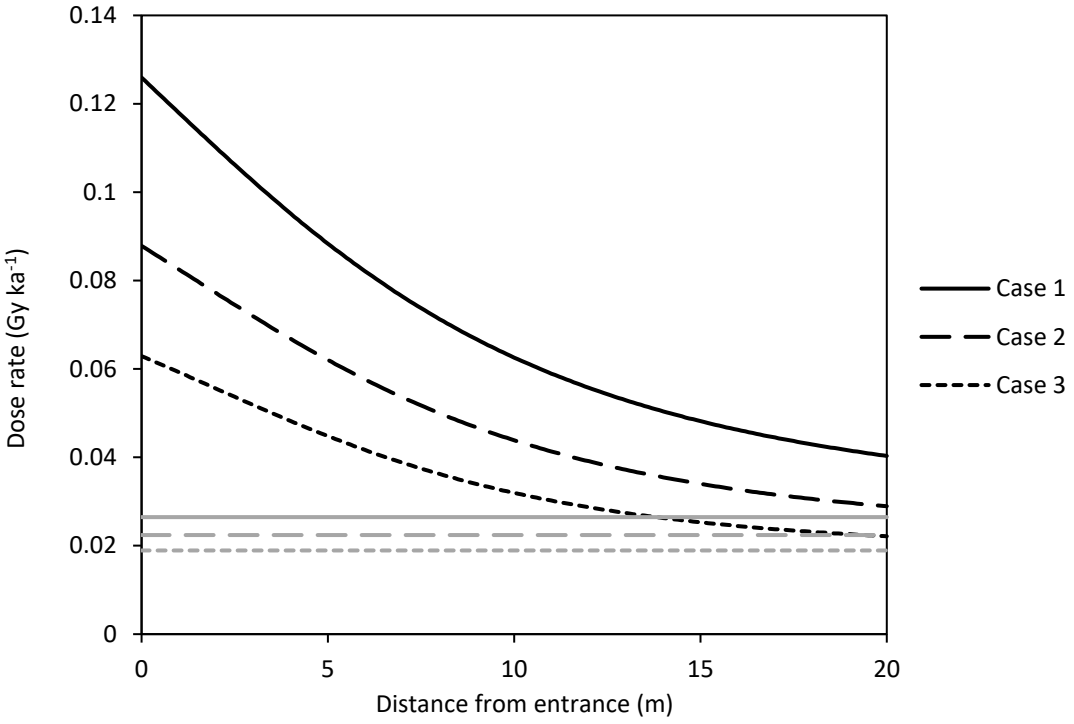


**FIG. 5-22.** Comparison of skyview-corrected and standard model cosmic dose rates on sample position within Taforalt cave. Three hypothetical samples are considered: sample beneath 1 m ash (Case 1), sample beneath 5 m ash and 1 m standard sediment (Case 2), sample beneath 5 m ash and 5 m standard sediment (Case 3). Black lines are skyview-corrected values, and grey lines are standard model. The cave roof has been estimated to be 20 m thick, with a density of 2.25 g $cm^{-3}$.

**TABLE 5-12.** Sample dose rates and calculation parameters. Samples denoted by bold text were collected in the Grey Series. Infill depth for these samples is total depth, and water content is 3.25 ± 1.50%. For all other samples, infill depth is depth in standard sediment (not including overlying 5 m of ash) and water content is 12.00 ± 5.00%.

| Sample | Grain Size (μm) | K (%) | Th (ppm) | U (ppm) | Infill Depth (m) | Dist. From Entrance (m) | Alpha ($10^{-2}$ Gy $ka^{-1}$) | Beta ($10^{-2}$ Gy $ka^{-1}$) | Gamma ($10^{-2}$ Gy $ka^{-1}$) | Cosmic ($10^{-2}$ Gy $ka^{-1}$) | Total Wet Dose Rate (Gy $ka^{-1}$) |
|---|---|---|---|---|---|---|---|---|---|---|---|
| TAF08-01 | 180-255 | 0.79 | 3.90 | 1.10 | 2.41 | 15.00 | 4.09 ± 2.07 | 67.51 ± 6.41 | 33.61 ± 1.87 | 3.04 ± 0.79 | 1.08 ± 0.07 |
| TAF08-02 | 180-255 | 0.51 | 2.40 | 0.60 | 2.02 | 15.00 | 3.33 ± 1.79 | 42.20 ± 4.05 | 26.83 ± 1.34 | 3.13 ± 0.85 | 0.72 ± 0.05 |
| TAF08-03 | 180-255 | 0.93 | 4.50 | 1.60 | 2.19 | 5.00 | 4.63 ± 2.32 | 82.50 ± 7.75 | 42.96 ± 2.15 | 5.60 ± 0.81 | 1.34 ± 0.09 |
| TAF08-04 | 180-255 | 0.90 | 4.70 | 1.50 | 1.87 | 5.00 | 4.61 ± 2.31 | 79.77 ± 7.48 | 42.96 ± 2.15 | 5.76 ± 0.81 | 1.30 ± 0.09 |
| TAF08-05 | 180-255 | 1.22 | 5.80 | 1.80 | 1.53 | 5.00 | 5.12 ± 2.58 | 104.93 ± 9.95 | 67.16 ± 5.68 | 5.93 ± 0.84 | 1.83 ± 0.12 |
| TAF08-06 | 180-255 | 1.25 | 5.90 | 1.70 | 1.66 | 5.00 | 5.07 ± 2.55 | 105.59 ± 10.06 | 67.12 ± 5.69 | 5.86 ± 0.82 | 1.84 ± 0.12 |
| TAF08-08 | 180-255 | 1.00 | 6.36 | 1.27 | 0.38 | 4.00 | 4.85 ± 2.48 | 86.59 ± 8.17 | 47.65 ± 2.38 | 7.06 ± 0.90 | 1.43 ± 0.10 |
| TAF08-10 | 180-255 | 1.72 | 6.60 | 1.85 | 0.92 | 8.00 | 5.36 ± 2.72 | 137.59 ± 13.39 | 50.67 ± 2.53 | 5.03 ± 0.88 | 1.95 ± 0.14 |
| TAF08-11 | 180-255 | 1.25 | 5.30 | 1.50 | 0.70 | 8.00 | 4.76 ± 2.39 | 102.51 ± 9.88 | 53.12 ± 2.66 | 5.13 ± 0.89 | 1.59 ± 0.11 |
| TAF08-12 | 180-255 | 1.52 | 6.40 | 1.75 | 0.44 | 8.00 | 5.23 ± 2.65 | 124.28 ± 12.01 | 55.56 ± 2.78 | 5.25 ± 0.93 | 1.85 ± 0.13 |
| TAF08-13 | 180-255 | 1.29 | 5.75 | 1.40 | 0.19 | 8.00 | 4.80 ± 2.42 | 105.12 ± 10.17 | 55.56 ± 2.78 | 5.37 ± 0.92 | 1.64 ± 0.11 |
| TAF08-14 | 180-255 | 1.08 | 5.10 | 1.40 | 1.20 | 6.00 | 4.63 ± 2.33 | 90.71 ± 8.67 | 56.38 ± 2.82 | 5.66 ± 0.90 | 1.54 ± 0.10 |
| TAF08-15 | 180-255 | 1.00 | 4.80 | 1.40 | 1.14 | 6.00 | 4.55 ± 2.29 | 85.04 ± 8.08 | 56.38 ± 2.82 | 5.69 ± 0.87 | 1.49 ± 0.10 |
| TAF08-16 | 180-255 | 1.16 | 5.90 | 1.50 | 0.68 | 6.00 | 4.91 ± 2.48 | 98.36 ± 9.37 | 48.88 ± 2.44 | 5.93 ± 0.88 | 1.64 ± 0.11 |
| **TAF08-17** | 180-255 | 0.74 | 2.12 | 0.62 | 0.42 | 20.00 | 3.75 ± 2.05 | 63.07 ± 4.67 | 25.53 ± 1.28 | 4.19 ± 2.15 | 0.97 ± 0.06 |
| TAF09-01 | 180-255 | 0.88 | 3.40 | 1.40 | 1.25 | 8.00 | 4.20 ± 2.12 | 75.30 ± 7.16 | 30.78 ± 1.54 | 4.89 ± 0.87 | 1.17 ± 0.08 |
| TAF09-08 | 180-255 | 0.81 | 3.90 | 1.20 | 2.86 | 5.50 | 4.17 ± 2.10 | 70.01 ± 6.64 | 28.30 ± 1.42 | 5.11 ± 0.78 | 1.06 ± 0.07 |
| TAF09-20 | 180-255 | 1.58 | 5.60 | 1.60 | 0.29 | 0.00 | 4.91 ± 2.47 | 124.48 ± 12.19 | 54.96 ± 2.75 | 9.37 ± 0.86 | 1.87 ± 0.13 |
| TAF09-21 | 180-255 | 0.96 | 4.30 | 1.30 | 0.66 | 0.00 | 4.35 ± 2.19 | 81.02 ± 7.74 | 57.36 ± 2.87 | 9.06 ± 0.83 | 1.45 ± 0.09 |
| TAF09-22 | 180-255 | 1.38 | 6.10 | 1.80 | 1.10 | 0.00 | 5.19 ± 2.62 | 115.21 ± 11.03 | 52.27 ± 2.61 | 8.71 ± 0.80 | 1.76 ± 0.12 |
| TAF09-23 | 180-255 | 1.16 | 5.20 | 1.80 | 1.38 | 0.00 | 4.96 ± 2.49 | 100.24 ± 9.50 | 50.24 ± 2.51 | 8.49 ± 0.79 | 1.60 ± 0.11 |
| **TAF09-24** | 180-255 | 0.52 | 1.40 | 0.50 | 1.02 | 5.50 | 3.43 ± 1.97 | 45.06 ± 3.31 | 24.10 ± 1.21 | 8.21 ± 1.19 | 0.81 ± 0.04 |
| **TAF09-25** | 180-255 | 0.68 | 1.70 | 0.60 | 1.84 | 5.50 | 3.61 ± 2.01 | 57.80 ± 4.29 | 30.25 ± 1.54 | 7.53 ± 1.05 | 0.99 ± 0.05 |
| TAF09-26 | 180-255 | 0.62 | 2.20 | 0.80 | 1.46 | 15.00 | 3.43 ± 1.82 | 50.89 ± 4.92 | 24.21 ± 1.21 | 3.28 ± 0.86 | 0.81 ± 0.06 |
| TAF09-26 | 180-255 | 0.62 | 2.20 | 0.80 | 1.46 | 15.00 | 3.43 ± 1.82 | 50.89 ± 4.92 | 24.21 ± 1.21 | 3.28 ± 0.86 | 0.81 ± 0.06 |
| TAF09-27 | 180-255 | 0.72 | 3.20 | 1.10 | 1.73 | 15.00 | 3.92 ± 1.99 | 62.04 ± 5.89 | 27.41 ± 1.37 | 3.20 ± 0.83 | 0.95 ± 0.07 |
| TAF09-34 | 180-255 | 0.61 | 3.00 | 0.80 | 4.15 | 15.00 | 3.63 ± 1.89 | 51.33 ± 4.89 | 30.46 ± 1.52 | 2.68 ± 0.73 | 0.85 ± 0.06 |
| TAF09-35 | 125-180 | 0.91 | 3.80 | 1.10 | 1.02 | 15.00 | 4.83 ± 2.43 | 77.03 ± 7.42 | 43.00 ± 2.86 | 3.40 ± 0.90 | 1.28 ± 0.08 |
|  | 180-255 |  |  |  |  |  | 4.07 ± 2.06 |  |  |  | 1.25 ± 0.05 |

**TABLE 5-12.** (Continued)

| Sample | Grain Size (µm) | K (%) | Th (ppm) | U (ppm) | Infill Depth (m) | Dist. From Entrance (m) | Alpha ($10^{-2}$ Gy $ka^{-1}$) | Beta ($10^{-2}$ Gy $ka^{-1}$) | Gamma ($10^{-2}$ Gy $ka^{-1}$) | Cosmic ($10^{-2}$ Gy $ka^{-1}$) | Total Wet Dose Rate (Gy $ka^{-1}$) |
|---|---|---|---|---|---|---|---|---|---|---|---|
| TAF09-36 | 125-180 | 0.83 | 2.90 | 0.80 | 1.05 | 15.00 | 4.16 ± 2.10 | 66.78 ± 6.55 | 39.83 ± 2.33 | 3.39 ± 0.91 | 1.14 ± 0.07 |
| | 180-255 | | | | | | 3.61 ± 1.88 | | | | 1.12 ± 0.07 |
| TAF09-37 | 125-180 | 0.83 | 3.30 | 0.90 | 1.24 | 15.00 | 4.42 ± 2.22 | 68.64 ± 6.66 | 39.85 ± 3.40 | 3.33 ± 0.88 | 1.16 ± 0.08 |
| TAF09-38 | 180-255 | 0.52 | 1.80 | 0.70 | 1.40 | 15.00 | 3.25 ± 1.77 | 42.96 ± 4.14 | 24.21 ± 1.21 | 3.29 ± 0.86 | 0.73 ± 0.05 |
| TAF09-39 | 125-180 | 0.97 | 3.90 | 1.00 | 1.67 | 15.00 | 4.75 ± 2.40 | 79.81 ± 7.76 | 42.16 ± 2.48 | 3.22 ± 0.86 | 1.30 ± 0.09 |
| | 180-255 | | | | | | 4.02 ± 2.04 | | | | 1.27 ± 0.08 |
| TAF09-40 | 125-180 | 0.56 | 2.60 | 1.10 | 1.73 | 15.00 | 4.38 ± 2.21 | 52.69 ± 4.92 | 37.44 ± 2.27 | 3.20 ± 0.86 | 0.98 ± 0.6 |
| | 180-255 | | | | | | 3.76 ± 1.94 | | | | 0.96 ± 0.6 |
| TAF10-01 | 180-255 | 0.96 | 3.78 | 0.85 | 5.00 | 13.00 | 3.87 ± 1.99 | 75.11 ± 7.38 | 25.33 ± 1.27 | 2.74 ± 0.69 | 1.07 ± 0.08 |
| TAF10-02 | 125-180 | 1.24 | 6.32 | 1.43 | 0.30 | 9.00 | 6.12 ± 3.21 | 106.32 ± 10.18 | 75.28 ± 3.76 | 4.98 ± 0.95 | 2.00 ± 0.13 |
| TAF10-05 | 125-180 | 1.33 | 6.77 | 1.62 | 0.45 | 9.00 | 6.50 ± 3.43 | 114.51 ± 10.93 | 75.28 ± 3.76 | 4.91 ± 0.90 | 2.05 ± 0.14 |
| TAF10-06 | 125-180 | 1.49 | 7.30 | 1.60 | 0.50 | 9.00 | 6.67 ± 3.57 | 125.74 ± 12.10 | 75.28 ± 3.76 | 4.89 ± 0.89 | 2.18 ± 0.15 |
| TAF10-07 | 125-180 | 1.57 | 8.22 | 1.65 | 0.55 | 9.00 | 7.06 ± 3.85 | 132.91 ± 12.76 | 75.28 ± 3.76 | 4.86 ± 0.93 | 2.25 ± 0.15 |
| TAF10-10 | 180-255 | 0.52 | 2.10 | 0.49 | 4.82 | 5.50 | 3.63 ± 2.02 | 45.97 ± 3.29 | 28.79 ± 1.76 | 5.73 ± 0.88 | 0.84 ± 0.04 |
| TAF10-11 | 125-180 | 1.11 | 5.48 | 1.35 | 0.20 | 5.50 | 5.72 ± 2.95 | 95.18 ± 9.09 | 54.51 ± 2.73 | 6.42 ± 0.94 | 1.56 ± 0.11 |
| TAF10-14 | 125-180 | 1.12 | 5.55 | 1.18 | 1.00 | 5.00 | 5.56 ± 2.88 | 94.34 ± 9.08 | 58.61 ± 2.93 | 6.21 ± 0.87 | 1.60 ± 0.11 |
| TAF10-16 | 180-255 | 0.87 | 3.49 | 1.13 | 1.85 | 0.00 | 4.01 ± 2.03 | 71.95 ± 6.92 | 37.15 ± 1.86 | 8.15 ± 0.76 | 1.22 ± 0.08 |
| TAF10-17 | 180-255 | 0.60 | 3.01 | 0.89 | 2.03 | 15.00 | 3.71 ± 1.91 | 51.96 ± 4.92 | 30.19 ± 2.05 | 3.13 ± 0.86 | 0.89 ± 0.06 |
| TAF10-18 | 125-180 | 0.67 | 2.91 | 0.99 | 1.97 | 16.00 | 4.38 ± 2.19 | 58.50 ± 5.55 | 31.36 ± 2.22 | 3.03 ± 0.85 | 0.97 ± 0.06 |

exception to this is sample TAF08-02, for which the single grain data is used due to the effects of super-saturation on multigrain aliquots (see Section 5.1.2.3). This view allows the consideration of OSL ages according to stratigraphic order and internal coherence. Each Group will be discussed, beginning with the Grey Series.

Four ages are available for the Grey Series, which create two disparate groups. Samples TAF09-24 (18.32 ± 1.21 ka) and TAF09-25 (19.43 ± 1.82 ka) are significantly older than TAF08-17 and TAF10-10 (both ~14.2 ka). Additionally, ages for TAF09-24/-25 and TAF10-10 are stratigraphically reversed. No intrinsic reason for this was discovered in the equivalent dose analyses. Single grain data for the two older samples revealed positive OSL qualities, i.e. numerous bright grains with relatively low overdispersion, and dose recovery was accurate.

Samples collected from the Upper Laminated sediments (Sectors 3 and 8) and the unstudied sediments of Sector 9 are generally in stratigraphic order, and do not suffer from any improbable age-depth relationships. Microsample ages are more variable and tend to be slightly younger than standard samples in Sector 3, but they correspond well with standard samples in Sector 8. Based on the OSL results from the base of Sectors 3 and 8, there may be a depositional hiatus between 30 and 40 ka.

There are, however, two pairs of adjacent samples (TAF08-05/06, TAF08-15/14) in Sector 8 that have reversed ages. One of these pairs overlaps at 1σ, but the other does not. The discrepancy between TAF08-05 and TAF08-06 is actually larger than it seems here due to the presence of the nearby limestone boulder (~ 2-3 cm from TAF08-05, ~ 7 cm from TAF08-06). Because no gamma-spectrometer measurements were made for these samples, the calculated gamma dose rate is higher than in reality. This effect is larger for sample TAF08-05, which is closer to the boulder, therefore its true age is likely to be slightly older. No particular reason for the reversal is apparent.

Sectors 1, 2, and the Deep Sounding are more problematic. There is little independent evidence for sediment age in the Deep Sounding, but stratigraphy suggests that ~170 ka is more

**TABLE 5-13.** Final ages for all samples and every measurement type. Ages in italic font indicate that fewer than 4 multigrain aliquots or 20 single grains were accepted for analysis, and therefore results should be treated with caution.

| Sample | Multigrain Age (ka) | Single Grain Age (ka) | VSA Age (ka) | Modelled Age (ka) |
|---|---|---|---|---|
| TAF08-01 | 106.8 ± 12.4[a] | 84.3 ± 10.5[a] | -- | 94.9 ± 9.6 |
| TAF08-02 | 134.5 ± 11.5[a] | 103.4 ± 12.7 | -- | 88.3 ± 8.9 |
| TAF08-03 | 44.0 ± 3.8 | -- | -- | 39.2 ± 2.2 |
| TAF08-04 | 39.7 ± 3.4 | -- | -- | 36.7 ± 2.3 |
| TAF08-05 | 30.8 ± 2.6 | -- | -- | 28.6 ± 1.6 |
| TAF08-06 | 24.0 ± 2.0 | -- | -- | 28.1 ± 1.5 |
| TAF08-08 | 28.5 ± 2.7 | -- | -- | -- |
| TAF08-10 | 31.3 ± 2.5 | -- | -- | 33.5 ± 2.0 |
| TAF08-11 | 28.4 ± 2.8 | -- | -- | 29.1 ± 1.6 |
| TAF08-12 | 22.9 ± 2.2 | 20.2 ± 1.8 | -- | 21.5 ± 1.3 |
| TAF08-13 | 20.0 ± 1.7 | 18.2 ± 1.4 | -- | 18.9 ± 1.0 |
| TAF08-14 | 26.2 ± 2.0 | -- | -- | 25.1 ± 1.3 |
| TAF08-15 | 29.7 ± 2.7 | -- | -- | 25.7 ± 1.5 |
| TAF08-16 | 22.7 ± 1.9 | -- | -- | 21.9 ± 1.4 |
| TAF08-17 | 14.2 ± 1.4 | -- | -- | 14.5 ± 1.3 |
| TAF09-01 | 39.8 ± 3.9 | -- | -- | 38.2 ± 2.5 |
| TAF09-08 | 44.2 ± 4.7 | -- | -- | 40.5 ± 2.4 |
| TAF09-20 | 18.6 ± 1.7 | -- | -- | 19.5 ± 1.8 |
| TAF09-21 | 25.1 ± 2.3 | -- | -- | 24.0 ± 1.6 |
| TAF09-22 | 26.1 ± 2.0 | -- | -- | 26.4 ± 1.5 |
| TAF09-23 | 28.3 ± 3.1 | -- | -- | 29.4 ± 2.2 |
| TAF09-24 | 18.3 ± 1.2 | 17.4 ± 1.0 | -- | 14.1 ± 1.7 |
| TAF09-25 | 19.4 ± 1.8 | 18.5 ± 1.6 | -- | 14.6 ± 1.5 |
| TAF09-26 | 80.9 ± 14.4 | 66.8 ± 5.8 | -- | 63.7 ± 3.4 |
| TAF09-27 | 91.4 ± 9.7[b] | *91.0 ± 11.0*[b] | -- | 82.1 ± 5.6 |
| TAF09-34 | *172.8 ± 13.9* | -- | -- | -- |
| TAF09-35 | -- | 38.7 ± 7.1 | 44.4 ± 3.6 | 42.9 ± 3.8 |
| TAF09-36 | -- | *66.4 ± 15.5* | 48.7 ± 3.4 | 51.5 ± 3.4 |
| TAF09-37 | 68.2 ± 8.2 | -- | 76.3 ± 9.2 | 59.6 ± 3.6 |
| TAF09-38 | -- | *57.2 ± 6.5* | -- | 63.2 ± 3.5 |
| TAF09-39 | -- | *35.1 ± 14.8* | 59.0 ± 5.0 | 66.8 ± 3.8 |
| TAF09-40 | 66.4 ± 5.8 | *74.8 ± 13.7* | -- | 74.5 ± 4.9 |
| TAF10-01 | 118.9 ± 14.6 | -- | -- | -- |
| TAF10-02 | 16.9 ± 1.6 | -- | -- | 17.0 ± 1.2 |
| TAF10-05 | 22.2 ± 2.4 | -- | -- | 20.7 ± 1.4 |
| TAF10-06 | 20.1 ± 1.6 | -- | -- | 22.0 ± 1.6 |
| TAF10-07 | 19.2 ± 1.8 | -- | -- | 29.1 ± 1.8 |
| TAF10-10 | 14.2 ± 1.0 | -- | -- | 14.9 ± 1.3 |
| TAF10-11 | 13.8 ± 1.1 | -- | -- | 16.4 ± 2.0 |
| TAF10-14 | 24.4 ± 1.9 | -- | -- | 24.4 ± 1.3 |
| TAF10-16 | 37.6 ± 3.4 | -- | -- | 35.4 ± 3.3 |
| TAF10-17 | 68.9 ± 4.6[b] | -- | -- | 86.6 ± 6.6 |
| TAF10-18 | 75.9 ± 7.7[b] | -- | -- | 78.0 ± 5.4 |

[a] Combined results from 220°/260° preheats

[b] 220° preheat

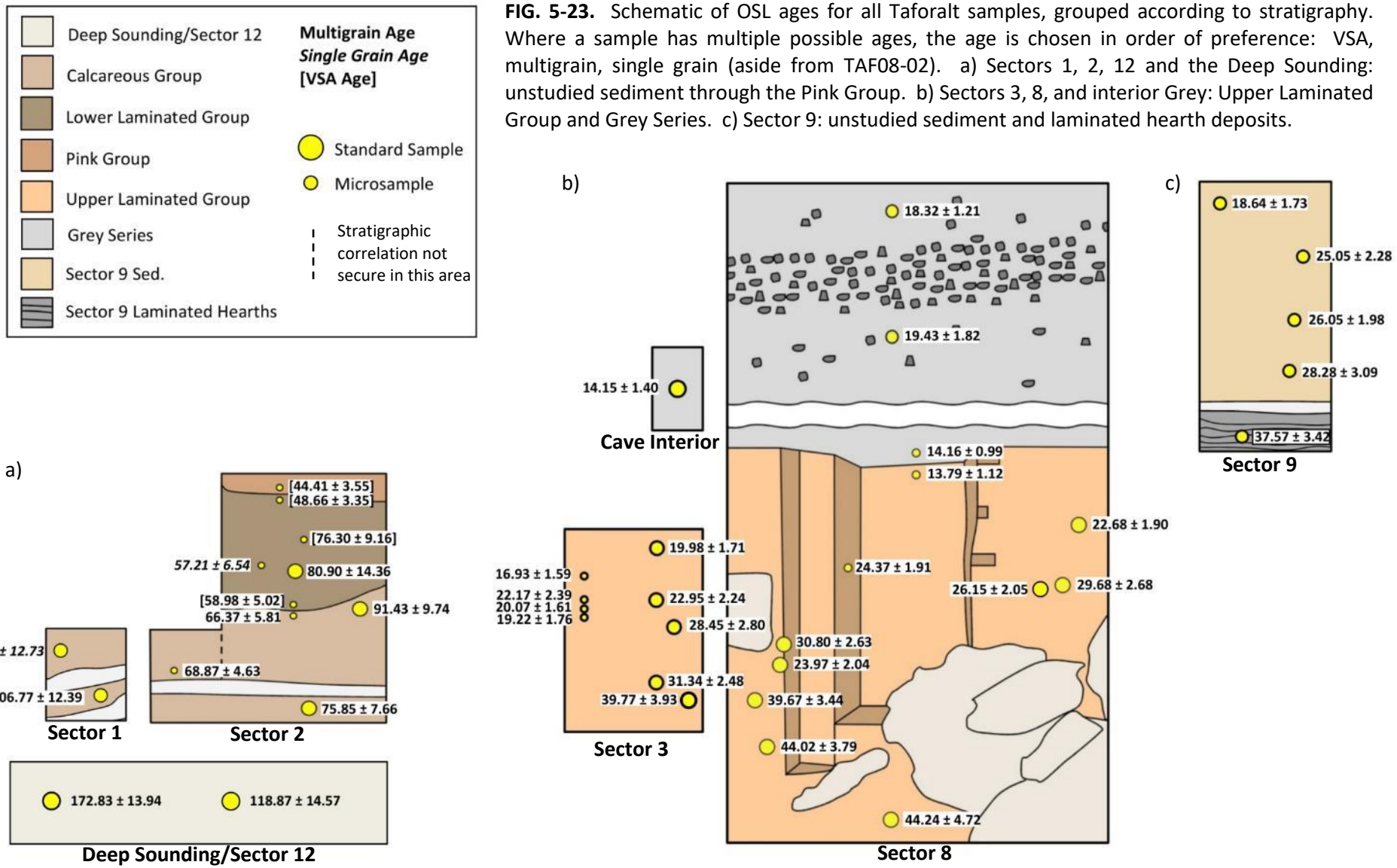


**FIG. 5-23.** Schematic of OSL ages for all Taforalt samples, grouped according to stratigraphy. Where a sample has multiple possible ages, the age is chosen in order of preference: VSA, multigrain, single grain (aside from TAF08-02). a) Sectors 1, 2, 12 and the Deep Sounding: unstudied sediment through the Pink Group. b) Sectors 3, 8, and interior Grey: Upper Laminated Group and Grey Series. c) Sector 9: unstudied sediment and laminated hearth deposits.

likely than ~119 ka. Nevertheless, neither age can be accepted or dismissed outright at this time. Concerns about the OSL characteristics of samples collected from Sectors 1 and 2 have been raised in the preceding sections. Dose recovery experiments indicated that certain grains may lead to a significant underestimate of the given dose in TAF08-01 (see Sections 5.1.1.1 and 5.1.1.2), and therefore the multigrain age (106.77 ± 12.39 ka) may be more reliable. Conversely, the presence of bright, super-saturating grains in TAF08-02 (Section 5.1.2.3) may cause significant age overestimation in the multigrain aliquots. In this case, the single grain age (103.40 ± 12.73 ka) would be more accurate. When considered together, the single grain age of TAF08-02 and multigrain age of TAF08-01 are coherent and plausible.

Of 10 samples from Sector 2, several are younger than expected based on the dating from Sector 1. Several points should be noted when considering data quality. First, gamma spectrometer measurements were only obtained for standard samples TAF09-26 (80.90 ± 14.36 ka) and TAF09-27 (91.43 ± 9.74 ka). These ages should therefore be considered the most secure. Second, both Calcareous Group samples TAF10-17 (68.87 ± 4.63 ka) and TAF10-18 (75.85 ± 7.66 ka) were collected from sediment with multiple calcareous concretions. This caused difficulties with sampling, and it is possible for the sediment to have been partially bleached at this time. However, if these two samples are excluded from consideration, microsamples TAF09-38 – TAF09-40 are still anomalously young for their stratigraphic position. It may also be questioned whether the Lower Laminated Group is likely to comprise 30 ka to 40 ka of sediment accumulation.

#### *5.1.4.1 Bayesian modeling*

The complete Bayesian model for all Taforalt OSL ages is summarized graphically in Fig. 5-24, and the model code is given in Appendix B. The model is essentially one large sequence, organized by sedimentological Group. For technical reasons, the code broke the cave into two main sequences, one of which was constrained to occur after the other. Ages were entered as

parameter-based equations, with two independent water content parameters-one for the 'typical' cave sediment, and one for the Grey Series.

An outlier model was used to input information concerning the likely reliability of data. All calculated ages (multigrain, single grain, and VSA) were incorporated into the model. Each OSL age was assigned either a low (0.05) or high (0.5) probability of being an outlier, based on information including sampling concerns, dose recovery experiments, and likelihood of saturation (Fig. 5-25). Previous experimentation with ages from Sectors 1 and 2 indicated that the largest changes in posterior probability occurred when 'unreliable' ages were completely excluded, and it was felt that the outlier model was a better reflection of the likelihood (but not certainty) that an age might not be accurate.

Calcareous Group samples are organized into sequences by sector, and ages within each sector are grouped by their stratigraphic relationship to nearby flowstones. Though it is likely that the flowstones in Sectors 1 and 2 are in fact the same, this has not been demonstrated via excavation and so has not been specified in the model. The stratigraphic sequence for the Lower Laminated and Pink Group samples was simpler: most ages were entered into a sequence with the exception of standard sample TAF09-26 and microsample TAF09-38, for which a phase was used. Upper Laminated sediments comprised three sequences: Sector 3 microsamples, Sector 3 standard samples, and Sector 8 samples. Positioning of samples in Sector 8 led to several pairs being considered as phases, because they were obtained at essentially the same location or for the same stratigraphic unit. The Grey Series phase included a sequence of ages obtained from the same face, as well one age (TAF08-17) determined from deposits towards the rear of the cave. Sector 9 ages were included as their own sequence, unconstrained by any links with sediments from the cave interior.

Modeled ages are listed in Table 5-13, and modeled Group boundaries are displayed in Fig. 5-26. According to these results, deposition of the Calcareous Group sediments began around 98.7 ± 11.7 ka and continued until 70.9 ± 5.3 ka, after which Lower Laminated sediments

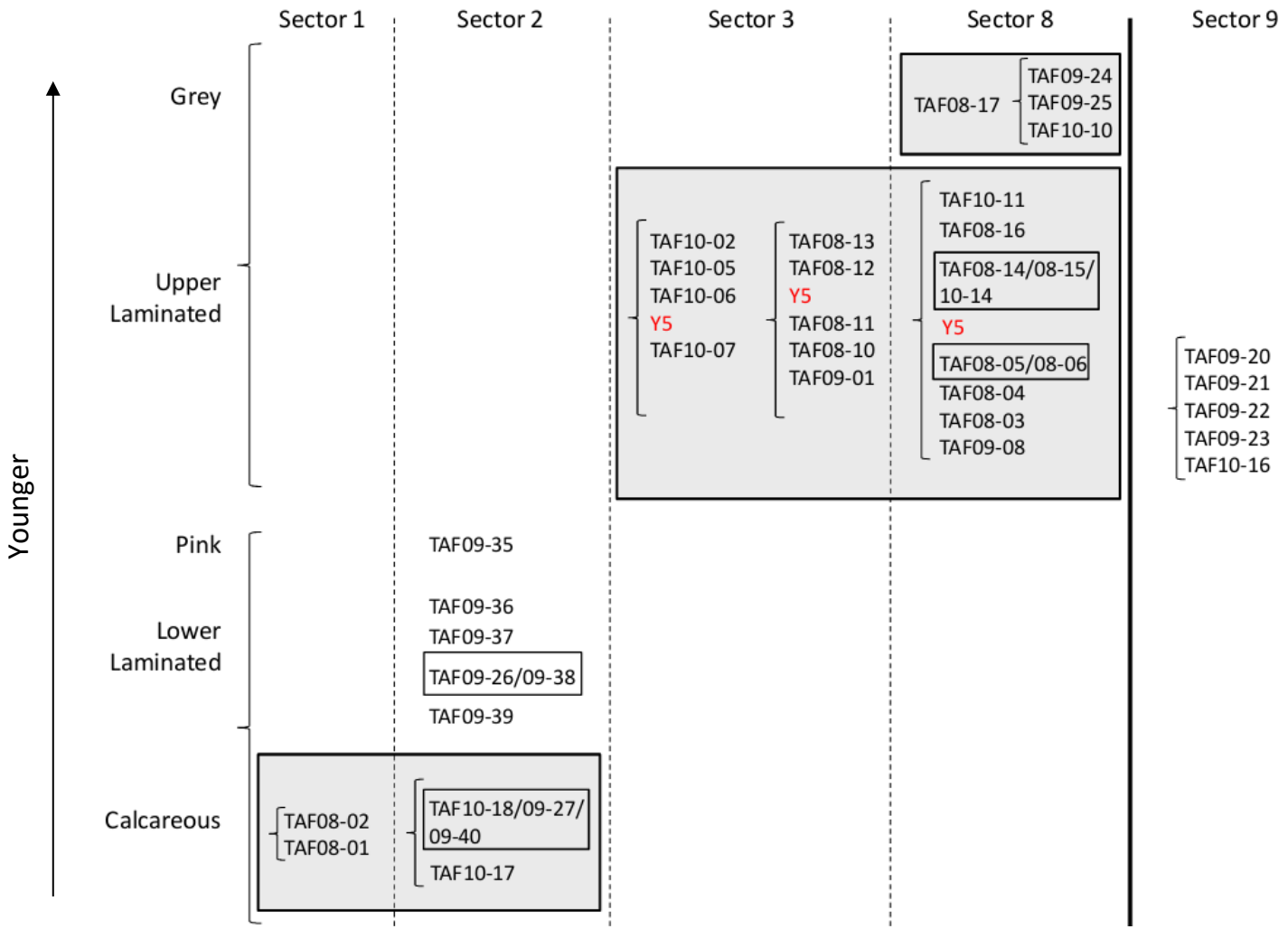


**FIG. 5-24.** Bayesian model schematic for Taforalt cave. Brackets indicate sequences, and boxes indicate phases. As an example, the Calcareous Group is modelled as a phase with two nested sequences, one of which contains another phase grouping. The main cave sequence comprises three unconnected sequences: Sectors 1 and 2, Sectors 3 and 8, and Sector 9. 'Y5' is a marker horizon for which a posterior probability (age) was suggested by the modelled ages.

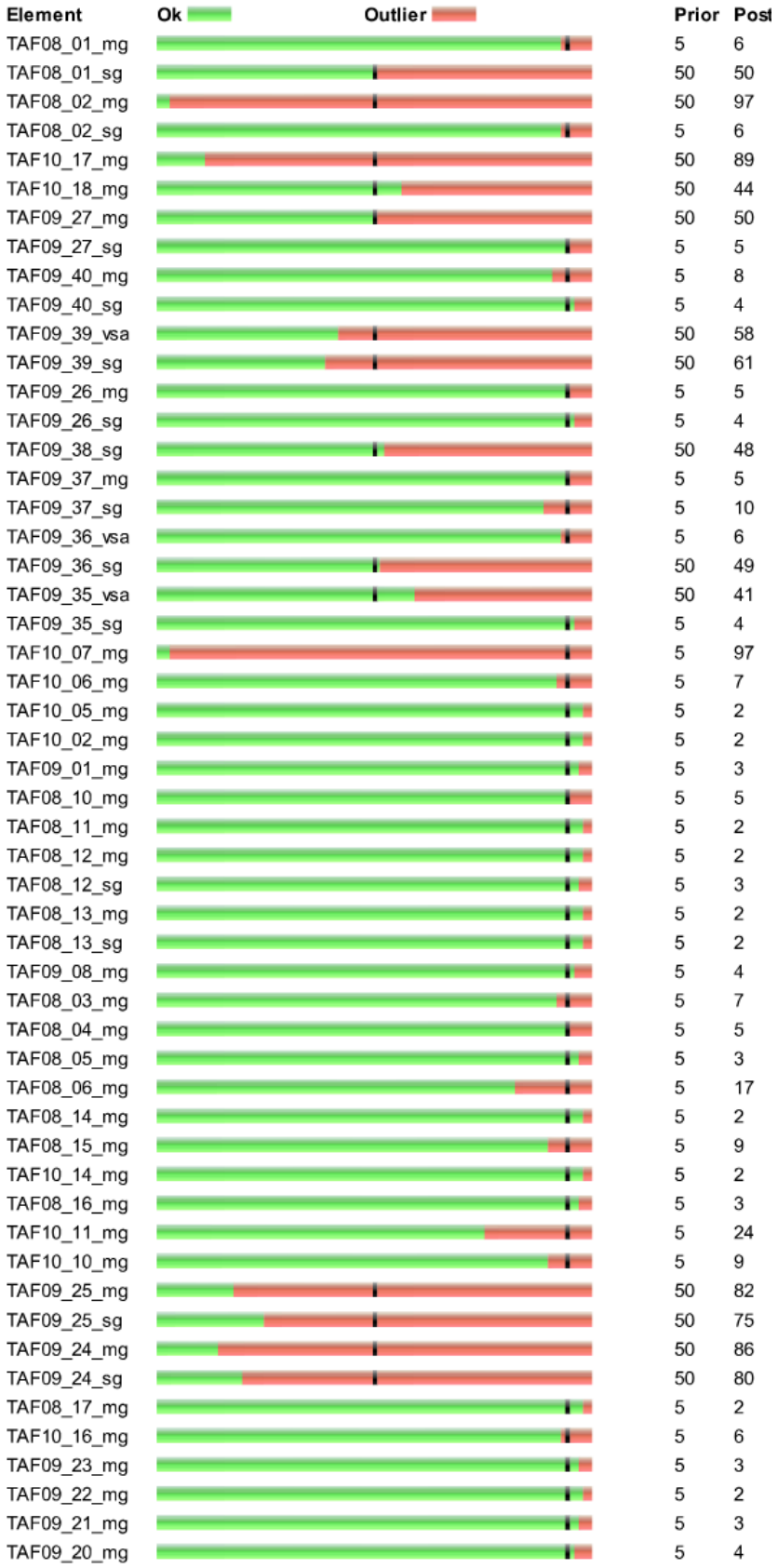


**FIG. 5-25.** Prior and posterior likelihoods that ages are outliers (%). Age names indicate the type of equivalent dose analysis used, and they are listed in stratigraphic order (oldest to youngest). This figure is adapted from that produced by OxCal v4.1.7 (Bronk Ramsey, 2009b; Bronk Ramsey et al., 2010).

a) Sector 9

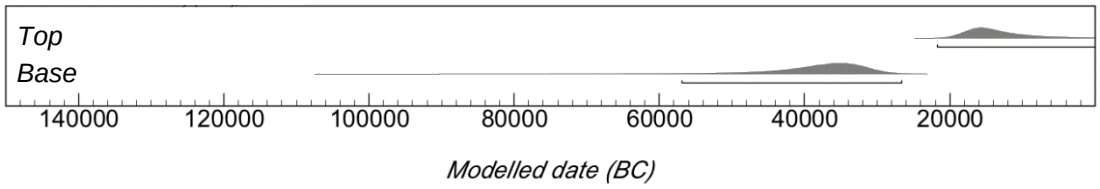


b) Sectors 3 and 8

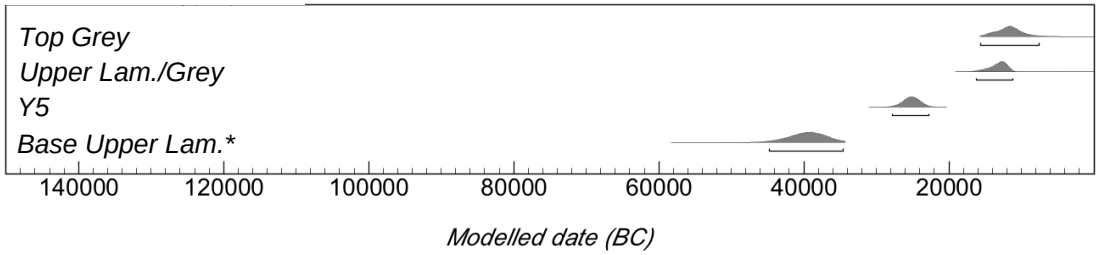


c) Sectors 1 and 2

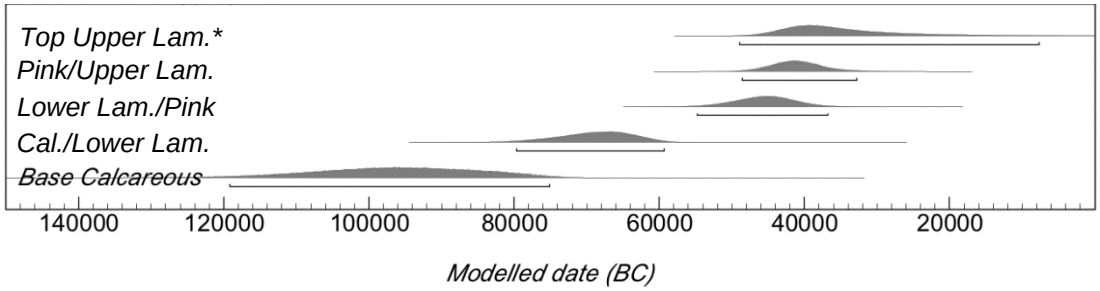


* Local base/top of Upper Laminated Group Sediments. No stratigraphic constraint relating these boundaries was entered in the model.

**FIG. 5-26.** Bayesian model results for Taforalt. Posterior probabilities are shown for boundaries (basal, top, and Group Boundaries) in each of the three major cave sequences. The modelled age for the marker horizon 'Y5' is also indicated. This figure is adapted from that produced by OxCal v4.1.7 (Bronk Ramsey et al, 2010).

were deposited until 47.5 ± 4.4 ka. The youngest sample measured in Sector 2 is from the ensuing Pink Group, and its modeled age is 42.9 ± 4.4 ka. The base of Sector 8, and the earliest Upper Laminated sample obtained for this study, dates to 38.2 ± 2.5 ka. Finally, the Grey Series sediments accumulated between 15.3 ± 1.3 ka and 13.5 ± 2.2 ka. Based on the modeled ages, it seems as though no significant hiatuses occur between Groups. Outlier probabilities (Fig. 5-25) are as expected, based on the previous discussion. Of 53 age estimates, the probability that each age was an outlier increased over the initial, assigned probability for 19 age estimates and stayed constant for 7.

## 5.2 Dar es-Soltan I

### 5.2.1 Dose recovery

Dose recovery experiments (see methods, Section 4.2.2.2) were performed on six aliquots each from five samples, which span the Dar es-Soltan I deposits. These comprised one sample each from Groups 1, 4, and 5 and two samples from Group 2. Aliquots from samples SOL1-05-01, -05B, -12, and -16 were bleached with both sunlight and LEDs (three aliquots each), and aliquots from sample SOL1-05-06 via the Minisys LEDs only; bleaching times for each experiment are given in Table 5-14. Though all rejection criteria were applied to these results, aliquots were only rejected for high IRSL response. This is presumed to be related to feldspar contamination, and it was highest for basal beach sand sample SOL1-05-01.

The number of accepted aliquots and results are summarized in Table 5-14 and Fig. 5-27. Including only accepted aliquots, all five samples have common or central ages that are within 10% of unity at a 1$\sigma$ error level, and two of five (SOL1-05-01, SOL1-05-06) have central values within 5% of the given dose. Most samples slightly underestimate the given dose, with only SOL1-05-16 returning a slightly higher dose estimate. There may be some dependence on the relationship between given dose and measured natural equivalent dose, but it is relatively weak (see Fig. 5-27b). Considered individually, more than three quarters of the measured aliquots gave central values within 10% of unity. The maximum difference for a single aliquot was 23%

**TABLE 5-14.** Dose recovery measurement parameters and results for Dar es-Soltan I samples.

| Sample | Bleaching Time (s) | Given Dose (Gy) | No. accepted aliquots | Recycling Ratio (μ ± 1σ) | Zero Ratio (μ ± 1σ) | Over-dispersion (%) | Normalized Recovered Dose |
|---|---|---|---|---|---|---|---|
| SOL1-05-01 | 100 | 71.5 ± 1.4 | 3 | 1.04 ± 0.02 | 0.00 ± 0.00 | -- | 0.97 ± 0.03 |
| SOL1-05-05B | 100 | 71.5 ± 1.4 | 5 | 1.03 ± 0.03 | 0.01 ± 0.00 | 2.81 ± 3.75 | 0.88 ± 0.02 |
| SOL1-05-06 | 300 | 47.0 ± 0.9 | 2 | 1.01 ± 0.00 | 0.00 ± 0.00 | -- | 0.98 ± 0.03 |
| SOL1-05-12 | 100 | 71.5 ± 1.4 | 6 | 1.01 ± 0.02 | 0.01 ± 0.00 | 6.87 ± 2.80 | 0.90 ± 0.03 |
| SOL1-05-16 | 100 | 4.8 ± 0.1 | 6 | 1.02 ± 0.03 | 0.01 ± 0.00 | -- | 1.08 ± 0.01 |

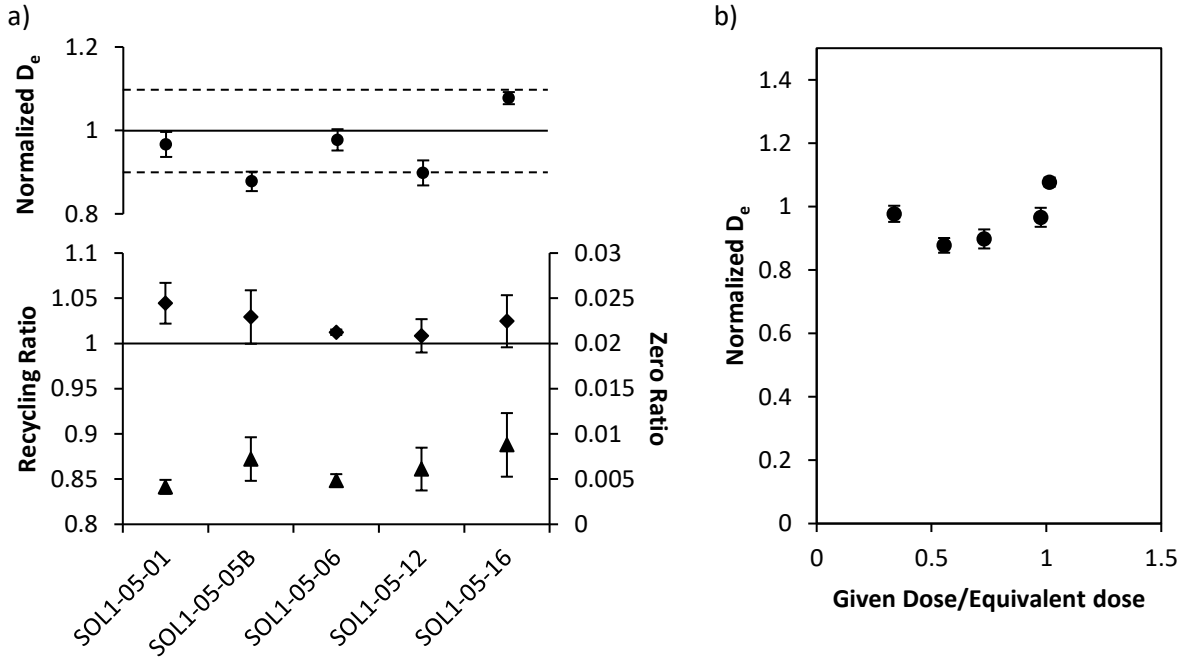


**FIG. 5-27.** Results of dose recovery experiments. a) Mean and standard deviation shown for normalized recovered doses, recycling ratios, and zero ratios. b) Relationship between dose recovery and proportion of the given dose to each sample's equivalent dose.

between given and recovered doses. Recycling ratios and zero ratios are well within the chosen limits for all samples. It is felt that these results are sufficient to suggest good SAR behavior for the quartz at Dar es-Soltan I.

### 5.2.2 Equivalent dose estimates

#### *5.2.2.1 Multigrain data*

Twenty-nine samples were measured with multigrain techniques. Between 6 and 18 aliquots were measured for each sample.

Rejection criteria were applied prior to further analysis (see Table 5-15). The most common reason for rejection was high IRSL response. Nearly two-thirds of the measured aliquots from the bedrock sandstone sample were rejected for high IRSL; the proportion rejected from the cave infill was variable. Group 1 samples yielded the lowest number of IRSL-responding aliquots overall. Recycling ratio and zero ratio caused few rejections with the exception of samples SOL1-05-20 and SOL1-05-21, for which 6 of 6 and 6 of 18 aliquots (respectively) were rejected for thermal transfer. Grains disaggregated from the bedrock sample, SOL1-05-21, have had a significantly different depositional and burial history than other samples, therefore this difference in behavior is not necessarily surprising. Sample SOL1-05-20, though, was collected only centimeters away from two other samples near the top of Group 1. Saturated aliquots are also present but rare, in both the bedrock and cave infill samples. More saturated aliquots were noted when samples were measured with fewer grains per aliquot (i.e. the DES08 samples).

The relative proportion of feldspars to quartz grains in the sediment seems to be quite low. First, samples measured with small diameter aliquots (~1-2 mm) were rarely rejected due to IRSL response, and the relative magnitudes of IRSL and OSL from larger aliquots were very different. For example, sample SOL1-05-05A, which was measured with 4-5 mm diameter aliquots, produced average IRSL signals of only 10.6% of the OSL response. Yet with the strict IRSL criteria, all 6 measured aliquots were rejected. By contrast, sample SOL1-05-21 (bedrock) has a mean IRSL response of nearly 60% of the subsequent OSL response, and yields several

**TABLE 5-15.** Multigrain aliquots excluded according to rejection criteria. The number of aliquots failing the IR rejection criteria has been indicated for each sample; where the aliquots were included in the final equivalent dose estimate, the number is given in parentheses. See text for discussion.

| | | | | Non-exclusive | | | | | | | | | |
|---|---|---|---|---|---|---|---|---|---|---|---|---|---|
| **Sample** | **# Meas.** | **>3σ** | **Tx Err.** | **RR** | **IR** | **Zero** | **Sat.** | **Super Sat.** | **Fit Err.** | **Neg. $D_e$** | **$D_e$ Err.** | **Not bracket** | **Accepted** |
| SOL1-05-01 | 6 | 0 | 0 | 1 | (1) | 0 | 0 | 0 | 0 | 0 | 0 | 0 | 5 |
| SOL1-05-02 | 6 | 0 | 0 | 0 | (1) | 0 | 0 | 0 | 0 | 0 | 0 | 0 | 6 |
| SOL1-05-03 | 6 | 0 | 0 | 0 | (0) | 0 | 0 | 0 | 0 | 0 | 0 | 0 | 6 |
| SOL1-05-04 | 6 | 0 | 0 | N/A | (1) | 0 | 0 | 0 | 0 | 0 | 0 | 0 | 6 |
| SOL1-05-05A | 6 | 0 | 0 | 0 | (6) | 0 | 0 | 0 | 0 | 0 | 0 | 0 | 6 |
| SOL1-05-05B | 6 | 0 | 0 | 0 | (2) | 0 | 0 | 0 | 0 | 0 | 0 | 0 | 6 |
| SOL1-05-06 | 12 | 0 | 0 | 0 | (9) | 0 | 0 | 0 | 0 | 0 | 0 | 0 | 12 |
| SOL1-05-07 | 6 | 0 | 0 | 0 | (3) | 0 | 0 | 0 | 0 | 0 | 0 | 0 | 6 |
| SOL1-05-08 | 6 | 0 | 0 | 0 | (5) | 0 | 0 | 0 | 0 | 0 | 0 | 0 | 6 |
| SOL1-05-09 | 12 | 0 | 0 | 0 | (7) | 0 | 0 | 0 | 0 | 0 | 0 | 0 | 12 |
| SOL1-05-10 | 12 | 0 | 0 | 2 | (3) | 0 | 0 | 0 | 0 | 0 | 0 | 0 | 10 |
| SOL1-05-11 | 6 | 0 | 0 | 0 | (3) | 0 | 0 | 0 | 0 | 0 | 0 | 0 | 6 |
| SOL1-05-12 | 6 | 0 | 0 | 0 | (2) | 0 | 0 | 0 | 0 | 0 | 0 | 0 | 6 |
| SOL1-05-13 | 6 | 0 | 0 | 0 | (1) | 0 | 0 | 0 | 0 | 0 | 0 | 0 | 6 |
| SOL1-05-14 | 6 | 0 | 0 | 0 | (0) | 0 | 0 | 0 | 0 | 0 | 0 | 0 | 6 |
| SOL1-05-15 | 6 | 0 | 0 | 0 | (5) | 0 | 0 | 0 | 0 | 0 | 0 | 0 | 6 |
| SOL1-05-16 | 6 | 0 | 0 | 0 | (0) | 0 | 0 | 0 | 0 | 0 | 0 | 0 | 6 |
| SOL1-05-17 | 6 | 0 | 0 | 0 | (0) | 0 | 0 | 0 | 0 | 0 | 0 | 0 | 6 |
| SOL1-05-18 | 6 | 1 | 0 | 0 | (3) | 0 | 0 | 0 | 0 | 0 | 0 | 0 | 5 |
| SOL1-05-19 | 6 | 0 | 0 | 1 | 2 | 0 | 0 | 0 | 0 | 0 | 3* | 0 | 1 |
| SOL1-05-20 | 6 | 0 | 0 | 5 | (4) | 6 | 0 | 0 | 0 | 0 | 0 | 0 | 0 |
| SOL1-05-21 | 18 | 0 | 0 | 2 | 11 | 6 | 0 | 1 | 0 | 0 | 2 | 0 | 3 |
| DES08-22 | 12 | 0 | 0 | 0 | (1) | 0 | 1 | 0 | 0 | 0 | 0 | 0 | 11 |
| DES08-24 | 12 | 1 | 1 | 0 | (0) | 1 | 0 | 0 | 0 | 0 | 0 | 0 | 10 |
| DES08-31 | 12 | 0 | 0 | 0 | (0) | 0 | 0 | 0 | 0 | 0 | 0 | 0 | 12 |
| DES08-32 | 12 | 0 | 0 | 0 | (0) | 0 | 1 | 0 | 0 | 0 | 0 | 2 | 9 |
| DES08-33 | 12 | 0 | 0 | 0 | (2) | 0 | 0 | 0 | 0 | 0 | 1 | 0 | 11 |
| DES08-34 | 12 | 0 | 0 | 3 | (0) | 0 | 0 | 0 | 0 | 0 | 1 | 0 | 8 |
| DES08-35 | 12 | 0 | 0 | 1 | (0) | 0 | 0 | 1 | 0 | 0 | 0 | 0 | 10 |

**TABLE 5-16.** Multigrain equivalent doses (central age model) calculated with and without IRSL-emitting aliquots. Only samples with IRSL-emitting aliquots that are acceptable by all other criteria are included.

| | IRSL accepted | | IRSL rejected | |
|---|---|---|---|---|
| **Sample** | **$D_e$ (Gy)** | **Overdispersion (%)** | **$D_e$ (Gy)** | **Overdispersion (%)** |
| SOL1-05-01 | 72.2 ± 4.8 | 11.47 ± 5.84 | 73.3 ± 5.6 | 12.38 ± 6.34 |
| SOL1-05-02 | 84.5 ± 4.6 | 12.16 ± 4.17 | 87.4 ± 4.8 | 11.08 ± 4.35 |
| SOL1-05-04 | 112.0 ± 6.7 | 11.80 ± 5.10 | 110.6 ± 8.0 | 13.53 ± 6.01 |
| SOL1-05-05B | 129.2 ± 9.1 | 15.62 ± 5.51 | 128.9 ± 12.5 | 17.97 ± 7.42 |
| SOL1-05-06 | 145.5 ± 8.0 | 17.40 ± 4.25 | 139.5 ± 14.7 | 16.35 ± 8.24 |
| SOL1-05-07 | 112.3 ± 8.4 | 16.89 ± 5.75 | 105.8 ± 3.7 | -- |
| SOL1-05-08 | 142.7 ± 4.4 | -- | 178.7 ± 18.0 | -- |
| SOL1-05-09 | 162.8 ± 11.1 | 21.13 ± 5.14 | 160.3 ± 17.2 | 22.76 ± 7.99 |
| SOL1-05-11 | 135.2 ± 6.0 | 8.53 ± 3.88 | 143.7 ± 9.0 | 8.92 ± 5.35 |
| SOL1-05-12 | 94.8 ± 3.8 | 7.49 ± 3.66 | 98.1 ± 4.8 | 6.80 ± 4.92 |
| SOL1-05-13 | 82.6 ± 5.3 | 14.77 ± 4.78 | 85.3 ± 5.7 | 14.18 ± 5.03 |
| SOL1-05-15 | 9.4 ± 0.4 | 9.40 ± 3.04 | 8.8 ± 0.3 | -- |
| SOL1-05-18 | 122.1 ± 8.5 | 15.34 ± 5.44 | 118.3 ± 4.0 | -- |
| SOL1-05-21 | 174.0 ± 18.6 | 27.02 ± 8.41 | 153.6 ± 17.7 | 14.95 ± 10.59 |
| DES08-22 | 47.9 ± 8.1 | 55.21 ± 11.99 | 47.5 ± 8.8 | 57.89 ± 13.17 |
| DES08-33 | 145.5 ± 11.2 | 23.21 ± 5.92 | 149.0 ± 13.9 | 25.92 ± 7.08 |

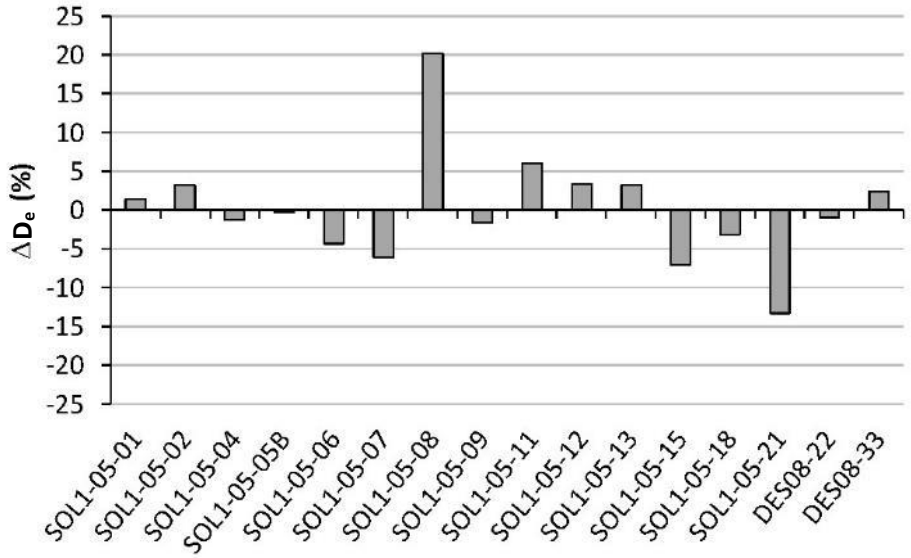


**FIG. 5-28.** Change in equivalent dose calculated with and without IRSL-emitting aliquots. ΔDe is given as percentage difference of the stricter rejection criteria (no IRSL).

aliquots that had IRSL responses of greater magnitude than the following OSL. Therefore the bedrock aliquots are clearly highly contaminated with feldspar, but the influence of rare feldspars on cave infill samples is more questionable.

To investigate the feldspar contamination issue, central equivalent dose values were calculated both with and without IRSL-rejected aliquots for the affected 17 samples. Results are summarized in Table 5-16 and Figure 5-28. There is no apparent systematic effect of removing slight IRSL-emitting aliquots: central equivalent doses increase and decrease as a result of this in approximately even numbers (the equivalent dose lowers for 9 and increases for 7) with a median of a -0.61%. For 11 of 17 samples, the absolute change is less than 5%, and a difference of more than 10% occurs for just two samples, SOL1-05-21 and SOL1-05-08.

For the latter two samples, the rejection of 'contaminated' aliquots led to a rejection of most measured aliquots. The low proportion of IRSL to OSL emission has already been discussed for sample SOL1-05-05A, and this is also the case for SOL1-05-08. The median natural IRSL emission expressed as a percentage of the following OSL is only 0.02%, and the maximum is 0.24% for aliquots of SOL1-05-08. It is most likely, therefore, that the significant equivalent dose difference for these samples is due to the high number of rejected aliquots, rather than to the effect of feldspars. Moreover, single grain analysis discussed in the next section demonstrates that feldspars are quite rare in the cave infill. Though it is certainly more technically correct to exclude the aliquots with any IRSL response, this analysis seems to indicate that the rejection of such data is not necessary to correct a systematic underestimation of equivalent dose due to feldspar contamination. Thus, this study uses the IRSL rejection criteria only for samples collected from either the aeolianite or the weathered aeolianite blocks in the cave infill (SOL1-05-01 and SOL1-05-19, respectively). This is due to the high number of feldspars noted during single grain analysis for these samples (Section 5.2.2.2, 5.2.2.3).

Population parameters are presented in Table 5-17. For those cave infill samples fitted with the central age model (i.e. overdispersion >0), overdispersion values range from 2.68 ±

**TABLE 5-17.** Distribution parameters for accepted multigrain aliquots by sample. Samples SOL1-05-21 and SOL1-05-19 use an IR exclusion criteria, but all other samples do not.

| Sample | Overdispersion (%) | Wtd. Skew. | Wtd. Kurt. | $D_e$ (Gy) |
|---|---|---|---|---|
| SOL1-05-01 | 11.47 ± 5.85 | 72.24 | -1.59 | 72.2 ± 4.8 |
| SOL1-05-02 | 12.16 ± 4.17 | 4.83 | -1.44 | 84.5 ± 4.6 |
| SOL1-05-03 | 14.78 ± 4.68 | 0.11 | 0.48 | 85.6 ± 5.4 |
| SOL1-05-04 | 11.80 ± 5.10 | 0.06 | -1.16 | 112.0 ± 6.7 |
| SOL1-05-05A | 8.56 ± 3.46 | 0.46 | -0.82 | 116.1 ± 4.8 |
| SOL1-05-05B | 15.62 ± 5.51 | -0.29 | -0.70 | 129.2 ± 9.1 |
| SOL1-05-06 | 17.40 ± 4.25 | 0.12 | -0.35 | 145.5 ± 8.0 |
| SOL1-05-07 | 16.89 ± 5.75 | -0.06 | -1.60 | 112.3 ± 8.5 |
| SOL1-05-08 | 0.00 | 0.72 | 3.45 | 142.7 ± 4.4 |
| SOL1-05-09 | 21.13 ± 5.14 | 0.58 | 1.02 | 162.8 ± 11.1 |
| SOL1-05-11 | 8.53 ± 3.88 | 0.75 | 2.51 | 135.2 ± 6.0 |
| SOL1-05-12 | 7.49 ± 3.66 | -0.04 | -0.87 | 94.8 ± 3.8 |
| SOL1-05-13 | 14.77 ± 4.78 | 1.05 | 3.66 | 82.6 ± 5.3 |
| SOL1-05-14 | 10.69 ± 4.50 | 0.11 | -1.39 | 40.9 ± 2.2 |
| SOL1-05-15 | 9.40 ± 3.04 | 0.48 | 0.43 | 9.4 ± 0.4 |
| SOL1-05-16 | 2.68 ± 2.23 | 0.23 | -0.10 | 4.7 ± 0.1 |
| SOL1-05-17 | 30.83 ± 9.26 | -0.29 | -2.26 | 71.7 ± 9.2 |
| SOL1-05-18 | 15.34 ± 5.44 | 0.08 | 2.33 | 122.1 ± 8.5 |
| SOL1-05-19 | 0.00 | -- | -- | 178.5 ± 24.6 |
| SOL1-05-21 | 14.95 ± 10.59 | -0.20 | -- | 153.6 ± 17.7 |
| DES08-22 | 55.21 ± 11.99 | 2.59 | 10.64 | 47.9 ± 8.1 |
| DES08-24 | 18.98 ± 5.15 | -0.47 | -1.43 | 34.9 ± 2.4 |
| DES08-31 | 22.65 ± 5.33 | -0.47 | -0.52 | 124.5 ± 8.8 |
| DES08-32 | 14.44 ± 4.21 | -0.22 | -0.82 | 130.2 ± 7.0 |
| DES08-33 | 23.21 ± 5.92 | 0.09 | 0.90 | 145.5 ± 11.2 |
| DES08-34 | 14.26 ± 4.23 | -0.21 | -0.49 | 97.2 ± 5.4 |
| DES08-35 | 22.00 ± 5.49 | 0.52 | 2.21 | 110.6 ± 8.1 |

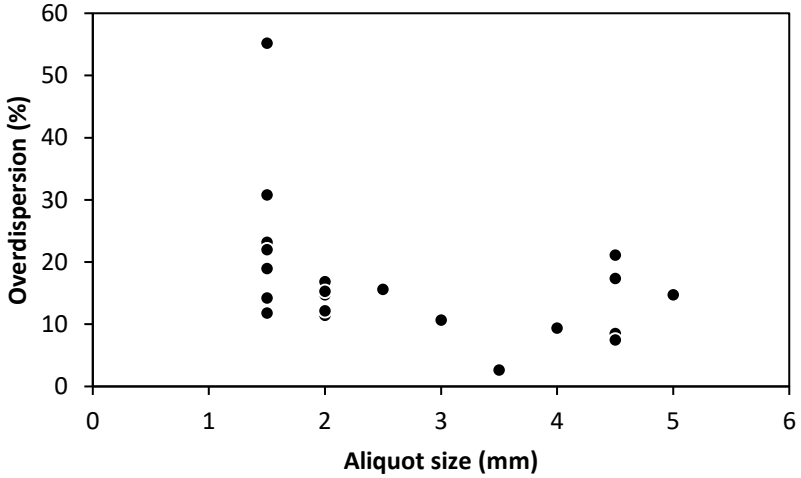


**FIG. 5-29.** The dependence of overdispersion on aliquot size. All samples with a calculable overdispersion were included. Overdispersion error bars have been excluded for visual clarity.

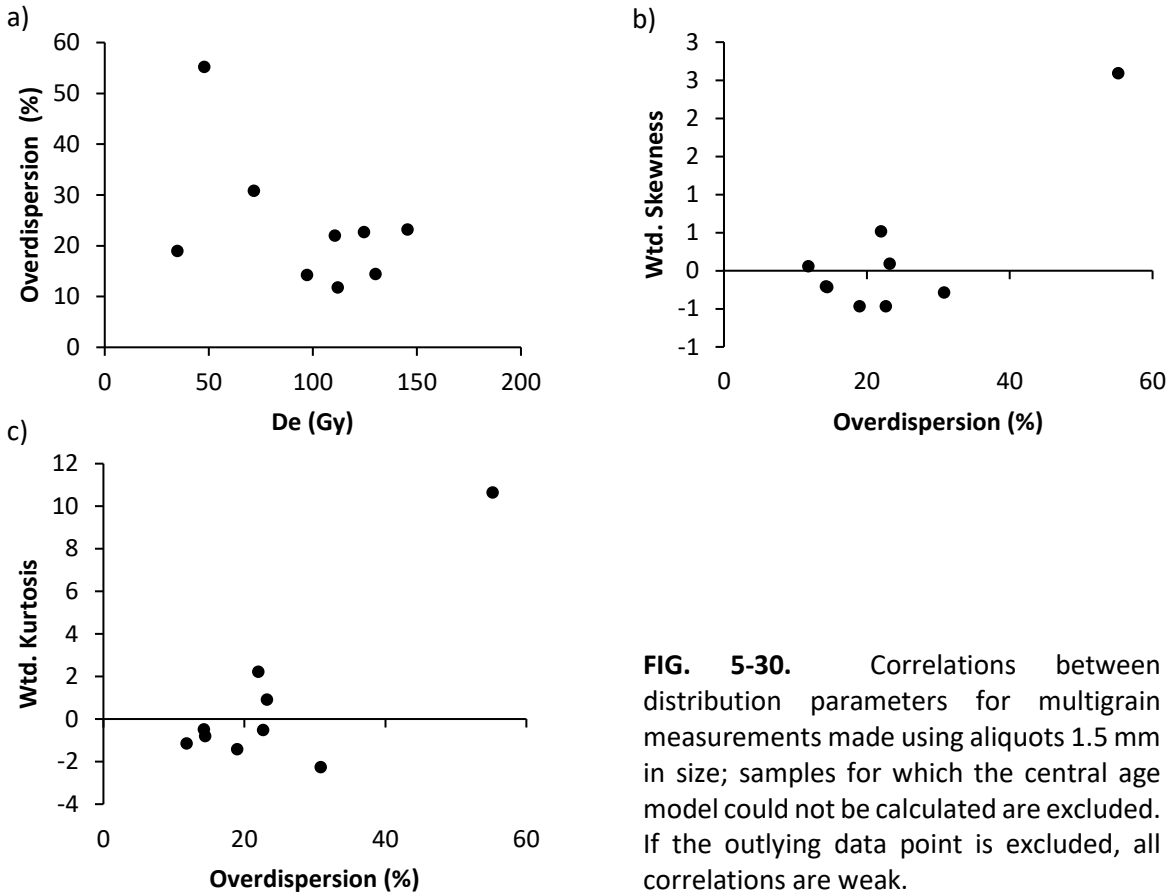


**FIG. 5-30.** Correlations between distribution parameters for multigrain measurements made using aliquots 1.5 mm in size; samples for which the central age model could not be calculated are excluded. If the outlying data point is excluded, all correlations are weak.

**TABLE 5-18.** Correlation coefficients for multigrain distribution parameters. a) All samples measured with 1.5 mm aliquots. b) Outlier (DES08-22) excluded.

| | $D_e$ (Gy) | Overdispersion | Wtd. Skewness | Wtd. Kurtosis |
|---|---|---|---|---|
| **De** | 1.00 | | | |
| **Overdispersion** | -0.50 | 1.00 | | |
| **Wtd. Skewness** | -0.34 | 0.84 | 1.00 | |
| **Wtd. Kurtosis** | -0.30 | 0.84 | 0.98 | 1.00 |

| | $D_e$ (Gy) | Overdispersion | Wtd. Skewness | Wtd. Kurtosis |
|---|---|---|---|---|
| **$D_e$** | 1.00 | | | |
| **Overdispersion** | -0.16 | 1.00 | | |
| **Wtd. Skewness** | 0.42 | -0.06 | 1.00 | |
| **Wtd. Kurtosis** | 0.53 | -0.02 | 0.79 | 1.00 |

2.23% to 55.21 ± 11.99%. However, before overdispersion values can be used to examine OSL behavior or sedimentary differences, aliquot size variations must be accounted for. Fig. 5-30 shows overdispersion plotted against the measured aliquot diameter. A negative relationship is apparent, and the correlation value between overdispersion and size is -0.42. Taking only samples with aliquots ~1.5 mm diameter, correlation coefficients were calculated (Table 5-18). Correlation values are highly dependent on sample DES08-22, which has the highest overdispersion and high kurtosis. With this sample included, overdispersion was strongly inversely correlated with equivalent dose (-0.50), and weighted skewness and kurtosis were strongly correlated with each other and with overdispersion (>0.84). If excluded, correlation values are much weaker: overdispersion is still weakly inversely correlated with equivalent doses (-0.16), and weighted kurtosis and skewness are strongly correlated with each other (0.79), but barely with overdispersion (-0.06, -0.02).

#### *5.2.2.2 Single grain data*

After analysis of initial multigrain data, fourteen samples were selected for single grain analysis. At least one sample from each sedimentary group of the cave infill has been analysed, as well as the grains disaggregated from the sandstone bedrock. For samples collected from within the cave, 300 to 600 grains were measured from each sample, while more than 1500 grains were measured from the bedrock sample.

Signal intensity

Light sum plots of these grains indicate that the natural signal profiles of most samples are relatively similar (Fig. 5-31). Exceptions to this are samples SOL1-05-21 and SOL1-05-06, which have a higher proportion of light from bright grains, and SOL1-05-16, for which light intensity is more evenly distributed.

Rejection criteria

The results of applying rejection criteria to the measured samples are summarized in Table 5-19 and Fig. 5-32. It should be noted that feldspar rejection criteria were only applied to

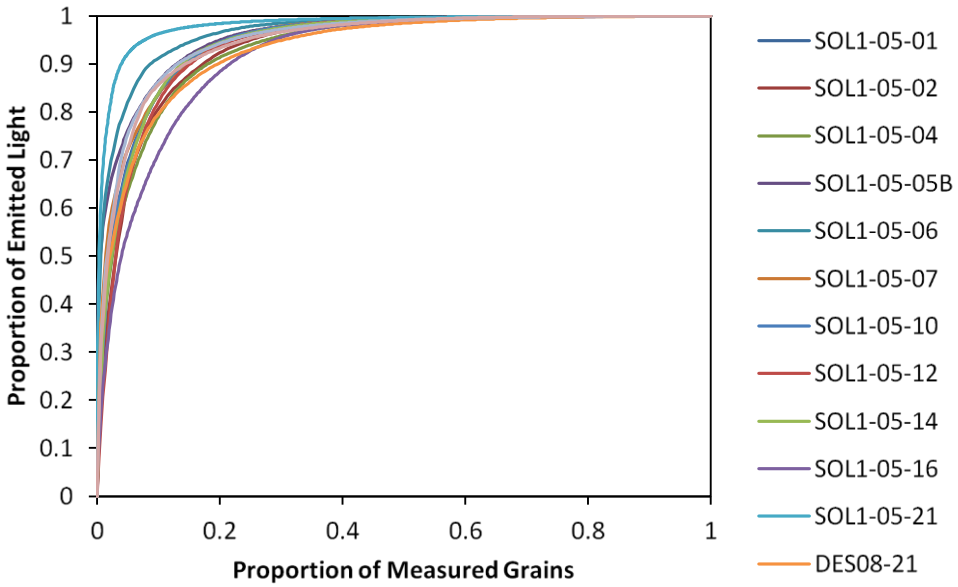


**FIG. 5-31.** Light sum graphs for measured single grains (natural signal, no background subtraction).

grains from samples SOL1-05-14, SOL1-05-16, and SOL1-05-21. However, feldspar contamination is low for measured single grain populations from the cave infill. Of the cave infill samples tested with the IR laser (see methods), one (SOL1-05-14) yielded only one probable feldspar from 500 grains, and SOL1-05-16 only 17 of 600 (~2.8%). SOL1-05-14, with the lower feldspar concentration, is sedimentologically more similar to the majority of tested samples than the midden sample 05-16. Second, IR LED stimulation of several single grain discs from a number of samples (Fig. 5-33) revealed essentially no IRSL signal from most of the analyzed grains.

The most significant result of this analysis is the difference between rejection profiles for cave infill samples vs. bedrock grains. For samples from the cave infill, between ~6 and 18% of grains were accepted, while only 1.2% of measured grains were accepted from the bedrock. This difference is due partially to the relatively high proportions of feldspars in the bedrock mineral extract, but it is primarily caused by the dimness of the bedrock grains in comparison to those

**TABLE 5-19.** Single grains (180-255 µm) excluded according to rejection criteria. Where the number measured is not a multiple of 100, stuck grains have been removed from the analysis.

| 220°C Preheat | | | | Non-exclusive | | | | | | | | |
|---|---|---|---|---|---|---|---|---|---|---|---|---|
| **Sample** | **Meas. (#)** | **>3σ** | **Tx Err.** | **RR** | **Zero** | **Sat.** | **Super-Sat.** | **Fit Err.** | **Neg. $D_e$** | **$D_e$ Err.** | **Not bracket** | **Accepted (#)** |
| SOL1-05-01 | 300 | 114 | 65 | 24 | 2 | 7 | 4 | 2 | 9 | 36 | 0 | 38 |
| SOL1-05-02 | 300 | 111 | 57 | 45 | 16 | 3 | 2 | 0 | 4 | 34 | 0 | 37 |
| SOL1-05-04 | 400 | 97 | 64 | 104 | 70 | 2 | 5 | 5 | 2 | 37 | 8 | 44 |
| SOL1-05-05B | 500 | 169 | 126 | 50 | 1 | 11 | 5 | 0 | 7 | 54 | 6 | 72 |
| SOL1-05-06 | 300 | 121 | 61 | -- | 15 | 11 | 11 | 6 | 5 | 31 | 16 | 23 |
| SOL1-05-07 | 300 | 128 | 57 | 21 | 8 | 2 | 4 | 3 | 3 | 31 | 5 | 41 |
| SOL1-05-10 | 300 | 96 | 67 | 47 | 6 | 4 | 3 | 1 | 5 | 23 | 8 | 45 |
| SOL1-05-12 | 300 | 114 | 70 | 24 | 2 | 5 | 0 | 0 | 7 | 29 | 0 | 50 |
| SOL1-05-14* | 500 | 240 | 121 | 35 | 5 | 3 | 1 | 1 | 4 | 18 | 11 | 62 |
| SOL1-05-16* | 600 | 343 | 60 | 61 | 5 | 1 | 0 | 0 | 2 | 16 | 0 | 109 |
| SOL1-05-21* | 1563 | 912 | 383 | 60 | 36 | 22 | 8 | 2 | 24 | 47 | 13 | 18 |
| DES08-21 | 297 | 118 | 53 | 30 | 15 | 10 | 2 | 1 | 0 | 29 | 4 | 39 |
| DES08-32 | 397 | 168 | 67 | 35 | 6 | 3 | 4 | 3 | 2 | 53 | 3 | 54 |
| DES08-34 | 299 | 104 | 45 | 29 | 14 | 15 | 7 | 2 | 2 | 47 | 5 | 36 |

*An IR laser was used to identify IRSL-emitting grains for these samples: 1, 17, and 87 grains were rejected from samples SOL1-05-14, -16, and -21, respectively.

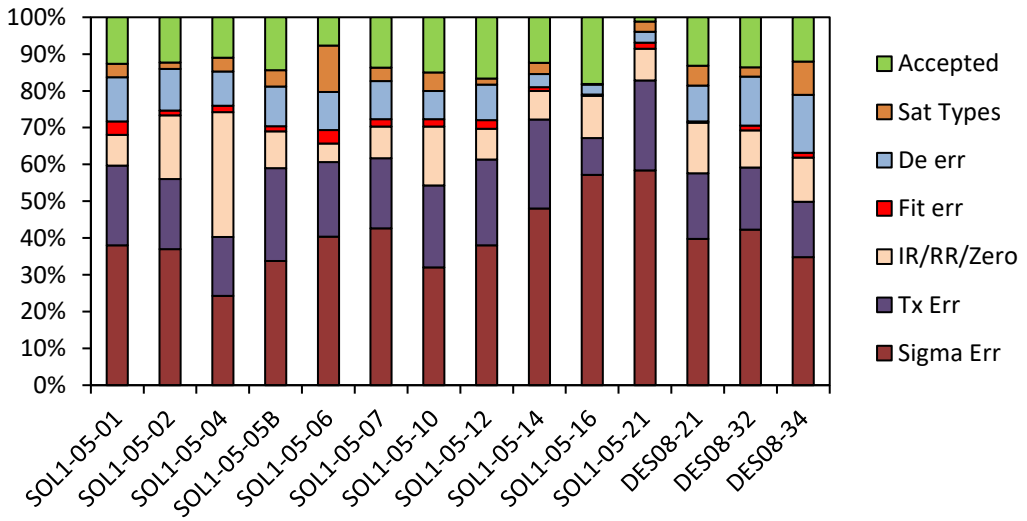


**FIG. 5-32.** Graphical comparison of proportion of grains rejected by each criterion.

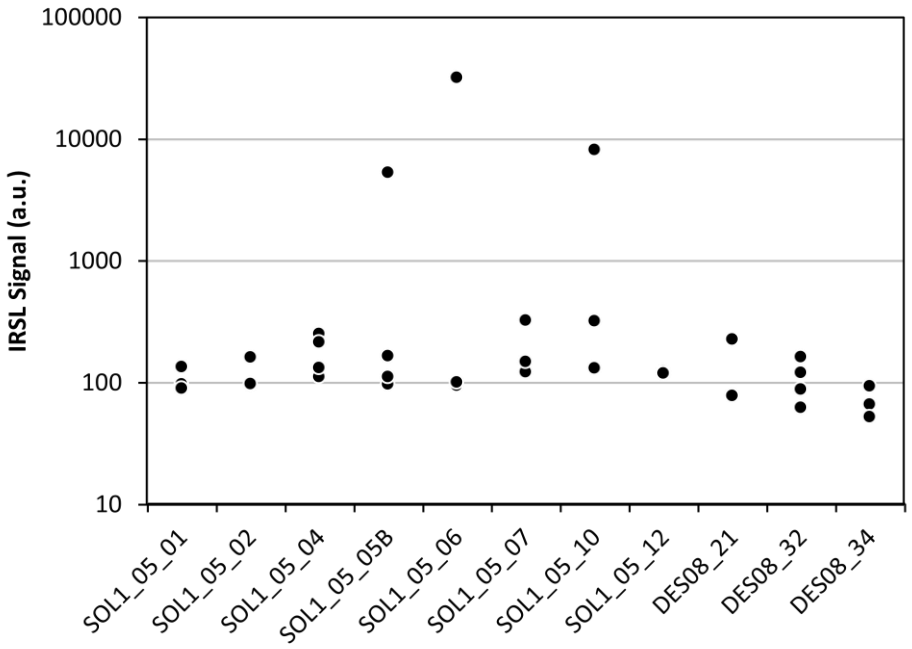


**FIG. 5-33.** Total IRSL signal (first 0.8 s of LED stimulation) for analyzed single grain aliquots. Samples stimulated by IR laser (SOL1-05-14, -16, and -21) are not included.

within the cave infill. Similar intensity discrepancies were noted between cave infill and the surrounding bedrock in Jacobs et al.'s (2006) study of Blombos cave and the surrounding Wankoe Formation. The mechanism for signal intensification of cave sediment grains is likely to be the repeated cycles of irradiation and stimulation involved in environmental transport, with grains becoming generally brighter as they travel further from the source bedrock (Pietsch et al., 2008).

Other notable outliers are samples SOL1-05-04, with an unusually high number of rejected grains due to recycling ratios, and SOL-05-16, which had only one saturated grain and no unbracketed grains (of 600 measured). Aside from SOL1-05-16, all other samples included saturated grains and all but one (SOL1-05-12) had super-saturated grains. Sample DES08-34 had the highest proportion of saturated-type grains, followed by Sample DES08-21.

Distribution characteristics

Distribution characteristics are summarized in Table 5-20 and Fig. 5-34. Overdispersion values tend to be high, ranging from 28.07 ± 4.00% to 47.14 ± 5.92% with more than half of samples having overdispersion values of at least 40%. Overdispersion levels are relatively constant for measured samples. Correlations between distribution characteristics were calculated for cave infill samples. Overdispersion is only very weakly correlated (0.16) with equivalent dose magnitude. Weighted skewness and kurtosis are moderately correlated with overdispersion, and strongly correlated with each other.

Regarding the variation of sample parameters, it is intriguing to compare measured grains from samples DES08-21 (38 grains) and SOL1-05-01 (39 grains), which were collected from several centimeters apart within the same soil layer in different years. It might be reasonably expected that the samples should return similar results. Single grains for these samples been prepared in the same manner, measured on the same machine, calibrated with the same data set, and evaluated by the same data fitting procedures. In the event, the measured distributions are not particularly similar. The central age model equivalent dose for each sample does not

**TABLE 5-20.** Distribution parameters for accepted single grain data.

| Sample | Overdispersion (%) | Wtd. Skew. | Wtd. Kurt. | CAM $D_e$ (Gy) |
|---|---|---|---|---|
| SOL1-05-01 | 43.12 ± 5.59 | 1.30 | 0.64 | 59.8 ± 4.5 |
| SOL1-05-02 | 47.14 ± 5.92 | 1.78 | 6.10 | 82.9 ± 6.7 |
| SOL1-05-04 | 46.52 ± 5.37 | 0.44 | 0.97 | 117.8 ± 8.6 |
| SOL1-05-05B | 42.16 ± 3.95 | 1.21 | 6.95 | 81.4 ± 4.3 |
| SOL1-05-06 | 39.84 ± 6.65 | 1.19 | 2.21 | 120.0 ± 10.6 |
| SOL1-05-07 | 43.53 ± 5.36 | 1.49 | 2.99 | 84.8 ± 6.1 |
| SOL1-05-10 | 40.37 ± 4.73 | 0.71 | 1.83 | 112.6 ± 7.2 |
| SOL1-05-12 | 41.22 ± 4.50 | 1.21 | 4.13 | 62.8 ± 3.8 |
| SOL1-05-14 | 31.80 ± 3.42 | 0.81 | 1.34 | 35.3 ± 1.6 |
| SOL1-05-16 | 44.08 ± 3.32 | 2.76 | 21.61 | 5.5 ± 0.3 |
| SOL1-05-21 | 39.11 ± 8.23 | -- | -- | 115.1 ± 11.9 |
| DES08-21 | 30.76 ± 4.35 | 0.84 | -0.03 | 49.7 ± 2.8 |
| DES08-32 | 41.57 ± 4.50 | 0.52 | 0.56 | 143.8 ± 8.6 |
| DES08-34 | 28.07 ± 4.00 | 0.11 | -0.52 | 100.5 ± 5.2 |

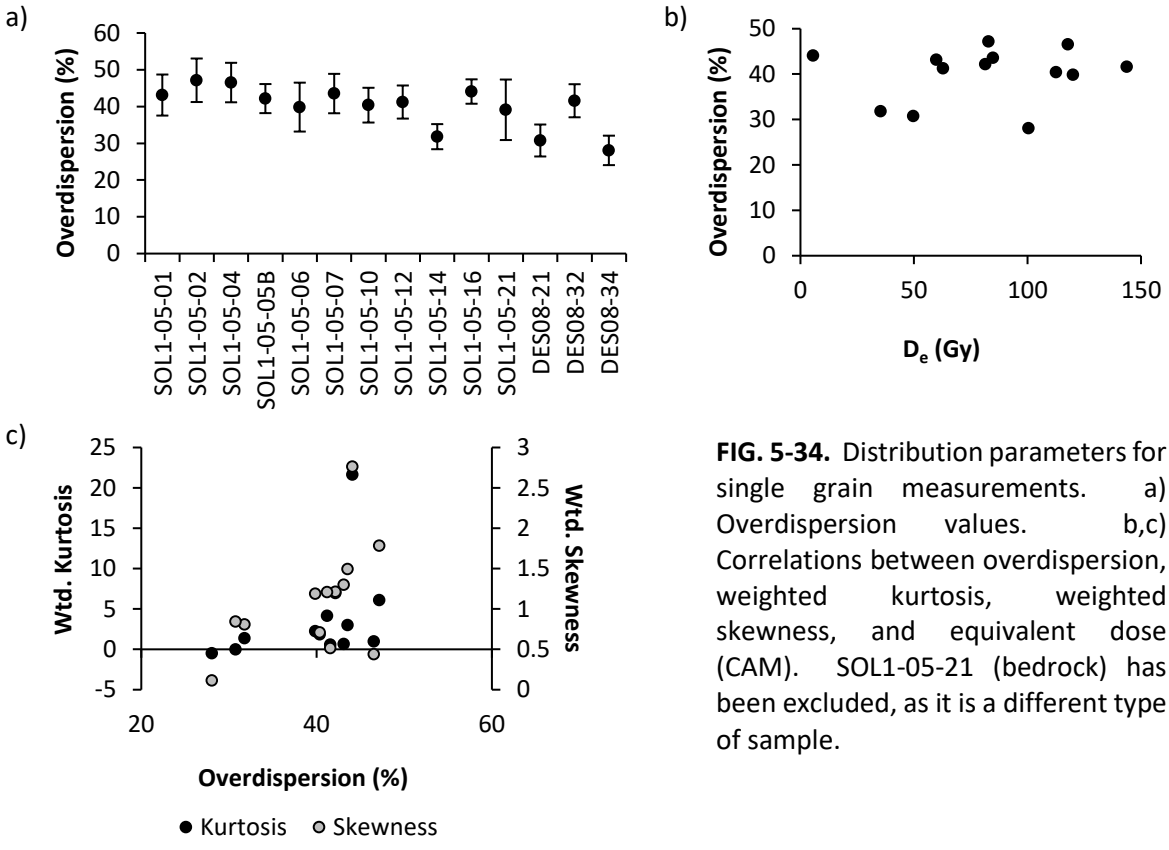


**FIG. 5-34.** Distribution parameters for single grain measurements. a) Overdispersion values. b,c) Correlations between overdispersion, weighted kurtosis, weighted skewness, and equivalent dose (CAM). SOL1-05-21 (bedrock) has been excluded, as it is a different type of sample.

**TABLE 5-21.** Correlation coefficients for single grain distribution parameters (SOL1-05-21 excluded).

| | $D_e$ (Gy) | Overdispersion | Wtd. Skewness | Wtd. Kurtosis |
|---|---|---|---|---|
| **$D_e$** | 1.00 | | | |
| **Overdispersion** | 0.15 | 1.00 | | |
| **Wtd. Skewness** | -0.63 | 0.51 | 1.00 | |
| **Wtd. Kurtosis** | -0.58 | 0.40 | 0.86 | 1.00 |

overlap at one sigma error, but does at a two sigma level. The calculated overdispersion is also dissimilar, with the lower dose sample having nearly 13% less overdispersion. According to a two-tailed t-test (unequal variance), the null hypothesis that these populations have the same mean is rejected (p=0.02). The cause of these differences is unknown.

All measured single grains are plotted in Fig. 5-35, with both CAM and FMM components indicated. Measured grains can range from ~20 to nearly 300 Gy within the same sample, as for SOL1-05-05B. Both long 'tailed' (e.g. SOL1-05-04, SOL1-05-07) and more symmetric distributions (e.g. DES08-34, SOL1-05-05B) are evident. Some high dose grains are clearly present in the low equivalent dose samples, such as SOL1-05-16, but these are rare and do not seem to particularly affect the CAM equivalent dose. Further evidence for the most appropriate age model is discussed in the next two sections, and the ensuing ages compared in Section 5.2.4.

Like the Taforalt samples, these samples may be examined in the context of other single grain studies on cave sites (see discussion at the end of Section 5.1.2.2 for examples from the scientific literature). Once again, the results of the rejection criteria analysis for the cave sediment samples are well within the reported ranges in the literature, though these grains are more highly luminescent than those from Taforalt. Equivalent dose distribution characteristics are also not unusual, though the typical overdispersion is on the higher side of those reported from cave sediments. Very similar distributions (see Fig. 5-36) have been reported from single grain studies on the nearby coastal sites of El Harhoura 2, El Mnasra, and Contrebandiers (Jacobs et al., 2011; Jacobs et al., 2012).

Interestingly, the OSL characteristics of the Dar es-Soltan bedrock are nearly identical to those found for that surrounding Contrebandiers (Jacobs et al., 2011), and it seems likely that they may be parts of the same fossilized dune system. Similar proportions of feldspar grains were measured by both groups though different methods were used (1.2% in this study and 1.6%/1.9% from Jacobs et al., 2011). The overdispersion values calculated for bedrock are also equivalent (this study: 39.11 ± 8.23%; Jacobs et al.,2011: 37 ± 4% and 39 ± 6%, as are the

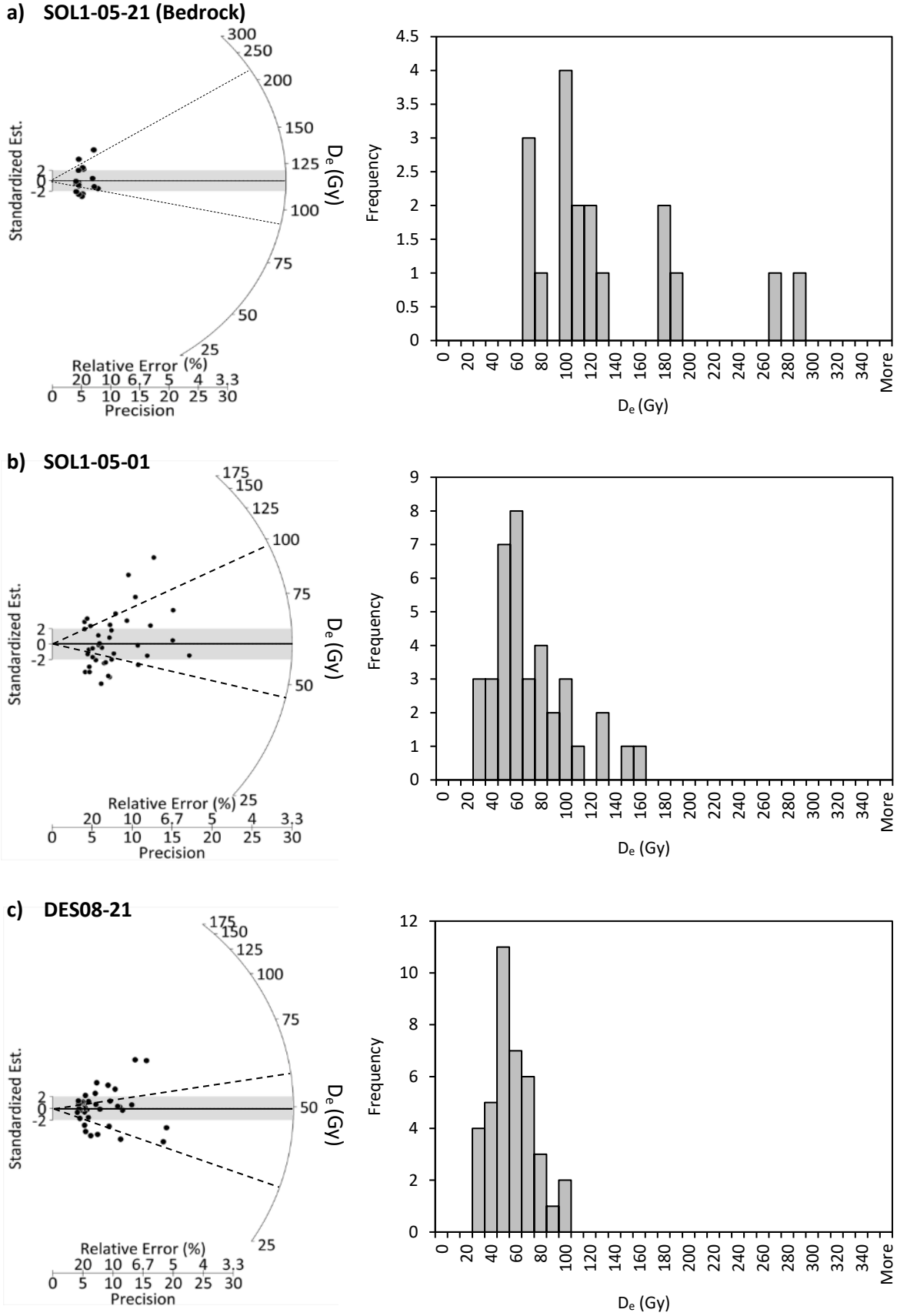


**FIG. 5-35.** Radial plots and histograms for single grain analyses. All samples are listed in order of depth: bedrock (a) then the base of the cave infill (b) to the top (n). Radial plots are centered at CAM estimates; note scale changes for both radial plots and histograms.

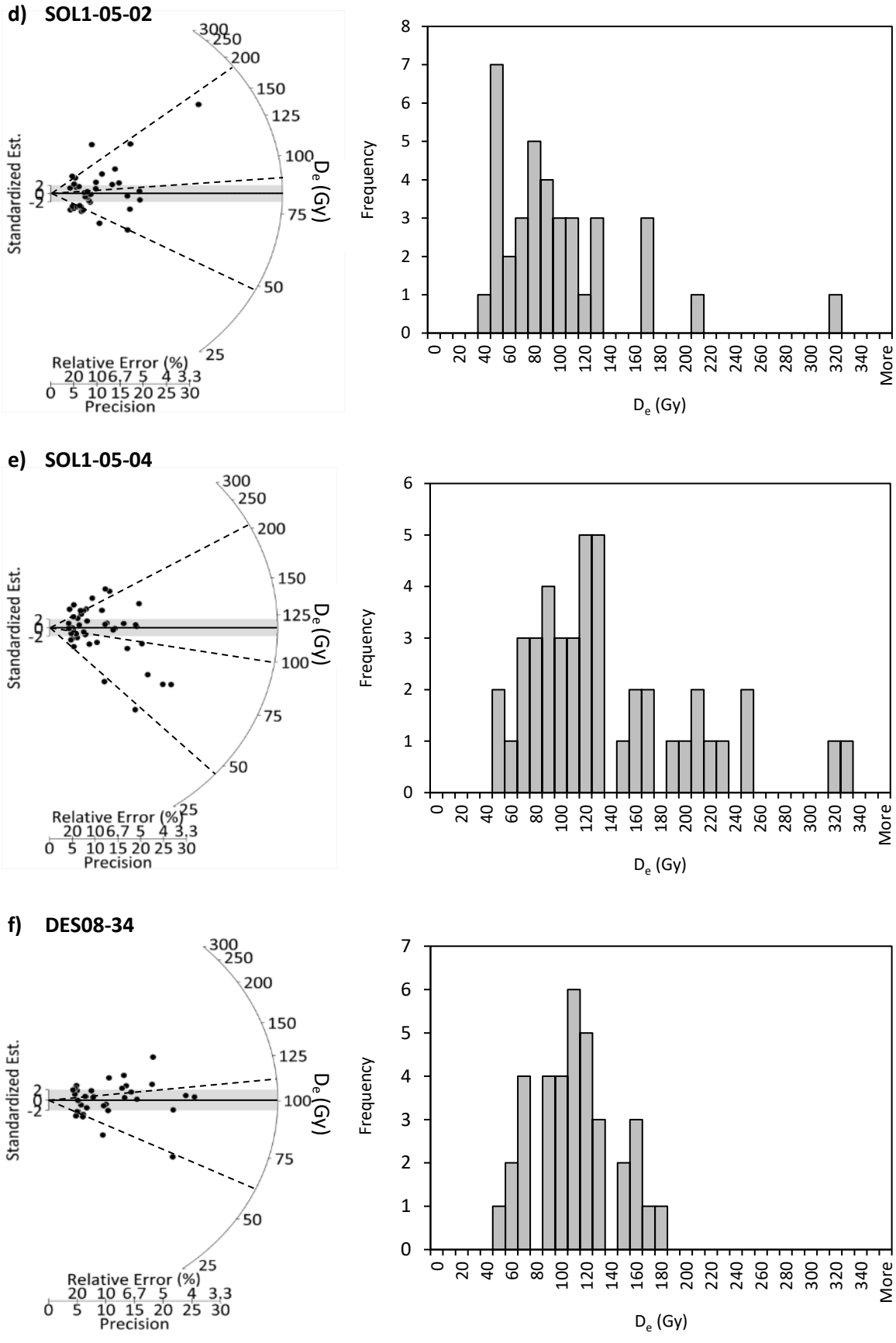


**FIG. 5-35.** (Continued)

**g) SOL1-05-05B**

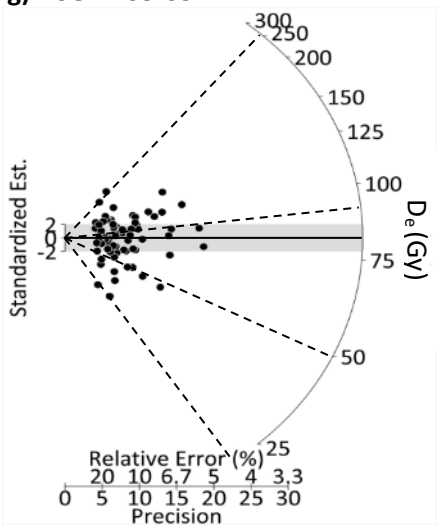


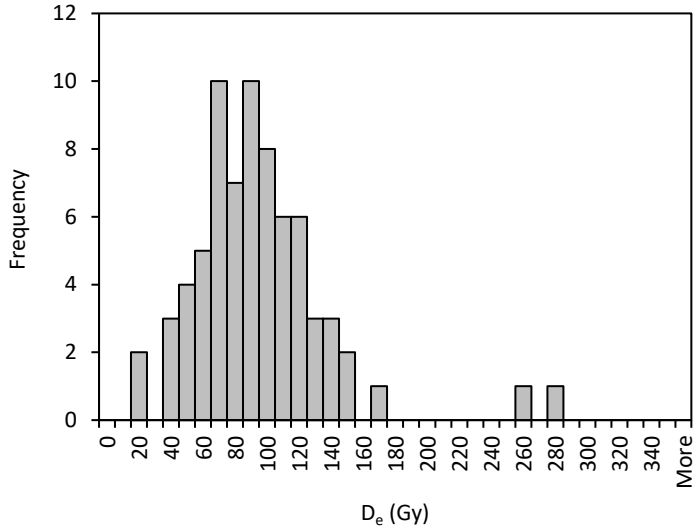


**h) SOL1-05-06**

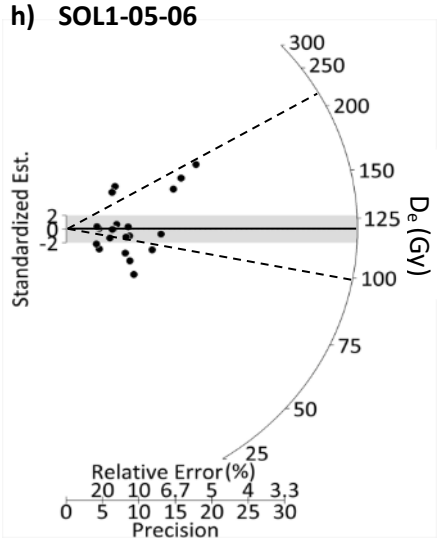


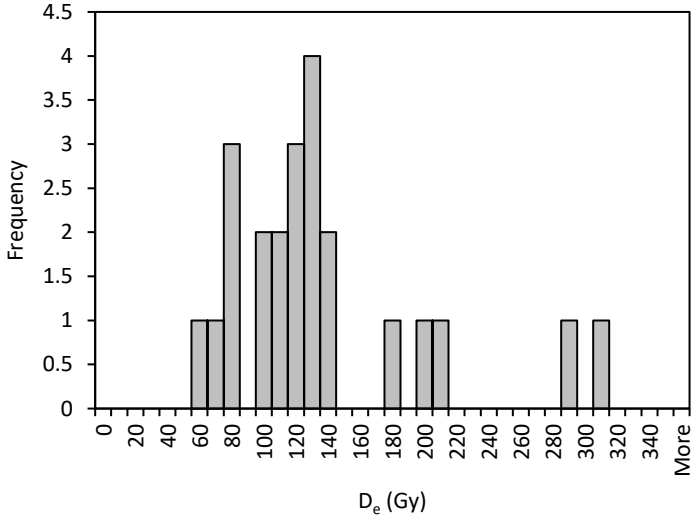


**i) SOL1-05-07**

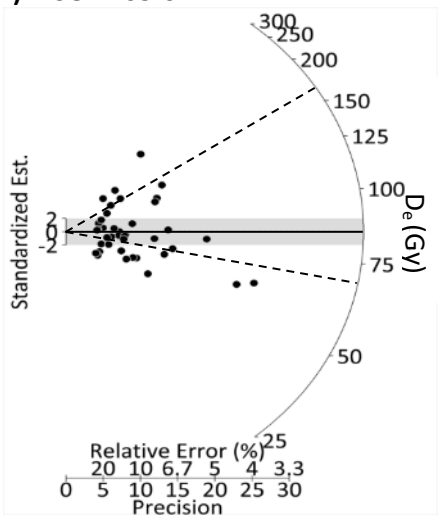


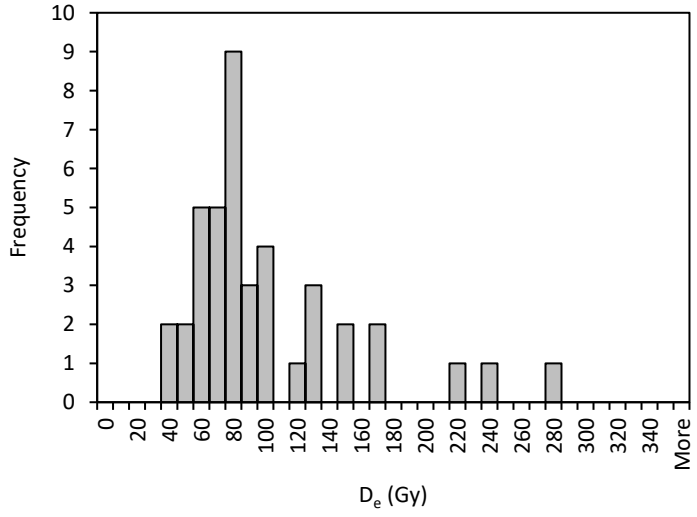


**FIG. 5-35.** (Continued)

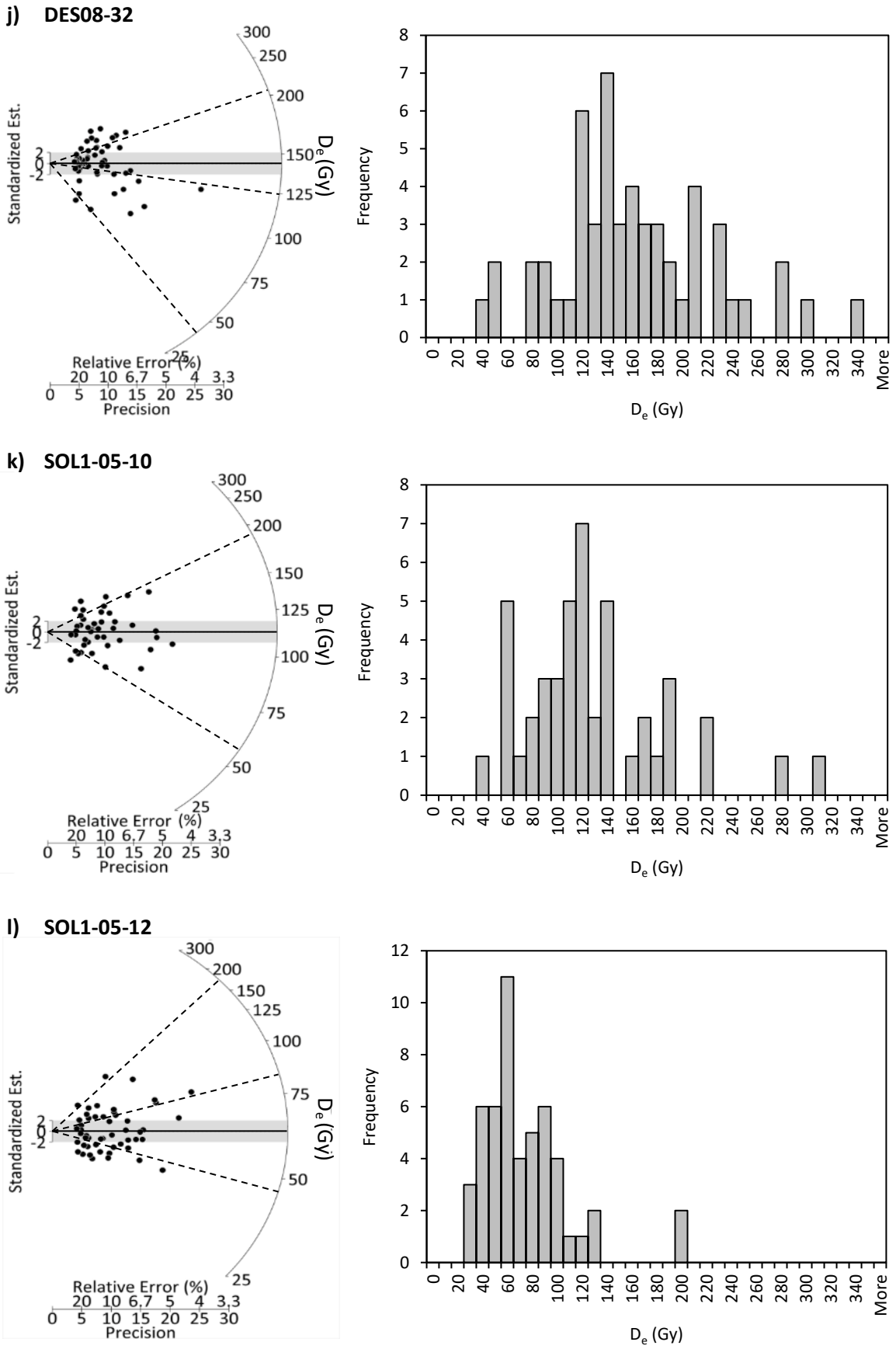


**FIG. 5-35.** (Continued)

**m) SOL1-05-14**

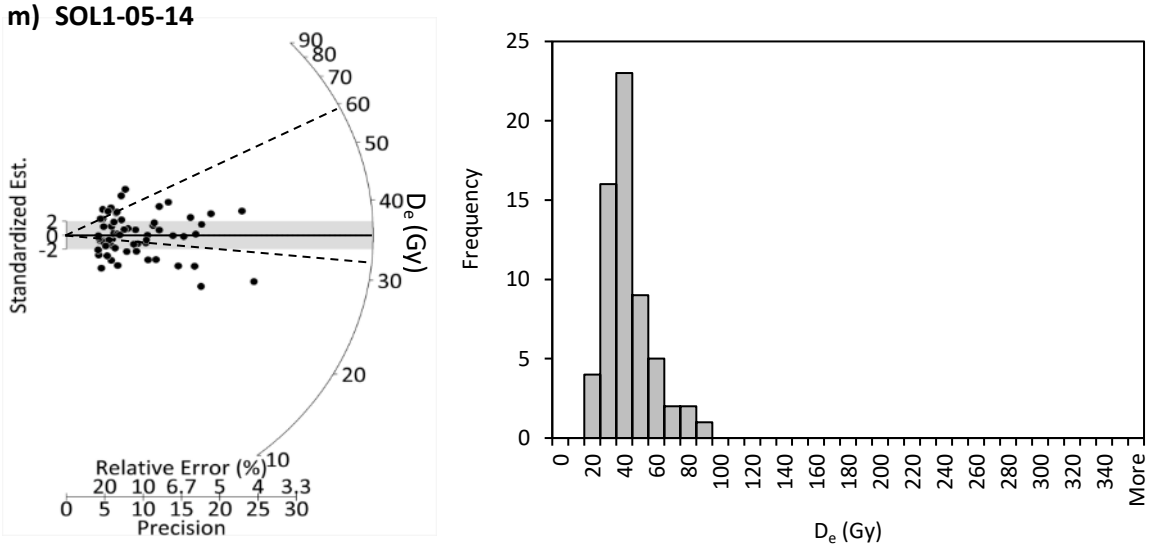


**n) SOL1-05-16**

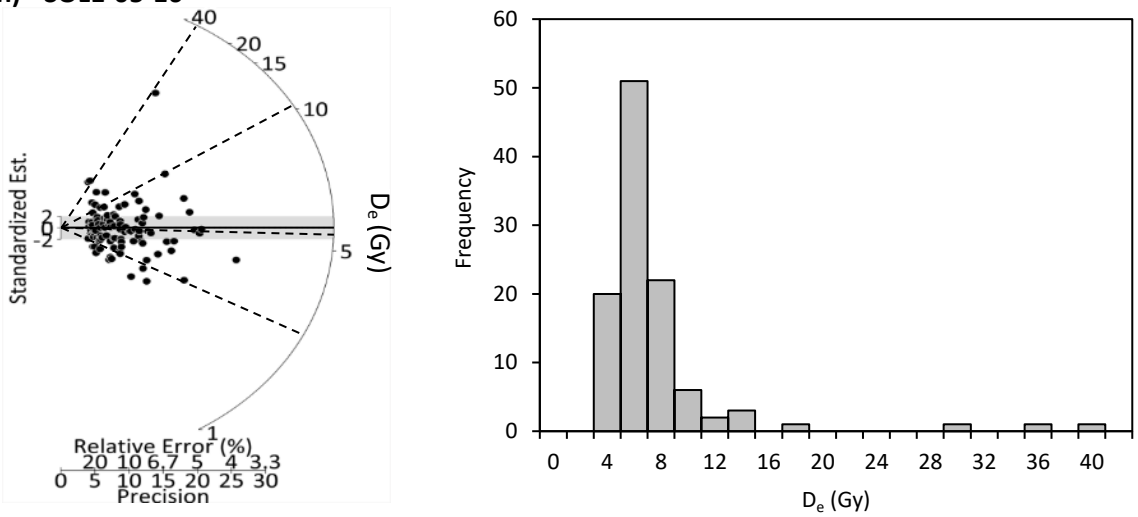


**FIG. 5-35.** (Continued)

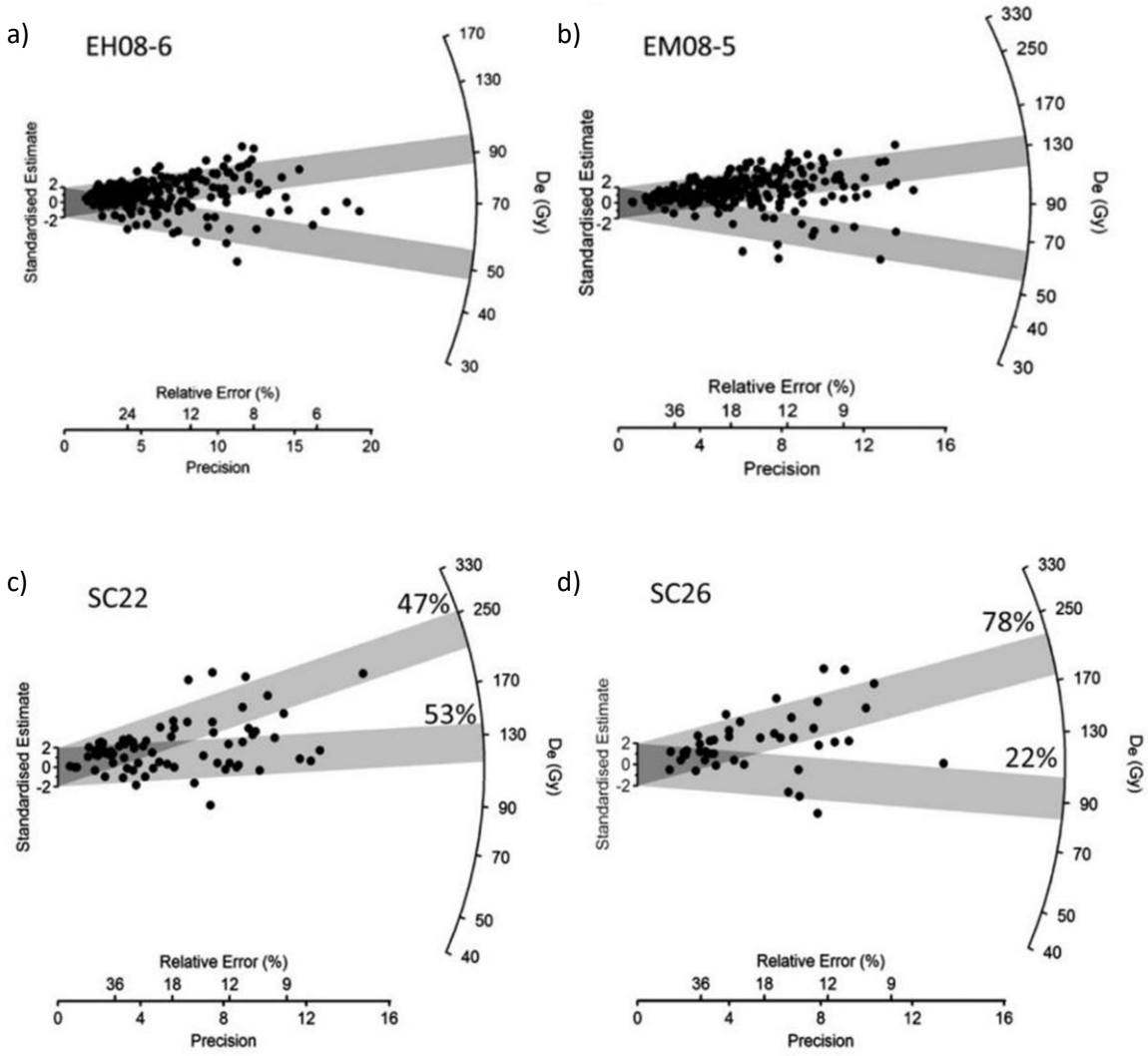


**FIG. 5-36.** Single grain equivalent dose distributions from other MSA cave sites on the Atlantic coast of Morocco. The finite mixture model has been used to fit the data. a,b) 'Scattered' samples from El Harhoura 2 and El Mnasra, respectively (Jacobs et al., 2012: 386). c,d) Calcareous sandstone bedrock from the site of Contrebandiers, collected from outside and within the cave, respectively (Jacobs et al., 2011: 3638).

measured equivalent dose distributions (see Fig. 5-36). Precise components fit with the FMM are different, however, due to varying values of overdispersion used in each model. Overall, the correspondence between results is high and supports the equivalent dose measurements made during this study.

#### *5.2.2.3 Equivalence of equivalent dose and burial dose*

Bioturbation

The lithostratigraphic description of Dar es-Soltan I noted bioturbation in most sediments, ranging in degree from low to extreme (Barton et al., 2009). Three types were noted: channels probably due to insect or molluscan burrowing (up to 20 mm in diameter), amorphous chambers, and root-related mixing, modern and ancient. Sediments from Groups 1 through 4 were noticeably bioturbated, with small-scale bioturbation particularly common in Groups 2 and 3. Within these groups, OSL samples were collected from locations where bioturbation appeared less present.

Partial bleaching

Accepted aliquots from four dose recovery experiments (SOL1-05-01, SOL1-05-05B, SOL1-05-12, and SOL1-05-16) have been pooled based on bleaching method (100 s of sunlight or LED). Normalized recovered doses for each group are displayed as box plots in Fig. 5-37. It is evident that the median of the sunlight bleached aliquots is slightly higher than that of the LED bleached aliquots, but this difference is too small to be significant. Bleaching efficiency under LEDs is high, with all 10 LED bleached aliquots decaying to less than 10% of their original signal by 3.6 s. It is clear that Dar es-Soltan I quartz bleaches relatively quickly, with no remnant signal.

However, the potential for incorporation of partially bleached grains into the cave sediment sequence is high. Two main routes are possible:

1. The incorporation of partially bleached quartz and feldspar grains weathered from the aeolianite bedrock,
2. Deposition of sediments, particularly the basal beach sands, under

restricted light conditions.

Considering the first route, the incorporation of aeolianite-derived grains into the cave infill is almost certainly occurring. It is known that significant weathering of the aeolianite bedrock has occurred, as large blocks have fallen from the roof of the cave and been incorporated throughout Group 4 deposits (towards the rear of the cave). Sample SOL1-05-19, which was collected from the weathered rind around one of these blocks, is close to saturation. Group 4 sediments (G4.5) also contain clasts of what are likely to be speleothem fragments derived from the roof of the cave (Barton et al., 2009). Accepting the existence of this input source, the effect of partially bleached grains on multigrain aliquots depends on the magnitude of the original signal, the relative proportion of these grains to those provided by other inputs, and the brightness of this quartz.

Grains from the bedrock were therefore characterized. Once disaggregated, coarse grains were measured according to single grain techniques and an IR laser was used to screen for feldspars. IRSL response was considered to be from a feldspar if the natural IRSL signal from the first 0.06 s was greater than 50 counts (a.u.); using the standard criteria for IRSL response (i.e. natural signal >3σ above background) was not appropriate as some very bright IRSL decay curves stayed essentially constant over the emission period. For bedrock sample SOL1-05-21, 1563 grains were measured, but only 18 quartz grains (1.2%) were accepted for equivalent dose analysis. 18 other grains were accepted based on SAR characteristics, but rejected as probable feldspars. The quartz central age equivalent dose is 115.11 ± 11.94 Gy, with an overdispersion value of 47.4 ± 8.5%. Feldspars comprise slightly over 7% of all measured grains, but emit 89.4% of the total OSL signal. Histograms of absolute grain brightness in Figure 5-38 show the significance of this difference. The brightest quartz grain emits only 1.5% as much signal as the brightest feldspar.

Two cave sequence samples, SOL1-05-14 (fine loamy sand, G5.1) and SOL1-05-16 (midden sample, G5.2), were also screened for feldspars. Midden sample SOL1-05-16 yields only

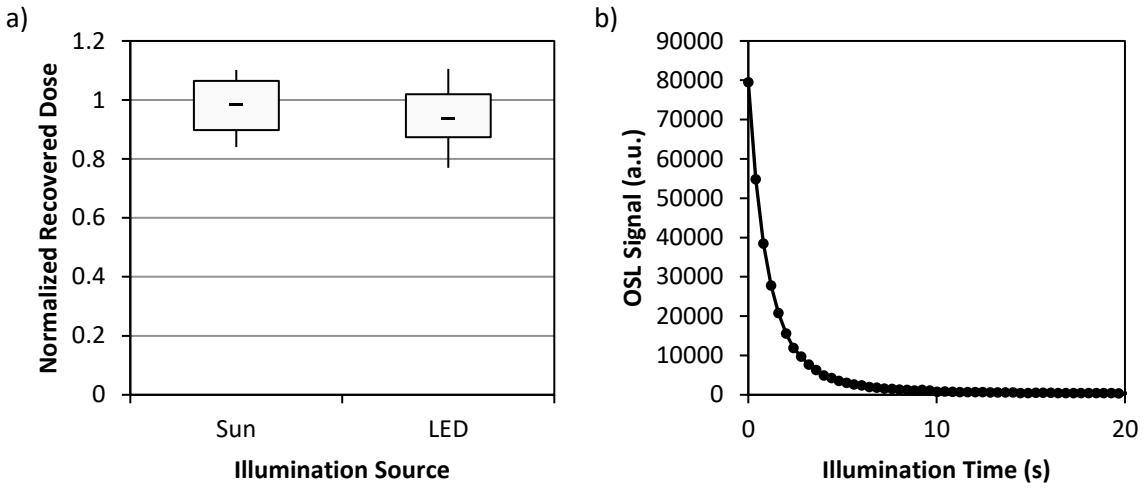


**FIG. 5-35.** Bleaching efficiency. a) Comparison of recovered doses from multigrain aliquots (all accepted dose recovery aliquots) bleached either by sunlight or with LEDs at various preheats. b) Typical natural signal bleaching with LEDs at 25°C.

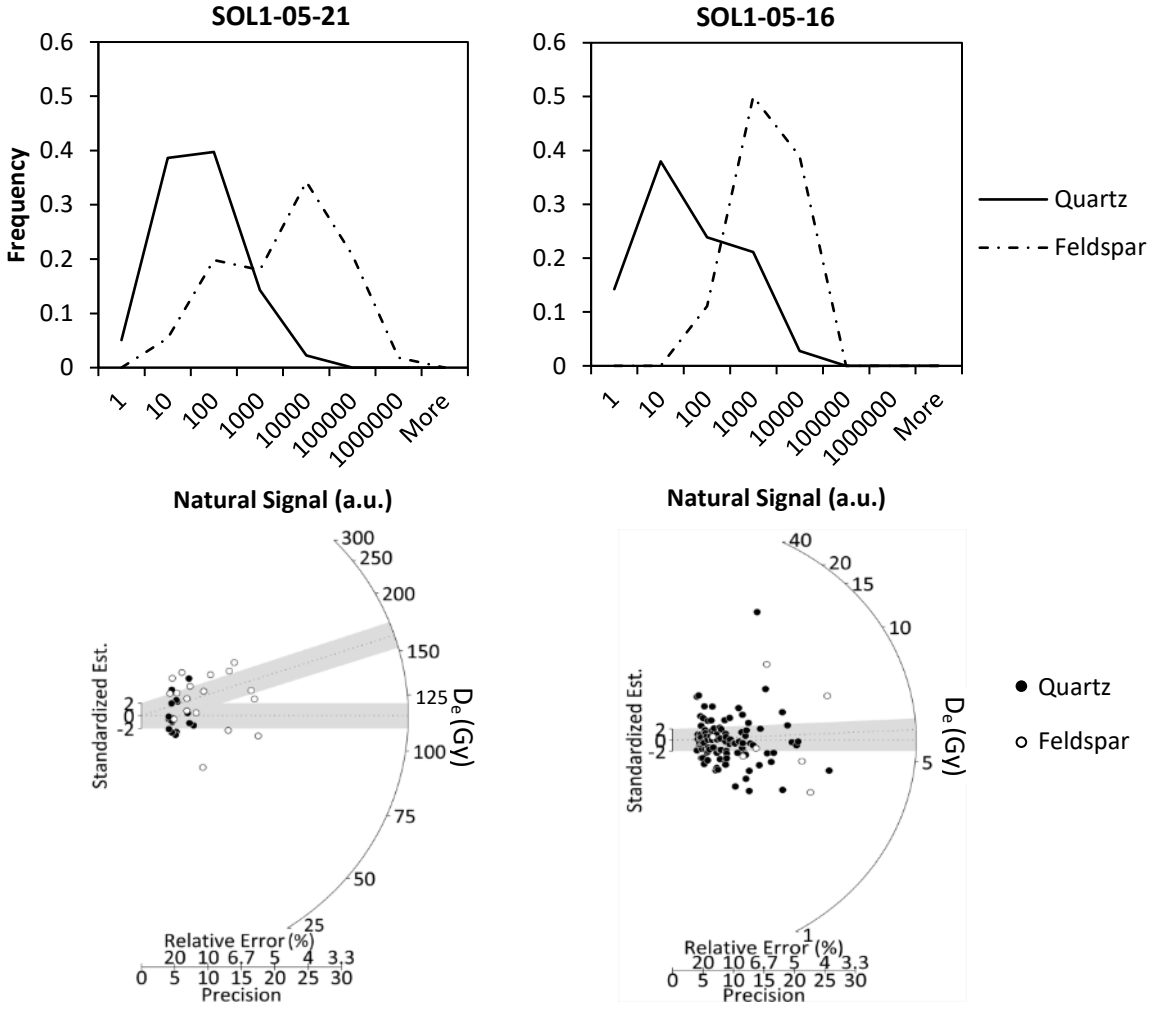


**FIG. 5-38.** Natural signals for feldspar and quartz in bedrock sample SOL1-05-21 and midden sample SOL1-05-16. It is clear that the influence of feldspars is much higher in the bedrock sample, due both to the number and brightness of these grains. For both samples, the feldspar equivalent dose is higher than the quartz equivalent dose.

3% feldspars, which contribute 21.6% of the total OSL signal. The more natural sand, SOL1-05-14, has 0.4% feldspars giving 4.5% of the OSL signal. In both samples, the brightest quartz grains are brighter than the brightest feldspars. If sample SOL1-05-16 and the bedrock sample are compared, it is clear that the bedrock quartz is relatively dim. Even though it has a equivalent dose of >100 Gy, the grain brightness profile of SOL1-05-21 is similar to that of SOL1-05-16, which only has a equivalent dose of ~5.5 Gy.

The second route—light restricted deposition of cave infill—is also possible, but it is more difficult to place constraints on the likelihood. It is known that there have been repeated flooding and pooling events in the cave, as these have been recorded by layer deformation and via sedimentary unconformities (Barton et al., 2009). In addition, the mouth of the cave is relatively small, so sediment that was not fully bleached during transport into the cave may not have experienced bleaching opportunities later (though this was somewhat rectified for later samples due to the hole that developed in the roof). However, it has also been shown that Dar es-Soltan I quartz is relatively easily bleached. Furthermore, no residual signals were found when equivalent dose measurements were made on modern beach sands in the region (J.-L. Schwenninger, pers. comm.). Therefore, it seems unlikely that this route would have a significant and systematic impact on cave sediments, but it should be kept in mind for anomalous samples.

### Microdosimetry

The sediments in the cave infill sequence are likely to be affected by microdosimetry issues, due to the presence of feldspars, shell fragments, carbonate and manganese concretions, and variable pore spaces in both very coarse (basal beach sands) and finely packed sediments (Nathan et al., 2003; Guérin et al., 2012). The bedrock, too, includes a high number of both feldspar hot-spots and shielding carbonate cements. It is impossible, without attempting detailed simulations, to incorporate all of these effects and predict the absorbed dose distribution for quartz grains of a particular sample. Nevertheless, the likelihood of this factor

should prevent overreliance on complex statistical manipulations of the measured equivalent dose distributions.

Saturation effects

Sample DES08-34 had the highest proportion of saturated/super-saturated grains at 7.4% (Table 5-19), but the median proportion for all measured samples was only ~2%. Moreover, correlation between central equivalent dose and saturation/super-saturation was only moderate (0.28), with certain samples having central equivalent doses of nearly 150 Gy and low levels of saturation. It seems likely that for certain samples, notably DES08-34, microdosimetry in relatively high dose sediments may lead to high overdispersion and therefore higher proportions of saturated grains. By excluding these grains and measuring only the lower dose populations, the ages of such samples may be underestimated. However, this issue is unlikely to systematically bias all high-dose OSL age estimates.

Supersaturating grains typically ranged in intensity from approximately the median grain intensity to several hundred times the median signal, corresponding to a maximum of a few percent of total emission intensity per sample. Only one exceptionally bright grain was noted. From sample SOL1-05-06, this grain was nearly 4900 times brighter than the grain median intensity, and its emissions comprised 39.8% of total signal from 300 grains. Overall, then, supersaturated grains are not likely to cause overestimation of equivalent dose in multigrain aliquots, but it is possible that certain rare aliquots may be subject to this.

#### *5.2.2.4 Age model*

In order to examine the effect of age model choice on data, CAM, MAM and FMM models were applied to all single grain data; overdispersion values of 20% and 30% were used for the MAM and FMM models. Calculated values are shown in Fig. 5-39. Overdispersion choice strongly affects the range (e.g. SOL1-05-21, DES08-34) and number (e.g. SOL1-05-05B, SOL1-05-16) of FMM components, as well as the value of the MAM and dominant FMM equivalent doses. Fig. 5-39c shows the difference in MAM value or dominant FMM component calculated using

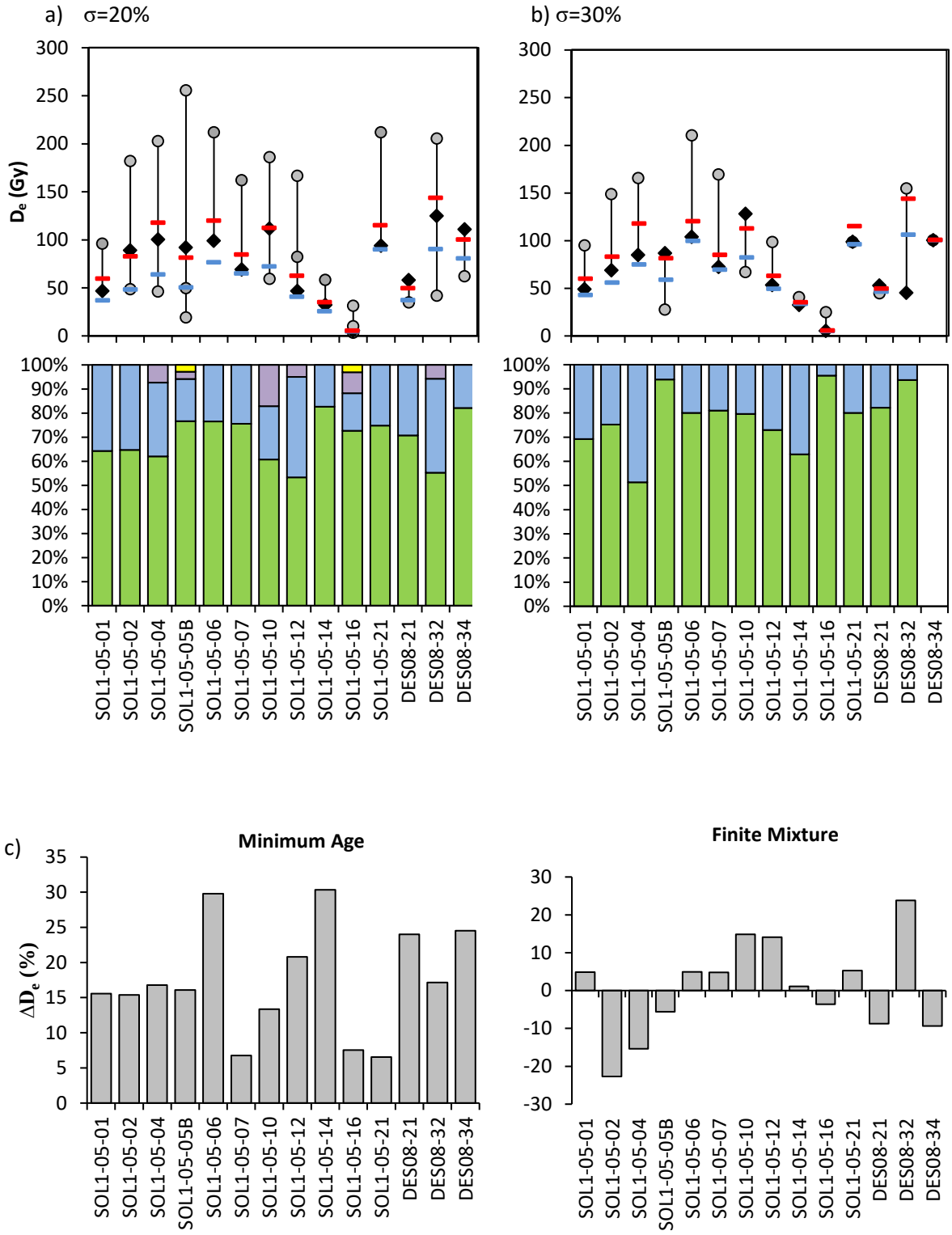


**FIG. 5-39.** Age model results for single grain data: a) σ=20%. b) σ=30%. Various age models are indicated as follows: central age equivalent dose (━), minimum age equivalent dose (━), and dominant (◆) and non-dominant (◎) FMM components. The bar charts underneath indicate grain proportions for each FMM component. c) Differences (%) in equivalent dose when assumed σ is changed to 30% from 20%.

30% overdispersion as a percentage of the value calculated for 20% overdispersion. MAM equivalent dose increases for all samples as overdispersion increases, whereas dominant FMM components increase or decrease depending on the sample. Calculated equivalent doses can differ by more than 30% for some samples due to a 10% change in assumed overdispersion.

Based on the preceding analysis of Dar es-Soltan I, it is felt that partial bleaching is not a significant factor therefore the minimum age model is not appropriate. Deciding between the central age model and finite mixture model is more difficult. On one hand, it seems unlikely that components calculated by the FMM can be attributed to a particular source, such as bioturbation or partial bleaching. Therefore, basing an age on a particular component could lead to significant inaccuracy. By allowing the model more freedom to identify modes in the data, however, equivalent dose values may be more robust than those calculated by the assumptions implicit in the central age model. Single grain ages will therefore be calculated according to both the CAM and FMM ($\sigma$ =20%) models and compared. Without further site data or independent age control, internal stratigraphic coherence of the final ages is the only way to evaluate the success of each model.

### 5.2.3 Dosimetry

#### *5.2.3.1 Sample parameters*

Measured water contents ranged from relatively low to nearly saturated, with a median value of ~12%. The basal, in situ beach sands at the base of the deposit contained less than 5% water by mass. Setting these samples aside, water content tended to increase with depth (Fig. 5-40). Sample SOL1-05-20—a sandy clay loam near the top of Group 1—yielded the highest water content value, 26.8%. As there was no evidence that measured sedimentary water content was dependent upon any confounding factors (such as excavation history), measured water contents were used for dose rate calculations.

A standard sediment density was used for cosmic dose calculations. The median density value for all tube samples was calculated to be 1.43 g $cm^{-3}$. A density of 2.3 g $cm^{-3}$ was chosen

for the sandstone within which the cave is formed (Natural Stone Council, 2010), and the overall thickness of the cave roof was estimated to be 3 m. No skyview correction was made for samples collected within the cave, due to the relatively small cave entrance. The hole in the cave roof will have increased the cosmic dose rate to Group 5 samples, but this cannot be estimated without on site measurements. Moreover, the placement of the numerous fallen boulders places this event fairly late in the cave's history. For the bedrock sample collected from the edge of the sandstone terrace, though, it was necessary to calculate shielded and unshielded cosmic dose. A minimum sediment path length of 5 cm was estimated as an average for the sample grains, and a skyview proportion of 50% was used in calculations.

Measured elemental concentrations are presented in Fig. 5-40 according to depth. Potassium and thorium are strongly depth dependent, and uranium values are less so. There is no clear correlation with present-day water content. Both sets of samples (2005 and 2008), for which elemental concentrations were measured in different laboratories, show the same depth-related trends for all three elements. Therefore this is likely to be an accurate reflection of the sediment rather than an artifact of the analysis. It is also apparent from these plots that elemental correlation is not as robust as expected for the whole cave infill. The potassium/thorium biplot (Fig. 5-41) demonstrates that potassium and thorium are highly correlated at low thorium levels, but this breaks down at ~3.7-3.8 ppm of Th. These high Th samples also seem to be enriched in uranium (Fig. 5-41), and it is possible that they are not in equilibrium. Correlation values for low and high thorium samples are listed in Table 5-22, and confirm what is apparent graphically. The anomalous values occur in sediment Groups 2 through 4 (i.e. from slightly over 3 m depth to 7 m). In fact, all of the samples taken from these sediments have high thorium levels, except for SOL1-05-06.

Gamma dose measurements were obtained on site for all but four dated samples. For comparison, expected gamma doses were also calculated from each sample's elemental concentration. Both sets of gamma values have been plotted in Fig. 5-42. On site and

calculated gamma dose rates reflect the same depth/dose rate dependence noted previously. There is no systematic difference between the two sets of values that might indicate disequilibrium. For the four samples without on site measurements, calculated gamma dose rates match expected values well and are thus adopted. While the calculated value for sample DES08-32 is more than 40% higher than the measured rate for a sample collected from a similar depth and sediment layer (SOL1-05-07), it is several meters away laterally. The calculated sample value is in fact very similar to the closer samples DES08-31 and -33, with on site dose rates of 0.62 and 0.58 Gy $ka^{-1}$, respectively. Dose rate information for all measured samples is given in Table 5-23.

### 5.2.4 Age estimates

Multigrain and single grain age estimates are given in Table 5-24, and plotted versus depth in Fig. 5-43. In some cases, sample depth has been slightly adjusted in order to maintain the correct stratigraphic order. Multigrain age estimates are in stratigraphic order until approximately 5 m depth, mid-way through Group 3 (G3.3). This level corresponds to sample SOL1-05-10, which yields an age of 96.4± 9.2 ka. Below this, age reversals are so common that it becomes difficult to suggest a robust age-depth model. Both Groups 2 and 3 yield ages ranging from 50 ka to 100 ka or greater, while Group 1 samples range from slightly below 100 ka to 150 ka. The oldest multigrain ages obtained from Group 1 are indistinguishable from the age calculated for the bedrock sample (147.8 ± 19.9 ka). Single grain data reproduce most of the age reversals evident in the multigrain data, whether CAM or FMM equivalent doses are used. The most significant systematic change is that single grain ages tend to be younger than multigrain (8 of 13 samples), in some cases significantly younger. These younger ages are not necessarily supported stratigraphically. For instance, either the CAM or FMM equivalent dose for the bedrock (SOL1-05-21) yields improbably young ages: 110.8 ± 13.8 ka and 90.2 ± 10.3 ka, respectively.

It is unlikely that bad SAR behavior is contributing in any significant degree to the age

anomalies noted in the sequence. The overall agreement between multigrain and single grain data, in which 'badly behaving' grains can be excluded, suggests that the SAR protocol is functioning correctly for the majority of grains. Dose recovery data also supports this interpretation. Super-saturation may adversely affect multigrain data occasionally, but as only one significant grain with this feature was found out of several thousands investigated, this would be a very rare occurrence. Examination of single grain data from cave infill and the bedrock characterization also suggested that bioturbation and partial bleaching were unlikely to contribute significantly. In particular, there is often no significant difference in single grain distribution between samples that are older than expected and comparatively young samples (e.g. SOL1-05-04 vs. SOL1-05-02 in Figure 5-35).

Instead, it seems likely that a combination of dosimetric effects is leading to the unusual age reversals. As noted in the previous section, elemental concentrations do not correlate as expected in Groups 2 through 4. Fig. 5-44 displays the multigrain age estimates for the cave infill, with samples that have high thorium levels (>3.7) highlighted. The only sample that may not be affected is SOL1-05-06, which has a multigrain age of 115.7 ± 11.7 ka. Plots of central equivalent dose and total dose rate against depth are also shown (Fig. 5-45). Both equivalent dose and dose rate first increase then decrease with depth. However, the calculated dose rates are significantly more variable than the corresponding equivalent doses. This is most obvious at the Group 1/Group 2 boundary, at a depth of ~7 m. While some dose rates increase abruptly at 7 m, the measured equivalent doses do not reflect this until further up the sequence at ~5 m. These data suggest that modern-day dose rates may not correspond to the average burial dose rates for a number of the samples. This will be discussed further in Section 7.1.2.

Further down in the sequence, age variations seem to be controlled by relatively minor fluctuations in the measured dose rate and equivalent dose. The superposition of these effects can significantly affect age estimates, particularly when dose rates are low as in Group 1. Again, this is likely to be due to both sediment variability as well as microdosimetric variation: ICP

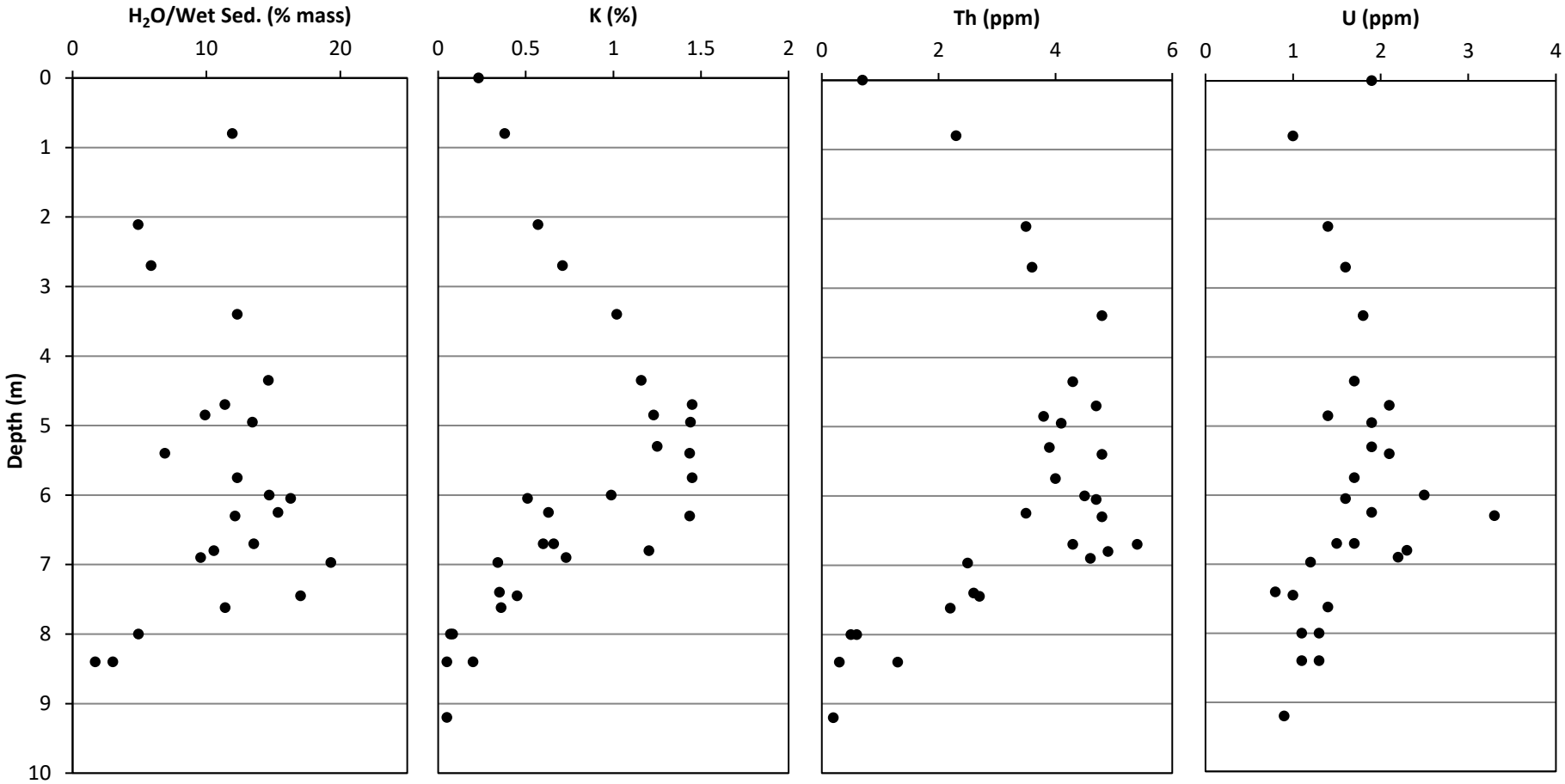


**FIG. 5-40.** Water content and elemental concentrations for all cave infill samples according to depth.

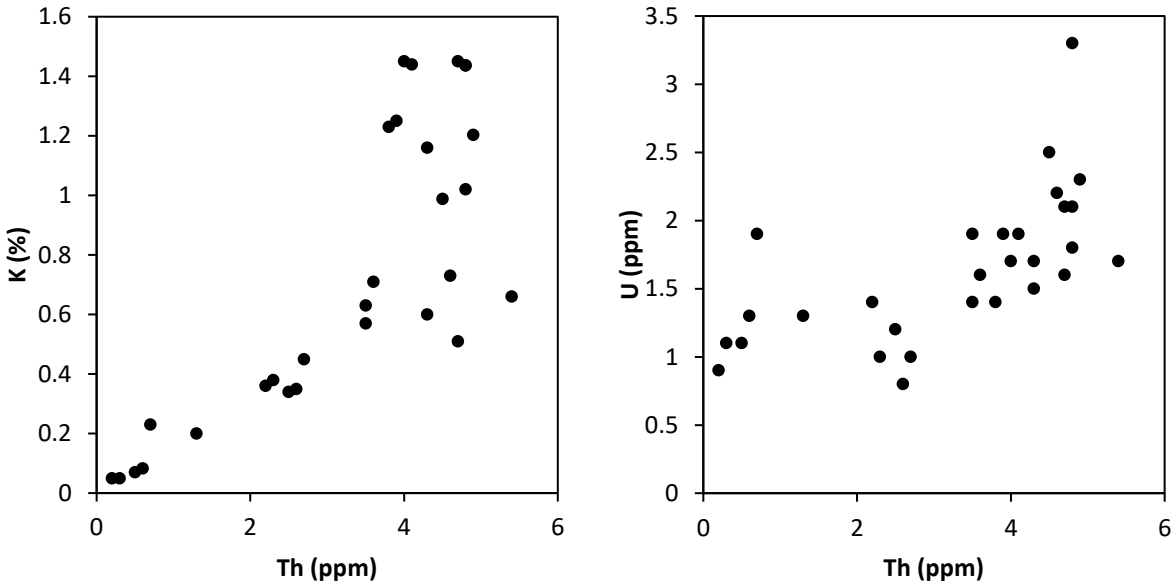


**FIG. 5-41.** Elemental biplots for measured samples (ICP-values).

**TABLE 5-22.** Correlation coefficients for ICP-measured elemental concentrations. a) All values. b,c) Clustered values: samples with <3.8 ppm Th (b) and >3.8 ppm Th (c).

a)

| | K | Th | U |
|---|---|---|---|
| **K** | 1.00 | | |
| **Th** | 0.80 | 1.00 | |
| **U** | 0.70 | 0.64 | 1.00 |

b)

| | K | Th | U |
|---|---|---|---|
| **K** | 1.00 | | |
| **Th** | 0.97 | 1.00 | |
| **U** | 0.43 | 0.26 | 1.00 |

c)

| | K | Th | U |
|---|---|---|---|
| **K** | 1.00 | | |
| **Th** | -0.32 | 1.00 | |
| **U** | 0.35 | 0.34 | 1.00 |

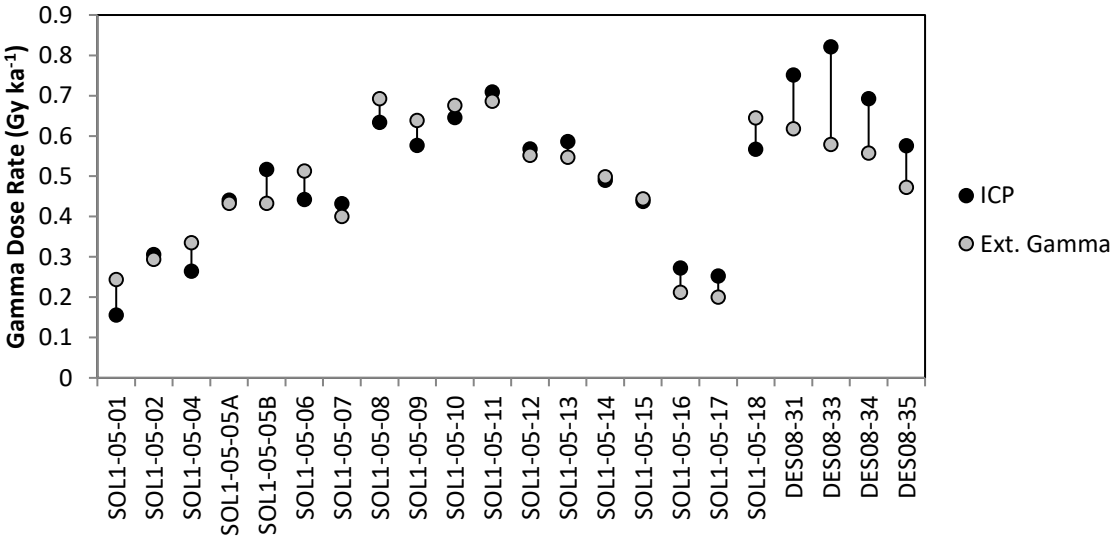


**FIG. 5-42.** Comparison between on-site gamma spectrometer measurements and gamma dose rates calculated from ICP-derived elemental concentrations. No systematic differences are apparent.

**TABLE 5-23.** Sample dose rates and calculation parameters. Gamma dose rates used in the final age calculations are shown in bold; on-site gamma spectrometer measurements were preferred for this purpose.

| Sample | K (%) | Th (ppm) | U (ppm) | $H_2O$ (%) | Infill Depth (m) | Alpha ($10^{-2}$ Gy $ka^{-1}$) | Beta ($10^{-2}$ Gy $ka^{-1}$) | Ext. Gamma ($10^{-2}$ Gy $ka^{-1}$) | Calc. Gamma ($10^{-2}$ Gy $ka^{-1}$) | Cosmic ($10^{-2}$ Gy $ka^{-1}$) | Total Wet Dose Rate (Gy $ka^{-1}$) |
|---|---|---|---|---|---|---|---|---|---|---|---|
| SOL1-05-01 | 0.07 | 0.50 | 1.10 | 5.00±5.00 | 8.00 | 3.60±2.05 | 18.50±1.69 | **24.4±1.22** | 15.58±1.33 | 6.88±6.19 | 0.53±0.07 |
| SOL1-05-02 | 0.36 | 2.20 | 1.40 | 11.40±5.00 | 7.62 | 3.93±2.04 | 41.36±3.70 | **29.41±1.47** | 30.56±2.58 | 7.07±6.71 | 0.82±0.08 |
| SOL1-05-03 | 0.45 | 2.70 | 1.00 | 17.04±5.00 | 7.45 | 3.42±1.76 | 40.30±3.81 | -- | **28.43±2.62** | 7.16±6.86 | 0.79±0.09 |
| SOL1-05-04 | 0.34 | 2.50 | 1.20 | 19.30±5.00 | 6.97 | 3.38±1.74 | 34.44±3.23 | **33.5±1.68** | 26.50±2.57 | 7.41±6.80 | 0.79±0.08 |
| SOL1-05-05A | 0.60 | 4.30 | 1.50 | 13.54±5.00 | 6.70 | 4.39±2.20 | 59.45±5.44 | **43.3±2.17** | 44.12±3.83 | 7.56±6.89 | 1.15±0.10 |
| SOL1-05-05B | 0.66 | 5.40 | 1.70 | 13.54±5.00 | 6.70 | 4.82±2.42 | 67.11±6.10 | **43.3±2.17** | 51.72±4.50 | 7.56±7.16 | 1.23±0.10 |
| SOL1-05-06 | 0.63 | 3.50 | 1.90 | 15.36±5.00 | 6.25 | 4.36±2.22 | 62.34±5.77 | **51.32±2.57** | 44.28±3.97 | 7.82±7.30 | 1.26±0.11 |
| SOL1-05-07 | 0.51 | 4.70 | 1.60 | 16.31±5.00 | 6.05 | 4.36±2.19 | 53.62±4.90 | **40.07±2.00** | 43.24±3.97 | 7.94±7.41 | 1.06±0.10 |
| SOL1-05-08 | 1.45 | 4.00 | 1.70 | 12.32±5.00 | 5.75 | 4.56±2.29 | 114.25±11.20 | **69.24±3.46** | 63.34±5.46 | 8.12±7.42 | 1.96±0.15 |
| SOL1-05-09 | 1.25 | 3.90 | 1.90 | 16.23±5.00 | 5.30 | 4.40±2.22 | 98.31±9.66 | **63.84±3.19** | 57.67±5.28 | 8.41±7.80 | 1.75±0.14 |
| SOL1-05-10 | 1.44 | 4.10 | 1.90 | 13.44±5.00 | 4.95 | 4.65±2.35 | 114.13±11.16 | **67.62±3.38** | 64.55±5.65 | 8.64±7.87 | 1.95±0.15 |
| SOL1-05-11 | 1.45 | 4.70 | 2.10 | 11.40±5.00 | 4.70 | 5.12±2.59 | 121.25±11.63 | **68.62±3.43** | 70.93±5.96 | 8.81±8.20 | 2.04±0.16 |
| SOL1-05-12 | 1.16 | 4.30 | 1.70 | 14.64±5.00 | 4.35 | 4.46±2.24 | 93.89±9.11 | **55.17±2.76** | 56.77±5.03 | 9.06±8.07 | 1.63±0.13 |
| SOL1-05-13 | 1.02 | 4.80 | 1.80 | 12.32±5.00 | 3.40 | 4.84±2.43 | 90.33±8.50 | **54.76±2.74** | 58.59±4.96 | 9.78±8.70 | 1.60±0.13 |
| SOL1-05-14 | 0.71 | 3.60 | 1.60 | 5.88±5.00 | 2.70 | 4.85±2.45 | 73.06±6.54 | **49.88±2.49** | 48.98±3.74 | 10.36±9.07 | 1.38±0.12 |
| SOL1-05-15 | 0.57 | 3.50 | 1.40 | 4.90±5.00 | 2.11 | 4.72±2.38 | 61.97±5.46 | **44.4±2.22** | 43.76±3.29 | 10.89±9.30 | 1.22±0.12 |
| SOL1-05-16 | 0.38 | 2.30 | 1.00 | 11.95±5.00 | 0.80 | 3.61±1.88 | 38.25±3.48 | **21.18±1.06** | 27.27±2.29 | 12.20±9.96 | 0.75±0.11 |
| SOL1-05-17 | 0.20 | 1.30 | 1.30 | 1.70±1.70 | 8.40 | 4.21±2.29 | 32.59±2.02 | **20.00±1.00** | 25.24±1.34 | 6.69±6.21 | 0.63±0.07 |
| SOL1-05-18 | 1.23 | 3.80 | 1.40 | 9.90±5.00 | 4.85 | 4.45±2.24 | 100.48±9.72 | **64.46±3.22** | 56.69±4.68 | 8.71±7.93 | 1.78±0.14 |
| SOL1-05-21 | 0.23 | 0.70 | 1.90 | 0.21±0.20 | 0.00 | 4.68±2.65 | 41.47±2.49 | **34.53±1.73** | 30.32±1.59 | 23.24±5.55 | 1.04±0.07 |
| DES08-22 | 0.05 | 0.30 | 1.10 | 3.01±3.00 | 8.40 | 3.66±2.12 | 17.16±1.35 | -- | **14.55±1.05** | 6.69±6.28 | 0.42±0.07 |
| DES08-24 | 0.05 | 0.20 | 0.90 | 3.40±3.00 | 9.20 | 3.43±3.03 | 14.50±1.12 | -- | **11.86±0.86** | 6.33±5.69 | 0.36±0.06 |
| DES08-31 | 1.44 | 4.80 | 2.10 | 6.91±5.00 | 5.40 | 5.52±2.80 | 128.07±12.01 | **61.75±3.09** | 75.12±5.86 | 8.34±7.71 | 2.04±0.16 |
| DES08-32 | 0.99 | 4.50 | 2.50 | 14.70±5.00 | 6.00 | 5.10±2.63 | 92.05±8.61 | -- | **61.58±5.44** | 7.97±7.21 | 1.67±0.13 |
| DES08-33 | 1.44 | 4.80 | 3.30 | 12.14±5.00 | 6.30 | 6.00±3.22 | 131.98±12.34 | **57.91±2.90** | 82.10±6.98 | 7.79±7.28 | 2.04±0.16 |
| DES08-34 | 1.20 | 4.90 | 2.30 | 10.57±5.00 | 6.80 | 5.39±2.75 | 109.66±10.22 | **55.76±2.79** | 69.23±5.70 | 7.51±7.07 | 1.78±0.14 |
| DES08-35 | 0.73 | 4.60 | 2.20 | 9.59±5.00 | 7.05 | 5.32±2.71 | 79.29±7.07 | **47.26±2.36** | 57.55±4.67 | 7.37±6.98 | 1.39±0.11 |

**TABLE 5-24.** Final ages for all samples for each measurement type.

| Sample | Multigrain Age (ka) | Single Grain Age (ka) | | Modelled Age (ka) |
|---|---|---|---|---|
| | | ***CAM*** | ***FMM*** | |
| DES08-21 | -- | 88.0 ± 12.6 | 102.7 ± 15.4 | -- |
| DES08-22 | 113.9 ± 26.2 | -- | -- | 116.4 ± 9.0 |
| DES08-24 | 96.6 ± 17.7 | -- | -- | 112.2 ± 7.5 |
| DES08-31 | 61.1 ± 6.4 | -- | -- | 68.1 ± 4.5 |
| DES08-32 | 78.1 ± 7.3 | 86.3 ± 8.4 | 74.9 ± 7.8 | 84.3 ± 5.7 |
| DES08-33 | 71.4 ± 7.8 | -- | -- | 83.1 ± 5.7 |
| DES08-34 | 54.5 ± 5.1 | 56.3 ± 5.2 | 62.1 ± 5.8 | 82.0 ± 5.5 |
| DES08-35 | 79.4 ± 8.6 | -- | -- | 85.3 ± 6.1 |
| SOL1-05-01 | 135.4 ± 20.5 | 112.1 ± 17.4 | 87.6 ± 13.2 | 121.2 ± 9.1 |
| SOL1-05-02 | 103.4 ± 11.8 | 101.3 ± 13.1 | 108.9 ± 14.1 | 112.6 ± 7.1 |
| SOL1-05-03 | 107.9 ± 13.5 | -- | -- | 113.9 ± 7.4 |
| SOL1-05-04 | 142.2 ± 17.3 | 149.6 ± 19.4 | 127.3 ± 15.8 | 122.4 ± 9.8 |
| SOL1-05-05A | 101.2 ± 9.7 | -- | -- | 96.7 ± 6.7 |
| SOL1-05-05B | 105.2 ± 11.7 | 66.3 ± 6.6 | 74.9 ± 7.2 | 97.1 ± 7.3 |
| SOL1-05-06 | 115.7 ± 11.7 | 95.4 ± 11.7 | 78.7 ± 15.7 | 100.3 ± 6.9 |
| SOL1-05-07 | 106.0 ± 12.8 | 80.0 ± 9.4 | 65.1 ± 6.8 | 97.1 ± 7.4 |
| SOL1-05-08 | 72.7 ± 6.0 | -- | -- | 71.9 ± 4.1 |
| SOL1-05-09 | 93.0 ± 9.7 | -- | -- | 74.8 ± 4.6 |
| SOL1-05-10 | 96.4 ± 9.2 | 57.7 ± 5.8 | 57.2 ± 6.5 | 75.4 ± 4.6 |
| SOL1-05-11 | 66.3 ± 5.9 | -- | -- | 69.7 ± 4.3 |
| SOL1-05-12 | 58.3 ± 5.4 | 38.6 ± 4.0 | 28.7 ± 3.1 | 57.3 ± 4.4 |
| SOL1-05-13 | 51.7 ± 5.4 | -- | -- | 53.3 ± 4.9 |
| SOL1-05-14 | 29.6 ± 3.1 | 25.5 ± 2.5 | 23.2 ±3.1 | 29.5 ± 2.4 |
| SOL1-05-15 | 7.7 ± 0.8 | -- | -- | 7.8 ± 0.6 |
| SOL1-05-16 | 6.2 ± 0.9 | 7.3 ± 1.1 | 7.1 ± 1.1 | 6.4 ± 0.7 |
| SOL1-05-17 | 113.0 ± 19.1 | -- | -- | 115.9 ± 8.3 |
| SOL1-05-18 | 68.5 ± 7.2 | -- | -- | 70.5 ± 4.4 |
| SOL1-05-21 | 147.8 ± 19.9 | 110.8 ± 13.8 | 90.2 ± 10.3 | -- |

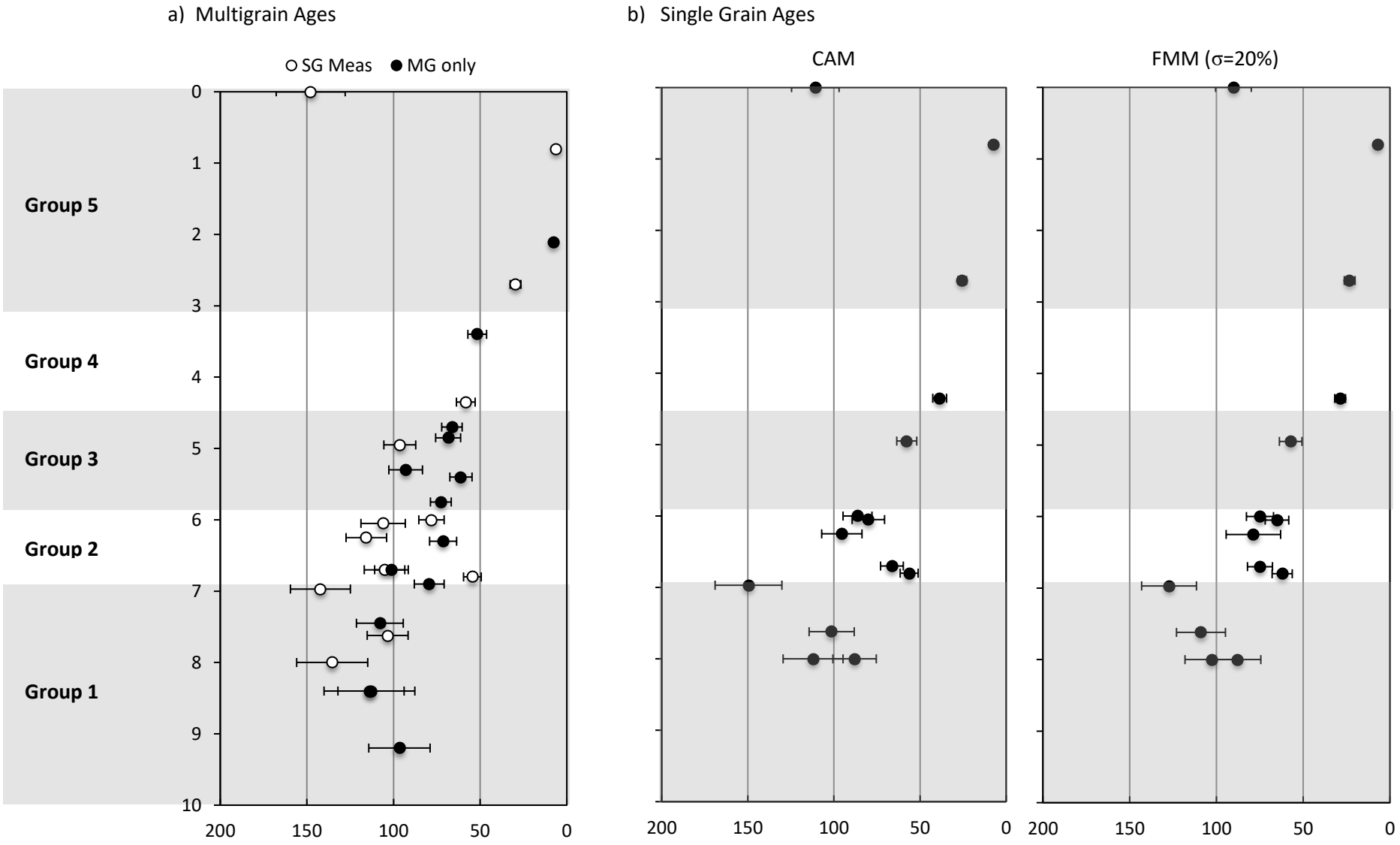


**FIG. 5-43.** Various types of age estimates plotted against depth for comparison. The sample at 0 m depth is the bedrock. Sample SOL1-05-19 (weathering ring) has not been plotted, as it is not a standard infill sample. a) Multigrain aliquot ages, with no IRSL exclusion except for the bedrock sample. Samples for which single grains have also been measured are plotted with white-filled points. b) Single grain age estimates are given based on both CAM and FMM age models.

elemental concentrations are probably not accurately reflecting the variation in sediment composition (particularly for the sand layers), and geometric effects are rendering invalid the usual methods of calculating dose rates (i.e. the infinite matrix approximation, see Guérin et al., 2012). If indeed these are the underlying causes, there is no theoretical reason why single grain data should be preferred over multigrain.

#### *5.2.4.1 Bayesian modeling*

Due to the numerous age-depth reversals, Bayesian modeling of the data was quite difficult. The initial model incorporated multigrain and single grain (CAM) ages and outlier analysis, but it was unsuccessful. Various simplified models were attempted, including multigrain and single grain ages (no outlier analysis) and multigrain ages only, in sequential stratigraphic order. Finally, a simple phase model was built and successfully run (Appendix B). All multigrain ages in each sedimentary Group were entered as a single phase, and the five Group phases were constrained by their stratigraphic order.

The modeled phase boundaries are shown in Fig. 5-46, and modeled OSL ages are listed in Table 5-24. It is apparent that the basal boundary for the cave infill (129.0 ± 12.4 ka) is not well constrained; this is due to the scatter in the Group 1 ages and the lack of stratigraphically lower data. Group transitions have been modeled at 105.8 ± 7.1 ka, 77.9 ± 4.8 ka, 64.4 ± 5.1 ka, 42.9 ± 5.1 ka, and 42.9.3 ± 8.3 ka. The value of this model is dependent upon the accuracy of the OSL age inputs. Bayesian analysis will not provide accurate ages if the input OSL data is systematically offset. However, this analysis functions as a 'best guess' based on the available OSL and stratigraphic data at this time.

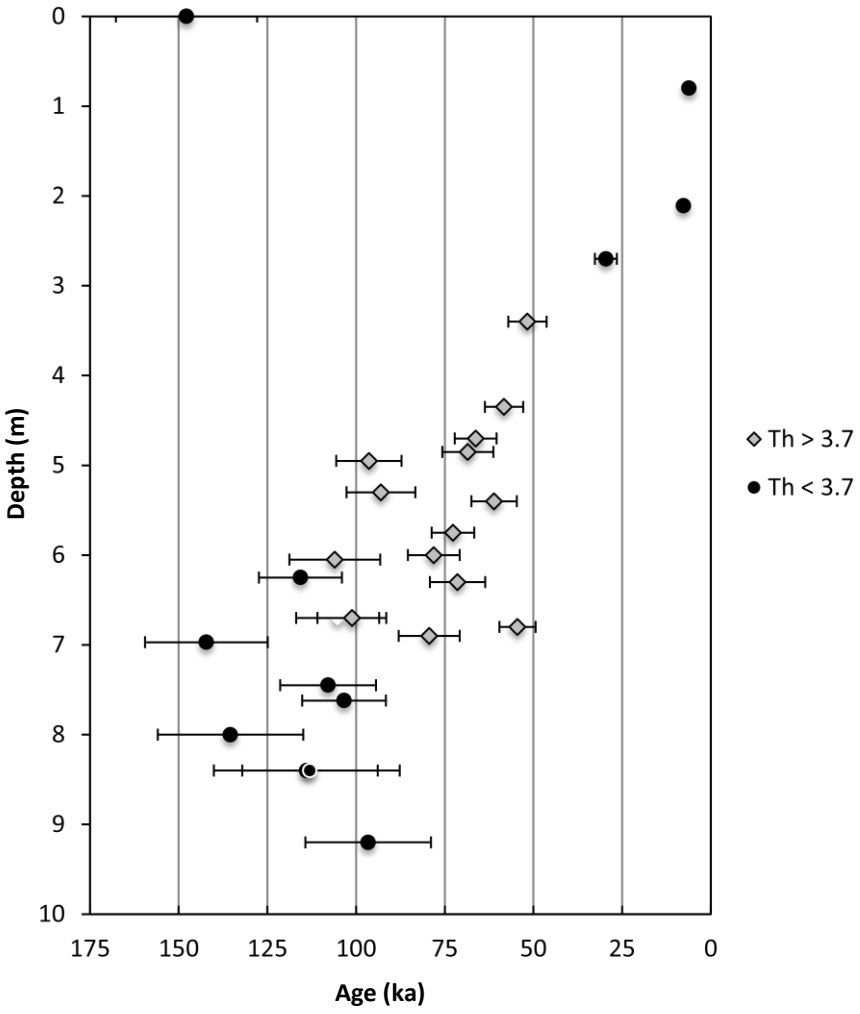


**FIG. 5-44.** Multigrain age estimates as for last figure, with high dose rate samples indicated.

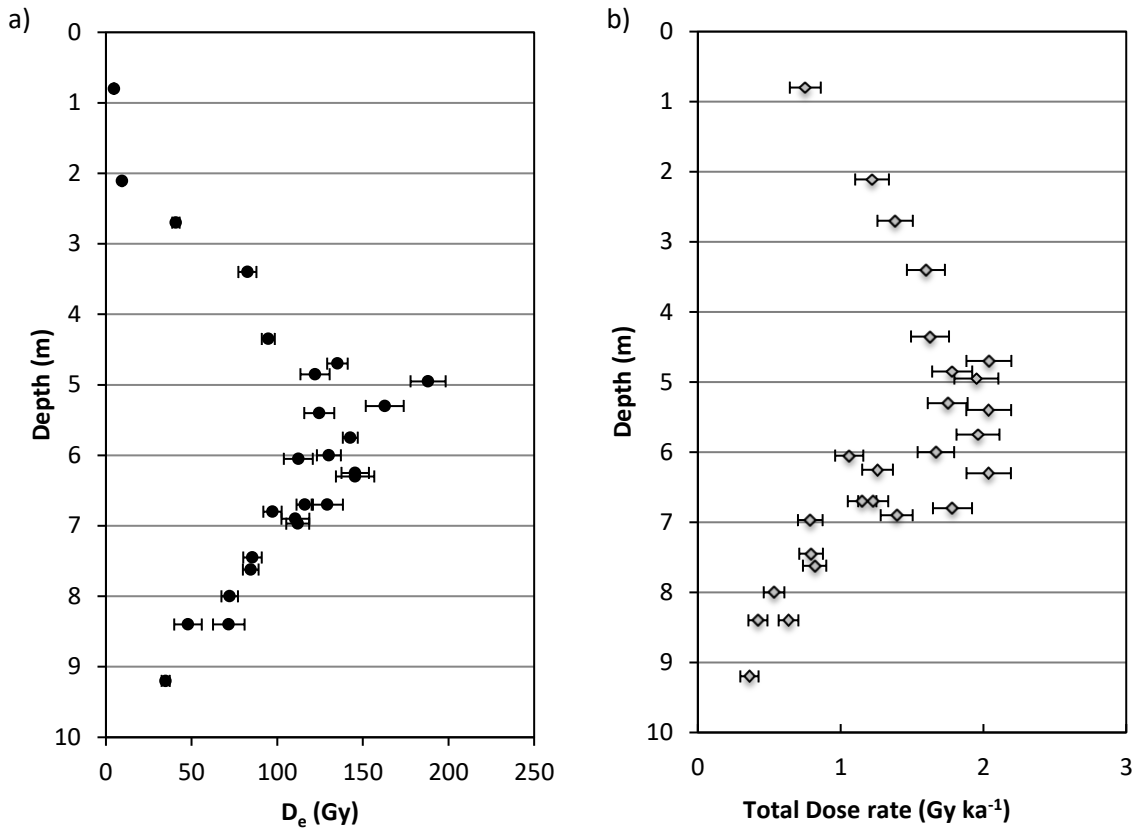


**FIG. 5-45.** Multigrain equivalent dose (a) and wet dose rates (b) plotted versus depth. There seems to be a disconnect between the trends for De and dose rate at ~ 7 m.

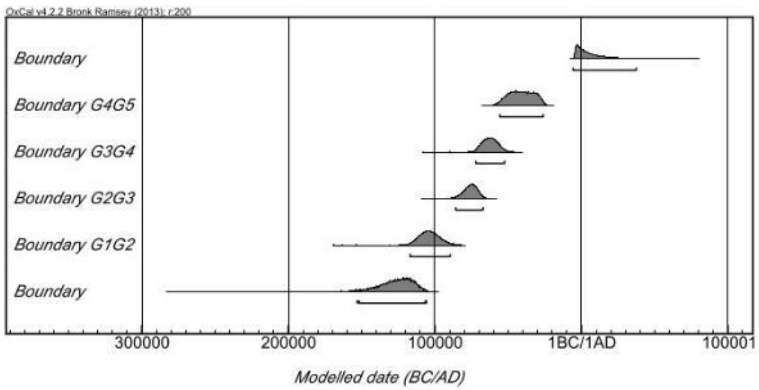


**FIG. 5-46.** Phase boundaries according to Bayesian modelling of multigrain ages (e.g. G1G2 indicates the Group 1/Group 2 boundary). This figure is adapted from that produced by OxCal v4.1.7 (Bronk Ramsey, 2010).

## 5.3 Rhafas

### 5.3.1 Dose recovery and preheat plateau

Due to the very limited amount of material available, a restricted dose recovery experiment was performed for subsample RHA-F-1B. More extensive dose recovery preheat plateau experiments were performed upon two other samples collected from Rhafas cave: RHA-05-01 and RHA-05-02 (see Section 3.2.3).

Six aliquots (1 mm in diameter) were prepared from RHA-F-1B quartz. These were split into two groups of three, and each group was bleached with blue LEDs (300 s at 25°C) prior to irradiation with either 27.3 ± 0.6 Gy or 113.8 ± 2.3 Gy. Each aliquot of one group was then assigned a regenerative dose preheat of 180°C, 220°C , or 260°C. Test dose preheats of 180°C were used. Fig. 5-47 displays the normalized recovered doses, recycling ratios, and zero ratios of these aliquots. Two aliquots were rejected for IR contamination (Table 5-25), but have been plotted on the figure for comparison. All recycling and zero ratios are well within rejection criteria limits. If all aliquots are considered as a single group, the normalized recovered dose of the four accepted aliquots is highly accurate at 1.00 ± 0.05 (σ=6.83 ± 3.83%). Including the two rejected aliquots gives 0.99 ± 0.06 (σ=12.55 ± 4.40%). If given dose and preheat are taken into account, underestimation of given dose may occur for high dose grains. There is not enough data, however, to confirm this possibility.

Preheat plateau test results for samples RHA-05-01 and RHA-05-02 are also shown in Fig 5-47. For each sample, aliquots were bleached with blue LEDs (300 s at 25°C) prior to being given a beta dose of 6.83 ± 0.14 Gy. Regenerative dose preheats of 180°C, 200°C, 220°C, 240°C, 260°C, and 280°C were applied to three or four aliquots per sample, and a test dose preheat of 220°C was used. Aliquots from both samples have been rejected for recycling ratio, zero ratio, and IRSL emission, and 7 of 24 aliquots from RHA-05-02 for dimness-related criteria (Table 5-25). Neither sample displays any notable dependence upon preheat temperature, though the zero ratio of RHA-05-01 may be somewhat preheat dependent. If each sample is treated as a single

**TABLE 5-25.** Rhafas dose recovery experiments: aliquots excluded according to rejection criteria.

a) RHA-F-1B

| | | | | Non-exclusive | | | | | | | | | |
|---|---|---|---|---|---|---|---|---|---|---|---|---|---|
| Preheat (°C); Dose | # Meas. | >3σ | Tx Err. | RR | IR | Zero | Sat. | Super-Sat. | Fit Err. | Neg. $D_e$ | $D_e$ Err. | Not bracket | Accepted |
| 180; 27 Gy | 1 | 0 | 0 | 0 | 1 | 0 | 0 | 0 | 0 | 0 | 0 | 0 | 0 |
| 220; 27 Gy | 1 | 0 | 0 | 0 | 0 | 0 | 0 | 0 | 0 | 0 | 0 | 0 | 1 |
| 260; 27 Gy | 1 | 0 | 0 | 0 | 0 | 0 | 0 | 0 | 0 | 0 | 0 | 0 | 1 |
| 180; 114 Gy | 1 | 0 | 0 | 0 | 0 | 0 | 0 | 0 | 0 | 0 | 0 | 0 | 1 |
| 220; 114 Gy | 1 | 0 | 0 | 0 | 0 | 0 | 0 | 0 | 0 | 0 | 0 | 0 | 1 |
| 260; 114 Gy | 1 | 0 | 0 | 0 | 1 | 0 | 0 | 0 | 0 | 0 | 0 | 0 | 0 |

b) RHA-05-01

| | | | | Non-exclusive | | | | | | | | | |
|---|---|---|---|---|---|---|---|---|---|---|---|---|---|
| Preheat (°C) | # Meas. | >3σ | Tx Err. | RR | IR | Zero | Sat. | Super-Sat. | Fit Err. | Neg. $D_e$ | $D_e$ Err. | Not bracket | Accepted |
| 180 | 4 | 0 | 0 | 2 | 0 | 0 | 0 | 0 | 0 | 0 | 0 | 0 | 2 |
| 200 | 4 | 0 | 0 | 0 | 2 | 0 | 0 | 0 | 0 | 0 | 0 | 0 | 2 |
| 220 | 4 | 0 | 0 | 0 | 0 | 0 | 0 | 0 | 0 | 0 | 0 | 0 | 4 |
| 240 | 4 | 0 | 0 | 1 | 0 | 0 | 0 | 0 | 0 | 0 | 0 | 0 | 3 |
| 260 | 4 | 0 | 0 | 0 | 1 | 0 | 0 | 0 | 0 | 0 | 0 | 0 | 3 |
| 280 | 4 | 0 | 0 | 1 | 0 | 0 | 0 | 0 | 0 | 0 | 0 | 0 | 3 |

c) RHA-05-02

| | | | | Non-exclusive | | | | | | | | | |
|---|---|---|---|---|---|---|---|---|---|---|---|---|---|
| Preheat (°C) | # Meas. | >3σ | Tx Err. | RR | IR | Zero | Sat. | Super-Sat. | Fit Err. | Neg. $D_e$ | $D_e$ Err. | Not bracket | Accepted |
| 180 | 3 | 0 | 0 | 1 | 0 | 0 | 0 | 0 | 0 | 0 | 0 | 0 | 2 |
| 200 | 3 | 2 | 0 | 1 | 0 | 1 | 0 | 0 | 0 | 0 | 0 | 0 | 0 |
| 220 | 3 | 1 | 0 | 0 | 0 | 0 | 0 | 0 | 0 | 0 | 0 | 0 | 2 |
| 240 | 6 | 0 | 0 | 0 | 0 | 0 | 0 | 0 | 0 | 0 | 0 | 0 | 6 |
| 260 | 3 | 1 | 1 | 0 | 0 | 0 | 0 | 0 | 0 | 0 | 0 | 0 | 1 |
| 280 | 3 | 1 | 0 | 1 | 0 | 0 | 0 | 0 | 0 | 0 | 0 | 0 | 1 |

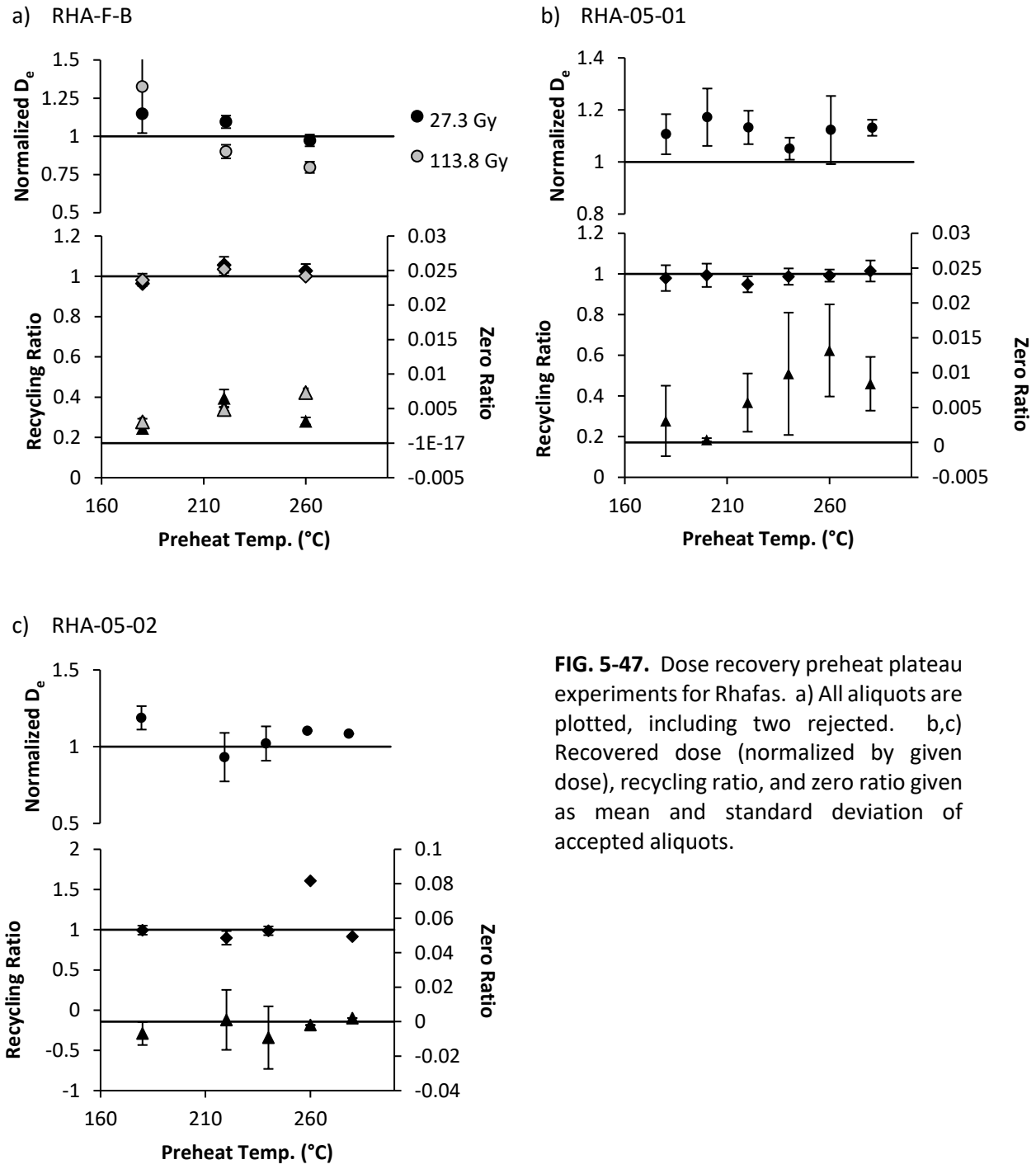


**FIG. 5-47.** Dose recovery preheat plateau experiments for Rhafas. a) All aliquots are plotted, including two rejected. b,c) Recovered dose (normalized by given dose), recycling ratio, and zero ratio given as mean and standard deviation of accepted aliquots.

group, recovered doses are 1.11 ± 0.02 Gy (central age) and 1.06 ± 0.03 Gy (common age) for RHA-05-01 and -02, respectively.

Though not ideal to use other samples from the same site to investigate dose recovery characteristics, this was attempted due to the lack of available sample material for tests. The limited evidence from RHA-F-1, however, suggests that it has better recycling ratio, zero ratio, and dose recovery characteristics than the other tested samples.

### 5.3.2 Equivalent dose estimates

Equivalent dose measurements were carried out on separate subsamples (Fig. 3-34), in order to preserve any bleaching gradient due to sample handling. The results, described below, did not support this hypothesis, so equivalent doses were pooled for age calculations.

#### *5.3.2.1 Multigrain aliquots*

Multigrain aliquots, 1 mm in diameter, were prepared from 90-180 μm grains. Six aliquots each were measured for subsamples B, C, E, and F, and twelve for subsample D. Five of six rejected aliquots were rejected based on recycling ratio; the final aliquot was unbracketed and seems to be saturated (Table 5-26). This is the only measured, saturated aliquot.

Distribution parameters for each of the subsamples tend to be controlled by the presence and extent of a high equivalent dose tail (Table 5-27b, Fig. 5-48a, 5-49a). Minimum equivalent dose values are consistent between subsamples: aliquots overlap (1 σ uncertainty) at ~23-24 Gy for all subsamples but B (slightly higher at ~28 Gy). Maximum dose aliquots vary significantly more in equivalent dose, and this correlates with distribution parameters such as skewness and kurtosis. Subsample D, with the highest dose aliquots, is the only distribution to be highly positively skewed (>1), and it has a similarly high kurtosis value. Other subsamples are much more symmetric (e.g. C, E, and F).

#### *5.3.2.2 Single grain*

Etched single grains were measured from subsamples B, C, D, and E, and unetched grains from subsample A. Subsamples B,C,D, and E are discussed first. Due to the lack of

mineral grains in the correct size fraction, standard single grain discs were not appropriate. Instead, single grains were mounted to standard multigrain aluminum discs and then measured as normal. For this analysis, the smallest grains were chosen from the 255-355 μm size fraction, and are estimated to be between 250 and 300 μm. The median natural signal was ~380 a.u., though individual grains were as much as 3000 times brighter (Fig. 5-50). Approximately half of grains generated a dose response curve, and only 4 grains were rejected for saturation or because they were unbracketed (Table 5-26b).

Single grain equivalent dose distributions are highly positively skewed for subsamples B and C (Table 5-27b). Minimum age model results ($\sigma$=20%) are similar, ranging from ~12 Gy to ~23 Gy, while central age values are influenced by the presence of high dose grains and therefore more disparate. High equivalent dose grains (i.e. >100 Gy) were detected in subsamples B,C, and E. They are probably present in D, as well, though more measurements would be necessary to confirm this.

The measurement of unetched large single grains from subsample A was intended as a quick and rudimentary test of the hypothesis that a bleaching gradient might be detected. Grains had dark coats, probably iron oxide, which was likely the cause of the high rejection rate (18 of 20 grains) for low signal and high test dose error (Table 5-26b). Two grains with valid dose response curves yielded equivalent dose values of 10.7 ± 1.2 Gy and >60 Gy (linear extrapolation).

#### *5.3.2.3 Age models and causes of overdispersion*

Based on the measured multigrain and single grain distributions, the subsampled grain populations are indistinguishable. For final age estimates, then, all multigrain and single grain measurements were pooled. Multigrain aliquots range from ~23 Gy to more than 200 Gy, with minimum age and central age values of 28.6 ± 1.8 Gy ($\sigma$=20%) and 41.2 ± 3.7 Gy. Overdispersion is high at 49.90 ± 6.41%.

**TABLE 5-26.** Rhafas multigrain aliquots excluded according to rejection criteria (by subsample).

b) Multigrain

| | | | | Non-exclusive | | | | | | | | | |
|---|---|---|---|---|---|---|---|---|---|---|---|---|---|
| **Sample** | **# Meas.** | **>3σ** | **Tx Err.** | **RR** | **IR** | **Zero** | **Sat.** | **Super-Sat.** | **Fit Err.** | **Neg. $D_e$** | **$D_e$ Err.** | **Not bracket** | **Accepted** |
| RHA-F-B | 6 | 0 | 0 | 0 | 0 | 0 | 0 | 0 | 0 | 0 | 0 | 0 | 6 |
| RHA-F-C | 6 | 0 | 0 | 0 | 0 | 0 | 0 | 0 | 0 | 0 | 0 | 0 | 6 |
| RHA-F-D | 12 | 0 | 0 | 3 | 0 | 0 | 0 | 0 | 0 | 0 | 0 | 1 | 5 |
| RHA-F-E | 6 | 0 | 0 | 0 | 0 | 0 | 0 | 0 | 0 | 0 | 0 | 0 | 6 |
| RHA-F-F | 6 | 0 | 0 | 1 | 0 | 0 | 0 | 0 | 0 | 0 | 0 | 0 | 5 |

a) Single Grain

| | | | | Non-exclusive | | | | | | | | |
|---|---|---|---|---|---|---|---|---|---|---|---|---|
| **Sample** | **Meas. (#)** | **>3σ** | **Tx Err.** | **RR** | **Zero** | **Sat.** | **Super-Sat.** | **Fit Err.** | **Neg. $D_e$** | **$D_e$ Err.** | **Not bracket** | **Accepted (#)** |
| RHA-F-A | 20 | 16 | 2 | 0 | 0 | 0 | 0 | 1 | 0 | 0 | 0 | 1 |
| RHA-F-B | 25 | 14 | 0 | 2 | 1 | 0 | 0 | 0 | 0 | 0 | 0 | 8 |
| RHA-F-C | 20 | 10 | 2 | 0 | 0 | 0 | 0 | 0 | 0 | 0 | 1 | 7 |
| RHA-F-D | 20 | 8 | 2 | 0 | 1 | 1 | 1 | 0 | 0 | 0 | 0 | 6 |
| RHA-F-E | 20 | 10 | 1 | 0 | 0 | 0 | 0 | 0 | 0 | 0 | 1 | 7 |

**TABLE 5-27.** Distribution parameters by subsample. As only 2 single grains were accepted for RHA-F-A, it has been excluded from table (b).

a) Multigrain

| **Sample** | **Overdisp. (%)** | **Skewness** | **Kurtosis** | **CAM $D_e$ (Gy)** | **MAM $D_e$ (Gy; σ=20%)** |
|---|---|---|---|---|---|
| RHA-F-B | 49.63 ± 14.49 | 1.39 | 1.39 | 46.5 ± 9.5 | 29.9 ± 4.0 |
| RHA-F-C | 22.68 ± 6.75 | -0.32 | -0.32 | 31.3 ± 2.9 | 28.0 ± 2.5 |
| RHA-F-D | 62.64 ± 15.83 | 2.62 | 2.62 | 47.0 ± 10.5 | 23.1 ± 3.9 |
| RHA-F-E | 51.27 ± 14.95 | 0.62 | 0.62 | 43.8 ± 9.2 | 26.3 ± 4.0 |
| RHA-F-F | 31.95 ± 10.32 | 1.24 | 1.24 | 37.7 ± 5.4 | 30.2 ± 3.9 |

b) Single Grain

| **Sample** | **Overdisp. (%)** | **Skewness** | **Kurtosis** | **CAM $D_e$ (Gy)** | **MAM $D_e$ (Gy; σ=20%)** |
|---|---|---|---|---|---|
| RHA-F-B | 119.88 ± 30.21 | 1.96 | 3.71 | 63.0 ± 26.79 | 16.3 ± 2.9 |
| RHA-F-C | 39.23 ± 11.03 | 1.34 | 0.74 | 30.3 ± 4.60 | 23.3 ± 2.7 |
| RHA-F-D | 22.20 ± 7.32 | -0.03 | -1.49 | 13.3 ± 1.29 | 12.0 ± 1.1 |
| RHA-F-E | 96.56 ± 26.05 | 1.44 | 0.70 | 35.5 ± 13.02 | 16.9 ± 2.0 |

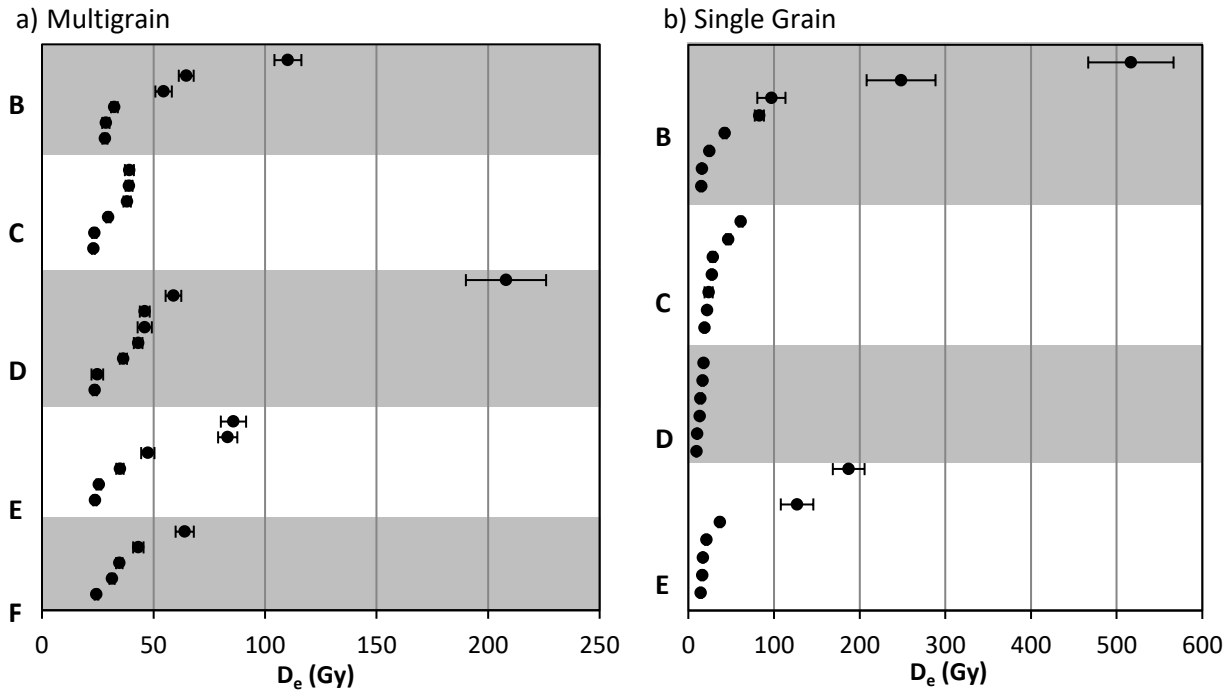


**FIG. 5-48.** Ranked multigrain (a) and single grain results (b) ordered by subsample.

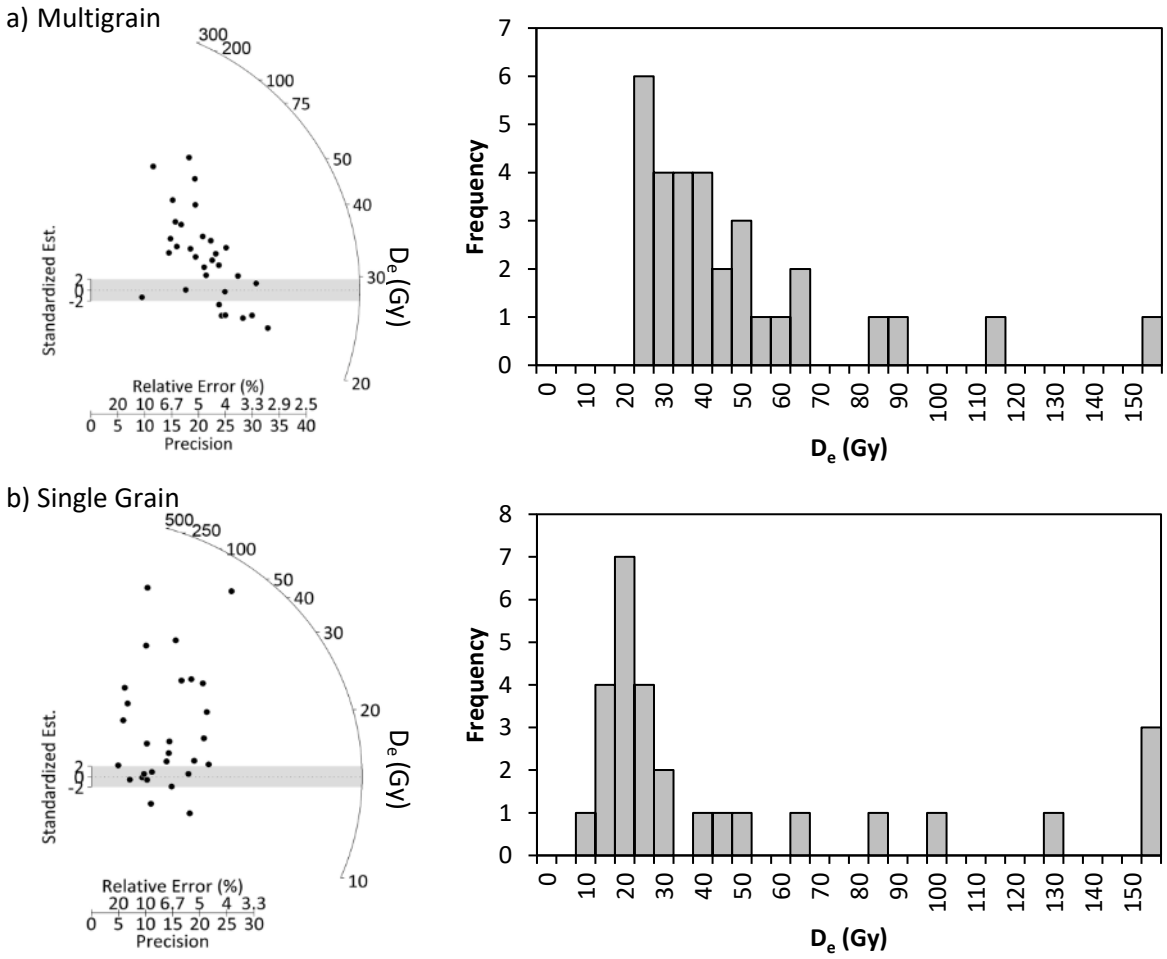


**FIG. 5-49.** Radial plots and histograms for pooled multigrain (a) and single grain results (b). The equivalent dose indicated on each radial plot is the minimum age model value (σ=20%).

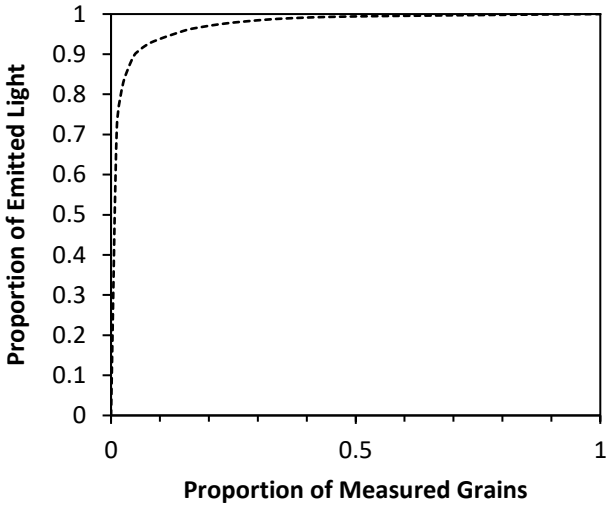


**FIG. 5-50.** Light sum for pooled single grains (natural signal, no background subtraction).

**TABLE 5-28.** Finite mixture model calculations for pooled single grains, σ=20% and 30%. a) LLIK values and accepted model (highlighted). Dose components of the accepted model and dominant component (highlighted) for σ=20% (b) and σ=20% (c).

a)

| *k* | σ=0.2 | σ=0.3 |
|---|---|---|
| **2** | -72.0 | -43.9 |
| **3** | -42.0 | -33.8 |
| **4** | -35.9 | -32.0 |
| **5** | -32.4 | --- |
| **6** | NAN | --- |

b) σ=20%

| | Comp. 1 | Comp. 2 | Comp. 3 | Comp. 4 | Comp. 5 |
|---|---|---|---|---|---|
| **$D_e$** | 16.19 ± 1.16 | 34.50 ± 5.19 | 80.19 ± 15.09 | 189.89 ± 41.81 | 513.06 ± 117.95 |
| **% grains** | 55.31 | 19.71 | 12.28 | 9.08 | 3.62 |

c) σ=30%

| | Comp. 1 | Comp. 2 | Comp. 3 |
|---|---|---|---|
| **$D_e$** | 17.79 ± 1.47 | 63.30 ± 11.46 | 273.85 ± 64.93 |
| **% grains** | 66.16 | 22.25 | 11.59 |

Single grains span a much wider range, from ~9 Gy to more than 500 Gy. Minimum age and central age values are 15.3 ± 1.1 ($\sigma$ =20%) and 32.5 ± 6.1 Gy, respectively. The calculated overdispersion is unusually high: 99.28 ± 0.13%. If the FMM model is applied (Table 5-28), the number of components varies depending on assigned overdispersion but the dominant component is ~16-17 Gy for both models. The highest dose component depends strongly on assigned overdispersion, calculated as ~500 Gy for $\sigma$ =20% but only ~270 Gy for $\sigma$ =30%.

Due to the unusual nature of this sample, determining the most appropriate age model is difficult. The overdispersion and range of the equivalent dose distribution indicate that some combination of partial bleaching, mixing, and microdosimetric effects is present. Beta-microdosimetry is certainly a factor, as the measured grains have been contained within bone. For grains next to the interior surface of the bone, the effective beta dose will have been approximately halved, assuming no uranium uptake (see next section). This effect, however, is not large enough to explain the full range of equivalent doses, and the low dose component would not be dominant if this were the only factor (based on geometrical considerations).

Partial bleaching or mixing could have occurred during post-excavation handling, but it is more likely to have occurred prior to excavation. At the time of sampling, the sediment was consolidated within the bone. Therefore it is unlikely to have been mixed with bleached sediment during post-excavation cleaning. There is also no bleaching gradient, which might support the case for such disturbance. It is possible that the bone fragment was filled with partially bleached sediment after excavation and before discovery, however, this seems unlikely to produce a consolidated core. On the other hand, it is quite possible for sediment mixing to have occurred during the bone's history, due to faunal burrowing or cycles of use and reburial.

Based on these considerations, a single age cannot be suggested at this time. Instead, a range of ages must be considered. The FMM dose components ($\sigma$=20%) will be used for this purpose as they provide a statistical measure of equivalent dose range and dominance, though it is unlikely the components reflect actual mixed populations.

### 5.3.3 Dosimetry

Dose rate calculation is also problematic. This section presents the atypical dose rate effects caused by the nature of the sample, summarizes beta and gamma dose rates calculated via a Monte Carlo model, then closes with a discussion of cosmic ray dose rate in light of the uncertainty as to the sample's burial location.

#### *5.3.3.1 Complications*

The primary complication in dose rate determination is due to the presence of bone in the sedimentary matrix. The infinite matrix assumption is no longer valid, therefore the standard, simple calculations of absorbed dose and dose attenuation cannot be used. In the simplest scenario, the substitution of carbonated hydroxyapatite for sediment shields some of the sediment within the bone, as the bone both displaces the sedimentary radioisotopes and increases radiation attenuation. It is also possible that the bone itself may serve as a source of radioisotopes, since bone is an open system and may absorb uranium from ground water. It is impossible to predict the net result of all effects for a general case: the shielding and bone-generated dose rate may tend to cancel each other out or one or the other may be dominant (Grün et al., 2005; Blackwell and Blickstein, 2000; Nathan and Grün, 2003).

Bone geometry results in variable beta dose rates to grains situated differently with respect to the interior of the bone. These geometric effects will be lowest for grains from the center of the femur cavity, and highest for any grains collected from the large pores of trabecular bone within the femur. Due to its longer range, gamma radiation is significantly more homogeneous across the sediment volume.

Two unusual sources of ionizing dose are insignificant and have therefore been disregarded in this analysis. The presence and decay of $^{14}C$ in the bone will add a small dose, but the deposited energy is negligible in comparison with standard sedimentary sources (R. Nathan, pers. comm.). Similarly, X-radiography of the femur will add only a few tenths of a milligray to the absorbed dose (Teeuwisse et al., 2007).

#### *5.3.3.2 Sample parameters*

Water content at the cave has not been reported by Mercier et al. (2007) for their samples, therefore the values was estimated as: 10.00 ± 3.85 %. This should account for periods of higher humidity, recognizable in the frequent carbonate deposits. The error was made as large as possible based on model constraints regarding error calculation.

The find location of the bone is unknown, so the cosmic dose rate was chosen to cover the range of possibilities. It is assumed that the original burial location is within the cave, based on discussions with site archaeologists. Dimensions of Rhafas cave were estimated from the author's photographs, online images, and the information given in Mercier et al. (2007). Minimum and maximum cosmic ray dose rates were estimated by assuming either the bone was a surface find at the cave entrance or it was buried under ~ 4 m of sediment at the maximum cave extent of 15 m (Mercier et al., 2007). The final cosmic ray dose was calculated by averaging these values and enlarging the error to span the calculated range: 37.65 ± 4.05 mGy $ka^{-1}$.

The uranium concentration in the bone fragment has not been measured. Depending on the age and environment of the bone, possible concentrations vary from < 1 ppm to > 20 ppm (Millard and Hedges, 1995; Blackwell and Blickstein, 2000). The current concentration of uranium in the sediment does not serve as an upper bound.

#### *5.3.3.3 Calculated dose rate*

Dose rates have been calculated for both the multigrain and single grain size fractions; the smaller multigrain crystals receive dose rates 1.1% higher than the larger single grains. Figure 5-51 shows the geometric effects of bone on beta and gamma dose rates calculated for the sediment core ($U_{bone}$ = 0 ppm). Variation due to model uncertainty is evident, however, no significant edge effects are apparent at this resolution. When all voxels are considered, though, the effect of the bone is apparent. Histograms of the total dose rate received by voxels per subsample vary depending on the particular geometry of the bone in that location, and the

distribution for the whole sediment core is negatively skewed (-1.17) due to bone shielding (Fig. 5-52).

Uranium content of the bone significantly affects the calculated dose rate. The minimum possible dose rate (i.e. $U_{bone}$ = 0 ppm) is 1.92 ± 0.05 Gy $ka^{-1}$. For bone with 15 ppm of Uranium, the dose rate is nearly 2.5 times higher: 4.76 ± 0.12 Gy $ka^{-1}$. In reality, this is an overestimate, though, due to the approximations made in this model. Uranium uptake in the bone was modeled as instantaneous at the moment of burial ('early uptake'). If uranium was absorbed more slowly, then this model will overestimate the dose rate due to the modern uranium concentration in the bone. Secular equilibrium was also assumed, which is not possible over the time scales involved (Blackwell and Blickstein, 2000); this means that any dose rate from the bone calculated assuming a certain U concentration will be an overestimate. With the available information, though, it is not possible to constrain such factors further.

### 5.3.4 Age estimates

If the dominant component of the single grain FMM model ($\sigma$ = 20%) is chosen for the age equation, the maximum possible age for the sediment core is 8.43 ± 0.64 ka. Depending on the uranium content, it could be significantly younger. Other dose components yield possible ages up to a maximum of 267.22 ± 61.80 ka for the highest dose, smallest component. Without further evidence, it is most parsimonious to suggest that the sediment within the bone is likely to be younger than ~8.5 ka.

It should be emphasized, however, that this technique suggests an age for the last burial of the bone, rather than for the bone itself. Final judgements on the significance of this fragment in the study of early modern *Homo sapiens* must therefore rely on anatomical analysis, further excavation, and perhaps the application of another dating technique such as U-series.

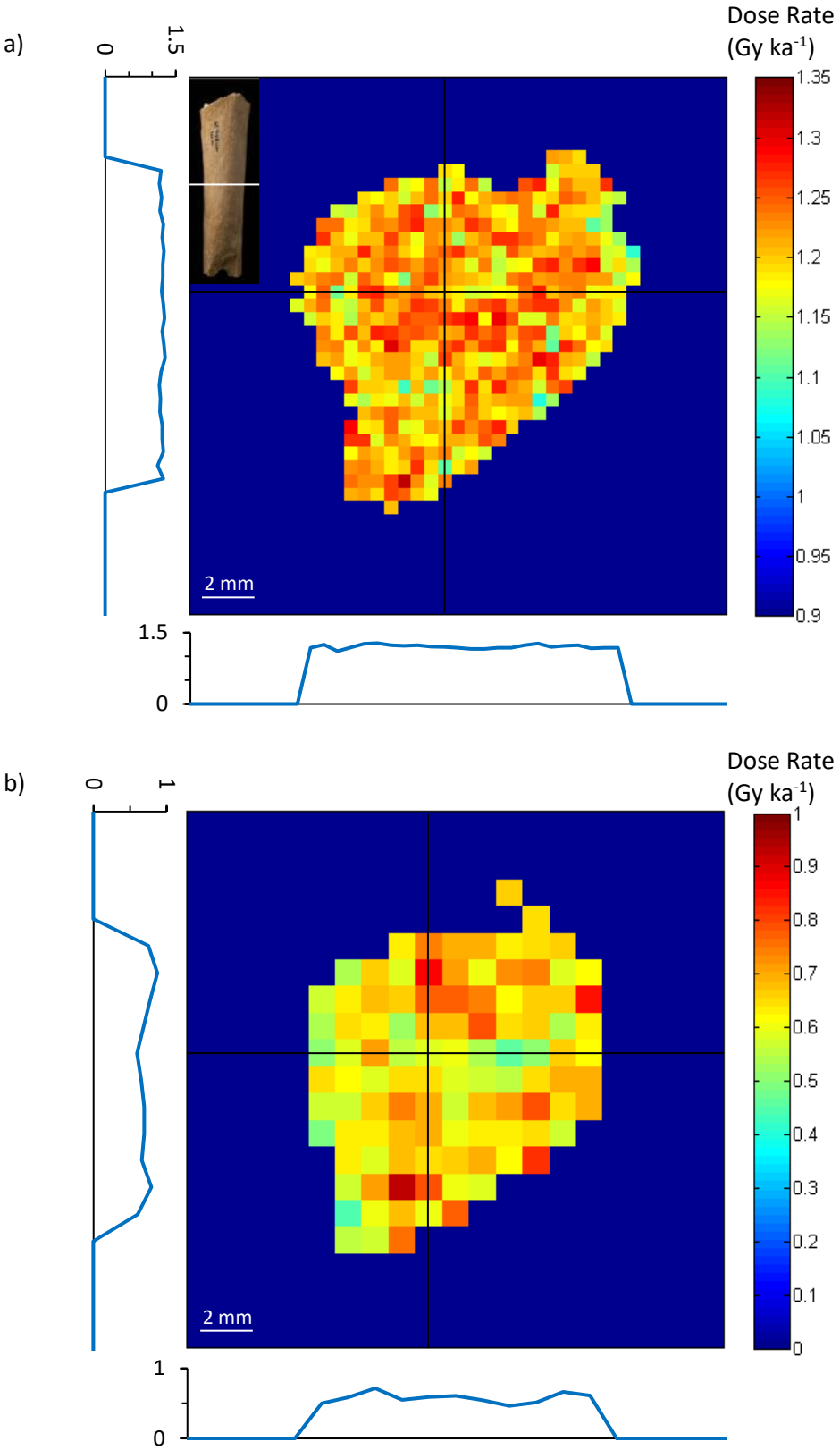


**FIG. 5-51.** Cross-section of modelled beta (a) and gamma (b) dose rates for sediment (135.0 ± 67.5 µm grains) at midpoint of bone ($U_{bone}$ = 0 ppm). The gamma dose rate model is lower resolution due to the larger range of gamma rays. Vertical and horizontal dose rate profiles (Gy ka$^{-1}$) are also displayed. Edge effects for beta and gamma dose rates are already insignificant at this resolution, though random variability due to the simulation is present.

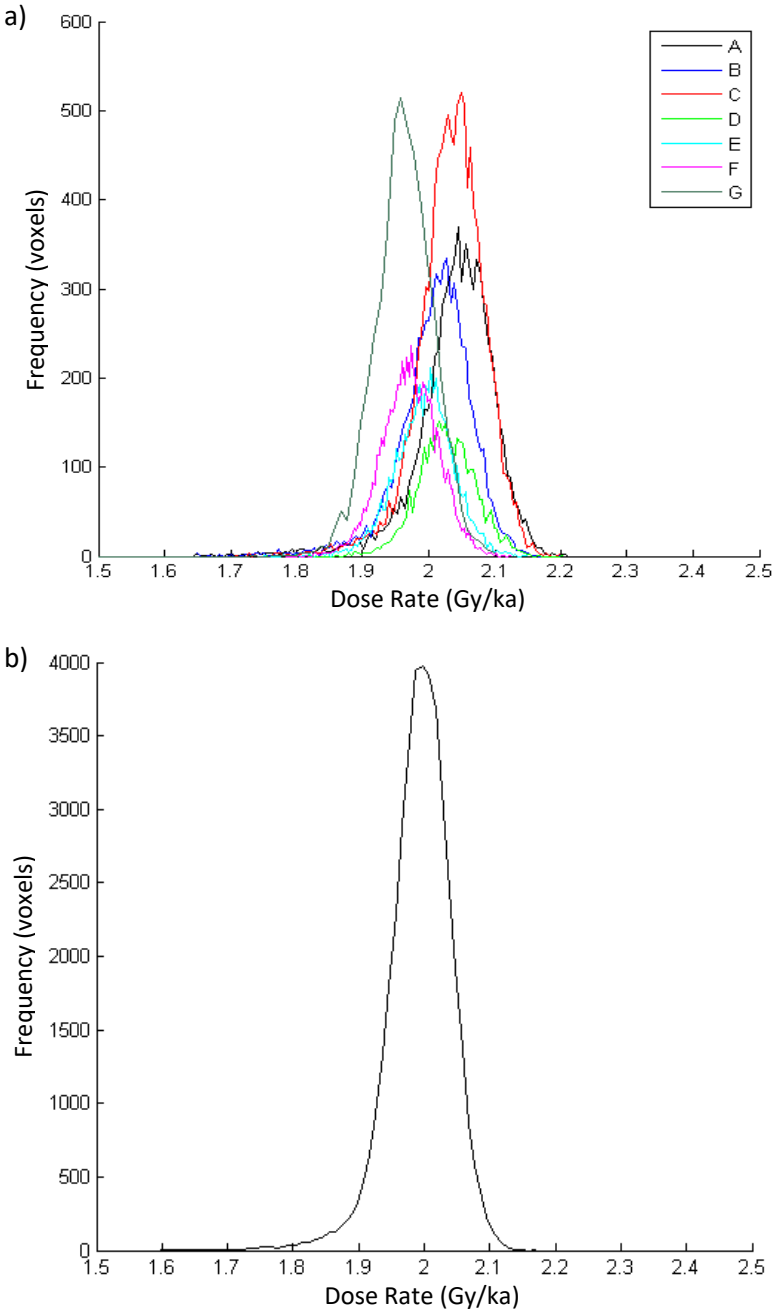


**FIG. 5-52.** Modelled total dose rate distributions (Gy $ka^{-1}$; $U_{bone}$ = 0 ppm): a) Sediment subsamples. The volume attributed to each subsample is approximate. b) Total sediment core: the outer boundaries of the sediment have been validated by CT scanning.

## 5.4 Chaperon Rouge II

Redating of Chaperon Rouge sample 724 b1 involved measurement of 24 multigrain aliquots, 500 single grains, and a single grain dose recovery experiment on 198 grains. Previous measurement details (Rhodes, 1990) are given in Appendix C.

### 5.4.1 Dose recovery

Two single grain discs (212-255 μm grains) were bleached for 300 s with blue LEDs at 25°C, and given a dose of 33.3 ± 0.7 Gy. Fifty-two grains were accepted (Table 5-29), and recovered doses from these grains are shown in Fig. 5-53. By all measures of the population's central tendency, the recovered dose is indistinguishable from the given dose at 1 sigma. The normalized average recovered dose is 0.99, with a standard deviation of 0.18, and the central age model yields 0.98 ± 0.02 (σ=11.7 ± 2.1%). Approximately 40% of measured grains have central estimates within 10% of the given dose, and 80.77% of accepted grains are within 2 sigma of the given dose. The dose recovery results suggest full confidence in the SAR characteristics of the measured grains.

### 5.4.2 Equivalent dose estimates

#### *5.4.2.1 Multigrain results*

Multigrain equivalent dose measurements were performed on aliquots of three different diameters (1-2 mm, 4 mm, and 8 mm, referred to as small, medium, and large). Assuming a hexagonal packing efficiency of 0.9069 for 180-255 μm grains on the surface of a sample disc, such measurements comprise approximately 40, 300, and 1200 grains, respectively. Twelve aliquots of the smallest size, and six each of the medium and large sizes were measured. Medium and large aliquots were irradiated using a Risø TL/OSL-DA-15 reader with low beta source heterogeneity.

Table 5-30 summarizes the numbers of aliquots rejected and the mean rejection values of accepted aliquots. Most aliquots passed SAR behavior characteristics with ease; only one aliquot of 24 was rejected due to recycling ratio. IRSL response seems to be correlated with

**TABLE 5-29.** Rejection criteria for single grain dose recovery.

| | | | | Non-exclusive | | | | | | | |
|---|---|---|---|---|---|---|---|---|---|---|---|
| **Sample** | **Meas. (#)** | **>3σ** | **Tx Err.** | **RR** | **Zero** | **Sat.** | **Super-Sat.** | **Fit Err.** | **Neg. $D_e$** | **$D_e$ Err.** | **Accepted (#)** |
| 724 b1 | 198 | 66 | 25 | 21 | 10 | 5 | 2 | 0 | 1 | 19 | 52 |

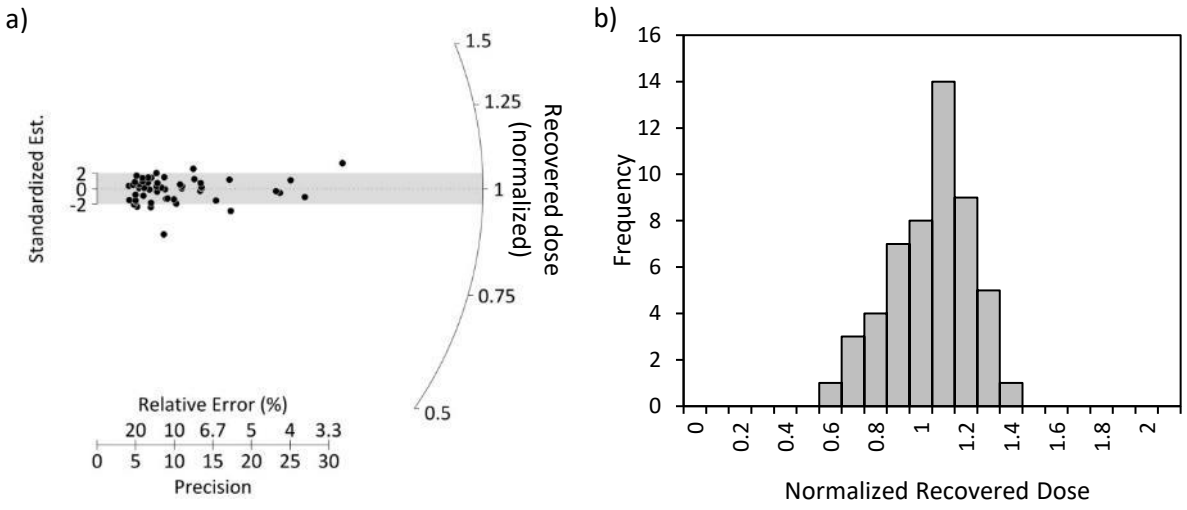


**FIG. 5-53.** Radial plot (a) and histogram (b) of recovered single grain equivalent doses. Recovered doses have been normalized by the given dose.

**TABLE 5-30.** Multigrain aliquots of 724 b1 excluded according to rejection criteria.

| | | | | Non-exclusive | | | | | | | | | |
|---|---|---|---|---|---|---|---|---|---|---|---|---|---|
| **Aliquot Size (mm)** | **# Meas.** | **>3σ** | **Tx Err.** | **RR** | **IR** | **Zero** | **Sat.** | **Super-Sat.** | **Fit Err.** | **Neg. $D_e$** | **$D_e$ Err.** | **Not bracket** | **Accepted** |
| 1-2 | 12 | 0 | 0 | 1 | 0 | 0 | 0 | 0 | 0 | 0 | 0 | 0 | 11 |
| 4 | 6 | 0 | 0 | 0 | 2* | 0 | 0 | 0 | 0 | 0 | 0 | 0 | 6 |
| 8 | 6 | 0 | 0 | 0 | 5* | 0 | 0 | 0 | 0 | 0 | 0 | 0 | 6 |

*Low IRSL detected, but aliquots not rejected—see text for details.

**TABLE 5-31.** Distribution parameters for accepted multigrain aliquots by aliquot size.

| **Aliquot Size (mm)** | **Overdispersion (%)** | **Skewness** | **Kurtosis** | **$D_e$ (Gy)** |
|---|---|---|---|---|
| 1-2 | 27.63 ± 6.03 | 1.64 | 3.42 | 30.8 ± 2.6 |
| 4 | 32.96 ± 9.72 | 1.19 | 2.06 | 42.5 ± 5.8 |
| 8 | 17.60 ± 5.50 | 2.14 | 4.73 | 43.2 ± 3.2 |

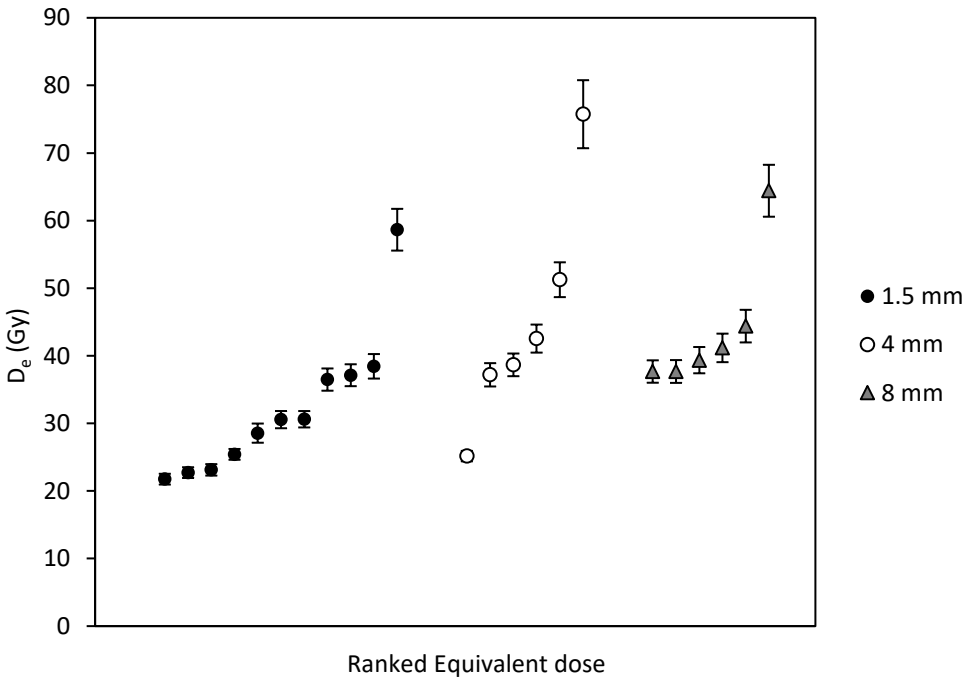


**FIG. 5-54.** Accepted multigrain equivalent doses by aliquot size, rank order.

aliquot size: 0 of 12 small aliquots, 2 of 6 medium aliquots, and 5 of 6 large aliquots were identified as producing a measurable IRSL signal. However, the magnitude of this natural IRSL signal averaged less than 4% of the subsequent OSL signal for the failing aliquots from each sample. Even if the IRSL step does not completely bleach contaminating feldspars, feldspar-based effects on the final equivalent dose should be minimal. Therefore the aliquots with IRSL response were retained in the subsequent analysis.

Results from the three aliquot sizes are shown in Fig. 5-54, and distribution statistics in Table 5-31. All three distributions are positively skewed, with the 8mm discs having the highest value. Population range does not depend in a clear way on aliquot size, as the 4 mm aliquots have a range almost double the ranges of the other two sizes. Given the rise in CAM equivalent dose value with aliquot size, it seems likely that significant equivalent dose heterogeneity exists on the single grain level.

#### *5.4.2.2 Single grain results*

Single grain analysis has been carried out upon 500 grains (212-255 μm), of which 130 were accepted for analysis (Table 5-32). IRSL screening comprised whole disc IR LED stimulation prior to the natural luminescence measurement. No significant IRSL response was detected. Signal emission is in general more evenly distributed amongst grains than other samples presented in this study (Fig. 5-55). Very bright grains do exist, e.g. one that contributed 12.5% of all emitted light. The brightest 10% of grains, however, contribute only 75.9% of the total signal emissions, which is relatively low compared to other samples in this study.

Equivalent doses from the accepted single grains are displayed in the radial plot and histogram shown in Fig. 5-56. Equivalent doses range from 2.5 ± 0.5 to 177.4 ± 41.7 Gy. The central age model returns a value of 21.3 ± 1.4 Gy, and indicates high overdispersion ($\sigma$ = 71.1 ± 4.56%). The 3- component minimum age model is controlled by the small number of very low dose grains: 5.9 ± 0.4 Gy is calculated for $\sigma$=20%, but only 0.7% of grains have this minimum dose. Finally, FMM values reflect the unusually broad equivalent dose distribution, as 5 and 4

components are fit for 20% and 30% overdispersion values, respectively (Table 5-33). Both assigned overdispersion values yield similar minimum, maximum, and peak components. In each case, the dominant peak is significantly lower than the CAM value: 13.6 ± 0.7 (σ=20%) and 15.0 ± 0.9 (σ=30%). A 20% overdispersion was used for age calculations, which seems to be a reasonable value for natural sediment, given the 11.7 ± 2.1% overdispersion measured during the single grain dose recovery.

One super-saturated and six saturated grains were recognized according to this study's criteria, together contributing 2.12% of the total natural emissions. Seven unbracketed grains, including the single brightest grain measured, contributed 14.7% of emissions. Based on visual inspection of dose response curves, most or all of these grains are likely to be saturated or super-saturated. These results suggest that the increase in $D_e$ with multigrain aliquot size is due to a relatively small number of bright, high dose or saturated grains in the sample.

#### *5.4.2.3 Comparison with prior study*

Previous equivalent dose measurements on large multigrain aliquots of this sample yielded an estimate of 46.0 ± 6.0 Gy (Rhodes, 1990). This study has replicated this result via multigrain measurements on 4 mm and 8 mm aliquots, which are indistinguishable at the 1 σ level from each other and the value reported by Rhodes (1990). This reproducibility is reassuring considering differences in measurement protocol between the two studies, namely the earlier normalized multiple aliquot protocol.

However, finer resolution equivalent dose measurement reveals an unexpected complexity in this sample. The single grain and even the smaller (1-2 mm) aliquots show that the measured equivalent dose decreases dramatically when the averaging effect of many hundreds of grains is removed. When faced with a single grain CAM $D_e$ that is less than half of the large multigrain aliquot $D_e$, numerous possibilities for sample heterogeneity must be considered. Partial bleaching of the sample during storage or preparation is unlikely, due to the

success in replicating large aliquot $D_e$ measurements. Similarly, differing grain response to the multiple

**TABLE 5-32.** Sample 724 b1: Single grains (212-255 μm) excluded according to rejection criteria (a) and distribution parameters for accepted grains (b).

a)

| | | | Non-exclusive | | | | | | | | |
|---|---|---|---|---|---|---|---|---|---|---|---|
| **Meas. (#)** | **>3σ** | **Tx Err.** | **RR** | **Zero** | **Sat.** | **Super-Sat.** | **Fit Err.** | **Neg. De** | **De Err.** | **Not bracket** | **Accepted (#)** |
| 500 | 199 | 69 | 37 | 35 | 6 | 1 | 0 | 0 | 26 | 7 | 130 |

b)

| **Overdisp. (%)** | **Skewness** | **Kurtosis** | **CAM De (Gy)** | **MAM De (Gy; σ=20%)** |
|---|---|---|---|---|
| 71.12 ± 4.56 | 3.30 | 17.97 | 21.3 ± 1.4 | 5.9 ±0.4 |

**TABLE 5-33.** Finite mixture model calculations for sample 724 b1, σ=20% and 30%. a) LLIK values and accepted model (highlighted). Dose components of the accepted model and dominant component (highlighted) for σ=20% (b) and σ=20% (c).

a)

| ***k*** | **σ=0.2** | **σ=0.3** |
|---|---|---|
| **2** | -246.9 | -175.5 |
| **3** | -153.2 | -136.0 |
| **4** | -135.3 | -130.1 |
| **5** | -128.7 | -130.1 |
| **6** | -127.8 | --- |

b) σ=20%

| | **Comp. 1** | **Comp. 2** | **Comp. 3** | **Comp. 4** | **Comp. 5** |
|---|---|---|---|---|---|
| **De** | 3.48 ± 0.31 | 13.63 ± 0.74 | 26.07 ± 3.91 | 43.41 ± 4.02 | 114.15 ± 18.49 |
| **% grains** | 5.39 | 38.84 | 28.19 | 25.23 | 2.35 |

c) σ=30%

| | **Comp. 1** | **Comp. 2** | **Comp. 3** | **Comp. 4** |
|---|---|---|---|---|
| **De** | 3.45 ± 0.44 | 15.03 ± 0.86 | 36.13 ± 2.26 | 113.00 ± 28.10 |
| **% grains** | 5.42 | 48.54 | 43.70 | 2.35 |

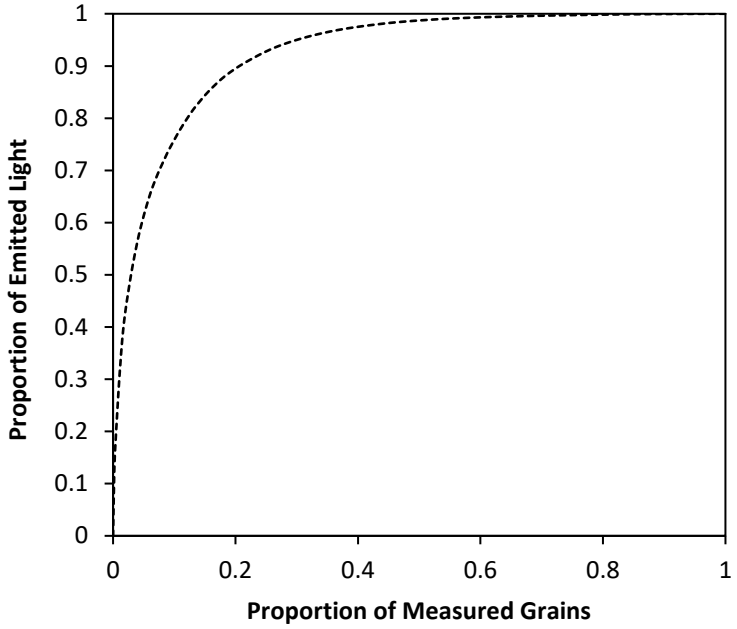


**FIG. 5-55.** Light sum for measured single grains of 724 b1 (natural signal, no background subtraction).

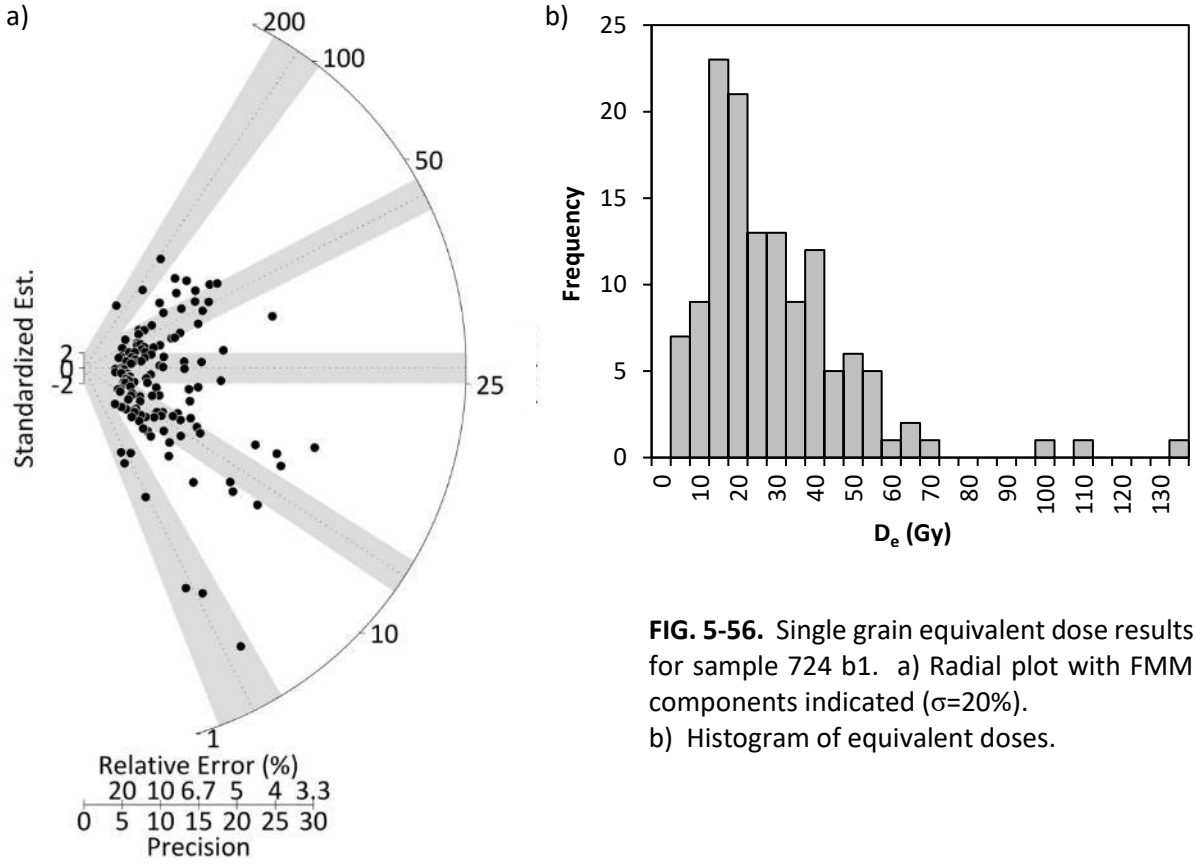


**FIG. 5-56.** Single grain equivalent dose results for sample 724 b1. a) Radial plot with FMM components indicated (σ=20%).
b) Histogram of equivalent doses.

aliquot methods and SAR protocol may be dismissed on several grounds. First, again, is the data replication. In addition, dose recovery experiments returned highly accurate single grain CAM estimates of given dose. It seems likely that the measured heterogeneity may be an accurate reflection of the sedimentary equivalent dose population.

Based on site characteristics, it is most likely that the unexpected equivalent dose distribution is due to bioturbation. Rhodes noted probable scorpion activity in the section, consisting of "D"-shaped burrows up to several centimeters in size (E. Rhodes, pers. comm.). Such activity could easily explain the presence of near modern grains. Partial bleaching can be ruled out because Chaperon Rouge is an open air site with aeolian sediment deposition. Microdosimetry also seems unlikely, based on a number of observations. The sample texture was relatively fine and homogeneous, and the lack of IRSL response from most aliquots indicates that the presence of feldspar 'hot-spots' is low. It is also difficult to suggest how the near-zero equivalent dose grains would have arisen, as there are no carbonate concretions apparent. A very similar dependence of equivalent dose on aliquot size was found for OSL samples collected from the open air site Lagoa do Bordoal (Portugal), and this pattern was likewise attributed to the effects of bioturbation (Forrest et al., 2003).

### 5.4.3 Age estimate

Given the problems outline in the previous section, it is difficult to suggest a final age for the sample. It is clear, however, that the single grain data must be regarded as more accurate than the multigrain. Therefore suggested ages are based on single grain-derived equivalent doses.

Accepting the dose rate of 1.12 ± 0.08 Gy $ka^{-1}$ calculated by Rhodes (1990), the CAM equivalent dose yields an age of 19.0 ± 1.8 ka. If, however, bioturbation is the main cause of the resulting distribution, then the oldest component derived by the FMM may be the best estimate. Based on the 20% sigma FMM results, the age becomes 101.9 ± 18.1 ka. This age is more than twice as old as that suggested previously, 41.1 ± 6.1 ka (Rhodes, 1990). Archaeologically, it is

plausible, yet this estimate must be regarded with caution due to the equivalent dose distribution characteristics. Further field work will be necessary to obtain a more accurate result.